Automatic regularization of finite element simulations of plasticity at finite strains

Mohamed Abatour

To cite this version:

Mohamed Abatour. Automatic regularization of finite element simulations of plasticity at finite strains. Mechanics [physics]. Université Paris sciences et lettres, 2022. English. NNT : 2022UPSLM085 . tel-04199280

HAL Id: tel-04199280
https://pastel.hal.science/tel-04199280

Submitted on 7 Sep 2023

PSL
UNIVERSITÉ PARIS

THÈSE DE DOCTORAT
DE L'UNIVERSITÉ PSL

Préparée à MINES Paris

Régularisation automatique des simulations par éléments finis de la plasticité en grandes déformations

Automatic regularization of finite element simulations of elastoplasticity at finite strains

Soutenue par
Mohamed ABATOUR
Le 16 novembre 2022

École doctorale n°621
Ingénierie des Systèmes, Matériaux, Mécanique, Energétique

Spécialité
Mécanique

Composition du jury :

Carl LABERGÈRE Professeur des universités, Université de technologie de Troyes	*Président*
Leong HIEN POH Professeur, National University of Singapore	*Rapporteur*
Stephan WULFINGHOFF Professeur, Université Christian-Albrecht de Kiel	*Rapporteur*
Mohamed JEBAHI Maître de conférences, Arts et Métiers ParisTech	*Examinateur*
Julia MERGHEIM Professeure, Université Friedrich-Alexander d'Erlangen-Nuremberg	*Examinateur*
Samuel FOREST Directeur de recherche, Mines Paris, CNRS	*Directeur de thèse*
Kais AMMAR Ingénieur de recherche, ARMINES	*Examinateur*
Nikolay OSIPOV Ingénieur, TRANSVALOR SA.	*Examinateur*

MINES PARIS | PSL

This thesis is dedicated to my family !

To my mother and my father !
To my brothers Rachid, Hicham, Mohcine, Nour-addine and Otman !

Acknowledgements

ⵏⴽⴽ ⴷ ⴰⵙⵏⴰⵎⵎⴰⵔ ⵉ ⴱⴱⴰ ⴷ ⵎⵎⴰ ⵅⴼ ⵡⴰⵏⵏⴰⵍ ⵏⵏⵓⵏ ⴷ ⵜⵥⵉⴹⵕⵜ ⵏⵏⵓⵏ ⴳ ⵜⵓⴷⵔⵜ ⵉⵏⵓ ⴰⴽⴽⵯ.
ⵉ ⴰⵢⵜⵎⴰ, ⵜⴰⵏⵎⵎⵉⵔⵜ ⵏⵏⵓⵏ ⵅⴼ ⵓⴱⴷⴷⴰⴷ ⵏⵏⵓⵏ ⴷⵉⴷⵉ ⴷ ⵉⵙⵙⵉⵎⵖⵓⵔⵏ ⵏⵏⵓⵏ.
ⵉ ⵜⴰⵡⵊⴰ ⵉⵏⵓ ⴰⴽⴽⵯ ⴷ ⵉⵎⴰⵔⴰⵏ ⴷ ⵉⵎⴷⴷⵓⴽⴽⵯⴰⵍ ⴷ ⵎⴰⴷ ⴰⴽⴽⵯ ⴷⵉⴷⵉ ⵉⴱⴷⴷⵏ, ⴰⵔ ⴰⵡⵏ ⵜⵜⴰⵣⵏⵖ ⴰⵙⵏⵉⵎⵎⵔ ⴷ ⵓⵙⵉⵜⴳ ⵉⴳⴳⵓⵜⵏ.
ⵉ ⵉⵙⵍⵎⴰⴷⵏ ⵉⵏⵓ ⵉⵅⴰⵜⴰⵔⵏ, ⴰⵡⴷ ⴽⵯⵏⵏⵉ ⴰⵔ ⴰⵡⵏ ⵜⵜⴰⵣⵏⵖ ⴰⵙⵉⵜⴳ ⴷ ⵓⵣⵔⴰⴽ ⵉⵣⴷⴷⵉⴳⵏ ⵅⴼ ⵎⴰⴷ ⵏⵏ ⵜⴳⴰⵎ ⴷ ⵜⵓⴳⴳⴰⵙ ⴷ ⵜⵣⵎⵎⴰⵔ ⴳ ⵓⵙⵍⵎⴷ ⵉⵏⵓ.

La réalisation de cette thèse a été possible grâce au concours de plusieurs personnes à qui je voudrais témoigner mes remerciements, mon respect et ma gratitude.

Tout d'abord, je tiens à remercier les membres du Jury pour avoir accepté d'examiner mon travail et pour leurs contributions scientifiques qui m'ont guidé tout au long de ma thèse. Merci à Karl Labergère de m'avoir fait l'honneur de présider le Jury. Je tiens à remercier Leong Hien Poh et Stephan Wulfinghoff pour leurs rapports détaillés et inspirants sur le manuscrit. Je remercie également Mohamed Jebahi pour les nombreuses discussions passionnantes sur les théories de la plasticité à gradient et Julia Mergheim pour sa participation au Jury.

Je tiens à exprimer toute ma reconnaissance à mon directeur de thèse, Samuel. Je le remercie pour sa patience, sa disponibilité et surtout ses judicieux conseils. Je remercie Kais pour son aide pour percer les mystères du code Z-set. Merci à Cristian de toutes les discussions intéressantes sur les polymères et les lois hyperélastiques. Un grand merci à mes encadrants de TRANSVALOR Nikolay et Stéphane de leur accompagnement et aide pour l'implémentation de toutes sortes de modèles et la réalisation de différentes simulations avec Z-set.

Merci à tous mes amis (docteurs ou futurs docteurs) avec qui j'ai vécu cette expérience pour les échanges passionnants que ce soit autour d'un café ou lors des conférences : Amar, Anass, Harris, Maxime, Flavien, Manon, Clément, ... Merci à tous mes camarades du bureau B127 : Vikram, Chiraz, Daniel, Vincent, Rami, ..., pour toutes les discussions et moments agréables. Merci également à mes colocataires Mouad et Amine de tous les moments que nous avons partagés ensemble.

J'adresse mes sincères remerciements à tous les chercheurs du centre des matériaux. Merci à mes professeurs lors de mon mastère DMS, Farida, Vladimir, Vladislav, Henry, Basile, Sébastien, Vincent, ... Un grand merci à mes encadrants du projet DMS Lucien et Stéphanie de leur aide précieuse pour réaliser et interpréter les résultats des différents essais expérimentaux. Je voudrais également remercier Abdennour, Yann de leur aide pour la réalisation de ses essais.

J'aimerais exprimer ma gratitude à tous les gens que j'ai pu rencontrer au centre des matériaux, trop nombreux pour les citer, qui ont eu la gentillesse de m'accueillir et de m'aider, de près ou de loin, pour accomplir mon travail.

Contents

Appendices 151

Nomenclature

Notations

$\underset{\sim}{\boldsymbol{F}}$	deformation gradient
$\underset{\sim}{\boldsymbol{C}}$	right Cauchy-Green strain tensor
$\underset{\sim}{\boldsymbol{E}}$	total Green-Lagrange strain tensor
$\underset{\sim}{\boldsymbol{B}}$	left Cauchy-Green strain tensor
$\underset{\sim}{\boldsymbol{\sigma}}$	Cauchy stress tensor
$\underset{\sim}{\boldsymbol{P}}$	Boussinesq (1st Piola-Kirchhoff) stress tensor
$\underset{\sim}{\boldsymbol{\Pi}}$	Piola (2nd Piola-Kirchhoff) stress tensor
$\underset{\sim}{\boldsymbol{\Pi}}^e$	Piola stress tensor in the intermediate configuration
$\underset{\sim}{\boldsymbol{M}}$	Mandel stress tensor
$\underset{\sim}{\boldsymbol{L}}$	velocity gradient tensor
$\underset{\sim}{\boldsymbol{D}}$	strain rate tensor
$\underset{\sim}{\boldsymbol{W}}$	spin tensor

Tensor notations

$\underline{\boldsymbol{a}} = a_i\ \underline{\boldsymbol{e}}_i$	first order tensor
$\underset{\sim}{\boldsymbol{A}} = A_{ij}\ \underline{\boldsymbol{e}}_i \otimes \underline{\boldsymbol{e}}_j$	second order tensor
$\underset{\sim}{\boldsymbol{A}}^T = A_{ji}\ \underline{\boldsymbol{e}}_i \otimes \underline{\boldsymbol{e}}_j$	transpose of a second order tensor
$\underset{\sim}{\boldsymbol{A}}^{-1}$	inverse of a second order tensor
$\underset{\sim}{\boldsymbol{A}}^{-T}$	inverse of a transpose of a second order tensor
$\mathrm{sym}(\underset{\sim}{\boldsymbol{A}}) = \dfrac{1}{2}(\underset{\sim}{\boldsymbol{A}}^T + \underset{\sim}{\boldsymbol{A}})$	the symmetric part of a second order tensor
$\mathrm{skw}(\underset{\sim}{\boldsymbol{A}}) = \dfrac{1}{2}(\underset{\sim}{\boldsymbol{A}} - \underset{\sim}{\boldsymbol{A}}^T)$	the anti-symmetric part of a second order tensor
$\underset{\simeq}{\boldsymbol{A}} = A_{ijk}\ \underline{\boldsymbol{e}}_i \otimes \underline{\boldsymbol{e}}_j \otimes \underline{\boldsymbol{e}}_k$	third order tensor
$\underset{\approx}{\boldsymbol{A}} = A_{ijklmn}\ \underline{\boldsymbol{e}}_i \otimes \underline{\boldsymbol{e}}_j \otimes \underline{\boldsymbol{e}}_k \otimes \underline{\boldsymbol{e}}_l \otimes \underline{\boldsymbol{e}}_m \otimes \underline{\boldsymbol{e}}_n$	sixth order tensor
$\underline{\boldsymbol{a}} \cdot \underline{\boldsymbol{b}} = a_i b_i$	scalar product
$\underset{\sim}{\boldsymbol{A}}\underset{\sim}{\boldsymbol{B}} = A_{ik}B_{kj}\ \underline{\boldsymbol{e}}_i \otimes \underline{\boldsymbol{e}}_j$	
$\underset{\sim}{\boldsymbol{A}} : \underset{\sim}{\boldsymbol{B}} = A_{ij}B_{ij}$	
$\mathrm{tr}(\underset{\sim}{\boldsymbol{A}} \cdot \underset{\sim}{\boldsymbol{B}}) = A_{ij}B_{ji}$	
$\underset{\sim}{\boldsymbol{A}} \otimes \underset{\sim}{\boldsymbol{B}} = A_{ij}B_{kl}\ \underline{\boldsymbol{e}}_i \otimes \underline{\boldsymbol{e}}_j \otimes \underline{\boldsymbol{e}}_k \otimes \underline{\boldsymbol{e}}_l$	
$\underset{\sim}{\boldsymbol{A}} \underline{\otimes} \underset{\sim}{\boldsymbol{B}} = A_{ik}B_{jl}\ \underline{\boldsymbol{e}}_i \otimes \underline{\boldsymbol{e}}_j \otimes \underline{\boldsymbol{e}}_k \otimes \underline{\boldsymbol{e}}_l$	
$\underset{\sim}{\boldsymbol{A}} \overline{\otimes} \underset{\sim}{\boldsymbol{B}} = A_{il}B_{jk}\ \underline{\boldsymbol{e}}_i \otimes \underline{\boldsymbol{e}}_j \otimes \underline{\boldsymbol{e}}_k \otimes \underline{\boldsymbol{e}}_l$	
$\underset{\approx}{\boldsymbol{A}} \,\vdots\, \underset{\simeq}{\boldsymbol{B}} = A_{ijklmn}B_{lmn}$	

Introduction

Context

The classical continuum theories for elastoplasticity are well established. Meanwhile, the absence of length scales makes these models unable to capture size effects observed in the mechanical behaviour of materials. Several experimental investigations showed that plasticity phenomena display a size effect or particularly the so-called *smaller is harder* effect. This effect depends on the wavelength of the variation of the deformation field. The conventional theories suffice when the deformation length scale is very large compared to the material length scale. Therefore, it becomes necessary to include the gradient terms in the constitutive equations when the deformation length scale is close to the material length scale. The internal length scale is related to the underlying material microstructure correlated to grain size in metals and inclusions in composite materials, or to the sample size (torsion of thin wires). Plastic strain gradients arise in different cases. First, the torsion and the bending loadings induce a finite plastic strain at the outer surface but zero along the neutral axis (see Fig. 1a and 1b). In addition, the presence of some plastic regions in an elastic medium (*e.g.*, the region at the tip of a crack or beneath an indenter; see Fig. 1c and 1d) induces plastic gradients. Plastic strain gradients results also from the microstructure itself (the presence of hard particles in a composite, grains, etc. as illustrated in Fig. 1e and 1f).

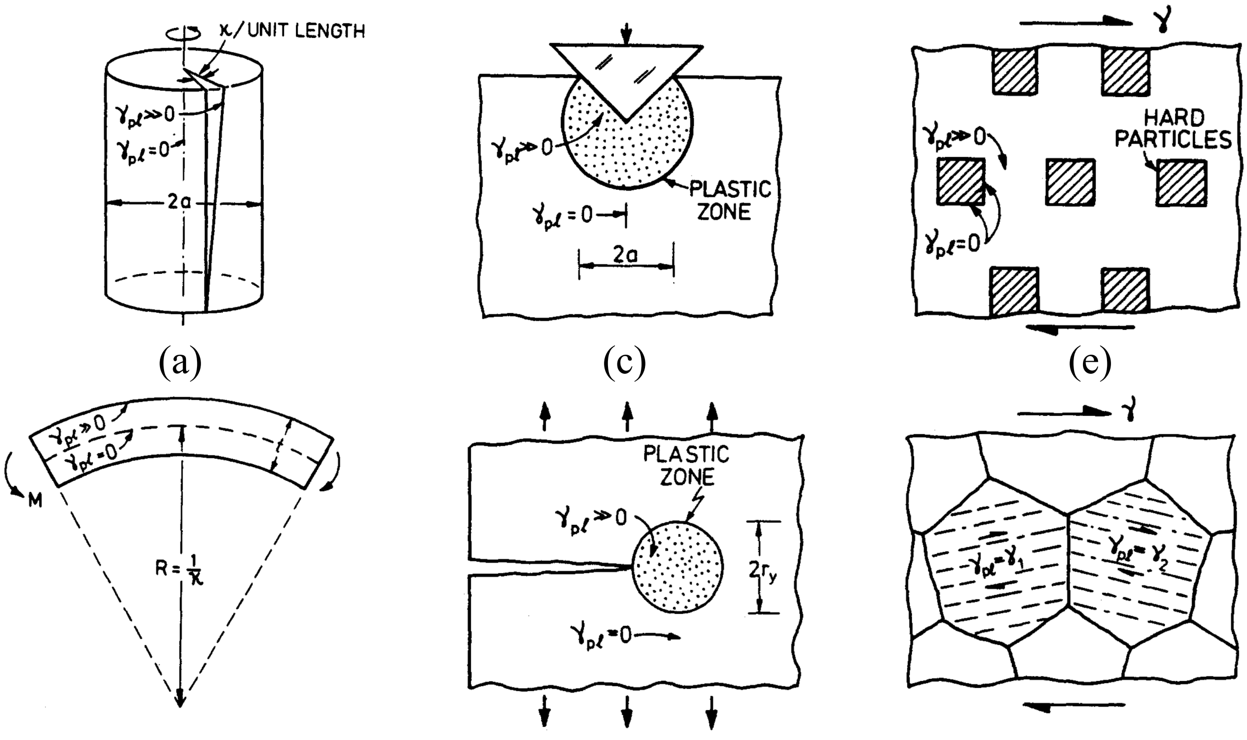

(a) (c) (e)

(b) (d) (f)

Figure 1: *Examples of applications where plastic strain gradients are induced [Fleck et al., 1994]*

On the other hand, the finite element simulation of plasticity and damage phenomena involving material softening using classical media is not satisfactory. The response of classical models exhibits a strong dependency on the mesh and the numerical methods. Explicit integration solvers are often adopted in order to obtain a satisfactory convergence rate especially when the mesh size is very small. The presence of material softening due to plasticity or damage is usually accompanied by strain localization phenomena. In an industrial context, reliable tools are necessary to provide more stable numerical solutions. A regularization of this model is often required to restore the ellipticity of differential equations and the well-posedness of the boundary value problem.

Plastic strain localization and damage occur in general for strain ranges that are beyond the scope of small strain models. Since the 1950s, a considerable number of studies were dedicated to investigating the subject of finite strain modelling. Because of their numerical efficiency and implementation ease, hypoelastic formulations are systematically used by the most widespread FEM software, *e.g.* ABAQUS, MARC, ANSYS, Z-set, etc. However, hypoelastic formulations have many drawbacks: the occurrence of an elastic dissipation due to the absence of elastic potential, the stress oscillations observed for problems involving large rotations, non-uniqueness of the convected derivatives, etc. These formulations are not general enough to model anisotropic elastoplasticity since the rotation of anisotropic axes is governed by the choice of the hypoelastic rate and not by a material-dependent quantity.

The numerical simulations of industrial processes and structural analysis require an increasing degree of certainty. Despite many decades of research on the subject, enhanced gradient models are not available for systematic use in commercial finite element codes. Even more important, a thermodynamically consistent finite strain formulation is not provided systematically in commercial software packages.

A brief state of the art

The finite strain modelling of elastoplasticity is still a subject of research. In particular, strain decomposition into elastic and plastic parts was a matter of debate for many decades. For example, several decompositions were suggested *e.g.* the additive decomposition of Green-Lagrange strain [Green and Naghdi, 1965], additive decomposition of the logarithmic strain [Miehe et al., 2002], the multiplicative decomposition [Mandel, 1973] or even no decomposition at all [Bertram, 1999]. Meanwhile, the formulation based on the multiplicative decomposition of the deformation gradient is widely accepted and used to model the constitutive behavior of metals, polymers [Lion, 2000], soil [Hashiguchi, 2019], concrete, ceramics, etc. Despite this widespread use of the multiplicative decomposition, its use is rather limited to some specific models in FEM codes.

The modeling of gradient theories can be traced back to the works of Mindlin [1964]; Eringen and Suhubi [1964]. Since then a panoply of theories has been proposed to model materials at different scales. They can be classified into two main categories referred to as generalized continuum theories: higher-order theories which enhance the kinematic description by additional degrees of freedom, and higher-grade theories in which the gradient of targeted variables is considered as an internal variable. The seminal work by Aifantis [1984] has proposed a modification of the flow stress in the classical von Mises model by adding terms related to the gradient and the Laplacian of the plastic deformation in order to represent the effect of the dislocation state on the macroscopic scale. The thermodynamical framework for this model was formulated years later as in [Gudmundson, 2004]. The compatibility with thermodynamics of some strain gradient theories is discussed in [Gurtin and Anand, 2009] based on the virtual power principle combined with the first two laws of thermodynamics.

Zoology of strain gradients has been the subject of many unifying attempts [Gudmundson, 2004; Kirchner and Steinmann, 2005; Forest and Sievert, 2003; Forest, 2009]:

- The approach based on non-local integral operators [Eringen, 2002; Bažant and Jirásek, 2002].
- Explicit strain gradients theories [Aifantis, 1984]: the explicit gradient plasticity theory requires an additional and nonstandard condition at the elastic-plastic boundary. Defining these boundaries becomes more complicated if the plastic zone grows during the deformation process. The set of resulting conditions cannot easily be met in the finite element implementation [Peerlings, 2007].

- Implicit strain gradient theories [Peerlings et al., 1996]: the explicit gradient of the plastic strain is replaced by the difference the conventional plastic strain and a nonlocal plastic strain. The nonlocal variable is the solution of a Helmholtz equation that involves its second gradient.
- The micromorphic approach: it was suggested by Eringen and Suhubi [1964]. It relies on the enrichment of the kinematics of the continuum by a non-symmetric second order tensor accounting for micro-deformations. Reduced theories are formulated by imposing internal constraints on the micro-deformation which allows for a decrease in the number of degrees of freedom, *e.g.* micropolar (Cosserat theory). This approach is applied to several phenomena including plasticity and damage [Forest, 2009; Saanouni and Hamed, 2013].

In general, the FEM implementation of higher-grade theories is more complex than higher-order ones [De Borst and Mühlhaus, 1992]. On the other hand, higher-order theories are, in most cases, a straightforward extension of the classical FEM implementation by adding supplementary degrees of freedom.

To the best of our knowledge, there exists no commercial or research finite element software that takes into account systematically the gradient-based theories. However, several implementations are carried out for some specific material models, *e.g.*, micromorphic plasticity and damage using VUMAT (explicit scheme) and a user element (VUEL) subroutines for ABAQUS [Diamantopoulou et al., 2017], a strain gradient formulation with a user element subroutine (UEL) and an implicit implementation (UMAT) in ABAQUS [Martínez-Pañeda et al., 2019], Aifantis's theory in ANSYS [Hashemi et al., 2013], explicit micromorphic formulation in VPS/Pam-Crash [Russo et al., 2022], micromorphic formulation etc.

Objectives

The main objective of this thesis is to provide a systematic and thermodynamically consistent approach to addressing elastoplasticity at finite strains in FEM codes. This objective is articulated around the following topics:

1. First, this approach seeks to extend the well-established elastoplasticity models at small strains to finite strains. It should cover a wide range of models which are commonly used in FEM codes, including different isotropic and kinematic hardening rules and internal variables. It is expected to be numerically efficient in the perspective of systematic use for industrial applications.
2. Second, the approach should also include enhanced gradient models in order to take into account size effects.
3. Third, the advocated approach is intended to cancel the spurious mesh dependency observed for classical models for strain localization phenomena.

Methodology

The proposed finite strain formulation is based on the multiplicative decomposition of the deformation gradient into thermoelastic and inelastic parts. All constitutive equations are expressed in the local isoclinic intermediate configuration. By this approach, isotropic and anisotropic plasticity models with various isotropic and kinematic hardening rules are re-usable in the framework of the multiplicative decomposition. Further, a supplementary constitutive equation for the plastic spin must be introduced which is in general omitted in common hypoelastic formulations.

The micromorphic approach is used to implement strain gradient elastoplasticity. This approach can be regarded as a relaxation of gradient models. The gradient models involve the gradient of some internal variables which requires a C^1-continuity [De Borst and Mühlhaus, 1992]. The fields of internal variables are not necessarily differentiable, *e.g.* the plastic strain in the neutral axis of a foil under bending. In contrast, the micromorphic approach introduces additional degrees of freedom that are dissociated from the internal variables. An alternative implementation of strain gradient theories employs Lagrange multipliers to weakly enforce the equality between non-local (degrees of freedom) and local variables (internal variables). Regarding numerical efficiency, the last implementation will be compared to the micromorphic model.

The proposed approach is implemented in the finite element software Z-set [2022]. The integration of constitutive equations is achieved using both explicit and implicit schemes, namely Runge-Kutta and θ-methods. The resolution of the global problem is carried out using quasi-Newton algorithms.

Thesis outline

This manuscript is organized as follows. Chapter 1 presents a systematic extension of constitutive equations to finite strains using the multiplicative decomposition and assuming an isoclinic intermediate configuration. It addresses the general case of multi-mechanism anisotropic thermo-elasto-(visco)plasticity. The proposed approach is applied to several loading cases including homogeneous volume element simulations and structural applications such as deep drawing and a turbine blade under creep. It is systematically compared to the response of hypoelastic formulations.

The chapter 2 proposes a general scalar-based micromorphic formulation at finite strains. In particular, models relying on the cumulative and the equivalent plastic strain are studied. For the sake of demonstration, only quadratic free energy potentials w.r.t. gradient terms are considered. The gradient can be either Lagrangian, Eulerian, or taken w.r.t. the intermediate configuration. The computational cost of micromorphic formulations is compared to the strain gradient theory implemented using Lagrange multipliers.

In chapter 3, a small strain formulation of micromorphic models based on symmetric second order tensors is proposed. Two models for which the micromorphic variable is associated with the total and the plastic strain are detailed. Analytical solutions are provided for simple extension and simple glide problems for elasticity and elastoplasticity. It is shown in particular that tensorial micromorphic models represent a plausible alternative to scalar based models.

The chapter 4 is divided into two main parts. The first one is dedicated to the study of some micromorphic models associated with saturating micromorphic variables. In the second part, the case of a composite material whose behavior exhibits both size effects and strain localization is considered. The necking formation and propagation are analyzed using a material behavior identified for a polymer material. The response of a unidirectional composite is shown to depend on the length scale due to plastic gradients in the confined matrix regions. A characteristic length scale is identified on the basis of experimental stress-strain curves obtained from a transverse compression test.

The chapter 5 summarises briefly the implementation of the proposed approach in the object-oriented software Z-set. This implementation includes a reformulation of constitutive equations in the framework of the multiplicative decomposition and supplementary constitutive equations for the plastic spin. An interface for the micromorphic formulation that covers scalar and tensorial models and energetic or dissipative models is illustrated.

Chapter 1

Systematic extension of constitutive laws to finite strain

Abstract This chapter presents a systematic and thermodynamically consistent extension of anisotropic thermo-elastoviscoplastic constitutive equations at finite strains. The formulation is based on the multiplicative decomposition of the deformation gradient into a thermoelastic and an inelastic part. This decomposition introduces an intermediate configuration considered to be isoclinic. The present framework covers a wide range of multi-mechanism (MM) elastoplastic models. The choice of suitable hyperelastic potential, hardening variables, and anisotropy evolution are discussed. Two definitions of the plastic spin are presented, the first one is derived from the general representation theorem, and the second one is obtained from the normality rule. The effect of the plastic spin is discussed in light of examples involving anisotropic plasticity. The response of the proposed formulation is compared with hypoelastic models in several volume element simulations and structural applications (deep drawing with anisotropic Hill plasticity model and a single crystal turbine blade). The implementation of this methodology in the commercial FE object-oriented code Z-set is detailed. We mainly show how to extend readily a wide range of small strain nonlinear constitutive models to finite deformations.

Résumé Une méthode d'extension systématique des lois de comportement établies dans le cadre des petites déformations aux transformations finies est présentée en se basant sur les principes de la thermodynamique des milieux continus. La méthode se base sur la décomposition multiplicative du gradient de transformation en une partie thermoélastique et une partie inélastique. Cette décomposition suppose l'existence d'une configuration intermédiaire considérée comme isocline relachée. Le présent formalisme couvre une large sélection de modèles élastoplastiques multi-mécanismes (MM). Le choix du potentiel hyperélastique approprié et des variables d'écrouissage est discuté. Pour modéliser l'anisotropie, un trièdre directeur est attaché au point matériel. La vitesse de rotation du trièdre directeur par rapport à l'élément de matière, est relié au taux de rotation dû à la plasticité est pris en compte. Deux définitions de ce taux de rotation sont présentées, la première se base sur le théorème des représentations tensorielles et la seconde est obtenue à partir de la loi de normalité. L'effet de la rotation plastique est discuté à la lumière d'exemples impliquant la plasticité anisotrope. La réponse de la formulation proposée est comparée aux modèles hypoélastiques à travers plusieurs applications sur un élément de volume et des calculs de structure ; à savoir : l'emboutissage d'une tôle avec un modèle de Hill ansiotrope et une aube de turbine monocristalline. L'implémentation de cette méthodologie dans le code commercial par éléments finis orienté objet Z-set est détaillée. Nous illustrons principalement comment étendre une librairie des lois de comportement nonlinéaires, disponible dans le code, en grandes déformations.

Contents

1.1 Introduction

Finite strain elastoplasticity, as observed in various materials, requires combined geometric and material nonlinear analysis of solids. Since the early sixties, a myriad of strategies have been developed to extend the well-established infinitesimal elastoplasticity theory to finite transformations [Green and Naghdi, 1965; Naghdi, 1990]. The widely used approach is the so–called hypoelastic formulations relying on additive decomposition of the total deformation rate into elastic and inelastic parts, and constitutive equations for objective stress rates [Truesdell, 1955; Hibbitt et al., 1970]. However, this framework has been the subject of much controversy. First, the constitutive equations are generally not integrable, which results in spurious energy dissipation in the elastic regime even prior to yield (see, *e.g.* [Kojić and Bathe, 1987; Lin et al., 2003; Brepols et al., 2014] among others). In order to recover the integrability of hypoelastic formulations, a logarithmic rate has been put forward by [Xiao et al., 1998, 1999]. However, it was shown in [Jiao and Fish, 2017] that the post-yield response of the logarithmic rate is inconsistent with the notion of elasticity. Second, the rate of elastic deformation is related to a non unique objective stress rate [Dienes, 1979; Nemat-Nasser, 1979]. In addition, some hypoelastic models are well-known to depend on the reference configuration, *e.g.* Green-Naghdi, and logarithmic rates [Shutov and Ihlemann, 2014]. Formulations relying upon the additive decomposition of the Green-Lagrange strain tensor were developed [Green and Naghdi, 1965]. Given that the considered strain measure is symmetric, the latter model cannot describe full anisotropy.

Another formulation based on the additive split of logarithmic strain was suggested by Miehe et al. [2002]. These formulations however imply a dependence of the choice of the reference configuration, meaning that the form of the constitutive laws is not left unchanged by the change of reference configuration [Shutov and Ihlemann, 2014].

Since the aforementioned models are unsatisfactory in describing finite deformations, several authors have put forward the necessity to introduce the multiplicative decomposition as a general way of describing the kinematics at finite strain [Kröner, 1959; Lee and Liu, 1967]. This decomposition assumes the existence of an intermediate configuration that is generally not unique. The concept of isoclinic intermediate configuration was proposed first by [Mandel, 1972, 1973]. Since then, several models relying upon the multiplicative decomposition and a hyperelastic potential for the stress have been developed (*e.g.* [Lion, 2000; Wallin et al., 2003; Menzel et al., 2005; Vladimirov et al., 2010; Brepols et al., 2014]). It is noteworthy to mention that there exist different versions of the multiplicative decomposition, *e.g.* considering a decomposition in the reverse order [Clifton, 1972; Lubarda, 1999], decomposition assuming symmetric elastic part or symmetric plastic part [Lee and Liu, 1967; Lubarda, 1991]. Alternatively, a rigorous presentation of this theory has been proposed by Bertram [1999] based on material isomorphisms. This approach defines a special class of materials described by elastic ranges that are independent of plastic deformation.

Constitutive modeling of kinematic hardening is still an active area of research even in the small strain regime [Bouby et al., 2015]. Kinematic hardening models at finite strain can be generally classified into two main groups; both are regarded as extensions of the Armstrong-Frederick model [Armstrong and Frederick, 1966]. The first one employs an evolution equation for the back stress, or the so-called 'Chaboche-type' model [Lemaitre and Chaboche, 1994]. The second one involves an additional multiplicative decomposition of the plastic part of the deformation gradient into storage and dissipative parts [Svendsen et al., 1998; Lion, 2000; Dettmer and Reese, 2004; Vladimirov et al., 2008, 2010]. The difference between different models becomes visible, particularly in cases where principal axes rotate, *e.g.* simple glide and torsion [Dogui and Sidoroff, 1985]. Significant differences are observed for the special case of linear kinematic hardening (Prager model) which leads to stress oscillations for Jaumann rate [Dogui and Sidoroff, 1985]. Meanwhile, many studies have shown that different extensions of the Armstrong-Frederick model yield, at least qualitatively, similar results [Tsakmakis, 1996a,b; Dettmer and Reese, 2004]. The differences are mainly due to second-order effects for loading conditions involving large rotations, apparent in simple shear [Dettmer and Reese, 2004; Tsakmakis and Willuweit, 2004].

At finite strain, the material does not undergo only macroscopic stretches and rotations but also rotations of its substructure described by some privileged directions called *directors*. The notion of plastic spin describes the evolution of material's directors with plasticity. As highlighted by several works (*e.g.* [Kratochvíl, 1973; Gurtin and Anand, 2005]), the plastic spin is undetermined for isotropic materials and is often assumed to vanish. Several constitutive equations for the plastic spin has been proposed independently by [Loret, 1983; Dafalias, 1983]. It has been argued that multiple plastic spins are required since each internal variable has a different nature and, consequently, a different rotating frame is required for each internal variable [Dafalias, 1993]. Furthermore, the plastic spin is useful to prevent stress oscillation, particularly in the case of the simple shear problem [Dafalias, 1983] when applied to elastoplastic materials with linear kinematic hardening. Constitutive modeling of plastic spin can be achieved through: (i) an additional ad-hoc constitutive equation [Loret, 1983; Dafalias, 1984; Ulz, 2011] (ii) generalized normality conditions [Mandel, 1973; Halphen and Son Nguyen, 1975; Itskov and Aksel, 2004].

The additive hypo-elastoplastic models are widely used in finite element codes for the sake of computational ease. Small deformation material models are adapted to large deformation problems with appropriate tangent operators and stress/strain measures. To our knowledge, there is no finite element software supporting a systematic extension of infinitesimal models using the multiplicative decomposition. Meanwhile, this approach is already used, exclusively, for some particular models, *e.g.* in MSC Marc [Hashiguchi, 2019], or by using user material subroutines in ABAQUS [Vladimirov et al., 2010; Brepols et al., 2014].

This chapter presents a generic and systematic extension of small strain models to finite deformations. The multiplicative decomposition of the deformation gradient into thermoelastic and inelastic parts is adopted. All constitutive equations are expressed in the local isoclinic intermediate configuration. Accordingly, the stress is related to the elastic strain through a hyperelastic law. Emphasis is put on the numerical implementation of the present formulation in a commercial finite element code provided with an object-oriented interface [Foerch et al., 1997]. By this approach, small strain models, including isotropic and anisotropic plasticity models with various isotropic and kinematic hardening rules, can be re-used in the framework of the multiplicative decomposition. On the other hand, unlike usual hypoelastic models, various constitutive equations for the plastic spin can be formulated within this framework.

This chapter is organized as follows. Section 1.2 presents a general thermodynamical framework for constitutive modeling of anisotropic finite strain thermo-elastoviscoplasticity based on the multiplicative decomposition. Kinematic assumptions and a thermodynamically consistent derivation of constitutive equations for multi-mechanism modeling are regarded. Different models describing kinematic hardening are discussed. Two constitutive choices of plastic spin are presented. In section 1.3, we describe the implementation of the present formulation in a commercial finite element code by taking advantage of its oriented object interface. Special attention is paid to the integration of constitutive equations and the construction of tangent matrices. Two integration schemes are adopted: using the exponential mapping or correcting residuals in order to fulfill the plastic incompressibility condition. Finally, the response of some particular models is presented in sections 1.4 and 1.5 for a volume element and structural applications, respectively. Through these applications, comparisons are made with hypoelastic formulations presented in appendix A.

1.2 General framework for elastoviscoplastic modeling at finite strains

1.2.1 Kinematics

The deformation gradient is multiplicatively split as

$$\underset{\sim}{\boldsymbol{F}} = \underset{\sim}{\boldsymbol{F}}^e \underset{\sim}{\boldsymbol{F}}^p \tag{1.1}$$

where $\underset{\sim}{\boldsymbol{F}}^e$ and $\underset{\sim}{\boldsymbol{F}}^p$ denote the thermoelastic and the inelastic parts, respectively, see Fig. 1.1. In contrast to $\underset{\sim}{\boldsymbol{F}}$, the parts $\underset{\sim}{\boldsymbol{F}}^e$ and $\underset{\sim}{\boldsymbol{F}}^p$ are not necessarily defined as gradients of one-to-one mappings. As a consequence of possible incompatibility of thermoelastic and plastic deformation fields, the intermediate configuration is local, *i.e.* it belongs to the immediate vicinity of a material point and is obtained from the current deformed configuration by a purely elastic unloading of this vicinity only. The volume changes due to elastic and plastic deformations are respectively denoted by

$$J_e = \det\left(\underset{\sim}{\boldsymbol{F}}^e\right) = \frac{\overline{\rho}}{\rho}, \quad J_p = \det\left(\underset{\sim}{\boldsymbol{F}}^p\right) = \frac{\rho_0}{\overline{\rho}} \tag{1.2}$$

and ρ, $\overline{\rho}$ and ρ_0 stand for the mass densities in current, intermediate and reference configurations, respectively. The decomposition (1.1), however, is not unique since any invertible transformation $\underset{\sim}{\boldsymbol{H}}$ can be introduced such that

$$\underset{\sim}{\boldsymbol{F}} = (\underset{\sim}{\boldsymbol{F}}^e \underset{\sim}{\boldsymbol{H}})(\underset{\sim}{\boldsymbol{H}}^{-1} \underset{\sim}{\boldsymbol{F}}^p) = \underset{\sim}{\boldsymbol{F}}^{e*} \underset{\sim}{\boldsymbol{F}}^{p*} \tag{1.3}$$

To remedy this concern, we shall define some material directors. These privileged directors are attached to some microstructural features and undergo a different transformation than the material. For solids, we can always define a triad of directors describing its microstructure (fibers, crystal lattice vectors, ...). In general, an infinity of directors may be identified for a material. Nevertheless, if the relative spin of all directors with respect to a single triad of directors is known, the problem shall be simplified by considering only this triad. It leads to the concept of local isoclinic intermediate configuration, advocated in [Mandel, 1973], where the material directors have the same inclination or orientation as in the reference configuration. The intermediate configuration is obtained by elastic virtual unloading, whereas the rigid-body rotation of directors is included in the thermoelastic part of the deformation gradient. The isoclinic local configuration is uniquely defined up to a symmetry operation belonging to the symmetry group of the material.

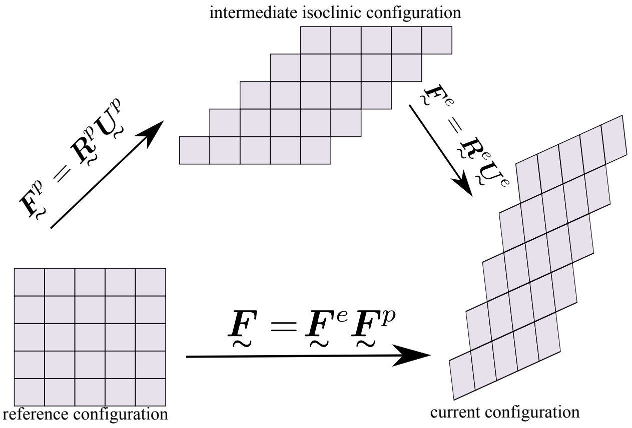

Figure 1.1: *Illustration of the local isoclinic intermediate configuration*

The velocity gradient is additively decomposed in the current configuration

$$\underset{\sim}{\boldsymbol{L}} = \underset{\sim}{\dot{\boldsymbol{F}}} \underset{\sim}{\boldsymbol{F}}^{-1} = \underset{\sim}{\boldsymbol{L}}^e + \underset{\sim}{\boldsymbol{F}}^e \overline{\underset{\sim}{\boldsymbol{L}}}^p \underset{\sim}{\boldsymbol{F}}^{e-1} \tag{1.4}$$

$\underset{\sim}{\boldsymbol{L}}^e$ is the purely elastic part of the velocity gradient and $\overline{\underset{\sim}{\boldsymbol{L}}}^p$ is referred to as the plastic deformation rate in the intermediate configuration. The latter, in turn, can be split into symmetric and skew-symmetric parts as

$$\begin{cases} \underset{\sim}{\boldsymbol{L}}^e = \underset{\sim}{\dot{\boldsymbol{F}}}^e \underset{\sim}{\boldsymbol{F}}^{e-1} = \underset{\sim}{\boldsymbol{D}}^e + \underset{\sim}{\boldsymbol{W}}^e \\ \overline{\underset{\sim}{\boldsymbol{L}}}^p = \underset{\sim}{\dot{\boldsymbol{F}}}^p \underset{\sim}{\boldsymbol{F}}^{p-1} = \overline{\underset{\sim}{\boldsymbol{D}}}^p + \overline{\underset{\sim}{\boldsymbol{W}}}^p \end{cases} \tag{1.5}$$

where $\underset{\sim}{\boldsymbol{D}}^e = \mathrm{sym}(\underset{\sim}{\boldsymbol{L}}^e)$, $\overline{\underset{\sim}{\boldsymbol{D}}}^p = \mathrm{sym}(\overline{\underset{\sim}{\boldsymbol{L}}}^p)$ are the elastic and the plastic strain rates, and $\underset{\sim}{\boldsymbol{W}}^e = \mathrm{skw}(\underset{\sim}{\boldsymbol{L}}^e)$ and $\overline{\underset{\sim}{\boldsymbol{W}}}^p = \mathrm{skw}(\overline{\underset{\sim}{\boldsymbol{L}}}^p)$ are the elastic and plastic spin tensors.

1.2.2 Thermodynamic framework

The local form of the Clausius-Duhem inequality expressed in the local current configuration is written as

$$\frac{\underset{\sim}{\boldsymbol{\sigma}} : \underset{\sim}{\boldsymbol{D}}}{\rho} - (\dot{\psi} + \dot{T}\eta) - \frac{1}{\rho}\frac{\underline{\boldsymbol{q}} \cdot \underline{\boldsymbol{g}}}{T} \geq 0, \qquad \underline{\boldsymbol{g}} = \boldsymbol{\nabla}_{\boldsymbol{x}} T \tag{1.6}$$

where $\underline{\boldsymbol{q}}$ is heat flux, $\underline{\boldsymbol{g}}$ is the current spatial gradient of temperature, and ψ, η designate the Helmholtz free energy and entropy densities per unit mass, respectively. The strain rate tensor $\underset{\sim}{\boldsymbol{D}} = \mathrm{sym}(\underset{\sim}{\boldsymbol{L}})$ is the work-conjugate of the symmetric Cauchy stress $\underset{\sim}{\boldsymbol{\sigma}}$. The volume density of internal forces w.r.t. the intermediate configuration is given by

$$J_e \underset{\sim}{\boldsymbol{\sigma}} : \underset{\sim}{\boldsymbol{D}} = \underset{\sim}{\boldsymbol{\Pi}}^e : \underset{\sim}{\dot{\boldsymbol{E}}}^e + \underset{\sim}{\boldsymbol{M}} : \overline{\underset{\sim}{\boldsymbol{L}}}^p \tag{1.7}$$

where

$$\begin{cases} \underset{\sim}{\boldsymbol{E}}^e = \frac{1}{2}\left(\underset{\sim}{\boldsymbol{C}}^e - \underset{\sim}{\boldsymbol{1}}\right), \qquad \underset{\sim}{\boldsymbol{C}}^e = \underset{\sim}{\boldsymbol{F}}^{eT} \underset{\sim}{\boldsymbol{F}}^e \\ \underset{\sim}{\dot{\boldsymbol{E}}}^e = \underset{\sim}{\boldsymbol{F}}^{eT} \underset{\sim}{\boldsymbol{D}}^e \underset{\sim}{\boldsymbol{F}}^e \\ \underset{\sim}{\boldsymbol{\Pi}}^e = J_e \underset{\sim}{\boldsymbol{F}}^{e-1} \underset{\sim}{\boldsymbol{\sigma}} \underset{\sim}{\boldsymbol{F}}^{e-T} \\ \underset{\sim}{\boldsymbol{M}} = J_e \underset{\sim}{\boldsymbol{F}}^{eT} \underset{\sim}{\boldsymbol{\sigma}} \underset{\sim}{\boldsymbol{F}}^{e-T} = \underset{\sim}{\boldsymbol{C}}^e \underset{\sim}{\boldsymbol{\Pi}}^e \end{cases} \tag{1.8}$$

$\underset{\sim}{\boldsymbol{\Pi}}^e$ and $\underset{\sim}{\boldsymbol{M}}$ denote, respectively, the Piola and Mandel stress tensors, expressed in the intermediate configuration. The Mandel stress tensor $\underset{\sim}{\boldsymbol{M}}$ is generally non-symmetric, in contrast to $\underset{\sim}{\boldsymbol{\Pi}}^e$. By expressing the dissipation inequality in the intermediate configuration, we obtain

$$\underset{\sim}{\boldsymbol{\Pi}}^e : \underset{\sim}{\dot{\boldsymbol{E}}}^e + \underset{\sim}{\boldsymbol{M}} : \overline{\underset{\sim}{\boldsymbol{L}}}^p - \rho_e(\dot{\psi} + T\eta) - \frac{\underline{\boldsymbol{q}}_e \cdot \underline{\boldsymbol{g}}_e}{T} \geq 0 \tag{1.9}$$

where $\underline{q}_e = J_e \underset{\sim}{\boldsymbol{F}}^{e-1}\underline{\boldsymbol{q}}$ and $\underline{g}_e = \underset{\sim}{\boldsymbol{F}}^{eT}\underline{\boldsymbol{g}}$. The specific free energy density $\psi(\underset{\sim}{\boldsymbol{E}}^e, T, \boldsymbol{\alpha}_I)$ is a function of elastic strain $\underset{\sim}{\boldsymbol{E}}^e$, temperature T and internal variables $\boldsymbol{\alpha}_I$ which are scalar and/or tensor quantities accounting for hardening properties. It follows that

$$\dot{\psi} = \frac{\partial\psi}{\partial \underset{\sim}{\boldsymbol{E}}^e} : \dot{\underset{\sim}{\boldsymbol{E}}}^e + \sum_I \frac{\partial\psi}{\partial\boldsymbol{\alpha}_I}\dot{\boldsymbol{\alpha}}_I + \frac{\partial\psi}{\partial T}\dot{T} \tag{1.10}$$

The Clausius-Duhem inequality takes the form:

$$\left(\underset{\sim}{\boldsymbol{\Pi}}^e - \overline{\rho}\frac{\partial\psi}{\partial \underset{\sim}{\boldsymbol{E}}^e}\right) : \dot{\underset{\sim}{\boldsymbol{E}}}^e + \underset{\sim}{\boldsymbol{M}} : \overline{\underset{\sim}{\boldsymbol{L}}}^p - \overline{\rho}\sum_I \frac{\partial\psi}{\partial\boldsymbol{\alpha}_I}\dot{\boldsymbol{\alpha}}_I - \overline{\rho}\left(\frac{\partial\psi}{\partial T} + \eta\right)\dot{T} - \frac{\underline{q}_e \cdot \underline{g}_e}{T} \geq 0 \tag{1.11}$$

The following state laws are adopted

$$\underset{\sim}{\boldsymbol{\Pi}}^e = \overline{\rho}\frac{\partial\psi}{\partial \underset{\sim}{\boldsymbol{E}}^e} \quad , \quad \eta = -\frac{\partial\psi}{\partial T} \tag{1.12}$$

so that the intrinsic dissipation remains as

$$\phi_{in} = \underset{\sim}{\boldsymbol{M}} : \overline{\underset{\sim}{\boldsymbol{L}}}^p - \overline{\rho}\sum_I \frac{\partial\psi}{\partial\boldsymbol{\alpha}_I}\dot{\boldsymbol{\alpha}}_I \geq 0 \tag{1.13}$$

together with the condition $\underline{q}_e \cdot \underline{g}_e \leq 0$. The condition (1.13) is satisfied for any process if there exists a convex potential Ω w.r.t. $\underset{\sim}{\boldsymbol{M}}$ and concave w.r.t. $\boldsymbol{A}_I$ such that

$$\overline{\underset{\sim}{\boldsymbol{L}}}^p = \frac{\partial\Omega(\underset{\sim}{\boldsymbol{M}}, \boldsymbol{A}_I)}{\partial\underset{\sim}{\boldsymbol{M}}} \quad , \quad \dot{\boldsymbol{\alpha}}_I = -\frac{\partial\Omega(\underset{\sim}{\boldsymbol{M}}, \boldsymbol{A}_I)}{\partial\boldsymbol{A}_I} \tag{1.14}$$

$\boldsymbol{A}_I$ are the thermodynamic forces associated with the state variables $\boldsymbol{\alpha}_I$:

$$\boldsymbol{A}_I = \overline{\rho}\frac{\partial\psi}{\partial\boldsymbol{\alpha}_I} \tag{1.15}$$

In the case of time–independent plasticity, the flow rule in Eq. (1.14) is rewritten

$$\overline{\underset{\sim}{\boldsymbol{L}}}^p = \dot{\lambda}\frac{\partial f(\underset{\sim}{\boldsymbol{M}}, \boldsymbol{A}_I)}{\partial\underset{\sim}{\boldsymbol{M}}} \tag{1.16}$$

where $f(\underset{\sim}{\boldsymbol{M}}, \boldsymbol{A}_I)$ is the yield function and $\dot{\lambda}$ denotes the plastic multiplier which can be determined by use of the consistency condition as

$$\dot{f}(\underset{\sim}{\boldsymbol{M}}, \boldsymbol{A}_I) = \frac{\partial f}{\partial\underset{\sim}{\boldsymbol{M}}} : \dot{\underset{\sim}{\boldsymbol{M}}} + \frac{\partial f}{\partial\boldsymbol{A}_I} : \dot{\boldsymbol{A}}_I = 0 \tag{1.17}$$

For viscoplasticity with a threshold, from Eq. (1.16) and Eq. (1.14), a viscoplastic multiplier can be defined as

$$\dot{\lambda} = \frac{\partial\Omega(\underset{\sim}{\boldsymbol{M}}, \boldsymbol{A}_I)}{\partial f(\underset{\sim}{\boldsymbol{M}}, \boldsymbol{A}_I)} \tag{1.18}$$

The existence of a convex potential from which the flow rule and the evolution law of internal variables are derived is sufficient to satisfy the dissipation inequality in Eq. (1.13), but it is not necessary.

1.2.3 Thermo-hyperelasticity

A myriad of free energy potentials are available to model hyperelasticity at finite strains. A widely used free energy potential is the so-called St. Venant-Kirchhoff model, as a straightforward generalization of

Hooke's law

$$\overline{\rho}\psi^e(\underset{\sim}{\boldsymbol{E}}^e) = \frac{1}{2}\underset{\sim}{\boldsymbol{E}}^e : \underset{\approx}{\mathbb{C}} : \underset{\sim}{\boldsymbol{E}}^e, \quad \text{with} \quad \underset{\sim}{\boldsymbol{E}}^e = \frac{1}{2}(\underset{\sim}{\boldsymbol{F}}^{eT}\underset{\sim}{\boldsymbol{F}}^e - \underset{\sim}{\boldsymbol{1}}) \tag{1.19}$$

where $\underset{\approx}{\mathbb{C}}$ is the fourth-order elasticity moduli. This non-polyconvex potential [Raoult, 1986] fails to respond appropriately in some cases *e.g.* the stress needed to shrink a bar to zero volume goes to zero which is physically unreasonable [Holzapfel, 2000]. This limitation is due to the fact that St. Venant-Kirchhoff model does not take into account the volume change appropriately. Several modified versions of this model are proposed in literature in order to circumvent the aforementioned limitation [Ciarlet, 1988; Holzapfel, 2000; Wallin and Ristinmaa, 2005] *e.g.* the isotropic neo-Hookean model

$$\overline{\rho}\psi^e(\underset{\sim}{\boldsymbol{E}}^e) = \frac{1}{2}\lambda(\log(J_e))^2 + \mu\left(\text{trace}(\underset{\sim}{\boldsymbol{E}}^e) - \log(J_e)\right) \tag{1.20}$$

λ and μ are Lamé coefficients. We mention that the proposed formulation is not restricted to a unique hyperelastic model. The model in Eq. (1.19) is proposed by default. In particular this choice is sufficient to represent the elastic part of the elastoplastic behavior of metals and alloys which are characterized by small elastic strains.

Two approaches for introducing thermoelasticity at finite strain may be distinguished. In the first approach, two configurations of material sample are considered: The initial configuration at uniform reference temperature, and the deformed configuration characterized by non-uniform stress and temperature fields [Bertram, 1999; Vujošević and Lubarda, 2002; Bertram, 2003]. The second approach has been proposed by [Lu and Pister, 1975; Teodosiu and Sidoroff, 1976; Vujošević and Lubarda, 2002; Lubarda, 2004] and by [Boyce et al., 1992; Kamlah and Tsakmakis, 1999; Lion, 2000] in the framework of thermo-elastoplasticity, where a supplementary intermediate configuration is considered. In the purely thermoelastic case, the deformation gradient is then split multiplicatively into thermal and elastic parts as

$$\underset{\sim}{\boldsymbol{F}} = \underset{\sim}{\boldsymbol{F}}^{el}\underset{\sim}{\boldsymbol{F}}^{\theta} \tag{1.21}$$

An alternative decomposition in the form of $\underset{\sim}{\boldsymbol{F}} = \underset{\sim}{\boldsymbol{F}}^{\theta}\underset{\sim}{\boldsymbol{F}}^{el}$ is suggested by Yu et al. [1997]. For isotropic materials, the two approaches yield identical or similar results [Lubarda, 2004]. When extended to anisotropic elastoplasticity, the latter approach gives rise to potential decompositions of the form $\underset{\sim}{\boldsymbol{F}} = \underset{\sim}{\boldsymbol{F}}^{el}\underset{\sim}{\boldsymbol{F}}^{\theta}\underset{\sim}{\boldsymbol{F}}^{p}$ and all permutations of this decomposition can be found in the literature[1] without unambiguous justification for the best–suited choice. That is why the first approach, see [Bertram, 2003], which relies on a unified thermoelastic deformation $\underset{\sim}{\boldsymbol{F}}^e$ is preferred in the following, so that superfluous sub-decompositions are avoided.

The thermoelastic part of the Helmholtz free energy ψ^{the} is defined as a function of the thermoelastic deformation tensor, still defined by Eq. (1.19), and temperature as

$$\overline{\rho}\psi^{the}(\underset{\sim}{\boldsymbol{E}}^e, T) = \overline{\rho}\psi^e(\underset{\sim}{\boldsymbol{E}}^e) - \Delta T\,\underset{\sim}{\boldsymbol{\beta}} : \underset{\sim}{\boldsymbol{E}}^e - C_\varepsilon T^2 \tag{1.22}$$

where $\underset{\sim}{\boldsymbol{\beta}}$ is a second order tensor describing thermal properties and C_ε is the specific heat at constant strain. If the free energy definition (1.19) is adopted, the stress is obtained as

$$\underset{\sim}{\boldsymbol{\Pi}}^e = \underset{\approx}{\mathbb{C}} : (\underset{\sim}{\boldsymbol{E}}^e - \underset{\sim}{\boldsymbol{\alpha}}_T\Delta T), \quad \underset{\sim}{\boldsymbol{\alpha}}_T = \underset{\approx}{\mathbb{C}}^{-1} : \underset{\sim}{\boldsymbol{\beta}} \tag{1.23}$$

where $\underset{\sim}{\boldsymbol{\alpha}}_T$ denotes the thermal expansion second order tensor which, for isotropic materials, can be reduced to only one scalar parameter as $\underset{\sim}{\boldsymbol{\alpha}}_T = \alpha_T\underset{\sim}{\boldsymbol{1}}$. Due to the fact that in usual materials thermal expansion always remains small, the proposed framework closely related to the usual small strain formulation will be sufficient.

---

[1] $\underset{\sim}{\boldsymbol{F}} = \underset{\sim}{\boldsymbol{F}}^{el}\underset{\sim}{\boldsymbol{F}}^{p}\underset{\sim}{\boldsymbol{F}}^{\theta}$ according to [Lion, 2000] and $\underset{\sim}{\boldsymbol{F}} = \underset{\sim}{\boldsymbol{F}}^{el}\underset{\sim}{\boldsymbol{F}}^{\theta}\underset{\sim}{\boldsymbol{F}}^{p}$ in [Boyce et al., 1992; Kamlah and Tsakmakis, 1999]

1.2.4 Multimechanism dissipation potential

The inelastic deformation observed on the macroscale has various origins at the level of material microstructure (dislocation slip, twinning, grain boundary sliding, viscosity and molecular orientation in polymers...). Each mechanism leads to a specific type of nonlinearity and constitutive equations. To sum up the contributions of all mechanisms, the total dissipation potential is written in the form

$$\Omega(\underset{\sim}{\boldsymbol{M}},\boldsymbol{A}_I) = \sum_k^N \Omega_k(\underset{\sim}{\boldsymbol{M}},\boldsymbol{A}_I) \tag{1.24}$$

Ω_k denotes the potential associated with the individual viscoplastic mechanism k. Each mechanism is characterized by several internal variables summarizing, at a given time, the material state and the influence of the past thermomechanical loading. The yield surface is defined in the stress-hardening variable (and temperature) space. For a given temperature and hardening, the elastic range is limited by the yield surface. It is a part of the vector space of dimension 9 of non-symmetric second order tensors denoted by $\mathscr{D}_e = \{\underset{\sim}{\boldsymbol{M}} / f(\underset{\sim}{\boldsymbol{M}},\boldsymbol{A}_I,T) \leq 0\}$. The condition $f(\underset{\sim}{\boldsymbol{M}},\boldsymbol{A}_I,T) = 0$ defines the yield surface and is chosen here of the form

$$f(\underset{\sim}{\boldsymbol{M}},\underset{\sim}{\boldsymbol{X}},R) = \left[\underset{\sim}{\boldsymbol{M}} - \underset{\sim}{\boldsymbol{X}}\right]_{eq} - R_0 - R(p,\boldsymbol{\alpha}_I) \tag{1.25}$$

where $[\diamond]_{eq}$ denotes an equivalent stress measure involving appropriate invariants of the tensor inside the brackets, R_0 is the initial yield stress, R describes the isotropic hardening law depending on the accumulated plastic strain p and internal variables $\boldsymbol{\alpha}_I$, and $\underset{\sim}{\boldsymbol{X}}$ is the back stress. Considering for instance the case of two internal variables $\boldsymbol{\alpha}_I = (\underset{\sim}{\boldsymbol{\alpha}}, r)$ and using Eq. (1.15), the associated forces $\underset{\sim}{\boldsymbol{X}}$ and R are obtained through

$$\underset{\sim}{\boldsymbol{X}} = \overline{\rho}\frac{\partial\psi}{\partial\underset{\sim}{\boldsymbol{\alpha}}}, \qquad R = \overline{\rho}\frac{\partial\psi}{\partial r} \tag{1.26}$$

where $\underset{\sim}{\boldsymbol{\alpha}}$ and r are the internal variables associated to kinematic and isotropic hardening, respectively. Multiple yield functions and multiple kinematic hardening variables can be used in the context of multimechanism approach, as proposed in [Cailletaud and Saï, 1995; Cailletaud, 2017]

It follows from Eq. (1.16) and (1.18) that the inelastic strain rate is the sum of the individual contributions of all mechanisms:

$$\underset{\sim}{\overline{\boldsymbol{L}}}^p = \sum_k^N \frac{\partial\Omega_k(\underset{\sim}{\boldsymbol{M}},\boldsymbol{A}_I)}{\partial\underset{\sim}{\boldsymbol{M}}} \tag{1.27}$$

This method circumvents the decomposition of the inelastic deformation into various contributions, often used in the literature in the form $\underset{\sim}{\boldsymbol{F}}^p = \underset{\sim}{\boldsymbol{F}}^{pl}\underset{\sim}{\boldsymbol{F}}^{v}\underset{\sim}{\boldsymbol{F}}^{d}\underset{\sim}{\boldsymbol{F}}^{tr}$... including plastic (rate–independent), viscoplastic, damage or transformation deformations. Such decompositions and all their possible permutations are hard to justify or define unambiguously. In contrast, each mechanism contributes incrementally to the inelastic deformation rate and can generally not be time–integrated into one single deformation part.

1.2.5 Kinematic hardening

In small strain theory, the use of Armstrong-Frederick–Chaboche models is widely accepted [Armstrong and Frederick, 1966; Frederick and Armstrong, 2007; Chaboche, 2008]. This model was enriched by a static recovery term, initially proposed by Lemaitre and Chaboche [1994]. This term allows for a full or partial recovery of the kinematic hardening variable. It has been demonstrated that the Armstrong-Frederick model does not admit a dissipation potential [Bouby et al., 2015] when used with a standard yield function [Besson et al., 2009]. Accordingly, this model is non standard. *Generalized standard materials* (GSM following [Halphen and Son Nguyen, 1975]) are characterized by a single potential to describe the yield function, the flow rule and the evolution laws for internal variables. Nonlinear kinematic hardening can be introduced in this GSM framework by modifying the yield function as follows [Besson et al., 2009]

$$f(\utilde{\boldsymbol{M}},\utilde{\boldsymbol{X}}) = [\utilde{\boldsymbol{M}}-\utilde{\boldsymbol{X}}]_{eq} - R_0 + \frac{D}{2C}\boldsymbol{J}^2(\utilde{\boldsymbol{X}}) \tag{1.28}$$

where C and D are material parameters related to kinematic hardening evolution and $\boldsymbol{J}(\diamond) = \sqrt{\frac{3}{2}(\diamond:\diamond)}$. Nevertheless, this modification Eq. (1.28) induces an isotropic hardening term in addition to the one describing the kinematic hardening effect. A different approach has been proposed in [de Saxcé, 1992] by introducing a new class of materials called *implicit standard materials*. This framework allows recovering an associative model.

The extension of the Armstrong-Frederick model to finite strain range can be achieved in several ways. This issue was investigated thoroughly in [Wallin et al., 2003; Dettmer and Reese, 2004; Tsakmakis and Willuweit, 2004]. A widely used approach is based on the multiplicative decomposition of the plastic part of the deformation gradient [Wallin et al., 2003; Dettmer and Reese, 2004; Brepols et al., 2014; Hashiguchi, 2019, 2020] into a storage part $\utilde{\boldsymbol{F}}^p_s$ and a dissipative part $\utilde{\boldsymbol{F}}^p_d$:

$$\utilde{\boldsymbol{F}}^p = \utilde{\boldsymbol{F}}^p_s\utilde{\boldsymbol{F}}^p_d \tag{1.29}$$

The free energy, depending on $\utilde{\boldsymbol{E}}^e$ and $\utilde{\boldsymbol{E}}^p_s = \frac{1}{2}(\utilde{\boldsymbol{F}}^{pT}_s\utilde{\boldsymbol{F}}^p_s - \utilde{\boldsymbol{1}})$, is split into elastic and kinematic hardening contributions as

$$\bar{\rho}\psi(\utilde{\boldsymbol{E}}^e,\utilde{\boldsymbol{E}}^p_s) = \bar{\rho}\psi^e(\utilde{\boldsymbol{E}}^e) + \bar{\rho}\psi^{\text{kin}}(\utilde{\boldsymbol{E}}^p_s) \tag{1.30}$$

The back stress acting on the local intermediate configuration is derived from

$$\utilde{\boldsymbol{X}} = \bar{\rho}\utilde{\boldsymbol{F}}^p_s\frac{\partial\psi^{\text{kin}}}{\partial\utilde{\boldsymbol{E}}^p_s}\utilde{\boldsymbol{F}}^{pT}_s \tag{1.31}$$

The dissipation inequality becomes

$$\utilde{\boldsymbol{M}} : \utilde{\boldsymbol{D}}^p - \bar{\rho}\frac{\partial\psi^{\text{kin}}}{\partial\utilde{\boldsymbol{C}}^p_s} : \dot{\utilde{\boldsymbol{C}}}^p_s \geq 0 \tag{1.32}$$

$$\left(\utilde{\boldsymbol{M}} - 2\bar{\rho}\utilde{\boldsymbol{F}}^p_s\frac{\partial\psi^{\text{kin}}}{\partial\utilde{\boldsymbol{C}}^p_s}\utilde{\boldsymbol{F}}^{pT}_s\right) : \utilde{\boldsymbol{D}}^p + 2\bar{\rho}\utilde{\boldsymbol{C}}^p_s\frac{\partial\psi^{\text{kin}}}{\partial\utilde{\boldsymbol{C}}^p_s} : \utilde{\boldsymbol{D}}^p_d \geq 0 \tag{1.33}$$

where

$$\utilde{\boldsymbol{C}}^p_s = \utilde{\boldsymbol{F}}^{p-T}_d\utilde{\boldsymbol{C}}^p\utilde{\boldsymbol{F}}^{p-1}_d \tag{1.34}$$

and

$$\dot{\utilde{\boldsymbol{C}}}^p_s = 2\utilde{\boldsymbol{F}}^{pT}_s\overline{\utilde{\boldsymbol{D}}}^p\utilde{\boldsymbol{F}}^p_s - 2\,\text{sym}\left(\utilde{\boldsymbol{C}}^p_s\utilde{\boldsymbol{D}}^p_d\right), \qquad \utilde{\boldsymbol{D}}^p_d = \text{sym}(\dot{\utilde{\boldsymbol{F}}}^p_d\utilde{\boldsymbol{F}}^{p-1}_d) \tag{1.35}$$

We denote by $\utilde{\boldsymbol{X}} = 2\bar{\rho}\utilde{\boldsymbol{F}}^p_s\dfrac{\partial\psi^{\text{kin}}}{\partial\utilde{\boldsymbol{C}}^p_s}\utilde{\boldsymbol{F}}^{pT}_s$ the back stress acting on the local intermediate configuration and by $\utilde{\boldsymbol{M}}_d = 2\bar{\rho}\utilde{\boldsymbol{C}}^p_s\dfrac{\partial\psi^{\text{kin}}}{\partial\utilde{\boldsymbol{C}}^p_s}$ a Mandel-like stress tensor. The evolution equations satisfying (1.33) are given by

$$\begin{cases} \overline{\utilde{\boldsymbol{D}}}^p = \dot{\lambda}\dfrac{\partial f}{\partial\utilde{\boldsymbol{M}}} \\ \utilde{\boldsymbol{D}}^p_d = \dot{\lambda}\dfrac{b}{c}\utilde{\boldsymbol{M}}_d \end{cases} \tag{1.36}$$

where b and c are material constants. For time-dependent plasticity, the plastic multiplier is given by $\dot{\lambda} = \dfrac{\partial\Omega}{\partial f}$ where Ω is the dissipation potential. Otherwise, the plastic multiplier $\dot{\lambda}$ is determined by applying the consistency condition $\dot{f} = 0$.

The proposed kinematic hardening model

As investigated in [Dettmer and Reese, 2004; Tsakmakis and Willuweit, 2004], different extensions of the Armstrong-Frederick model lead to qualitatively similar results if the material parameters are selected appropriately. Another formulation of the kinematic hardening model with both static and dynamic recovery terms is adopted here avoiding any further decomposition of $\underset{\sim}{\boldsymbol{F}}^p$ and resulting from the non-associative evolution equation as

$$\underset{\sim}{\boldsymbol{X}} = \frac{2}{3} C \underset{\sim}{\boldsymbol{\alpha}}, \qquad \dot{\underset{\sim}{\boldsymbol{\alpha}}} = \overline{\underset{\sim}{\boldsymbol{D}}}^p - \dot{\lambda} D \underset{\sim}{\boldsymbol{\alpha}} - \frac{3}{2}\left(\frac{J(\underset{\sim}{\boldsymbol{X}})}{M}\right)^m \frac{\underset{\sim}{\boldsymbol{X}}}{J(\underset{\sim}{\boldsymbol{X}})} \tag{1.37}$$

where C, D, m and M are material parameters. The second term in the right describes the dynamic recovery and the third one is responsible for static recovery. This evolution equation must be complemented by the initial value of $\underset{\sim}{\boldsymbol{\alpha}}$.

Remark 1. *The kinematic hardening variable* $\underset{\sim}{\boldsymbol{\alpha}}$ *in Eq. (1.37) is symmetric provided that its initial value is symmetric. This rule can be generalized to a non-symmetric kinematic hardening variable by substituting* $\overline{\underset{\sim}{\boldsymbol{D}}}^p$ *in Eq. (1.37) by* $\overline{\underset{\sim}{\boldsymbol{L}}}^p$

$$\dot{\underset{\sim}{\boldsymbol{\alpha}}} = \overline{\underset{\sim}{\boldsymbol{L}}}^p - \dot{\lambda} D \underset{\sim}{\boldsymbol{\alpha}} - \frac{3}{2}\left(\frac{J(\underset{\sim}{\boldsymbol{X}})}{M}\right)^m \frac{\underset{\sim}{\boldsymbol{X}}}{J(\underset{\sim}{\boldsymbol{X}})} \tag{1.38}$$

It follows that $\underset{\sim}{\boldsymbol{X}}$ *is generally not symmetric, like the Mandel stress tensor. We mention also that a model with non-symmetric internal variable of kinematic hardening has been proposed in [Itskov and Aksel, 2004].*

A more accurate description of a large variety of experimental stress-strain curves is possible by combining several independent kinematic hardening variables [Lemaitre and Chaboche, 1994] such that

$$\underset{\sim}{\boldsymbol{X}} = \sum_{i=0}^{N_X} \underset{\sim}{\boldsymbol{X}}_i, \qquad \underset{\sim}{\boldsymbol{X}}_i = \frac{2}{3} C_{ij} \underset{\sim}{\boldsymbol{\alpha}}_j \tag{1.39}$$

where N_X is the total number of kinematic hardening variables associated with (visco)-plastic mechanisms. C_{ij} is a matrix describing the interaction between kinematic hardening variables.

1.2.6 Plastic spin

We define the velocity gradient tensor $\overline{\underset{\sim}{\boldsymbol{L}}}$ as the pull back of $\underset{\sim}{\boldsymbol{L}}$ to the intermediate configuration. It can then be split into purely elastic and plastic parts as

$$\overline{\underset{\sim}{\boldsymbol{L}}} = \underset{\sim}{\boldsymbol{F}}^{e-1} \underset{\sim}{\boldsymbol{L}} \underset{\sim}{\boldsymbol{F}}^e = \overline{\underset{\sim}{\boldsymbol{L}}}^e + \overline{\underset{\sim}{\boldsymbol{L}}}^p \tag{1.40}$$

noting

$$\overline{\underset{\sim}{\boldsymbol{L}}}^e = \underset{\sim}{\boldsymbol{F}}^{e-1} \dot{\underset{\sim}{\boldsymbol{F}}}^e = \underset{\sim}{\boldsymbol{F}}^{e-1} \underset{\sim}{\boldsymbol{L}}^e \underset{\sim}{\boldsymbol{F}}^e \qquad \text{and} \qquad \overline{\underset{\sim}{\boldsymbol{L}}}^p = \dot{\underset{\sim}{\boldsymbol{F}}}^p \underset{\sim}{\boldsymbol{F}}^{p-1} \tag{1.41}$$

Strain rate and spin tensors expressed in the intermediate isoclinic configuration are derived as

$$\overline{\underset{\sim}{\boldsymbol{L}}} = \overline{\underset{\sim}{\boldsymbol{D}}} + \overline{\underset{\sim}{\boldsymbol{W}}}, \qquad \overline{\underset{\sim}{\boldsymbol{L}}}^e = \overline{\underset{\sim}{\boldsymbol{D}}}^e + \overline{\underset{\sim}{\boldsymbol{W}}}^e, \qquad \overline{\underset{\sim}{\boldsymbol{L}}}^p = \overline{\underset{\sim}{\boldsymbol{D}}}^p + \overline{\underset{\sim}{\boldsymbol{W}}}^p \tag{1.42}$$

The plastic deformation is induced by various mechanisms as mutual slips between material particles (crystals in metals, soil particles, etc.) without causing the rotation of the substructure defined by appropriate directors. Hence, the rotation and stretch of the substructure is induced only by the elastic distortion, including additional rigid body rotation, both included in $\underset{\sim}{\boldsymbol{F}}^e$. Accordingly, the spin of the substructure $\overline{\underset{\sim}{\boldsymbol{W}}}^e$ is independent of plastic deformation. Therefore, $\overline{\underset{\sim}{\boldsymbol{W}}}^e$ is given by subtracting the plastic spin from the total spin as follows

$$\overline{\underset{\sim}{\boldsymbol{W}}}^e = \overline{\underset{\sim}{\boldsymbol{W}}} - \overline{\underset{\sim}{\boldsymbol{W}}}^p = \operatorname{skw}(\underset{\sim}{\boldsymbol{F}}^{e-1} \dot{\underset{\sim}{\boldsymbol{F}}}^e) \tag{1.43}$$

One should note that if the plastic spin $\overline{\underset{\sim}{W}}^p$ vanishes, the spin of directors will coincide with the material rotation rate.

Two important classes of plastic spin constitutive laws are distinguished in the literature. The first one is derived from normality rules whereas the second one follows from the application of tensor representation theorems.

Plastic spin derived from the tensor representation theorem

A general explicit expression of plastic spin has been proposed independently by [Dafalias, 1983; Loret, 1983] using the tensor representation theorem as

$$\begin{aligned}\overline{\underset{\sim}{W}}^p =& \beta_1(\underset{\sim}{a}\underset{\sim}{s} - \underset{\sim}{s}\underset{\sim}{a}) + \beta_2(\underset{\sim}{a}^2\underset{\sim}{s} - \underset{\sim}{s}\underset{\sim}{a}^2) + \beta_3(\underset{\sim}{a}\underset{\sim}{s}^2 - \underset{\sim}{s}^2\underset{\sim}{a}) \\ &+ \beta_4(\underset{\sim}{a}\underset{\sim}{s}\underset{\sim}{a}^2 - \underset{\sim}{a}^2\underset{\sim}{s}\underset{\sim}{a}) + \beta_5(\underset{\sim}{s}\underset{\sim}{a}\underset{\sim}{s}^2 - \underset{\sim}{s}^2\underset{\sim}{a}\underset{\sim}{s}) + \cdots \end{aligned} \tag{1.44}$$

where $\underset{\sim}{s}$ is the stress measure, $\underset{\sim}{a}$ denotes an internal variable and β_i are material parameters. $\underset{\sim}{a}$ can be also regarded as structure variables [Van der Giessen, 1991; Aravas, 1994]. For instance, for a unidirectional composite described by a director $\underline{n}$ [Fares and Dvorak, 1991], $\underset{\sim}{a} = \underline{n} \otimes \underline{n}$. This allows to describe the evolution of the material substructure or directors [Ulz, 2011]. To the best of our knowledge, all the studies of models including plastic spin make use only of the first order approximation of Eq. (1.44). By doing so, the plastic spin expressed in terms of Mandel's stress tensor is given by

$$\overline{\underset{\sim}{W}}^p = \beta(\underset{\sim}{M}\overline{\underset{\sim}{D}}^p - \overline{\underset{\sim}{D}}^p\underset{\sim}{M}) \tag{1.45}$$

This model is used to describe the evolution of anisotropic axes [Dafalias, 1993; Ulz, 2011] where β is a parameter having the dimension of the inverse of stress. $\overline{\underset{\sim}{W}}^p$ vanishes as long as $\underset{\sim}{M}$ and $\overline{\underset{\sim}{D}}^p$ are coaxial.

Plastic spin derived from the normality rule

According to this approach, the plastic spin is derived naturally from the normality rule as the skew-symmetric part of $\overline{\underset{\sim}{L}}^p$

$$\overline{\underset{\sim}{W}}^p = \mathrm{skw}(\overline{\underset{\sim}{L}}^p) = \mathrm{skw}\left(\frac{\partial\Omega(\underset{\sim}{M}, \boldsymbol{A}_I)}{\partial\underset{\sim}{M}}\right) \tag{1.46}$$

This model of plastic spin will be studied in the case of crystal plasticity (see section 1.4.6).

1.3 Implementation in an object oriented FEM code

1.3.1 Object oriented architecture

The full description of the implementation of a generic formulation of constitutive equations in an object–oriented code, like the Z-set software[2] used in the present work, is detailed in [Foerch et al., 1997; Besson et al., 2009]. The software is designed such that material models are implemented independently from the FEM. Therefore, the material library can be used by other FEM codes. This is made possible by proper interfaces between the FEM software and the material library Z-mat. The implementation of a generic material behaviour requires the following ingredients:

- `grad`: the imposed variables *e.g.* $\underset{\sim}{F}$. It allows driving the behaviour externally.
- `flux`: returned variable associated to a `grad` variable. It represents the response of the behavior law to the application of `grad` variable, *e.g.* Cauchy stress $\underset{\sim}{\sigma}$, Boussinesq stress $\underset{\sim}{P}$
- `EP`: external parameters as temperature, humidity, grain size, ... `EP` are set by the user and thus always known in advance.

---

[2] See `www.zset-software.com`

- `VINT`: Integrated variables which are to be integrated over a given time increment in order to update `flux`, *e.g.* $\underset{\sim}{\boldsymbol{F}}^e$, $\boldsymbol{\alpha}_I$, ...

- `VAUX`: auxiliary variables do not define the material state directly, and they are kept for output. They may be useful in post-processing.

- `COEFF`: material parameters appearing as coefficients introduced in constitutive laws. They may depend on `EP`, `VINT` and `VAUX`.

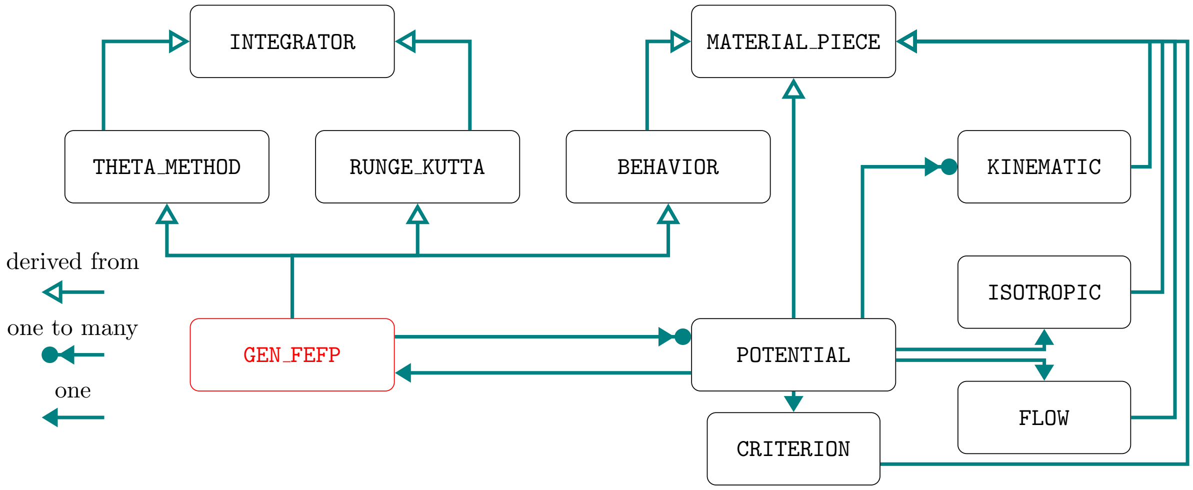

Figure 1.2: *A diagram showing the organization of some objects used to build material behaviors.*

Fig. 1.2 describes the implementation of a class named `GEN_FEFP` derived from `BEHAVIOR`. This class allows to consider various inelastic mechanisms through the class `POTENTIAL`. Each potential includes a flow rule (time-independent plasticity, Norton power law...), several isotropic and kinematic hardening rules. The internal variables associated with kinematic hardening (*i.e.* $\underset{\sim}{\alpha}$) are held by the corresponding `KINEMATIC` object. Explicit and implicit integration of constitutive equations are handled by `RUNGE_KUTTA` and `THETA_METHOD` classes, respectively. The `CRITERION` object specifies the yield surface (von Mises, Tresca, Hill, ...). This implementation allows a minimum programming effort since all the required classes to build a material behavior (except `GEN_FEFP`) are already implemented and used in the framework of other formulations (small strain, hypoelasto-plasticity, ...).

1.3.2 Global resolution of equilibrium equations

The current (resp. reference) configuration of the body at time t (resp. t_0) is called V (resp. V_0) with boundary ∂V (resp. ∂V_0). The latter can be split into the sub–boundaries ∂V^u and ∂V^{tr} such that $\partial V = \partial V^u \cup \partial V^{tr}$ and $\partial V^u \cap \partial V^{tr} = \emptyset$, where Dirichlet and Neumann conditions are respectively prescribed. Corresponding surfaces ∂V_0^u and ∂V_0^{tr} are defined on the reference boundary of the body. The space of kinematically admissible displacements field is the set of sufficiently regular displacement functions that satisfies

$$\mathscr{K} = \{\underline{\boldsymbol{u}}(\underline{\boldsymbol{x}}) | \underline{\boldsymbol{u}} = \underline{\tilde{\boldsymbol{u}}}(\underline{\boldsymbol{x}}) \quad \text{if} \quad \underline{\boldsymbol{x}} \in \partial V^u\} \tag{1.47}$$

knowing that $\underline{\tilde{\boldsymbol{u}}}$ is the prescribed displacement field on ∂V^u. Virtual displacements are set to zero over ∂V^u defining the space of virtual displacements as

$$\mathscr{V} = \{\underline{\boldsymbol{\eta}}(\underline{\boldsymbol{x}}) | \underline{\boldsymbol{\eta}}(\underline{\boldsymbol{x}}) = 0 \quad \text{if} \quad \underline{\boldsymbol{x}} \in \partial V^u\} \tag{1.48}$$

The surface tractions are prescribed over the region ∂V^{tr}.

Following [Neto et al., 2008] among others, the initial boundary value problem amounts to find a displacement field $\underline{\boldsymbol{u}} \in \mathscr{K}$ that satisfies

$$\mathscr{W}(\underline{\boldsymbol{u}},\underline{\boldsymbol{\eta}}) = 0, \quad \forall \underline{\boldsymbol{\eta}} \in \mathscr{V} \tag{1.49}$$

where the virtual work functional under finite deformation is given by

$$\mathscr{W}(\underline{\boldsymbol{u}},\underline{\boldsymbol{\eta}}) = \int_{V_0} \left(\underset{\sim}{\boldsymbol{P}} : \nabla_X \underline{\boldsymbol{\eta}} - \underline{\boldsymbol{b}}.\underline{\boldsymbol{\eta}}\right) dV - \int_{\partial V_0^{tr}} \underline{\boldsymbol{t}}.\underline{\boldsymbol{\eta}} dS \tag{1.50}$$

where $\underline{\boldsymbol{b}}$ and $\underline{\boldsymbol{t}}$ denote the reference body force and surface traction fields, respectively. $\underset{\sim}{\boldsymbol{P}}$ stands for the Boussinesq stress tensor. The linearization of Eq. (1.49) at a given state defined by the field $\underline{\boldsymbol{u}}^*$ is written

$$\mathscr{W}(\underline{\boldsymbol{u}}^*,\underline{\boldsymbol{\eta}}) + D\mathscr{W}(\underline{\boldsymbol{u}}^*,\underline{\boldsymbol{\eta}})[\Delta\underline{\boldsymbol{u}}] = 0, \quad \forall \underline{\boldsymbol{\eta}} \in \mathscr{V} \tag{1.51}$$

where $D\mathscr{W}(\underline{\boldsymbol{u}}^*,\underline{\boldsymbol{\eta}})[\Delta\underline{\boldsymbol{u}}]$ is the directional derivative of $\mathscr{W}(\underline{\boldsymbol{u}}^*,\underline{\boldsymbol{\eta}})$ in the direction of $\Delta\underline{\boldsymbol{u}}$. For convenience, the force and surface traction fields on ∂V_0^{tr} are assumed to be independent of the displacement field. Then,

$$\begin{aligned}
D\mathscr{W}(\underline{\boldsymbol{u}}^*,\underline{\boldsymbol{\eta}})[\Delta\underline{\boldsymbol{u}}] &= \frac{d}{d\varepsilon}\left(\mathscr{W}(\underline{\boldsymbol{u}}^* + \varepsilon\Delta\underline{\boldsymbol{u}},\underline{\boldsymbol{\eta}})\right)\bigg|_{\varepsilon=0} &\quad (1.52)\\
&= \frac{d}{d\varepsilon}\left(\int_{V_0} \underset{\sim}{\boldsymbol{P}}(\underset{\sim}{\boldsymbol{F}}^* + \varepsilon\Delta\underset{\sim}{\boldsymbol{F}}) : \nabla_X \underline{\boldsymbol{\eta}}\right)\bigg|_{\varepsilon=0} &\quad (1.53)\\
&= \frac{d}{d\varepsilon}\left(\int_{V_0} \left[\underset{\sim}{\boldsymbol{P}}(\underset{\sim}{\boldsymbol{F}}^*) + \Delta\underset{\sim}{\boldsymbol{P}}(\underset{\sim}{\boldsymbol{F}}^*, \varepsilon\Delta\underset{\sim}{\boldsymbol{F}})\right] : \nabla_X \underline{\boldsymbol{\eta}}\right)\bigg|_{\varepsilon=0} &\quad (1.54)\\
&= \int_{V_0} \left[\frac{\partial \underset{\sim}{\boldsymbol{P}}}{\partial \Delta\underset{\sim}{\boldsymbol{F}}}\bigg|_{\underset{\sim}{\boldsymbol{F}}^*} : \Delta\underset{\sim}{\boldsymbol{F}}\right] : \nabla_X \underline{\boldsymbol{\eta}} &\quad (1.55)
\end{aligned}$$

where

$$\Delta\underset{\sim}{\boldsymbol{F}} = \nabla_X(\Delta\underline{\boldsymbol{u}}), \qquad \underset{\sim}{\boldsymbol{F}}^* = \underset{\sim}{\boldsymbol{1}} + \nabla_X \underline{\boldsymbol{u}}^* \tag{1.56}$$

The Boussinesq stress tensor $\underset{\sim}{\boldsymbol{P}}$ is related to Kirchhoff's stress tensor $\underset{\sim}{\boldsymbol{\tau}}$ by

$$\underset{\sim}{\boldsymbol{P}} = \underset{\sim}{\boldsymbol{\tau}}\underset{\sim}{\boldsymbol{F}}^{-T} \tag{1.57}$$

The tangent modulus is computed as

$$\underset{\approx}{\mathscr{A}} = \frac{\partial \underset{\sim}{\boldsymbol{P}}}{\partial \Delta\underset{\sim}{\boldsymbol{F}}}\bigg|_{\underset{\sim}{\boldsymbol{F}}^*} = \frac{\partial \underset{\sim}{\boldsymbol{\tau}}}{\partial \Delta\underset{\sim}{\boldsymbol{F}}}\bigg|_{\underset{\sim}{\boldsymbol{F}}^*} \underset{\sim}{\boldsymbol{F}}^{-T} + \underset{\sim}{\boldsymbol{\tau}} \frac{\partial \underset{\sim}{\boldsymbol{F}}^{-T}}{\partial \Delta\underset{\sim}{\boldsymbol{F}}}\bigg|_{\underset{\sim}{\boldsymbol{F}}^*} \tag{1.58}$$

or in index notation

$$\mathscr{A}_{ijkl} = \frac{\partial \tau_{ip}}{\partial \Delta F_{kl}} F^{-1}_{jp} - \tau_{ip} F^{-1}_{jk} F^{-1}_{lp} \tag{1.59}$$

By approximating the domain V_0 with a finite number of elements n_{el} denoted by V_0^e, the discrete form of the virtual work (1.50) is written

$$\sum_{e=0}^{n_{el}} \int_{V_0^e} \left([\boldsymbol{B}]^T\{\boldsymbol{P}\} - [\boldsymbol{N}^T]\{\boldsymbol{b}\}\right) dV - \sum_{e=0}^{n_{el}} \int_{\partial V_0^{tr,e}} [\boldsymbol{N}]^T\{\boldsymbol{t}\}\, dS = 0 \tag{1.60}$$

$[\boldsymbol{N}]$ and $[\boldsymbol{B}]$ denote the interpolation matrix and the discrete material gradient operator, respectively (see appendix B.1). The element stiffness matrix is given by

$$[\boldsymbol{K}^e] = \int_{V_0^e} [\boldsymbol{B}]^T[\mathscr{A}][\boldsymbol{B}] dV \tag{1.61}$$

Table 1.1: *Iterative resolution algorithm of the incremental boundary value problem*

```
Result: Compute the displacement $\underline{\boldsymbol{u}}_{n+1}$ at $t_{n+1}$
(i) Set initial guess $\underline{\boldsymbol{u}}^{(0)}_{n+1}$ , $k = 1$
while $k < N^{max}_{iter}$ do
    (ii) $\underline{\boldsymbol{u}}^{(k)}_{n+1} = \underline{\boldsymbol{u}}^{(k-1)}_{n+1} + \Delta\underline{\boldsymbol{u}}^{(k)}$
    (iii) $\underset{\sim}{\boldsymbol{F}}^{(k)}_{n+1} = \underset{\sim}{\boldsymbol{1}} + \nabla_X \underline{\boldsymbol{u}}^{(k)}_{n+1}$
    (iv) Update stress and state variables using constitutive equations
    (v) Compute consistent tangent moduli $\underset{\approx}{\mathscr{A}}^c$
    (vi) Calculate residuals $\mathfrak{R}\left(\underline{\boldsymbol{u}}^{(k)}_{n+1}\right) = f^{int}\left(\underline{\boldsymbol{u}}^{(k)}_{n+1}\right) - f^{ext}_{n+1}$
    if convergence then
        go to next increment n+1 (i)
    else
        (vii) Compute global stiffness matrix $[\boldsymbol{K}]^g$
        (viii)$\Delta\underline{\boldsymbol{u}}^{(k+1)} = -[\boldsymbol{K}^g]^{-1}\mathfrak{R}$    , k←k+1
    end
end
```

The global stiffness matrix is obtained by assembling the element tangent stiffness matrices as

$$[\boldsymbol{K}^g] = \mathop{\mathsf{A}}_{e=1}^{n_{el}} ([\boldsymbol{K}^e]) \tag{1.62}$$

The linear set of equations to be solved for $\Delta\underline{\boldsymbol{u}}$ iteratively is given by

$$[\boldsymbol{K}]^g \Delta\underline{\boldsymbol{u}} = -\mathfrak{R}(\underline{\boldsymbol{u}}) \tag{1.63}$$

where

$$\mathfrak{R}\left(\underline{\boldsymbol{u}}\right) = f^{int}\left(\underline{\boldsymbol{u}}\right) - f^{ext} \tag{1.64}$$

The global internal and external forces are written

$$f^{int} = \mathop{\mathsf{A}}_{e=1}^{n_{el}} \left(\int_{V_0^e} [\boldsymbol{B}]^T \{\boldsymbol{P}\} dV \right) \tag{1.65}$$

$$f^{ext} = \mathop{\mathsf{A}}_{e=1}^{n_{el}} \left(\int_{V_0^e} [\boldsymbol{N}^T]\{\boldsymbol{b}\} dV + \int_{\partial V_0^{tr,e}} [\boldsymbol{N}]^T \{\boldsymbol{t}\} dS \right) \tag{1.66}$$

The consistent tangent moduli $\underset{\approx}{\mathscr{A}}^c$ are calculated from the implicit incremental constitutive equations as

$$\frac{\partial \underset{\sim}{\boldsymbol{\tau}}(\alpha_n, \underset{\sim}{\boldsymbol{F}}_{n+1})}{\partial \Delta \underset{\sim}{\boldsymbol{F}}_{n+1}} = \frac{\partial \underset{\sim}{\boldsymbol{\tau}}(\alpha_n, \underset{\sim}{\boldsymbol{F}}_{n+1})}{\partial \Delta \underset{\sim}{\boldsymbol{F}}^e_{n+1}} \frac{\partial \Delta \underset{\sim}{\boldsymbol{F}}^e_{n+1}}{\partial \Delta \underset{\sim}{\boldsymbol{F}}_{n+1}} \tag{1.67}$$

The general iterative resolution algorithm of the incremental boundary value problem is summarized in Table 1.1.

1.3.3 Integration of constitutive equations

The set of time–integrated variables is given by

$$\mathscr{V}_{int} = \left\{ \underset{\sim}{\boldsymbol{F}}^e \middle| \, p_1, \, \boldsymbol{\alpha}_1; \, \cdots ; \, p_n, \, \boldsymbol{\alpha}_n \right\} \tag{1.68}$$

p_i is the accumulated inelastic strain associated with the i-th mechanism, $\boldsymbol{\alpha}_i$ denote internal variables describing both isotropic (*e.g.* r_i) and kinematic hardening (*e.g.* $\underset{\sim}{\boldsymbol{\alpha}}_i$) specific to each mechanism. Semicolons in (1.68) represent the separation between different mechanisms. A distinction between $\boldsymbol{\alpha}_i$ and p_i was considered so that partial derivatives required by integration methods can be implemented efficiently. The model for each deformation mechanism will be defined by the following system of elementary equations via the `POTENTIAL` interface:

- Plasticity criteria $f_i(\underset{\sim}{\boldsymbol{M}}, p_i, \boldsymbol{\alpha}_i)$: Each criterion depends on the Mandel stress tensor, the accumulated plastic strain and variables that describe multi-kinematic hardening. Only the case where a criterion is associated with one and only one dissipation potential is discussed in the following. Alternative models involving multi-mechanisms and one single unified criterion can be found in [Cailletaud, 2017]. The implementation of this kind of models is discussed thoroughly in [Foerch et al., 1997].

- Flow rule: The plastic multiplier is defined in two ways. For time-independent plasticity, $\dot{\lambda}$ must fulfill the consistency condition Eq. (1.17). In the rate–dependent case, the multiplier is defined as the derivative of dissipation potential Ω_i w.r.t. the yield function f_i Eq. (1.18). It follows that

  $$\underset{\sim}{\boldsymbol{L}}^p_i = \dot{\lambda}_i \frac{\partial f_i}{\partial \underset{\sim}{\boldsymbol{M}}} = \dot{\lambda}_i \underset{\sim}{\boldsymbol{N}}_i \tag{1.69}$$

  with $\underset{\sim}{\boldsymbol{N}}_i$ being the inelastic flow direction.

- Isotropic and kinematic hardening laws take the generic form

  $$\dot{\boldsymbol{\alpha}}_i = \dot{\lambda}_i \boldsymbol{m}_i - \dot{\boldsymbol{q}}_i \tag{1.70}$$

  where $\boldsymbol{m}_i$ is the hardening potential normal and $\dot{\boldsymbol{q}}_i$ represents the time derivative of the hardening variable evolution due to static recovery effects. Note that in case of associated plasticity, $\boldsymbol{m}_i = \dfrac{\partial f}{\partial \boldsymbol{A}_i}$, meaning that the hardening potential normal is simply given by the normal to the yield surface. For instance, $\underset{\sim}{\boldsymbol{m}}_i = \underset{\sim}{\boldsymbol{N}}_i - \dfrac{3D_i}{2C_i} \underset{\sim}{\boldsymbol{X}}_i$ for nonlinear kinematic hardening. The evolution of the nonlinear isotropic hardening variable r, from Eq. (1.14), writes $\dot{r} = \dot{\lambda}(1 - \dfrac{R}{Q})$ which imply that $m = 1 - \dfrac{R}{Q}$. The integrated variable r is related to R by $R = bQr$ (see Eq. (1.15)), with the material parameters b and Q. The latter model can be integrated analytically (cf. Eq. (1.105) in Section 1.5), which allows to reduce the number of time–integrated variables in the code.

Two integration methods for ordinary differential equations have been implemented for the present general formulation. The first one is explicit, namely second or fourth order Runge-Kutta methods with automatic time–stepping, the second one is implicit: θ-method resolved using the iterative Newton-Raphson scheme. Each inelastic deformation mechanism is accounted for within the class `POTENTIAL`. This class provides the increment of integrated variables for explicit integration and residuals for implicit integration. Each `POTENTIAL` object possesses various methods with regard to the model definition (isotropic and kinematic hardening, yield criteria, ...). The implementation supports an unlimited number of `POTENTIAL` objects with possible interactions. In case of interactions, another class is dedicated to add interaction terms appropriately. The expression of $\underset{\sim}{\boldsymbol{L}}^p$ is calculated through summation of all potential contributions according to Eq. (1.27), in addition to the supplementary ad-hoc constitutive equation for the plastic spin.

`RUNGE_KUTTA`: the integration of variables is based on the calculation of the rate of $\mathcal{V}_{int}$. For viscoplastic cases, the plastic multiplier is calculated using the flow rule. For time-independent plasticity, the increment

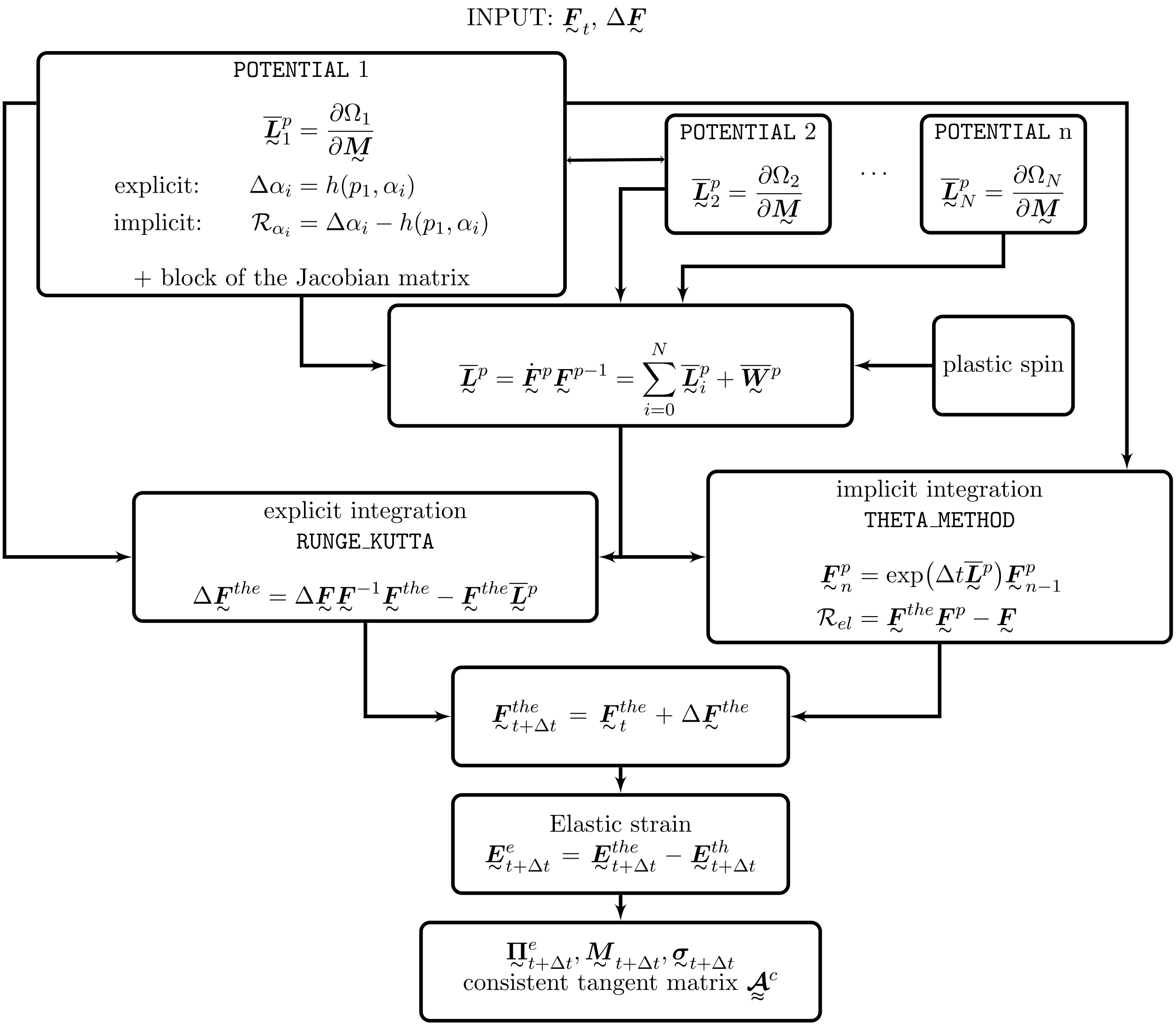

Figure 1.3: *Diagram showing explicit and implicit integration methods. Each* `POTENTIAL` *provides the update of associated internal variables and the corresponding block of the Jacobian matrix.*

of the plastic multiplier is derived from the consistency condition as

$$\begin{aligned} 2\underset{\sim}{N} : \left[\underset{\sim}{\mathbf{1}} \underline{\otimes} \underset{\sim}{\boldsymbol{\Pi}}^e + \frac{1}{2}\underset{\sim}{C}^e . \underset{\approx}{\mathbb{C}}\right] : \left(\underset{\sim}{F}^{eT}\underset{\sim}{D}\underset{\sim}{F}^e - \underset{\sim}{C}^e \sum_{i,\dot\lambda_i\neq\dot p}^{N} \underset{\sim}{\overline{L}}_i^p\right) \\ + \frac{\partial f}{\partial \boldsymbol{A}_i} : \sum_i^N \frac{\partial \boldsymbol{A}_i}{\partial \boldsymbol{\alpha}_i}\dot{\boldsymbol{\alpha}}_i + \frac{\partial f}{\partial p_i}\dot p_i + \frac{\partial f}{\partial \mathrm{EP}} : \dot{\mathrm{EP}} = 0 \end{aligned} \tag{1.71}$$

`THETA_METHOD:` $\theta = 0$ corresponds to the explicit Euler method and $\theta = 1$ results in the so-called backward Euler method. The constitutive equations are expressed in the residual form as follows

$$\underline{\mathscr{R}} = \begin{pmatrix} \mathscr{R}_{el} \\ \mathscr{R}_{p_i} \\ \mathscr{R}_{\alpha_i} \end{pmatrix} \tag{1.72}$$

where

$$\mathscr{R}_{el} = \underset{\sim}{\boldsymbol{F}}^e \underset{\sim}{\boldsymbol{F}}^p - \underset{\sim}{\boldsymbol{F}} \qquad \text{or} \qquad \mathscr{R}_{el} = \Delta \underset{\sim}{\boldsymbol{F}}^e - \Delta \underset{\sim}{\boldsymbol{F}} \underset{\sim}{\boldsymbol{F}}^{-1} \underset{\sim}{\boldsymbol{F}}^e_{cor} + \underset{\sim}{\boldsymbol{F}}^e_{cor} \sum_{i=0}^{N} \Delta p_i \underset{\sim}{\boldsymbol{N}}_i \tag{1.73}$$

$$\mathscr{R}_{p_i} = f_i(\underset{\sim}{\boldsymbol{M}}, \boldsymbol{A}_i) \qquad \text{or} \qquad \mathscr{R}_{p_i} = \Delta p_i - \Delta t \frac{\partial \Omega}{\partial f_i} \quad \text{(viscoplasticity)} \tag{1.74}$$

$$\mathscr{R}_{\alpha_i} = \Delta \boldsymbol{\alpha}_i - \Delta p_i \boldsymbol{m}_i - \Delta t \dot{\boldsymbol{q}}_i \tag{1.75}$$

N being the total number of mechanisms. The residual in Eq. (1.73)-left involves the use of the exponential mapping which satisfies the plastic incompressibility [Weber and Anand, 1990; Miehe, 1996]. Its linearization requires the expression of the derivative of the exponential of a second order tensor w.r.t. a second order tensor. As $\underset{\sim}{\boldsymbol{L}}^p$ is in general non symmetric, calculating these terms is a non-trivial task. In that case, the infinite series representation is used and truncated [Dettmer and Reese, 2004; Hashiguchi, 2019]. Alternatively, in Eq. (1.73)b, the plastic incompressibility is not satisfied anymore. For this reason, the elastic part of the deformation gradient is corrected at each iteration as

$$\underset{\sim}{\boldsymbol{F}}^e_{cor} = \left(\frac{\det \underset{\sim}{\boldsymbol{F}}}{\det \underset{\sim}{\boldsymbol{F}}^e} \right)^{\frac{1}{3}} \underset{\sim}{\boldsymbol{F}}^e \tag{1.76}$$

The values of all associated forces and parameters evaluated at an intermediate time designated by θ are

$$\mathscr{V}^{t+\theta\Delta t}_{int} = \mathscr{V}^{t}_{int} + \theta \Delta \mathscr{V}_{int} \tag{1.77}$$

The set of equations (1.73,1.74,1.75) can be gathered in the following form

$$\underline{\mathscr{R}}(\mathscr{V}^{t+\theta\Delta t}_{int}, \Delta \mathscr{V}_{int}) = 0 \tag{1.78}$$

Since Eq. (1.78) is highly nonlinear, it is usually solved by means of a Newton method which requires the calculation of the Jacobian matrix [J]. The new estimate of $\Delta \mathscr{V}^{k+1}_{int}$ is then given by

$$\Delta \mathscr{V}^{k+1}_{int} = \Delta \mathscr{V}^{k}_{int} - [J]^{-1} \underline{\mathscr{R}}^k \tag{1.79}$$

where

$$[J] = \left. \frac{\partial \underline{\mathscr{R}}}{\partial \Delta \mathscr{V}_{int}} \right|_{k+1} \tag{1.80}$$

and $\mathscr{R}^k$ denotes the local residual at the k-th iteration. The variation of $\mathscr{R}$ resulting from the variation of v_{int} and $\underset{\sim}{\boldsymbol{F}}$ vanishes as well

$$\delta \underline{\mathscr{R}} = \frac{\partial \underline{\mathscr{R}}}{\partial \Delta \mathscr{V}_{int}} \delta \Delta \mathscr{V}_{int} + \frac{\partial \underline{\mathscr{R}}}{\partial \Delta F} \delta \Delta \underset{\sim}{\boldsymbol{F}} = 0 \tag{1.81}$$

which implies that, after convergence, the inverted Jacobian matrix relates the change of Δv_{int} with respect to a change in $\Delta \underset{\sim}{\boldsymbol{F}}$ as

$$\delta \Delta \mathscr{V}_{int} = - \left(\frac{\partial \underline{\mathscr{R}}}{\partial \Delta v_{int}} \right)^{-1} \frac{\partial \underline{\mathscr{R}}}{\partial \Delta F} \delta \Delta \underset{\sim}{\boldsymbol{F}} \tag{1.82}$$

The expression of the Jacobian matrix is detailed in the appendix (C.1). By using Eq. (1.82), one can calculate the term $\dfrac{\partial \Delta \underset{\sim}{\boldsymbol{F}}^e}{\partial \Delta \underset{\sim}{\boldsymbol{F}}}$ in Eq. (1.67).

1.4 Applications to volume element simulations

The capabilities of the model formulation and its implementation are illustrated in this section in the case of complex homogeneous loading conditions. The tests are therefore performed at the material point level and require the integration of constitutive equations. Some original features of the models are highlighted.

1.4.1 Cyclic closed deformation path

Hypoelastic formulations are well known to result in some spurious predictions under complex loading conditions. For instance, when a closed strain cycle is applied, the resulting stress cycle is not necessarily closed. This issue was investigated theoretically [Kojić and Bathe, 1987; Lin et al., 2003] and numerically [Brepols et al., 2014] in the case of purely mechanical loadings. In this example, the response of finite strain formulations is investigated in the thermoelastic domain for two different loading cases. In both cases, we consider two hypoelastic constitutive models for the Cauchy stress based on the Jaumann and Green-Naghdi rates and a hyperelastic model given by Eq. (1.23).

Case 1: A cyclic and non-proportional mechanical loading is applied (see Fig. 1.4-a). Accordingly, the applied deformation gradient and the resulting Cauchy stress tensor have the following forms

$$\begin{pmatrix} F_{11}(t) & F_{12}(t) & 0 \\ 0 & 1 & 0 \\ 0 & 0 & 1 \end{pmatrix} \quad \text{and} \quad \underset{\sim}{\sigma} = \begin{pmatrix} \sigma_{11} & \sigma_{12} & 0 \\ \sigma_{12} & \sigma_{22} & 0 \\ 0 & 0 & \sigma_{33} \end{pmatrix} \tag{1.83}$$

where the functions $F_{11}(t)$ and $F_{12}(t)$ are prescribed.

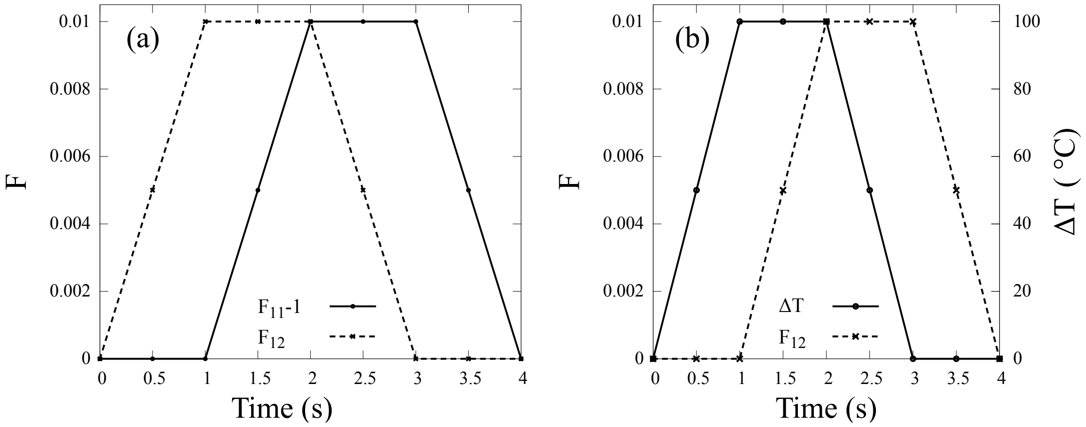

Figure 1.4: *Illustration of loading conditions corresponding to (a) case 1, (b) case 2*

Case 2: Is concerned with a non-proportional thermomechanical loading described in Fig. 1.4-b and corresponding to prescribed shear $F_{12}(t)$ and temperature variation $\Delta T(t)$. The deformation gradient is imposed as

$$\underset{\sim}{F} = \begin{pmatrix} 1 & F_{12}(t) & 0 \\ 0 & F^*_{22} & 0 \\ 0 & 0 & F^*_{33} \end{pmatrix} \quad \text{and} \quad \underset{\sim}{\sigma} = \begin{pmatrix} \sigma_{11} & \sigma_{12} & 0 \\ \sigma_{12} & 0 & 0 \\ 0 & 0 & 0 \end{pmatrix} \tag{1.84}$$

F^*_{22} and F^*_{33} are determined by the analysis in such a way that the conjugate Cauchy stress components vanish. The component σ_{11} does not vanish due to the applied temperature and to the Poynting effect. The figures 1.5 and 1.6 depict an elastically non-consistent response of the two hypoelastic formulations, namely Jaumann and Green-Naghdi. When a closed strain cycle is applied, residual stresses remain at the end of each cycle. Consequently, due to the accumulation of residual stresses during the deformation process, the resulting stress drifts away over cycles. In contrast, for a hyperelastic model, no residual stresses are detected after each cycle, *i.e.* all stress components return back to zero. As suggested by Xiao et al. [1998], some hypoelastic models, *e.g.* based on the logarithmic rate, produce consistent results compared to hyperelastic models. Nevertheless, in the case of elastoplasticity, these rates are no longer integrable [Jiao and Fish,

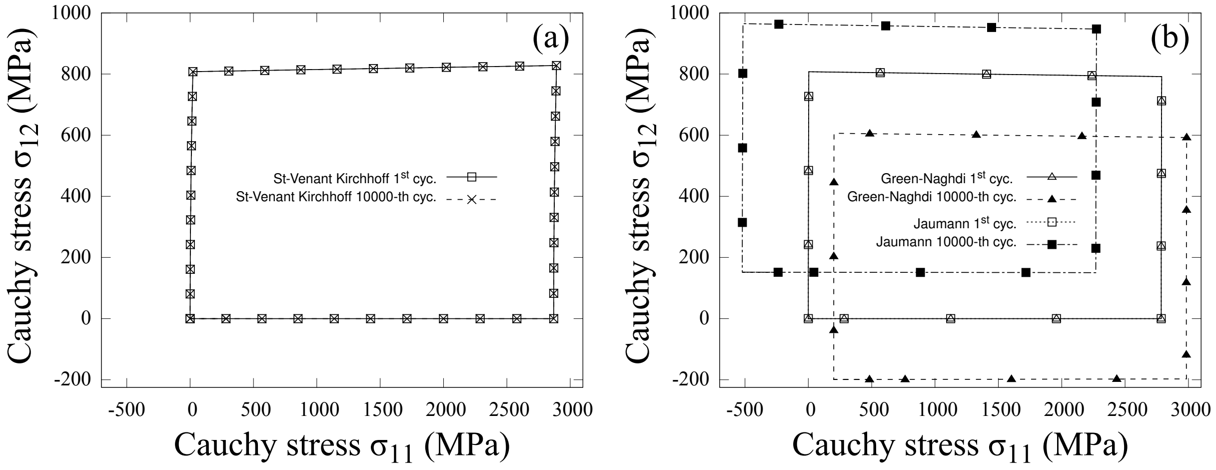

Figure 1.5: *Case 1, the resulting stress during the first and the 10000th cycles for (a) hyperelastic material (b) hypoelastic materials. Young's modulus* $E = 210000$ *MPa, and Poisson ratio* $\nu = 0.3$.

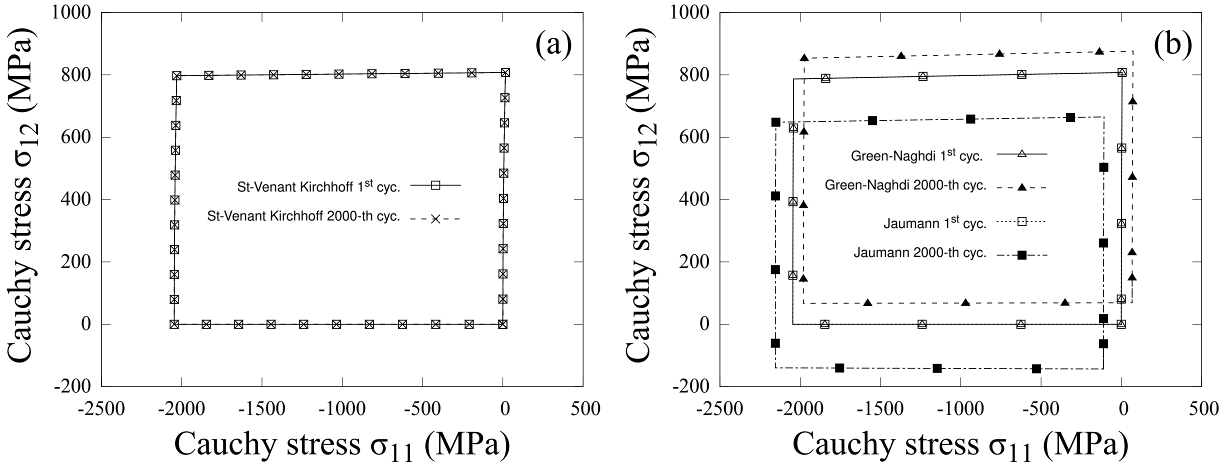

Figure 1.6: *Case 2, the resulting stress during the first and the 2000th cycles for (a) hyperelastic material (b) hypoelastic materials.* $E = 210000$ *MPa,* $\nu = 0.3$ *and* $\alpha_T = 10^{-4} K^{-1}$

2017]. It has been shown that any hypoelastic law is integrable in the case of proportional loading *i.e.* for deformation processes depending on a single parameter [Truesdell and Noll, 1965].

1.4.2 Simple glide with kinematic hardening

The deformation gradient for a simple glide test has the form

$$\underset{\sim}{\boldsymbol{F}} = \begin{pmatrix} 1 & \gamma(t) & 0 \\ 0 & 1 & 0 \\ 0 & 0 & 1 \end{pmatrix} \tag{1.85}$$

In this section, a comparison is drawn between the elastoplastic models previously presented by looking at the classical cases of monotonic and cyclic simple shear. The kinematic hardening contribution ψ^{kin} to the free energy is given in the Neo-Hookean form [Dettmer and Reese, 2004; Hashiguchi, 2019]

$$\psi^{\mathrm{kin}}(\underset{\sim}{\boldsymbol{E}}_s^p) = c\left(\mathrm{tr}(\underset{\sim}{\boldsymbol{E}}_{\mathrm{s}}^{\mathrm{p}}) - \log\left(\det \underset{\sim}{\boldsymbol{F}}_{\mathrm{s}}^{\mathrm{p}}\right)\right) \tag{1.86}$$

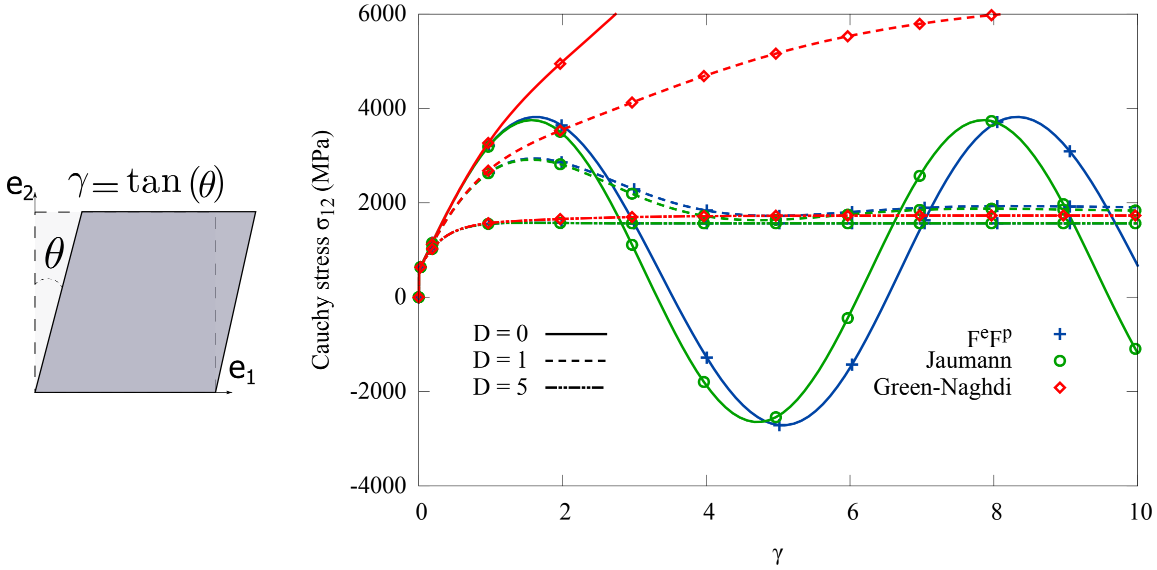

Figure 1.7: *Monotonic simple glide test for different formulations of elastoplasticity with kinematic hardening: Stress oscillations in the case of Jaumann rate and the multiplicative decomposition if $D = 0$. These oscillations are suppressed as the parameter D increases. Values of material parameters: $C = 10000$ MPa, $R_0 = 1000$ MPa.*

In the case of linear kinematic hardening, significant differences are found between the various formulations as shown in Fig. 1.7 and Fig. 1.8. Fig. 1.7 depicts a spurious oscillatory response of both multiplicative and Jaumann formulations. In contrast, the model based on the Green-Naghdi rate predicts that σ_{12} increases monotonically. The model based on the multiplicative decomposition of the plastic part of the deformation gradient does not display oscillations as depicted in Fig. 1.8-a. These oscillations can be suppressed by increasing the value of the parameter D from Eq. (1.37). By doing so, kinematic hardening saturates rapidly which leads to almost the same predictions by different models. Accordingly, when the dynamic recovery term is sufficiently high (compared to the storage part), the saturation rate of the various models becomes similar.

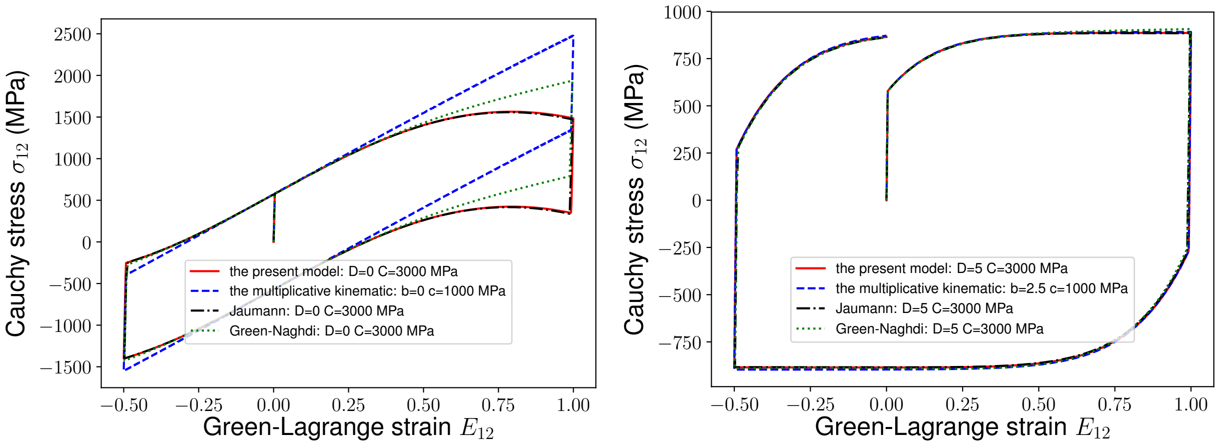

(a) (b)

Figure 1.8: *Cyclic simple glide loading: (a) linear ($D = 0$) (b) nonlinear kinematic hardening with dynamic recovery.*

1.4.3 Static recovery of kinematic hardening

In this example, the effect of the static recovery of the kinematic hardening is illustrated. It corresponds to the last term in the evolution equation Eq. (1.37). This term introduces time-dependent material behavior even in the absence of viscosity. We consider a von Mises surface yield given by

$$f(\underset{\sim}{M},R) = \left((\underset{\sim}{M}-\underset{\sim}{X})^{dev} : (\underset{\sim}{M}-\underset{\sim}{X})^{dev}\right)^{1/2} - R_0 \tag{1.87}$$

where $(\diamond)^{dev}$ denotes the deviatoric part. The back stress $\underset{\sim}{X} = \frac{2}{3}C\underset{\sim}{\alpha}$ and the evolution of $\underset{\sim}{\alpha}$ follows the constitutive equation (1.37). This model is applied to relaxation and creep tests.

Relaxation test under simple glide

A simple glide test is considered according to the following conditions

$$\underset{\sim}{F} = \begin{pmatrix} 1 & \gamma(t) & 0 \\ 0 & 1 & 0 \\ 0 & 0 & 1 \end{pmatrix}, \qquad \gamma(t) = \begin{cases} \dfrac{t}{2} & 0 \le t \le 1 \\ \dfrac{1}{2} & 1 \le t \le 4 \end{cases} \tag{1.88}$$

which corresponds to monotonic glide followed by a constant shear value inducing stress relaxation in order to highlight the impact of the static recovery term. The material response is shown in Fig. 1.9 for three different sets of values of material parameters (m,M). The following features can be observed

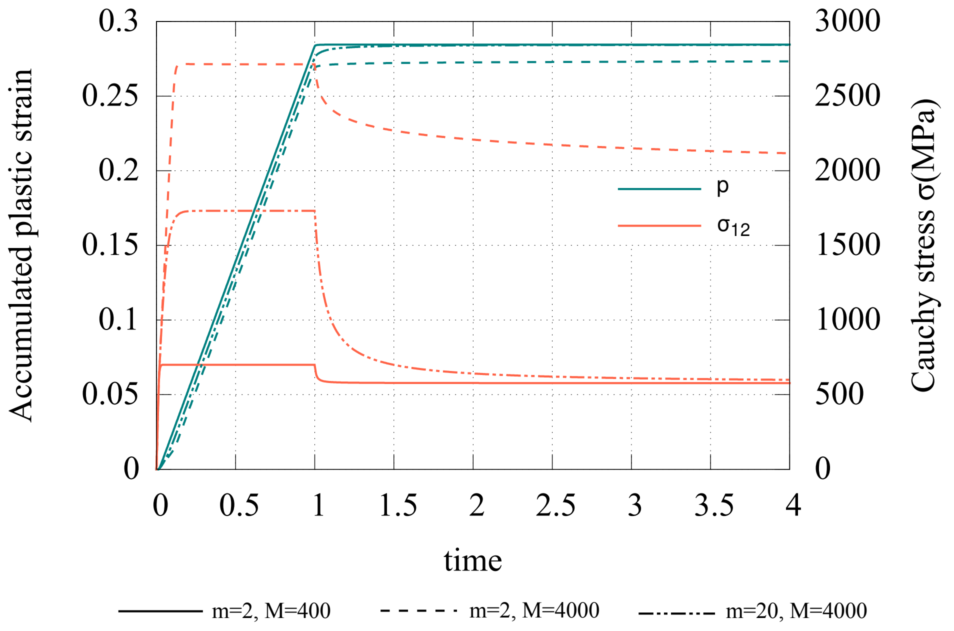

Figure 1.9: *Relaxation test: Higher values of m and lower values of M result in a faster recovery of kinematic hardening.* $C = 300000$ *MPa,* $D = 20$*. Parameter M in MPa.*

- $0 \le t \le 1$: During this time interval, the applied shear is monotonically increasing. After yielding, there is a competition between different terms in Eq. (1.37): storage part, dynamic and static recoveries. For given parameters C and D, a higher value of parameter M or a lower value of parameter m allow for slower recovery of the kinematic hardening leading to a higher value of σ_{12} (see Fig. 1.9).
- $1 \le t \le 4$: The imposed shear strain is constant *i.e.* $\dot{\underset{\sim}{F}} = 0$. Consequently, the variation of the accumulated plastic strain is low due to small elastic strain since $\overline{\underset{\sim}{L}}^p = -\underset{\sim}{F}^{e-1}\dot{\underset{\sim}{F}}^e$ during a relaxation

test. Therefore, the evolution of the kinematic hardening variable reduces to

$$\dot{\underset{\sim}{\alpha}} \approx -\frac{3}{2}\left(\frac{J(\underset{\sim}{X})}{M}\right)^m \frac{\underset{\sim}{X}}{J(\underset{\sim}{X})} \tag{1.89}$$

The recovery rate increases then with higher values of the power m (resp. lower values of M).

In metals, this effect occurs significantly at high temperature due to thermal activation. In fact, the crystalline structure of the metal is partially recovered by annihilation of dislocations and redistribution of point defects [Lemaitre and Chaboche, 1994]. This relaxation of internal stresses generally results in a decrease of the mechanical resistance.

Creep test

In this example, the imposed deformation components are $F_{ij} = 0$ for $i \neq j$ and $\{ij\} \neq \{12\}$. F_{11}, F_{22}, F_{33} and F_{12} are set to be free. The imposed Cauchy stress component σ_{12} is given by

$$\sigma_{12} = \begin{cases} 1000t \text{ MPa}, & 0 \leq t \leq 1 \\ 1000 \text{ MPa}, & 1 \leq t \leq 4 \end{cases} \tag{1.90}$$

and the remaining components of Cauchy stress tensor will vanish. The material response is shown in Fig. 1.10. It is important to note that the used model does not include any viscosity, meaning that the yield condition is exactly fulfilled. The creep deformation is induced solely by the static relaxation of the back-stress that has developed during the loading stage (see Eq. (1.37)):

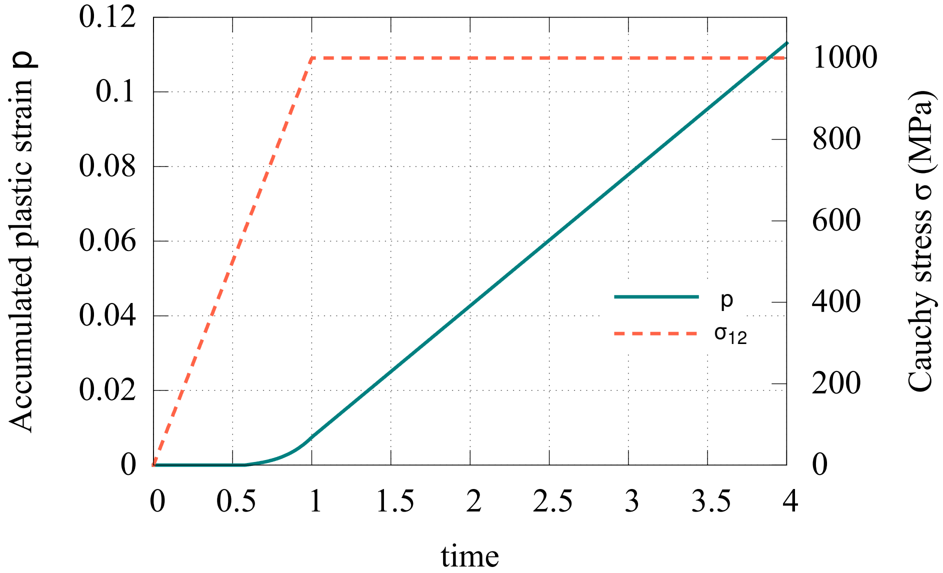

Figure 1.10: *Plastic flow during a creep test.*

- $0 \leq t \leq 1$: As the imposed stress increases, the accumulated plastic strain increases after yielding ($\sigma_{12} = \sqrt{3}R_0$).
- $1 \leq t \leq 4$: According to the consistency condition, the kinematic hardening does not evolve since the applied stress is constant. Therefore, the plastic multiplier is constant and the accumulated plastic multiplier increases linearly. Due the static recovery term, the model becomes time-dependent. In other words, if the static recovery term is omitted, then $\dot{\underset{\sim}{\alpha}} = 0 \Rightarrow \dot{p} = 0$.

1.4.4 Application to a von Mises-based multimechanism model

The concept of multimechanism modeling is applied in this section to the isotropic von Mises plasticity. A model is introduced involving two inelastic mechanisms and two plasticity criteria, called 2M2C in the terminology defined in the references [Cailletaud and Saï, 1995; Cailletaud, 2017]. The yield function, flow rule and evolution equations adopted for this example are as follows

$$f_p(\underset{\sim}{\boldsymbol{M}},\underset{\sim}{\boldsymbol{X}}_p)=\left((\underset{\sim}{\boldsymbol{M}}-\underset{\sim}{\boldsymbol{X}}_p)^{dev}:(\underset{\sim}{\boldsymbol{M}}-\underset{\sim}{\boldsymbol{X}}_p)^{dev}\right)^{1/2}-R_{0p} \tag{1.91}$$

$$f_v(\underset{\sim}{\boldsymbol{M}},\underset{\sim}{\boldsymbol{X}}_v)=\left((\underset{\sim}{\boldsymbol{M}}-\underset{\sim}{\boldsymbol{X}}_v)^{dev}:(\underset{\sim}{\boldsymbol{M}}-\underset{\sim}{\boldsymbol{X}}_v)^{dev}\right)^{1/2}-R_{0v} \tag{1.92}$$

$$\dot{v}=\left\langle\frac{f_v}{K}\right\rangle^n,\ \dot{p}=\frac{\underset{\sim}{\boldsymbol{N}}_p:\left(\underset{\sim}{\boldsymbol{1}}\,\underline{\otimes}\,\underset{\sim}{\boldsymbol{\Pi}}^e+\frac{1}{2}\underset{\sim}{\boldsymbol{C}}^e\cdot\underset{\approx}{\mathbb{C}}\right):\left(\underset{\sim}{\boldsymbol{F}}^{eT}\underset{\sim}{\boldsymbol{D}}\underset{\sim}{\boldsymbol{F}}^e-\dot{v}\,\underset{\sim}{\boldsymbol{C}}^e\underset{\sim}{\boldsymbol{N}}_v\right)}{\underset{\sim}{\boldsymbol{N}}_p:\left[(\underset{\sim}{\boldsymbol{1}}\,\underline{\otimes}\,\underset{\sim}{\boldsymbol{\Pi}}^e+\frac{1}{2}\underset{\sim}{\boldsymbol{C}}^e\cdot\underset{\approx}{\mathbb{C}}):(\underset{\sim}{\boldsymbol{C}}^e\underset{\sim}{\boldsymbol{N}}_p)\right]+\frac{1}{3}C_p\underset{\sim}{\boldsymbol{N}}_p:\underset{\sim}{\boldsymbol{m}}_p} \tag{1.93}$$

$$\dot{\underset{\sim}{\boldsymbol{\alpha}}}_p=\dot{p}\left(\frac{\partial f_p}{\partial\underset{\sim}{\boldsymbol{M}}}-D_p\underset{\sim}{\boldsymbol{\alpha}}_p\right),\quad\dot{\underset{\sim}{\boldsymbol{\alpha}}}_v=\dot{v}\left(\frac{\partial f_v}{\partial\underset{\sim}{\boldsymbol{M}}}-D_v\underset{\sim}{\boldsymbol{\alpha}}_v\right) \tag{1.94}$$

$$\begin{pmatrix}\underset{\sim}{\boldsymbol{X}}_p\\ \underset{\sim}{\boldsymbol{X}}_v\end{pmatrix}=\frac{2}{3}\begin{pmatrix}C_p & C_{pv}\\ C_{vp} & C_v\end{pmatrix}\begin{pmatrix}\underset{\sim}{\boldsymbol{\alpha}}_p\\ \underset{\sim}{\boldsymbol{\alpha}}_v\end{pmatrix} \tag{1.95}$$

The first plastic mechanism associated with the yield function f_p is rate–independent, whereas the second one is viscoplastic. The (visco)plastic multipliers are computed either by a power law or the consistency condition, according to Eq. (1.93). The material parameters used in the following examples are given in Table 1.2.

Consider now a simple tensile/compressive test under strain control, divided into five stages. The resulting stress state is uni-axial (σ_{11}). The response of the model for two distinct strain rates is given in Fig. 1.11. The following observations can be made:

- $F_{11}=1.1\,t$, for $0\leq t\leq t_1$ (tension): The (v) mechanism is active first because the corresponding yield stress is taken as $R_{0v}=0$. But after a while, the mechanism (p) is activated once the threshold R_p is reached. In fact, the activation of an inelastic mechanism will depend on the associated initial yield stress and also on the hardening properties of the other mechanism. Higher strain rates induce more plastic strain, while lower strain rates result in more viscoplastic strain.

- $F_{11}=1.1$, for $t_1\leq t\leq t_2$: During this stage the imposed strain is maintained at a constant value. The inelastic deformation remains quasi–constant accompanied by stress relaxation due to dynamic recovery of kinematic hardening.

- $F_{11}=1.1-0.1(t-t_2)$, for $t_2\leq t\leq t_3$ (unloading+compression): The plastic yielding in compression occurs at a rather large stress level due to the Bauschinger effect.

- $F_{11}=0.9$, for $t_3\leq t\leq t_4$: The imposed strain is constant. A quasi–constant inelastic deformation and stress relaxation due to kinematic hardening recovery are observed.

- $F_{11}=0.9+0.1(t-t_4)$, for $t_4<t<t_5$ (unloading phase). At $F_{11}=1$, the residual stress does not vanish due to kinematic hardening.

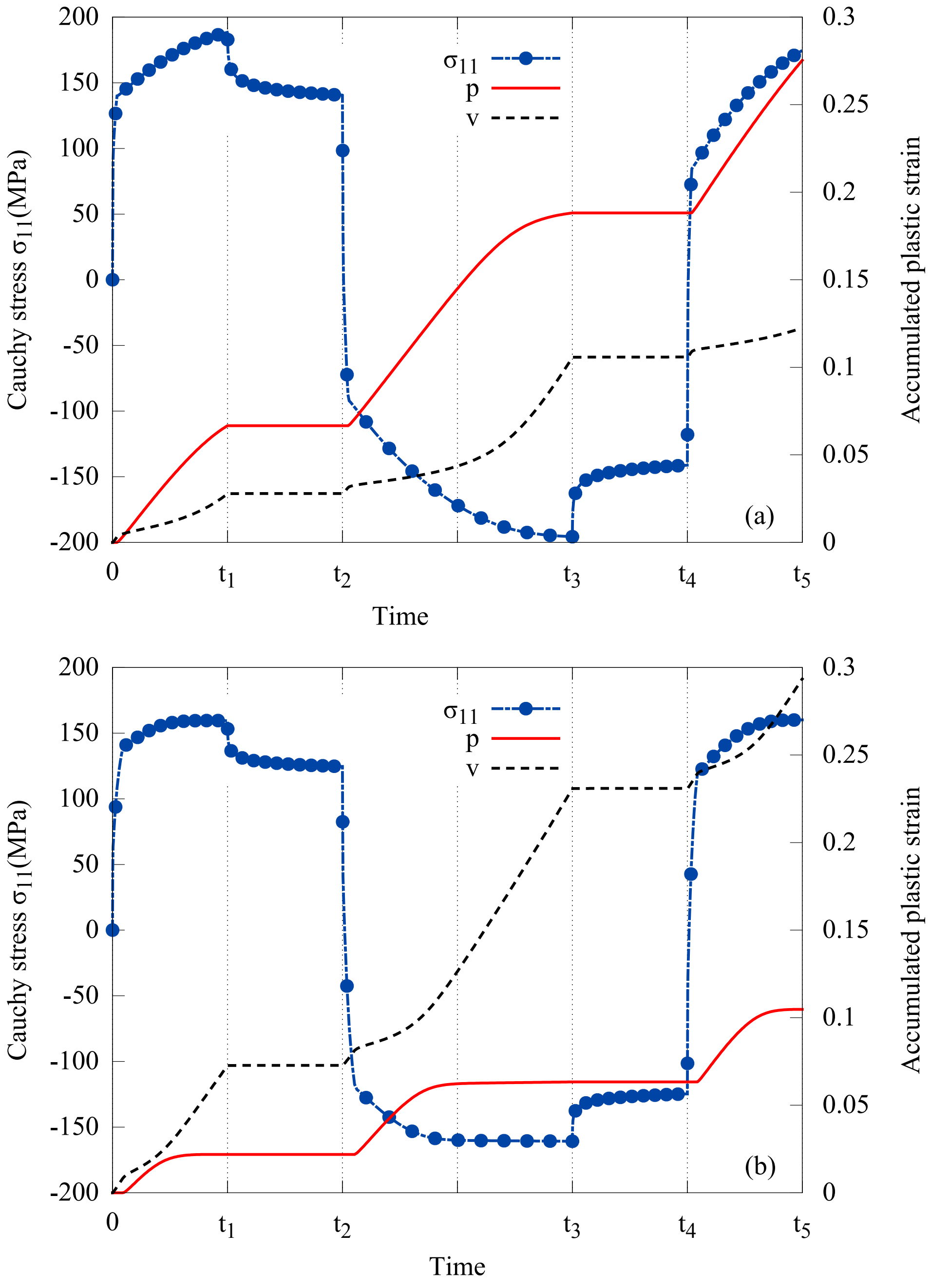

Figure 1.11: *Tension/compression test for two deformation rates* $\dot{F}_{11} = 0.1\ s^{-1}$ *(a) and* $\dot{F}_{11} = 0.001\ s^{-1}$ *(b). Model with a time-independent and a viscoplastic mechanism.*

E	ν	K	n	R_{0v}	C_v	D_v	R_{0p}	C_p	D_p
(MPa)	(-)	(MPa$^{\frac{1}{n}}$)	(-)	(MPa)	(MPa)	(-)	(MPa)	(MPa)	(-)
210000	0.3	120	7	0	20000	200	140	1000	10

Table 1.2: *Material parameters for a model with two inelastic mechanisms:* (p) *time-independent plastic and* (v) *viscoplastic.* $C_{pv} = C_{vp} = 0$ *MPa.*

1.4.5 Plastic spin in anisotropic plasticity

The effect of plastic spin on the response of a Hill perfectly plastic material is illustrated in this example. Hill's yield criterion is expressed in terms of Mandel stress tensor in the form

$$f(\underset{\sim}{M}) = \Big(F(M_{22}-M_{33})^2 + G(M_{33}-M_{11})^2 + H(M_{11}-M_{22})^2 + 2NM_{12}^2 + 2LM_{23}^2 + 2MM_{13}^2 \Big)^{1/2} - R_0 \tag{1.96}$$

where F, G, H, N, M, L are material parameters characterizing the anisotropy of plasticity. This yield function reduces to von Mises if $F = G = H = 0.5$ and $H = N = M = 1.5$.

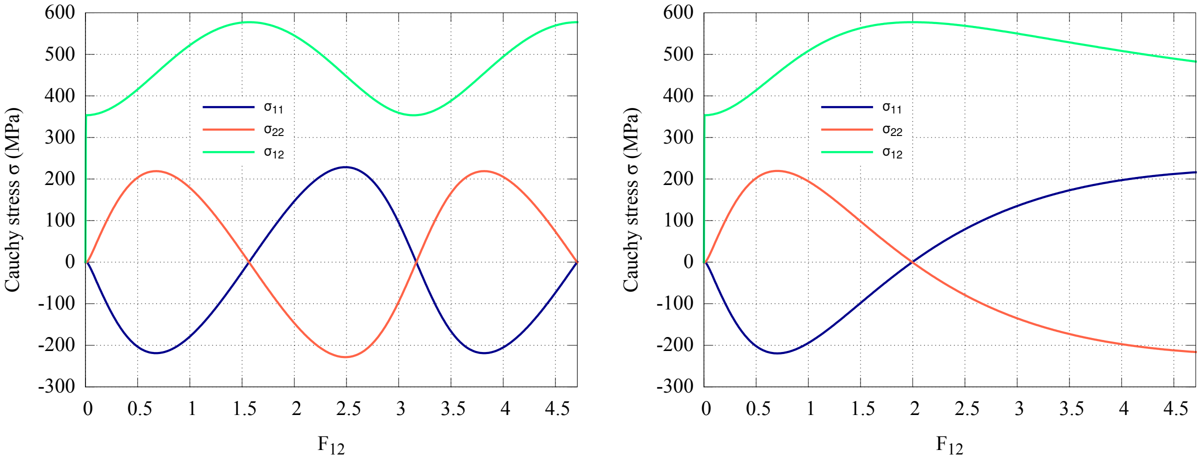

Figure 1.12: *Hypoelastoplastic material response under simple glide loading. Jaumann (left) and Green-Naghdi (right) formulations. Coefficients of Hill's yield criterion used in this simulation:* $F = G = H = 0.5$*,* $L = M = 1.5$*,* $N = 4$*, initial yield stress* $R_0 = 1000\,MPa$*.*

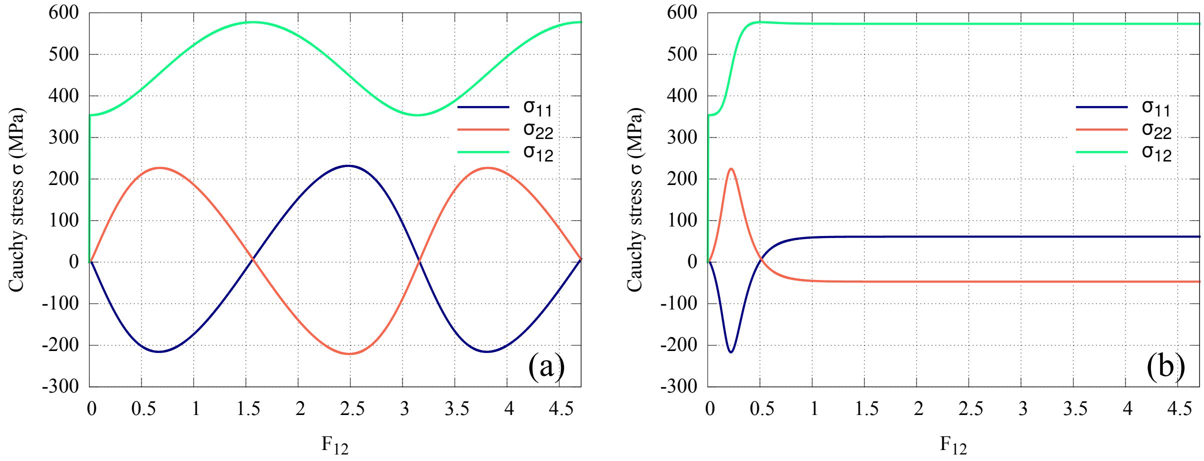

Figure 1.13: *Effect of plastic spin on stress values in the case of simple glide loading. (a) Without plastic spin i.e.* $\beta = 0\ MPa^{-1}$ *(b) with plastic spin* $\beta = 0.01\ MPa^{-1}$*. Multiplicative plasticity model with yield stress* $R_0 = 1000\ MPa$*, Hill yield criterion coefficients* $F = G = H = 0.5$*,* $L = M = 1.5$*,* $N = 4$*.*

A simple glide test is considered with constant shear rate in the plane $(1,2)$. When the hypoelastic-plastic model is used with the Jaumann derivative, the continuum under a constant shear strain rate $\dot{\gamma}$ rotates endlessly at the spin $\dot{\theta}^W = -\frac{\dot{\gamma}}{2}$. Consequently, the spin of directors is equal to $\dot{\theta}^W_{dir} = \dot{\theta}^W = -\frac{\dot{\gamma}}{2}$. The value of σ_{12} oscillates between $\frac{R_0}{\sqrt{2N}}$ at $F_{12} = \gamma = k\pi\,(k \in \mathbb{N})$ and a peak (or valley) value $\frac{R_0}{\sqrt{F+G+4H}}$ at $\gamma = \frac{2k+1}{2}\pi\,(k \in \mathbb{N})$. In the case of the Green-Naghdi formulation, the spin of directors is equal to $\dot{\theta}^R_{dir} = -\frac{2\dot{\gamma}}{4+\gamma^2}$. Therefore, the rotation angle converges to $\pi/2$ as γ goes to infinity. This is illustrated by Fig. 1.13.

The responses of the proposed model are shown in Fig. 1.14. If the plastic spin vanishes *i.e.*

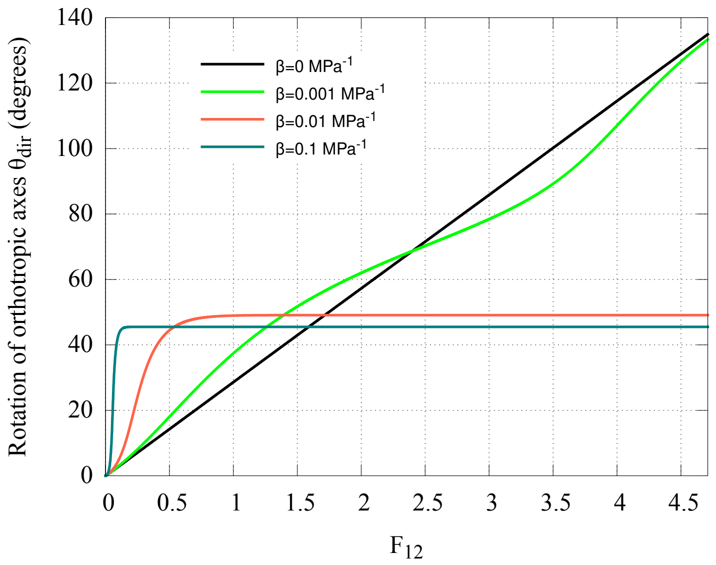

Figure 1.14: *Directors' spin for various values of parameter β during a simple glide test for a Hill perfectly plastic material and multiplicative decomposition. When $\beta = 0\mathrm{MPa}^{-1}$, the rotation rate of directors is constant and coincides with the material spin.*

$\beta = 0\mathrm{MPa}^{-1}$, for small elastic stretches, the proposed model without plastic spin and the model based on Jaumann derivative have the same response. This means that the orthotropic axes rotate at the same rate as the continuum $\dot{\theta} = -\dot{\gamma}/2$. In contrast, as shown in Fig. 1.13, when $\beta \neq 0\mathrm{MPa}^{-1}$, the spin of the substructure is different from material spin. In fact, as the value of β increases, the spin induced by $\overline{\underset{\sim}{\boldsymbol{W}}}^p$ balances out the material spin. Further, if β is sufficiently high, the rotation of directors saturates rapidly at an angle of $\approx \pi/4$. The rate of directors' spin is illustrated in Fig. 1.14 for several values of the plastic spin parameter β: constant spin for $\beta = 0$, rapid saturation for high values and oscillatory response for intermediate values.

1.4.6 Plastic spin: crystal plasticity

Crystal plasticity represents one of the few physical situations for which the plastic spin of crystal directors is precisely known. The spin of directors uniquely results from the slip of N^s systems on specific crystallographic planes and along specific slip directions. The dissipation potential is expressed in terms of the Schmid yield function f^s associated with each slip system s

$$f^s = \left| \underset{\sim}{\boldsymbol{M}} : \underset{\sim}{\boldsymbol{N}}^s - x^s \right| - \tau_c^s \qquad \text{with} \qquad \underset{\sim}{\boldsymbol{N}}^s = \underline{\boldsymbol{l}}^s \otimes \underline{\boldsymbol{n}}^s \tag{1.97}$$

where τ_c^s denotes the critical resolved shear stress (CRSS) for the s-th slip system, $\underline{\boldsymbol{l}}^s$ and $\underline{\boldsymbol{n}}^s$ are, respectively, the slip direction and the normal to the slip plane. The resolved Mandel shear stress $\tau^s = \underset{\sim}{\boldsymbol{M}} : \underset{\sim}{\boldsymbol{N}}^s$ is the driving force for activation of the s-th slip system. Kinematic hardening has been introduced by Méric et al. [1991] in the crystal plasticity framework, in the form of a back stress variable x^s obeying the following evolution rule

$$\dot{\alpha}^s = \dot{\gamma}^s - D|\dot{\gamma}^s|\alpha^s, \qquad x^s = C\alpha^s \tag{1.98}$$

where C, D are the kinematic hardening material parameters. For the sake of demonstration, a power law potential is considered

$$\Omega(\underset{\sim}{\boldsymbol{M}}, \underset{\sim}{\boldsymbol{N}}^s) = \sum_{s=0}^{N_s} \frac{K}{n+1} \left\langle \frac{|\underset{\sim}{\boldsymbol{M}} : \underset{\sim}{\boldsymbol{N}}^s - x^s| - \tau_c^s}{K} \right\rangle^{n+1} \tag{1.99}$$

where n and K are viscosity material parameters and $<\cdot>$ denotes the Macauley brackets. Further, a non-linear hardening law is adopted for the CRSS τ_c^s given by

$$\tau_c^s = \tau_c^{\mathscr{F}(r)} + \sum_{r=0}^{N_s} H^{sr}\left(1 - \exp\left(-b^{\mathscr{F}(r)}\gamma_{cum}^r\right)\right) \tag{1.100}$$

$\mathscr{F}(r)$ identifies the slip system family to which the slip system r belongs (for example basal and prismatic system families in HCP crystals), N_s is the total number of slip systems and γ_{cum}^r denotes the accumulated plastic slip. The matrix H^{sr} accounts for interactions between slip systems. The evolution of the plastic slip variables γ^s follows as

$$\dot{\gamma}^s = \left\langle \frac{|\underset{\sim}{\boldsymbol{M}} : \underset{\sim}{\boldsymbol{N}}^s - x^s| - \tau_c^s}{K} \right\rangle^n \operatorname{sign}\left(\underset{\sim}{\boldsymbol{M}} : \underset{\sim}{\boldsymbol{N}}^s - \mathrm{x}^s\right) \tag{1.101}$$

According to the normality rule (1.27), the plastic deformation rate reads

$$\overline{\underset{\sim}{\boldsymbol{L}}}^p = \sum_{s=0}^{N_s} \dot{\gamma}^s \underset{\sim}{\boldsymbol{N}}^s \tag{1.102}$$

and the plastic spin writes

$$\overline{\underset{\sim}{\boldsymbol{W}}}^p = \sum_{s=0}^{N_s} \dot{\gamma}^s \operatorname{skw}\left(\underline{\boldsymbol{l}}^s \otimes \underline{\boldsymbol{n}}^s\right) \tag{1.103}$$

As an illustration, the simple glide kinematics (1.85) is imposed to a face centered cubic (FCC) single crystal. The single crystal model response is compared to two *fake* crystal models in order to highlight the importance of properly characterizing the plastic spin. In the *fake* models no plastic spin is introduced and Jaumann or Green–Naghdi hypoelastic laws are used instead of the actual plastic spin (1.103). The responses of the three models are shown in Fig. 1.15. The material is perfectly plastic, with an initial CRSS value $\tau_c^s = 100$ MPa. The simple glide loading direction 1 initially coincides with the crystal direction [100], whereas the direction 2 initially coincides with the crystal direction $[0\bar{1}1]$. The octahedral slip system family of the FCC crystal is employed and contains 12 slip systems. The reference solution based on the multiplicative decomposition and plastic spin predicts a saturation of stress levels after $F_{12} = 2$ shear. In contrast, the *fake* crystal responses exhibit oscillatory stress evolutions. It is noteworthy that the stress component σ_{33} vanishes for hypoelastic models. On the other hand, the approach based on the multiplicative decomposition includes a plastic spin derived from the dissipation potential. This model of plastic spin dictates the spin of directors independently of material rotation (see Fig. 1.16). In addition, the σ_{33} does not vanish according to the present model contrary to the hypoelastic formulations.

Furthermore, the rotation rate tends to zero for the crystal orientation considered in the present example, which is not the case for Jaumann rate. The comparison with experimental results confirms that the rotation of anisotropic axes of a single crystal does not follow the material rotation [Peeters et al., 2001; Duchene et al., 2008]. Clearly, the *fake* crystal plasticity models are physically inadequate. Note that oscillatory responses can be observed for special crystal orientations within the framework of multiplicative crystal plasticity, see [Le et al., 2020].

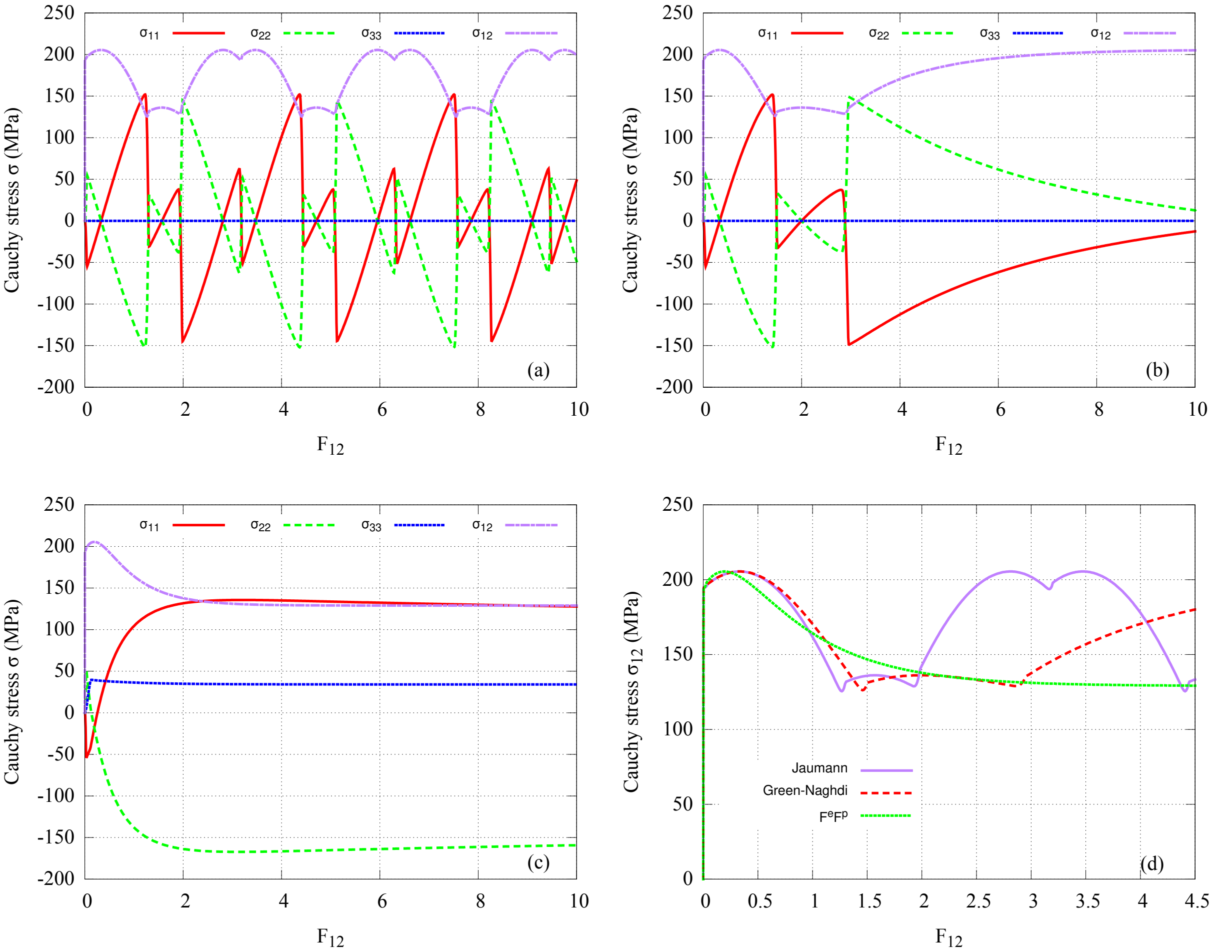

Figure 1.15: *The effect of plastic spin in the case of a simple glide loading of a FCC single crystal for three different finite strain formulations: Jaumann (a) and Green-Naghdi(b) rates (with no plastic spin) and the multiplicative decomposition (c). (d) comparison of σ_{12} for all three formulations.*

1.4.7 Crystal plasticity with system interactions

The interaction matrix in Eq. (1.100) has the general form

$$\boldsymbol{H} = \left(\begin{array}{c:c:c:c} Q_1\boldsymbol{H}_1 & Q_1 h_2^1 & \dots & Q_1 h_n^1 \\ \hdashline Q_2 h_2^1 & Q_2\boldsymbol{H}_2 & \dots & Q_2 h_n^2 \\ \hdashline \vdots & \vdots & \ddots & \vdots \\ \hdashline Q_n h_n^1 & Q_n h_n^2 & \dots & Q_n\boldsymbol{H}_n \end{array} \right) \tag{1.104}$$

where Q_i is the isotropic hardening parameter associated with each slip system family i, H_i matrices denote the self-hardening coefficients, and h_m^n denotes the latent hardening parameters (hardening of slip systems belonging to the family n caused by slip systems belonging to the family m). The table 1.3 shows typical

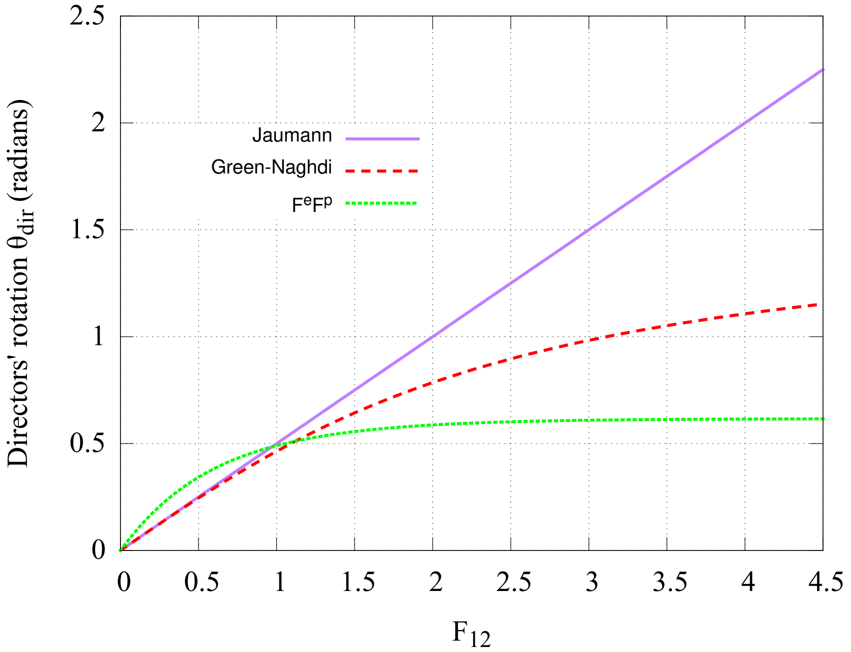

Figure 1.16: *The spin of material directors in the case of a simple glide loading for three different finite strain formulations of crystal plasticity: Jaumann and Green-Naghdi rates and the multiplicative decomposition*

material constants for a single crystal with octahedral and cubic slip system families. Such combination of octahedral and cube slip system families are encountered in single crystal Nickel–based superalloys [Méric et al., 1991].

K_1	n_1	$\tau_c^{(1)}$	Q_1	b_1	H_1	K_2	n_2	$\tau_c^{(2)}$	Q_2	b_2	H_2
(MPa$^{1/n_1}$)	(-)	(MPa)	(MPa)	(-)	(-)	(MPa$^{1/n_2}$)	(-)	(MPa)	(MPa)	(-)	(-)
0.1	20	100	50	50	1	0.1	20	100	100	100	1

Table 1.3: *Material parameters for octahedral (1) and cubic (2) slip systems with isotropic hardening.*

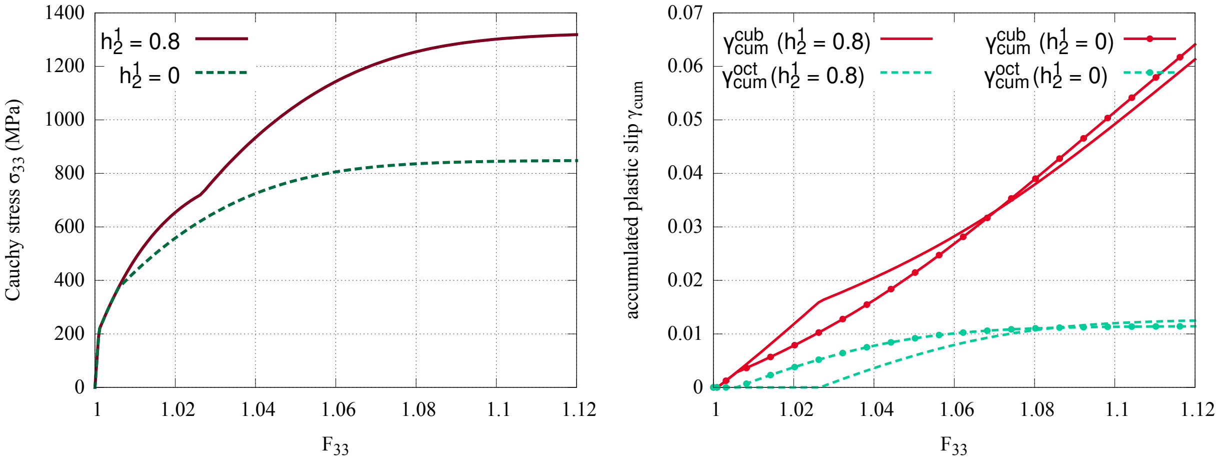

Figure 1.17: *A single crystal including two slip system families (octahedral an cubic) in tension along* $< 111 >$. *γ_{cum}^{cub} (resp. γ_{cum}^{oct}) denotes the accumulated cubic (resp. octahedral) plastic slip.*

Fig. 1.17 shows the influence of latent hardening parameter h_2^1 on the activation of slip systems. In fact, if $h_2^1 = 0$, the cubic slip systems are activated as soon as $\sigma_{33} \approx \dfrac{3\sqrt{2}}{2}\tau_c^{(2)}$ (according to Schmid's law, neglecting the overstress due to viscoplasticity), and the octahedral slip systems are activated when $\sigma_{33} \approx \dfrac{3\sqrt{6}}{2}\tau_c^{(1)}$. If $h_2^1 > 0$, the octahedral slip systems will be activated later since the corresponding critical resolved shear increases due to accumulated cubic plastic slip according to Eq. (1.100). This is the manifestation of latent hardening between slip system families.

1.5 Structural applications

The proposed generic formulation and implementation are now illustrated in the case of structural components subjected to various loading conditions. The model predictions and computational efficiency are compared to those obtained by standard approaches involving hypo-elastoviscoplastic models.

1.5.1 Application 1: Deep drawing for anisotropic materials

The present approach is applied first to the three dimensional problem of cup deep drawing. This problem is common in literature and solved using various finite strain formulations, see [Ulz, 2011; Vladimirov et al., 2010]. The geometry of the test is described in Fig. 1.18.

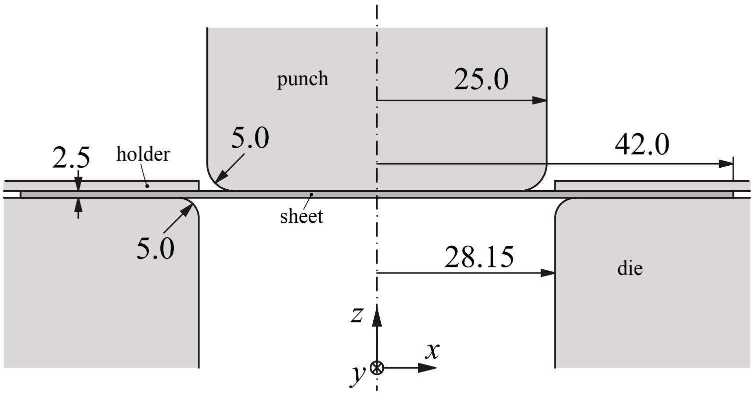

Figure 1.18: *Schematic view of the cup drawing process. No friction is considered between sheet and tools. The die, punch and the holder are assumed to be linear elastic with a Young modulus of* $E = 10^6$ *MPa and a Poisson ratio* $\nu = 0.3$. *Lengths in mm.*

A time-independent elastoplastic model is considered with a Hill yield function as in Eq. (1.96). A nonlinear isotropic hardening rule is adopted in the form

$$R(p) = R_0 + Q(1 - \exp(-cp)) \tag{1.105}$$

Here the value of the initial yield stress is $R_0 = 253$ MPa, the isotropic hardening parameters are chosen as $c = 14$ and $Q = 215$ MPa. The parameters of Hill's yield function are set to $F = G = H = N = 0.5$ and $L = M = 1.5$. Herein, only a quarter of the cup is analyzed due to the orthotropic material symmetry. The mesh of the sheet contains 900 C3D8 hexahedral solid elements (linear interpolation with 8 Gauss points per element), with 3 elements in the thickness direction. The plate is initially circular. The tools are modeled as rigid surfaces and are completely fixed except the punch which is pushed in z-direction to a total displacement of $u_z = -40$ mm.

Fig. 1.19 shows the distribution of the accumulated plastic strain and the deformed configuration. If the plastic spin vanishes, the maximal values of the accumulated plastic strain are located along the directions of the material symmetry x- and y- axes. When plastic spin is taken into account by means of parameter

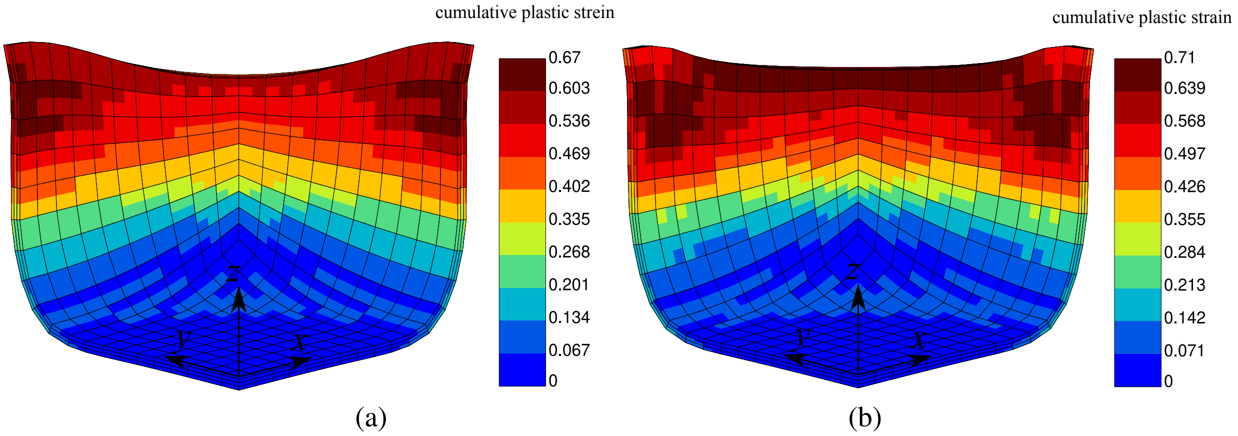

Figure 1.19: *Accumulated plastic strain induced by cup drawing in an anisotropic elastoplastic plate: (a) Without plastic spin* $\beta = 0\ MPa^{-1}$*, (b) with plastic spin* $\beta = 0.01\ MPa^{-1}$

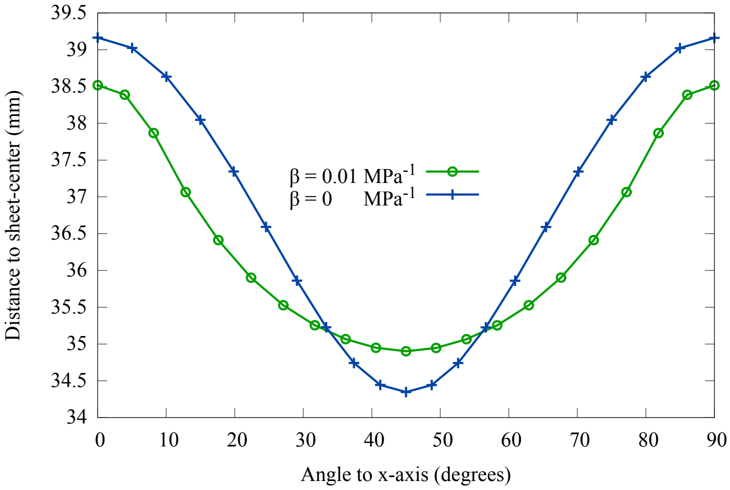

Figure 1.20: *Distance of rim to the sheet center versus angle to x-axis. The curve shows the earing pattern for two values of the parameter* β*.*

β from Eq. (1.45), the distribution of accumulated plastic strain tends to be more isotropic for $\beta = 0.01$ MPa^{-1}.

The earing profile after forming is depicted in Fig. 1.20 for two values of the parameter β. The edge of the sheet has a wavy shape. As the value of β increases, the edge shows less pronounced wave-shape. Similar results were reported in [Ulz, 2011] for an isotropic elastic and a transverse isotropic Hill-type plastic model. The hypoelastic version of this model yields similar results to the present approach, including the wavy shape of the cup and the distribution of plastic strains. The present formulation, however, is advantageous since a supplementary plastic spin describing the evolution of anisotropy axes can be incorporated in the model.

1.5.2 Application 2: Turbine blade with single crystal plasticity

In the following, the behavior of a nickel-based superalloy single crystal turbine blade subjected to creep at high temperature is studied. During their operation, turbine blades are subjected to centrifugal forces induced by the rotation (∼ 20000 RPM) of the turbine disc in addition to gas pressure. During one flight, the turbine blades are subjected to high and non-uniform temperatures (maximum temperature ∼ 1200°C), which will induce thermal strains. The thermomechanical loading is maintained for a longer time, compared to the nominal in-service conditions, at the maximum temperature(∼ 640°C at the root and

$\sim$ 1200°C at the tip). The mesh of the turbine blade geometry contains 1366 linear C3D8 hexahedral solid elements. We consider two initial orientations of the crystal. The first one is such that the crystal directions triplet ($[100]-[010]-[001]$) coincide with the orthogonal basis vectors triplet (x_1,x_2,x_3). For the second orientation, the crystal is tilt by 15° in the x_1-x_3 plane. The objective is to assess the impact of crystal misorientation on the thermomechanical response of the blade.

The material model has 18 slip systems potentially active, 12 octahedral $\{110\}<111>$ and 6 cubic slip systems $\{110\}<100>$. The constitutive equations of the model including kinematic hardening law were given in Sec. 1.4.6. Typical values of the material parameters used in the simulation can be found in [Méric and Cailletaud, 1991]. Cubic elasticity moduli, the coefficient of isotropic thermal expansion, critical resolved shear stresses, viscoplastic flow parameters and nonlinear kinematic hardening parameters are identified as functions of temperature.

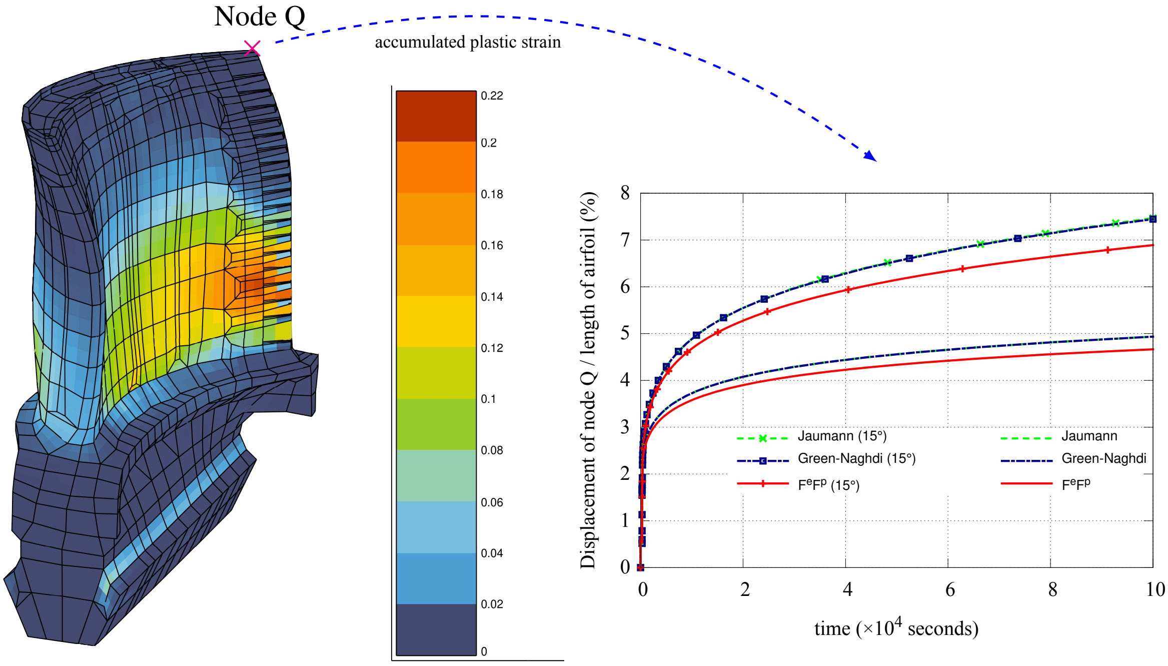

Figure 1.21: *(a) The accumulated plastic strain in a turbine blade subjected to creep at high temperature. (b) Displacement of the node Q as a function of time: comparison of different finite deformation formulations.*

Fig. 1.21 shows that both hypoelastic formulations yield similar creep results. The present model prediction slightly differs and the difference increases with time. The difference between various formulations becomes apparent when an initial rotation of 15° around y-axis is considered. Fig. 1.22 shows the relative rotation of material directors with respect to material rotation for the present model. For hypoelastic formulations, the spin of directors coincides with material rotation which is not the case for the model based on the multiplicative decomposition. The multiplicative crystal plasticity model assumes a relative rotation of crystal directors with respect to material lines, induced by the plastic spin (1.103). An initial misorientation of 15° leads to slightly larger relative rotation of crystal directors, as shown in Fig. 1.22. This result explains the fact that the difference in creep predicted by various formulations is much more pronounced for an initial misorientation of 15° compared to 0°. It must be underlined that the presented crystal plasticity formulations based on corotational frames are physically unsound but represent standard extensions of small strain crystal plasticity.

1.5.3 Computational efficiency of the approach

The present formulation is compared to two hypoelastic formulations, Jaumann (J) and Green-Naghdi (GN) rates, in terms of computational efficiency. We consider four examples of structural applications and different material models. In addition to the applications discussed previously, we carry out a tensile test on

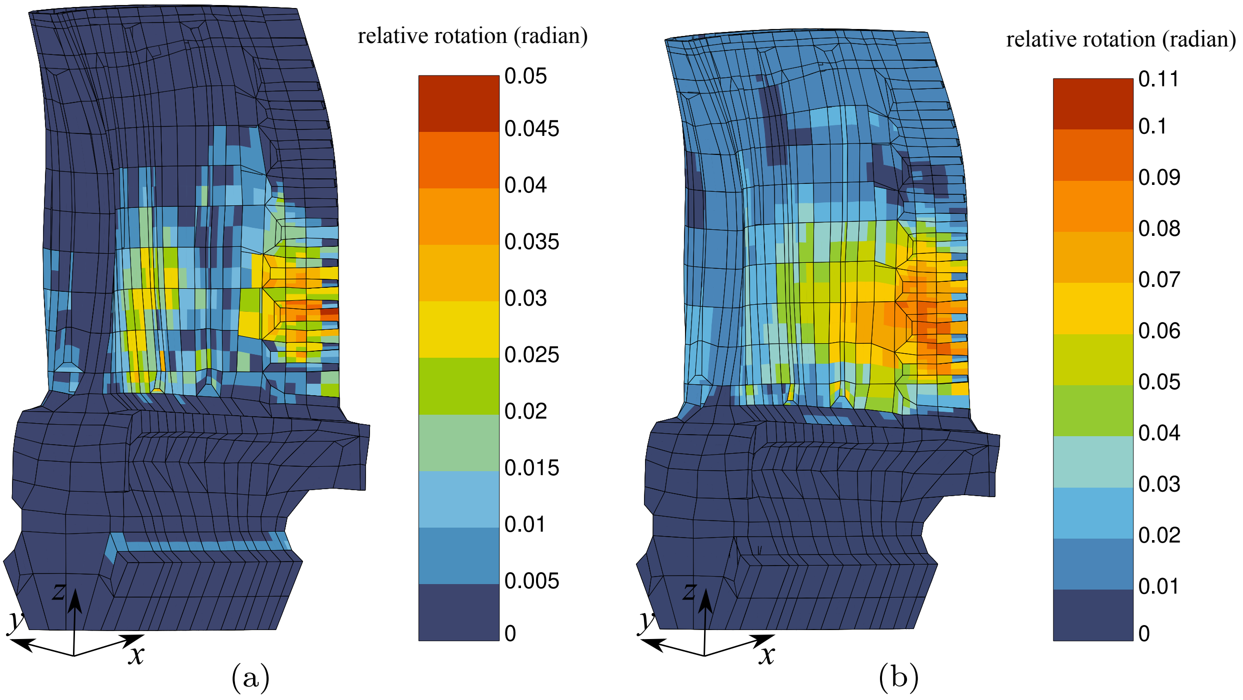

Figure 1.22: *Relative rotation of crystal directors w.r.t. material lines for the multiplicative-based model in two cases (a) ideal* $< 1001 >$ *orientation of the blade, (b) deviation of 15° around y-axis.*

a notched specimen with 323703 nodes corresponding to 73920 C3D20R quadratic elements with reduced integration. A von Mises plasticity model is adopted with initial yield stress $R_0 = 300$ MPa.The parameter values for nonlinear isotropic and kinematic hardening are taken as $Q = 400$ MPa, $b = 2.5$, $C = 5700$ MPa and $D = 17$, as in [Vladimirov et al., 2008]. The results predicted by different formulations (hypoelastic and multiplicative models) turn out to be almost identical in this isotropic case. Fig. 1.23 depicts the obtained accumulated plastic strain field. The objective of this example is to illustrate the performance of the approach for a problem with almost one million degrees of freedom.

Note that the integration of constitutive equations is carried out using a fully implicit integration method ($\theta = 1$). The time increment is set to the same value for all the formulations (if it does not converge, the time increment is divided by 2). Comparison results for various formulations are presented in Fig. 1.24. Computations were carried out on processors of type Intel(R) Xeon(R) CPU E5-2650 v4 @ 2.20GHz. It is found that the formulation based on the multiplicative decomposition leads to a slightly higher computational cost compared to hypoelastic formulations (+15%–20%). This is due to the fact that more operations are implied by the systematic use of non–symmetric tensors in the algorithm. Besides, the total number of iterations for convergence of global equilibrium, is slightly higher for the model based on the multiplicative decomposition. In spite of that, the computational cost is still reasonable compared to formulations common in commercial FEM software. The slight increase in computation time is counter–balanced by additional possibilities in the modeling of anisotropic inelasticity.

1.6 Conclusion

This chapter demonstrates that elasto-viscoplastic models based on the multiplicative decomposition of the deformation gradient are now mature for a systematic use in commercial finite element codes for structural computations. The proposed generic constitutive framework overcomes the shortcomings of standard formulations used in most available FE codes and based on hypoelastic laws and limited description of anisotropic behavior. It has been shown that the computing efficiency is comparable to the standard approach, although slightly less advantageous. The use of a thermodynamically consistent formulation of

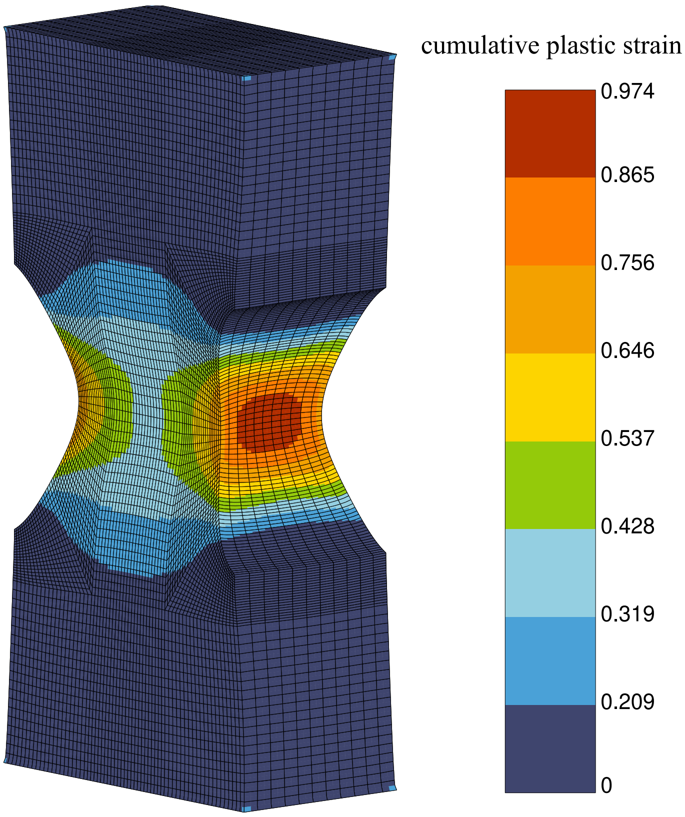

Figure 1.23: *Cumulative plastic strain in a notched specimen subjected to tensile loading using the multiplicative decomposition based model.*

constitutive equations ensures increased reliability of model predictions.

The proposed extension of constitutive equations at finite strain relies upon the multiplicative decomposition of the deformation gradient and a hyperelastic relation between stress and elastic strain measures. The other characteristic feature is the expression of plasticity laws in terms of the Mandel stress tensor, which is generally non-symmetric. The approach accommodates contributions of many deformation mechanisms combining thermo-plasticity, viscosity and possibly damage, without resorting to arbitrary further multiplicative decompositions of elastic or plastic parts of the deformation gradient. Instead, the rates of multimechanism contributions are added in the viscoplastic flow rule. Anisotropy is incorporated via the consideration of directors and associated structural tensors and plastic spin concept which are often absent in existing standard formulations. It was illustrated in the case of Hill's criterion and crystal plasticity.

Two numerical integration methods of the nonlinear evolution equations are proposed. First, the elastic or the plastic part of the deformation gradient is integrated using an exponential map. In general, this method involves calculating the exponential of a non-symmetric second-order tensor and its derivative, which is not an easy task. An alternative integration method is considered, which consists of correcting the elastic part of the deformation gradient to enforce the plastic incompressibility. The present framework is illustrated through various models, including isotropic and anisotropic (visco)-plasticity with isotropic and kinematic hardening. Most formulations exist in the literature but a few are original: nonlinear non-symmetric kinematic hardening rule including dynamic and static recovery terms. In the case of linear kinematic hardening, models based on the Jaumann rate and the multiplicative decomposition exhibit stress oscillations extensively discussed in the literature. However, regarding nonlinear kinematic hardening including dynamic recovery term, the various models provide similar predictions for a proper choice of material parameters.

The capabilities of the present formulation are illustrated through elementary industrial applications. The effect of plastic spin on the evolution of anisotropy described by a triad of directors was evaluated in the case of cup drawing. This effect cannot be neglected, particularly for materials showing a high

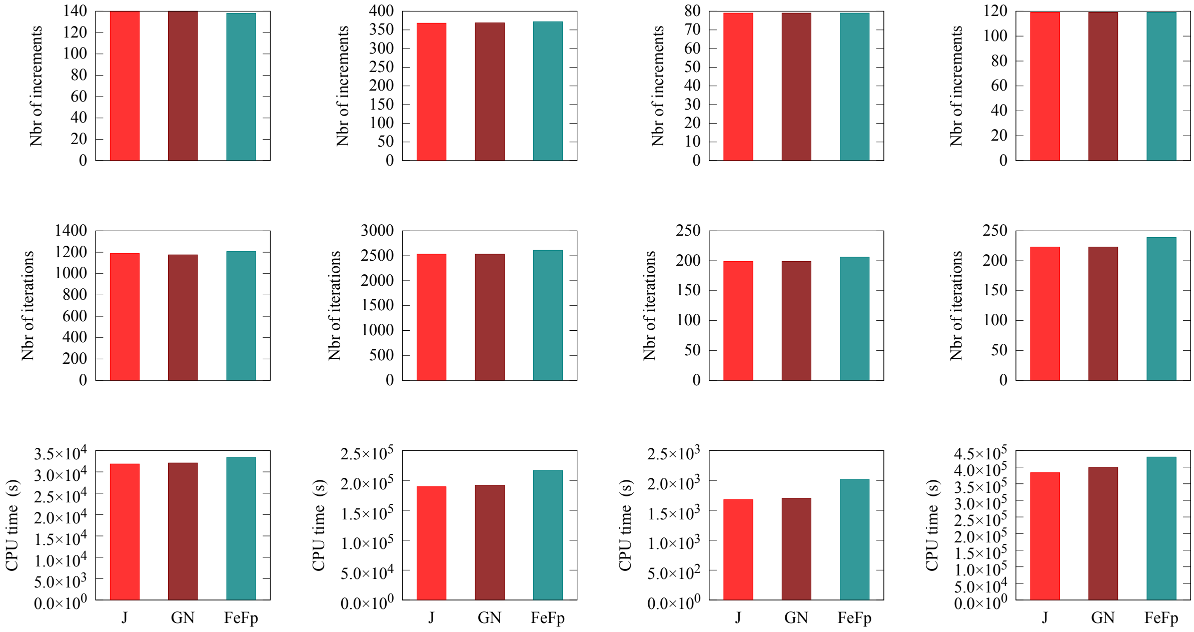

(a) (b) (c) (d)

Figure 1.24: *Comparison of the total number of increments, total number of iterations and CPU time for different formulations. Applications: (a) deep drawing with 900 C3D8 elements (1324 nodes), (b) deep drawing with 19500 C3D8 elements (26564 nodes), (c) turbine blade under creep with 1366 C3D8 elements (2498 nodes), (d) Notched specimen with 73920 C3D20R elements (323703 nodes). Simulations are run on 24 CPUs.*

degree of anisotropy under large plastic deformation. The comparison between hypo-elastoplastic models applied to crystal plasticity shows that the result heavily depends on the objective stress rate. The crystal plasticity model based on the multiplicative decomposition remains the reference model in that case and was successfully validated by experiments, especially the rotation of crystal directors with respect to loading axes.

Meanwhile, further research is necessary to develop yield criteria in terms of the generally non-symmetric Mandel stress tensor [Itskov and Aksel, 2004; Ulz, 2011]. The identification of the constitutive equations for the plastic spin requires more experimental investigations at large deformations. Furthermore, non-symmetric internal variables (*e.g.* kinematic hardening) are to be considered. Examples showing applications to compressible elastoviscoplastic materials could also be provided. Non associated flow rules for applications to granular media should also be envisaged.

It is hoped that the present results can increase the interest of the engineering computation community towards the systematic use of physically consistent nonlinear constitutive equations.

Chapter 2

Scalar elastoplastic micromorphic continua

Abstract Gradient plasticity has been studied extensively over the past forty years to model size effects and to regularize finite element simulations involving localization phenomena. This chapter discusses the pros and the cons of gradient plasticity models based on the gradient of scalar plastic variables, in particular the gradient of cumulative plastic strain. It proposes benchmark tests for modeling the size effects and localization of plastic strain. Analytical solutions for the simple slip case are provided. These solutions are used to validate the FE implementation. We focus on the micromorphic approach as a practical method for the implementation of gradient plasticity in finite element codes. A comparison of three distinct micromorphic formulations of time-independent plasticity in finite deformations is presented. These formulations are based on multiplicative decomposition of the deformation gradient and quadratic potentials with respect to the gradient terms. The performance of micromorphic models is compared to that of gradient plasticity models based on Lagrange multipliers. Several problems with monotonic and cyclic loading, including confined plasticity in simple glide and tension, bending and torsion in large deformations are treated. Limitations of the model based on the cumulative plastic strain are discussed in the case of bending and torsion. These limitations can be overcome by the use of the equivalent plastic strain gradient model, or the use of tensor micromorphic variables. This last type of model will be the subject of the chapter 3.

Résumé La plasticité à gradient a fait l'objet de plusieurs études au cours des quarante dernières années afin de modéliser les effets d'échelle et de régulariser les simulations par éléments finis des phénomènes de localisation. Ce chapitre aborde les avantages et les inconvénients des modèles de la plasticité à gradient basés sur le gradient des variables plastiques scalaires, en particulier le gradient de la déformation plastique cumulée. Il propose des tests de référence pour la modélisation des effets d'échelle et de la localisation de la déformation plastique. Nous proposons des solutions analytiques dans le cas du glissement simple. Ces solutions sont utilisées pour valider l'implémentation EF. Nous nous focalisons sur l'approche micromorphe, en tant que méthode pratique pour l'implémentation de la plasticité à gradient dans les codes par éléments finis. Nous proposons une comparaison de trois formulations micromorphes distinctes de la plasticité indépendante du temps en transformations finies. Ces formulations sont basées sur la décomposition multiplicative du gradient de transformation et sur des potentiels quadratiques par rapport aux termes du gradient. La performance numérique des modèles micromorphes est comparée à celle des modèles de plasticité à gradient basés sur les multiplicateurs de Lagrange. Plusieurs problèmes avec chargements monotones et cycliques ont été traités, y compris la plasticité confinée en glissement simple et en tension, la flexion et la torsion en grandes déformations. Des limitations du modèle basé sur le gradient de la déformation plastique cumulée sont discutés dans le cas de la flexion et de la torsion. Ces limitations peuvent être surmontées par l'utilisation du modèle à gradient de la déformation plastique équivalente, ou l'utilisation des variables micromorphes tensorielles. Ce dernier type de modèles sera l'objet du chapitre 3.

Contents

2.1 Introduction

Many experiments have revealed the size-dependent nature of metal plasticity characterized by intrinsic length scales interacting with small specimen dimensions, *e.g.*, grain size effects in thin films [Venkatraman and Bravman, 1992], bending of thin foils [Stölken and Evans, 1998], torsion of copper wires reviewed in [Fleck and Hutchinson, 1997] until more recent experiments on confined plasticity in thin films [Mu et al., 2016]. In general, a *smaller is stronger* effect has been reported. The presence of plastic strain gradients leads to enhanced hardening due to the generation of geometrically necessary dislocations [Nye, 1953; Ashby, 1970; Fleck and Hutchinson, 1993]. The conventional plasticity theory is well established and is predictive to some extent. However, the size effects cannot be captured by classical models since no length scale enters the constitutive equations.

On the other hand, strain-softening leads to ill-posed boundary value problems in classical continuum theories. This is due to the loss of ellipticity of the governing partial differential equations in the rate-independent case. The numerical simulations are therefore sensitive to mesh size [de Borst et al., 1995], orientation of element edges [Hien Poh and Swaddiwudhipong, 2009; Mazière and Forest, 2015] and element types. Various types of regularization methods are studied in literature relying on non-local integral operators [Botta et al., 2005], gradient formulations [de Borst et al., 1999] or extra-degrees of freedom for smoothing strain or damage fields [Peerlings et al., 1996]. Further, this spurious mesh dependency can also be solved partially for rate-dependent models [Needleman, 1988] where the intrinsic length scale increases for high rate sensitive materials.

The mechanics of generalized continua enables the introduction of characteristic lengths into constitutive equations of materials with microstructure. For instance, the micromorphic approach is first proposed in [Eringen and Suhubi, 1964; Suhubi and Eringen, 1964]. In this theory, a deformable triad of directors is defined at each material point. Higher-order theories are constructed then by associating tensors of various orders with material points [Germain, 1973]. These tensors can be related to either deformation tensors or internal variables. Various micromorphic models using scalar and tensor variables accounting for elasticity, plasticity, and damage have been suggested in [Forest, 2009; Saanouni and Hamed, 2013; Kiefer et al., 2018]. In crystal plasticity, models with one micromorphic variable accounting for plastic strain in all slip systems are used in order to decrease the number of additional degrees of freedom [Wulfinghoff and Böhlke, 2012; Ling et al., 2018; Scherer et al., 2019, 2020].

Finite strain modeling of elastoplasticity has been studied for decades and is still the subject of current research. The widely used approach to extend the well-established infinitesimal elastoplasticity theory to finite deformations is the so-called hypoelastic formulation relying on the additive decomposition of the total deformation rate into elastic and inelastic parts, and constitutive equations for objective stress rates. However, these formulations suffer from several shortcomings. For instance, spurious energy dissipation in the elastic regime before yield and at post-yield. Formulations relying upon the additive decomposition of the Green-Lagrange strain tensor were developed for isotropic materials in [Green and Naghdi, 1965] and the additive split of logarithmic strain was suggested in [Miehe et al., 2002]. Several authors have advocated the multiplicative decomposition as a general way of describing the kinematics at finite strain [Kröner, 1959; Lee and Liu, 1967]. This decomposition assumes the existence of an intermediate configuration that is generally not unique. The concept of isoclinic intermediate configuration was proposed first in [Mandel, 1973] to overcome this limitation.

A general framework for the formulation of generalized continuum constitutive equations at finite deformations based on the multiplicative decomposition was proposed in [Forest and Sievert, 2003] for Cosserat, strain gradient, micromorphic and gradient of internal variable media. These models are applicable to the modeling of size effects in plasticity of materials as well as the simulation of strain localization phenomena. As summarised in [Forest, 2016], finite strain formulations for strain gradient plasticity lead to distinct regularisation operators. Non-coaxial deformations, such as simple glide, reveal significant differences between finite strain formulations, as recently discussed for the micromorphic approach of plasticity in [Friedlein et al., 2022]. In particular, the formulation based on additive logarithmic strain decomposition under non-coaxial deformation yields a softer response and eventually leads to early strain localization compared to the multiplicative elastoplasticity. Further investigations on Lagrangian and Eulerian non-local effects were conducted by , *e.g.* [Steinmann, 1999; Geers et al., 2001, 2003; Geers, 2004]. According to these works, various formulations deviate from each other at finite strain, but with no clear preference. It remains that only few studies were dedicated to the computational analysis of strain gradient plasticity at large deformations, see for instance in [Martinez-Paneda and Niordson, 2016] based on the gradient of the plastic strain tensor, and [Anand et al., 2012; Zhang et al., 2018; Ling et al., 2018] for the gradient of scalar variables.

The present work focuses on the micromorphic approach based on the gradient of scalar variables because this class of models remains rather easy to implement in FE codes in the case of rate-independent elasto-plasticity, and provides computationally efficient simulations due to the reduced number of additional degrees of freedom. Several issues related to the particular choice of scalar micromorphic variable are reported in the literature. First, the micromorphic enhancement may lead to a negative isotropic hardening and ultimately to a non-physical negative radius of elastic domain [Poh et al., 2011]. Further, scalar variables do not account for flow direction [Wulfinghoff et al., 2014]. A scalar enhanced model has been proposed in [Jebahi and Forest, 2021] at small strain to solve this conceptual problem. The model involves a back-stress that is undeterminate at zero plastic strain. A tensorial gradient plasticity model was proposed in [Poh et al., 2011] to address the aforementioned issues but this model remains numerically expensive.

The numerical implementation of strain gradient theories has been widely investigated. An implementation of strain gradient plasticity based on Lagrange multipliers has been proposed in [Lorentz and Benallal, 2005]. It consists in duplicating the considered variable, one is local and one is non-local and these two variables are then enforced to be equal. An augmented Lagrangian term was introduced to prevent plastic strain oscillations [Chen et al., 2020, 2022]. The computational cost of micromorphic and Lagrange multiplier-based approaches are compared for a rate-(in)dependent single crystal model [Scherer et al., 2020]. For that case, the authors suggest that the computational performance can be improved by considering the Lagrange multiplier-based formulation.

The objective of the present work is to provide a series of benchmark tests addressing both size effects in hardening plasticity and simulation of localization phenomena to evaluate the performance of the approach both theoretically and computationally and investigate its limitations. The analysis is limited to the isothermal case for the sake of brevity although extensions to thermomechanics are possible [Forest, 2009; Felder et al., 2022]. Verification of the proposed finite implementation is performed via analytical solutions at small strains for hardening and softening plasticity. The considered boundary value problems are simulated according to three distinct formulations of the model at finite deformations. At finite strain, the gradient of the micromorphic variable is defined with respect to (w.r.t.) either the reference, current or intermediate configurations. The free energy potential is assumed to be a quadratic form w.r.t. to one of this gradient variables. This results in three distinct models that will be compared throughout this work for monotonic and cyclic loading conditions. The present approach is applied to size effects in two cases. First, plastic gradients are induced by particular boundary conditions applied to the micromorphic variable corresponding to confined plasticity. Further, gradients emerge from the geometry of the loading in the case of bending and torsion applications. The torsion case is considered in 3D in order to evaluate the computational efficiency of the model and their implementation. Finally, the capability of these models to cancel the spurious mesh dependency is investigated through applications involving strain localization. The present approach is compared in terms of computational cost to the Lagrange multiplier-based approach. This chapter reviews several aspects of micromorphic plasticity but also present novel features. First, the three finite deformations frameworks are compared for the first time to highlight the differences at large deformations under complex loading. Second, the analysis of cyclic shear, tension and bending using several models shows significantly different material responses ranging from unbounded size-dependent isotropic hardening to several types of size-dependent kinematic hardening. In particular, a new model based on the gradient of an equivalent strain measure at finite deformation is proposed and shown to solve some drawbacks of the initial approach. Then, original applications are presented for plastic strain localization in shear and tension. A new analytical solution is presented for shear localization describing the micromorphic model response in detail and thus providing sophisticated verification of the FE implementation. An anisotropic gradient contribution is finally proposed showing the interplay between two length scales during double shear banding in a plate in tension.

The outline of this chapter is as follows. The general micromorphic approach for finite strain gradient plasticity is presented in section 2.2. The special case of scalar micromorphic variables is put forward. Three different finite strain formulations are discussed relying upon gradient variables defined w.r.t. reference, current and intermediate configurations. A strain gradient plasticity model based on Lagrange multipliers is revisited. The finite element implementation is discussed briefly. The capability of different micromorphic formulations to predict size effects is discussed in section 2.3 for a unit cell subjected to simple glide and tension under confined plasticity boundary conditions. In section 2.4, size effects in the case of bending of a two-dimensional foil and torsion of a cylindrical bar are investigated. The case of strain localization is addressed in section 2.5 for a unit cell subjected to simple glide and a plate under tension. Finally, the computational efficiency and the limitations of the approach are discussed in section 2.6.

2.2 Model formulation at finite deformation and FE implementation

According to the classical Cauchy continuum theory, the material body is characterized by a set of degrees of freedom $DOF0 = \{\underline{\boldsymbol{u}}\}$ and state variables $STATE0 = \{\underset{\sim}{\boldsymbol{F}}, T, \alpha_I\}$. The displacement field, the deformation gradient, and temperature are denoted respectively by $\underline{\boldsymbol{u}}$, $\underset{\sim}{\boldsymbol{F}}$, and T, whereas α_I represent scalar and tensor internal variables accounting for hardening/softening properties. The micromorphic approach proposed in [Forest, 2009] at small strains and in [Forest, 2016] at finite deformations, is a systematic enhancement of the classical continuum and constitutive theory to account for size and microstructure internal length effects. Supplementary degrees of freedom, denoted by χ, associated with selected internal variables are introduced, *i.e.* $DOF = \{\underline{\boldsymbol{u}}, \chi\}$. Indeed, the micromorphic variables and related internal variables have the same tensor rank and physical dimension. The set of material state variables is enriched by the micromorphic variable χ and its gradient $\nabla\chi$, *i.e.* $STATE = \{\underset{\sim}{\boldsymbol{F}}, T, \alpha_I, \chi, \nabla\chi\}$. In what follows, notations are used for a scalar micromorphic variable, even though similar equations are valid for tensor variables as well, but the present work addresses exclusively the case of scalar variables.

2.2.1 Reduced micromorphic elasto(visco)plasticity: kinematics and balance equations

The deformation gradient is decomposed multiplicatively following [Kröner, 1959; Lee and Liu, 1967; Mandel, 1973] into elastic and inelastic parts as

$$\underset{\sim}{\boldsymbol{F}} = \underset{\sim}{\boldsymbol{F}}^e \underset{\sim}{\boldsymbol{F}}^p \tag{2.1}$$

Following Mandel [1973], the isoclinic local intermediate configuration, where the material directors describing the anisotropic material behavior have the same inclination or orientation as in the reference configuration, is adopted. This intermediate configuration is then uniquely defined up to an element of the material symmetry group.
The total, elastic and plastic relative volume changes are denoted by J, J_e and J_p, respectively:

$$J = \frac{\rho_0}{\rho} = \det\{\underset{\sim}{\boldsymbol{F}}\} \quad , \quad J_e = \frac{\overline{\rho}}{\rho} = \det\{\underset{\sim}{\boldsymbol{F}}^e\} \quad , \quad J_p = \frac{\rho_0}{\overline{\rho}} = \det\{\underset{\sim}{\boldsymbol{F}}^p\} \tag{2.2}$$

where ρ, $\overline{\rho}$ and ρ_0 denote the mass density in the current, intermediate and reference local configurations, respectively. The Lagrangian gradient of additional degrees of freedom $\underline{\boldsymbol{K}} = \dfrac{\partial\chi}{\partial\underline{\boldsymbol{X}}}$ and the Eulerian gradient $\underline{\boldsymbol{k}} = \dfrac{\partial\chi}{\partial\underline{\boldsymbol{x}}}$ are related by

$$\underline{\boldsymbol{k}} = \underset{\sim}{\boldsymbol{F}}^{-T} \underline{\boldsymbol{K}} \tag{2.3}$$

Likewise, a generalized variable $\overline{\underline{\boldsymbol{K}}}$ can be defined w.r.t. the intermediate configuration as

$$\overline{\underline{\boldsymbol{K}}} = \underset{\sim}{\boldsymbol{F}}^{p-T} \underline{\boldsymbol{K}} = \underset{\sim}{\boldsymbol{F}}^{eT} \underline{\boldsymbol{k}} \tag{2.4}$$

The power density of internal forces expressed w.r.t. the current configuration, $\mathscr{P}^{(i)}$, is given by

$$\mathscr{P}^{(i)} = \underset{\sim}{\boldsymbol{\sigma}} : \underset{\sim}{\boldsymbol{D}} + a\dot{\chi} + \underline{\boldsymbol{b}} \cdot \dot{\underline{\boldsymbol{k}}} \quad , \quad \forall \underline{\boldsymbol{x}} \in \Omega \tag{2.5}$$

with $\underset{\sim}{\boldsymbol{\sigma}}$ is the Cauchy stress, a and $\underline{\boldsymbol{b}}$ are generalized stresses associated with the micromorphic variable and its first gradient. By neglecting volume forces for the sake of brevity, the principle of virtual power is written w.r.t. the current configuration as follows

$$\int_D \mathscr{P}^{(i)} dV = \int_{\partial D} (\underline{\boldsymbol{t}}.\dot{\underline{\boldsymbol{u}}} + a^c \dot{\chi})\, dS \quad , \quad \forall D \subset \Omega \tag{2.6}$$

where D is a sub-domain of the current configuration Ω of the body. External forces arise from macroscopic surface traction $\underline{\boldsymbol{t}}$ and a generalized surface traction a^c related to the micromorphic variable. The application of the virtual power principle, w.r.t. the generalized set of independent degrees of freedom, leads to the static balance laws in the current configuration in the form

$$\begin{cases} \mathrm{div}\,\underset{\sim}{\boldsymbol{\sigma}} &= \underline{\mathbf{0}} \\ \mathrm{div}\,\underline{\boldsymbol{b}} &= a \end{cases} \quad \forall \underline{\boldsymbol{x}} \in \Omega \qquad \begin{cases} \underline{\boldsymbol{t}} &= \underset{\sim}{\boldsymbol{\sigma}} \cdot \underline{\boldsymbol{n}} \\ a^c &= \underline{\boldsymbol{b}} \cdot \underline{\boldsymbol{n}} \end{cases} \quad \forall \underline{\boldsymbol{x}} \in \partial\Omega \tag{2.7}$$

where $\underline{\boldsymbol{n}}$ denotes the outward surface unit normal. The power density of internal forces expressed w.r.t. the reference configuration $\mathscr{P}_0^{(i)} = J\mathscr{P}^{(i)}$ is given by

$$\mathscr{P}_0^{(i)} = \underset{\sim}{\boldsymbol{P}} : \dot{\underset{\sim}{\boldsymbol{F}}} + a_0\dot{\chi} + \underline{\boldsymbol{b}}_0 \cdot \dot{\underline{\boldsymbol{K}}} \;\; , \;\; \forall \underline{\boldsymbol{X}} \in \Omega_0 \tag{2.8}$$

where the generalized stresses a_0 and $\underline{\boldsymbol{b}}_0$ are related to a and $\underline{\boldsymbol{b}}$ by

$$a_0 = \frac{\rho_0}{\rho}a = Ja, \qquad \underline{\boldsymbol{b}}_0 = J\underset{\sim}{\boldsymbol{F}}^{-1}\underline{\boldsymbol{b}} \tag{2.9}$$

and $\underset{\sim}{\boldsymbol{P}} = J\underset{\sim}{\boldsymbol{\sigma}}\underset{\sim}{\boldsymbol{F}}^{-T}$ is the Boussinesq stress tensor. In the reference configuration, Eq. (2.6) becomes

$$\int_{D_0} \mathscr{P}_0^{(i)} dV_0 = \int_{\partial D_0} (\underline{\boldsymbol{T}}.\dot{\underline{\boldsymbol{u}}} + a_0^c\dot{\chi})\, dS_0 \quad , \quad \forall D_0 \subset \Omega_0 \tag{2.10}$$

where D_0 is a subdomain of the reference configuration Ω_0. Furthermore, the balance laws write

$$\begin{cases} \mathrm{Div}(\underset{\sim}{\boldsymbol{P}}) &= \underline{\mathbf{0}} \\ \mathrm{Div}(\underline{\boldsymbol{b}}_0) &= a_0 \end{cases} \quad \forall \underline{\boldsymbol{X}} \in \Omega_0 \qquad \begin{cases} \underline{\boldsymbol{T}} &= \underset{\sim}{\boldsymbol{P}} \cdot \underline{\boldsymbol{n}}_0 \\ a_0^c &= \underline{\boldsymbol{b}}_0 \cdot \underline{\boldsymbol{n}}_0 \end{cases} \quad \forall \underline{\boldsymbol{X}} \in \partial\Omega_0 \tag{2.11}$$

where $\underline{\boldsymbol{n}}_0$ is the outward surface normal and $\underline{\boldsymbol{T}}$ is the surface traction measured on the reference boundary ∂D_0. Likewise, the power density of internal forces is rewritten w.r.t. the intermediate local configuration[1] $\overline{\mathscr{P}}^{(i)} = J_e\mathscr{P}^{(i)}$ as

$$\overline{\mathscr{P}}^{(i)} = \frac{1}{2}\underset{\sim}{\boldsymbol{\Pi}}^e : \dot{\underset{\sim}{\boldsymbol{C}}}^e + (\underset{\sim}{\boldsymbol{M}} + \overline{\underline{\boldsymbol{K}}} \otimes \overline{\underline{\boldsymbol{b}}}) : \overline{\underset{\sim}{\boldsymbol{L}}}^p + \overline{a}\dot{\chi} + \overline{\underline{\boldsymbol{b}}} \cdot \dot{\overline{\underline{\boldsymbol{K}}}} \tag{2.12}$$

where $\overline{\underline{\boldsymbol{b}}} = J_e\underset{\sim}{\boldsymbol{F}}^{e-1}\underline{\boldsymbol{b}} = \dfrac{1}{J_p}\underset{\sim}{\boldsymbol{F}}^p\underline{\boldsymbol{b}}_0$ and $\overline{a} = J_e a = \dfrac{a_0}{J_p}$. The Cauchy-Green elastic strain measure defined on the intermediate local configuration is $\underset{\sim}{\boldsymbol{C}}^e = \underset{\sim}{\boldsymbol{F}}^{eT}\underset{\sim}{\boldsymbol{F}}^e$. The Piola stress tensor w.r.t. the intermediate local configuration is $\underset{\sim}{\boldsymbol{\Pi}}^e = J_e\underset{\sim}{\boldsymbol{F}}^{e-1}\underset{\sim}{\boldsymbol{\sigma}}\underset{\sim}{\boldsymbol{F}}^{e-T}$ and $\underset{\sim}{\boldsymbol{M}} = \underset{\sim}{\boldsymbol{C}}^e\underset{\sim}{\boldsymbol{\Pi}}^e$ denotes the Mandel stress tensor. The expression of the virtual power w.r.t. the various local configurations are related by the following

$$\frac{\overline{\mathscr{P}}^{(i)}}{\overline{\rho}} = \frac{\mathscr{P}^{(i)}}{\rho} = \frac{\mathscr{P}_0^{(i)}}{\rho_0} \tag{2.13}$$

2.2.2 On three forms of the Helmholtz free energy potential

The mass specific Helmholtz free energy density function for classical elasto(visco)plasticity models, ψ^{ref}, depends on the elastic strain tensor $\underset{\sim}{\boldsymbol{C}}^e$, internal variables $\boldsymbol{\alpha}_I$, both quantities attached to the intermediate local configuration, according to Besson et al. [2009].

The next constitutive choice is to select the dependence of the free energy potential on the micromorphic variables. For that purpose, the total free energy is split into two functions in the form:

$$\psi = \psi^{ref} + \psi^{\chi} \tag{2.14}$$

---

[1] To establish this expression, the following equation was used

$$\dot{\underline{\boldsymbol{K}}} = \underset{\sim}{\boldsymbol{F}}^{pT}\dot{\overline{\underline{\boldsymbol{K}}}} + \dot{\underset{\sim}{\boldsymbol{F}}}^{pT}\overline{\underline{\boldsymbol{K}}}$$

where the micromorphic contribution is incorporated into the function ψ^χ. The latter is chosen to depend explicitly on one internal variable taken from the set $\boldsymbol{\alpha}_I$, on the micromorphic variable χ and on either $\underline{\boldsymbol{k}}, \underline{\boldsymbol{K}}$ or $\overline{\underline{\boldsymbol{K}}}$. In that way, three distinct functions, $\psi^\chi(\boldsymbol{\alpha}_I, \chi, \underline{\boldsymbol{k}}), \psi_0^\chi(\boldsymbol{\alpha}_I, \chi, \underline{\boldsymbol{K}}), \overline{\psi}^\chi(\boldsymbol{\alpha}_I, \chi, \overline{\underline{\boldsymbol{K}}})$, can be considered that differ only by the choice of the third argument.

Conversion between the three free energy potentials

The free energy potential is an isotropic function of its arguments, the arguments including structural tensors in the case of anisotropic materials [Boehler, 1987; Zheng, 1994]. In particular, the dependence on the gradient of the micromorphic variable must fulfill this requirement. This allows for conversion of free energy function from one set of arguments to the others:

$$\begin{aligned}\psi(\underset{\sim}{C}^e, \boldsymbol{\alpha}_I, \chi, \underline{\boldsymbol{k}}) &= \psi(\underset{\sim}{C}^e, \boldsymbol{\alpha}_I, \chi, \underset{\sim}{F}^{-T}\underline{\boldsymbol{K}})\\ &= \psi(\underset{\sim}{C}^e, \boldsymbol{\alpha}_I, \chi, \underset{\sim}{U}^{-T}\underline{\boldsymbol{K}})\\ &=: \psi_0(\underset{\sim}{C}^e, \underset{\sim}{C}, \boldsymbol{\alpha}_I, \chi, \underline{\boldsymbol{K}}) \end{aligned} \tag{2.15}$$

by virtue of space isotropy principle applied at the second line. The right stretch tensor $\underset{\sim}{U} = \underset{\sim}{C}^{1/2}$ was introduced. It is apparent from this expression that a function $\psi(\underset{\sim}{C}^e, \boldsymbol{\alpha}_I, \chi, \underline{\boldsymbol{k}})$ cannot be converted into a function $\psi_0(\underset{\sim}{C}^e, \boldsymbol{\alpha}_I, \chi, \underline{\boldsymbol{K}})$. The conversion is only possible if adding the right Cauchy–Green as an argument. On the other hand,

$$\begin{aligned}\psi(\underset{\sim}{C}^e, \boldsymbol{\alpha}_I, \chi, \underline{\boldsymbol{k}}) &= \psi(\underset{\sim}{C}^e, \boldsymbol{\alpha}_I, \chi, \underset{\sim}{F}^{e-T}\overline{\underline{\boldsymbol{k}}})\\ &= \psi(\underset{\sim}{C}^e, \boldsymbol{\alpha}_I, \chi, \underset{\sim}{U}^{e-T}\overline{\underline{\boldsymbol{k}}})\\ &=: \overline{\psi}(\underset{\sim}{C}^e, \boldsymbol{\alpha}_I, \chi, \overline{\underline{\boldsymbol{k}}}) \end{aligned} \tag{2.16}$$

In that case, conversion from a function $\psi(\underset{\sim}{C}^e, \boldsymbol{\alpha}_I, \chi, \underline{\boldsymbol{k}})$ to a function of the form $\overline{\psi}(\underset{\sim}{C}^e, \boldsymbol{\alpha}_I, \chi, \overline{\underline{\boldsymbol{k}}})$ is always possible.

In the present work, quadratic contributions to the free energy density w.r.t. either $\underline{\boldsymbol{k}}, \underline{\boldsymbol{K}}$ or $\overline{\underline{\boldsymbol{k}}}$, will be considered for simplicity. In the isotropic case, a quadratic contribution with respect to $\underline{\boldsymbol{k}}$ takes the form:

$$\frac{1}{2}A\|\underline{\boldsymbol{k}}\|^2 = \frac{1}{2}A\underline{\boldsymbol{k}}\cdot\underline{\boldsymbol{k}} \tag{2.17}$$

where A is a constant material parameter regarded as a higher order modulus. It is apparent that a quadratic contribution w.r.t. $\underline{\boldsymbol{k}}$ can be converted into non–quadratic expressions for $\underline{\boldsymbol{K}}$ and $\overline{\underline{\boldsymbol{k}}}$, in the following ways:

$$\frac{1}{2}A\underline{\boldsymbol{k}}\cdot\underline{\boldsymbol{k}} = \frac{1}{2}A\underline{\boldsymbol{K}}\cdot\underset{\sim}{C}^{-1}\cdot\underline{\boldsymbol{K}} = \frac{1}{2}A\overline{\underline{\boldsymbol{K}}}\cdot\underset{\sim}{C}^{e-1}\cdot\overline{\underline{\boldsymbol{K}}} \tag{2.18}$$

As a consequence, adopting a quadratic contribution w.r.t. $\underline{\boldsymbol{K}}, \underline{\boldsymbol{k}}$ or $\overline{\underline{\boldsymbol{K}}}$ leads to three *distinct* material models. The corresponding responses will be compared in the various examples handled in the following.

The case of an anisotropic contribution of $\underline{\boldsymbol{K}}, \underline{\boldsymbol{k}}$ or $\overline{\underline{\boldsymbol{K}}}$ will also be considered and the discussion is postponed to section 2.5.2.

2.2.3 Exploitation of entropy principle and constitutive equations

The entropy principle in its local form is now exploited with the simplifying assumption of non-dissipative generalized stresses (a, $\underline{\boldsymbol{b}}$, a_0, $\underline{\boldsymbol{b}}_0$, $\overline{a}$ and $\overline{\underline{\boldsymbol{b}}}$). Three formulations are presented depending on the use of $\underline{\boldsymbol{K}}, \overline{\underline{\boldsymbol{K}}}$ or $\underline{\boldsymbol{k}}$ as an argument of the free energy potential:

Eulerian formulation The dissipation inequality is written as:

$$\mathscr{P}^{(i)} - \rho\dot{\psi} \geq 0 \tag{2.19}$$

The rate of change of free energy density is evaluated as

$$\dot{\psi}(\underset{\sim}{\boldsymbol{C}}^e, \alpha_I, \chi, \underline{\boldsymbol{k}}) = \frac{\partial \psi}{\partial \underset{\sim}{\boldsymbol{C}}^e} : \dot{\underset{\sim}{\boldsymbol{C}}}^e + \frac{\partial \psi}{\partial \boldsymbol{\alpha}_I} \dot{\boldsymbol{\alpha}}_I + \frac{\partial \psi}{\partial \chi} \dot{\chi} + \frac{\partial \psi}{\partial \underline{\boldsymbol{k}}} \cdot \dot{\underline{\boldsymbol{k}}} \tag{2.20}$$

By substituting Eq. (2.5) and the previous equation in the dissipation inequality Eq. (2.19), the Clausius–Duhem inequality is obtained

$$\left(\frac{1}{2J_e} \underset{\sim}{\boldsymbol{\Pi}}^e - \rho \frac{\partial \psi}{\partial \underset{\sim}{\boldsymbol{C}}^e} \right) : \dot{\underset{\sim}{\boldsymbol{C}}}^e + \frac{1}{J_e} \underset{\sim}{\boldsymbol{M}} : \underset{\sim}{\overline{\boldsymbol{L}}}^p + \left(a - \rho \frac{\partial \psi}{\partial \chi} \right) \dot{\chi} + \left(\underline{\boldsymbol{b}} - \rho \frac{\partial \psi}{\partial \underline{\boldsymbol{k}}} \right) \cdot \dot{\underline{\boldsymbol{k}}} - \rho \frac{\partial \psi}{\partial \boldsymbol{\alpha}_I} \dot{\boldsymbol{\alpha}}_I \geq 0 \tag{2.21}$$

where the Mandel stress tensor $\underset{\sim}{\boldsymbol{M}}$ is the driving force for plastic flow. Since Eq. (2.21) holds true for any mechanical process (*i.e.* for any $\dot{\underset{\sim}{\boldsymbol{C}}}^e$, $\dot{\chi}$ and $\dot{\underline{\boldsymbol{k}}}$), and assuming that the conjugate functions do not depend on these increments, the following state laws are derived

$$\underset{\sim}{\boldsymbol{\Pi}}^e = 2\overline{\rho} \frac{\partial \psi}{\partial \underset{\sim}{\boldsymbol{C}}^e} \quad , \quad a = \rho \frac{\partial \psi}{\partial \chi} \quad , \quad \underline{\boldsymbol{b}} = \rho \frac{\partial \psi}{\partial \underline{\boldsymbol{k}}} \quad , \quad \boldsymbol{A_I} = \overline{\rho} \frac{\partial \psi}{\partial \boldsymbol{\alpha}_I} \tag{2.22}$$

The latter equation defines the thermodynamic forces $\boldsymbol{A_I}$ associated with the internal variables $\boldsymbol{\alpha}_I$. The residual dissipation rate takes the form

$$\underset{\sim}{\boldsymbol{M}} : \underset{\sim}{\overline{\boldsymbol{L}}}^p - \boldsymbol{A_I} \dot{\boldsymbol{\alpha}}_I \geq 0 \tag{2.23}$$

The previous condition of positive dissipation is automatically satisfied when there exists a convex potential $\Omega(\underset{\sim}{\boldsymbol{M}}, \boldsymbol{A_I})$ providing the flow rule and evolution equations for the internal variables:

$$\underset{\sim}{\overline{\boldsymbol{L}}}^p = \frac{\partial \Omega}{\partial \underset{\sim}{\boldsymbol{M}}} \quad , \quad \dot{\boldsymbol{\alpha}}_I = -\frac{\partial \Omega}{\partial \boldsymbol{A_I}} \tag{2.24}$$

The existence of such a dissipation potential is convenient but not necessary.

Lagrangian formulation Alternatively, the Lagrangian version of the Clausius–Duhem inequality reads

$$\left(\frac{J_p}{2} \underset{\sim}{\boldsymbol{\Pi}}^e - \rho_0 \frac{\partial \psi_0}{\partial \underset{\sim}{\boldsymbol{C}}^e} \right) : \dot{\underset{\sim}{\boldsymbol{C}}}^e + J_p \underset{\sim}{\boldsymbol{M}} : \underset{\sim}{\overline{\boldsymbol{L}}}^p + \left(a_0 - \rho_0 \frac{\partial \psi_0}{\partial \chi} \right) \dot{\chi} + \left(\underline{\boldsymbol{b}}_0 - \rho_0 \frac{\partial \psi_0}{\partial \underline{\boldsymbol{K}}} \right) \cdot \dot{\underline{\boldsymbol{K}}} - \rho_0 \frac{\partial \psi_0}{\partial \boldsymbol{\alpha}_I} \dot{\boldsymbol{\alpha}}_I \geq 0 \tag{2.25}$$

and constitutive equations are derived as follows

$$\underset{\sim}{\boldsymbol{\Pi}}^e = 2\overline{\rho} \frac{\partial \psi_0}{\partial \underset{\sim}{\boldsymbol{C}}^e} \quad , \quad a_0 = \rho_0 \frac{\partial \psi_0}{\partial \chi} \quad , \quad \underline{\boldsymbol{b}}_0 = \rho_0 \frac{\partial \psi_0}{\partial \underline{\boldsymbol{K}}} \quad , \quad \boldsymbol{A_I} = \bar{\rho} \frac{\partial \psi_0}{\partial \boldsymbol{\alpha}_I} \tag{2.26}$$

The equations (2.23) and (2.24) apply in this case as well.
A drawback of the two previous constitutive formulations is that they combine variables defined on different local configurations. Appropriate push-forward or pull-back operations make it possible to consider variables all defined on the intermediate local configuration, as proposed in [Forest, 2016]. For that purpose, use is made of the variable $\overline{\underline{\boldsymbol{K}}}$ which is the pull-back of $\underline{\boldsymbol{k}}$ to the intermediate local configuration.

Formulation w.r.t. the intermediate configuration In that case, the dissipation inequality was derived in [Forest, 2016] as

$$\left(\frac{1}{2} \underset{\sim}{\boldsymbol{\Pi}}^e - \overline{\rho} \frac{\partial \overline{\psi}}{\partial \underset{\sim}{\boldsymbol{C}}^e} \right) : \dot{\underset{\sim}{\boldsymbol{C}}}^e + (\underset{\sim}{\boldsymbol{M}} + \overline{\underline{\boldsymbol{K}}} \otimes \overline{\underline{\boldsymbol{b}}}) : \underset{\sim}{\overline{\boldsymbol{L}}}^p + \left(\overline{a} - \overline{\rho} \frac{\partial \psi}{\partial \chi} \right) \dot{\chi} + \left(\overline{\underline{\boldsymbol{b}}} - \overline{\rho} \frac{\partial \overline{\psi}}{\partial \overline{\underline{\boldsymbol{K}}}} \right) . \dot{\overline{\underline{\boldsymbol{K}}}} - \overline{\rho} \frac{\partial \overline{\psi}}{\partial \boldsymbol{\alpha}_I} \dot{\boldsymbol{\alpha}}_I \geq 0 \tag{2.27}$$

The state laws are adopted in a form such that no dissipation is associated to the generalized stress $\overline{\underline{\boldsymbol{b}}}$:

$$\underset{\sim}{\boldsymbol{\Pi}}^e = 2\overline{\rho}\frac{\partial \overline{\Psi}}{\partial \underset{\sim}{\boldsymbol{C}}^e} \quad , \quad \overline{a} = \overline{\rho}\frac{\partial \overline{\Psi}}{\partial \chi} \quad , \quad \overline{\underline{\boldsymbol{b}}} = \overline{\rho}\frac{\partial \overline{\Psi}}{\partial \overline{\underline{\boldsymbol{K}}}} \quad , \quad \boldsymbol{A_I} = \overline{\rho}\frac{\partial \overline{\Psi}}{\partial \alpha_I} \tag{2.28}$$

The mechanical dissipation takes a specific form in that case:

$$\left(\underset{\sim}{\boldsymbol{M}} + \underset{\sim}{\boldsymbol{X}}^b\right) : \overline{\underset{\sim}{\boldsymbol{L}}}^p - \boldsymbol{A_I}\dot{\alpha}_I \geq 0 \tag{2.29}$$

where

$$\underset{\sim}{\boldsymbol{X}}^b = \overline{\underline{\boldsymbol{K}}} \otimes \overline{\underline{\boldsymbol{b}}} \tag{2.30}$$

is an additional contribution to the Mandel stress tensor acting as a kinematic-hardening variable that naturally emerges from the formulation w.r.t. the intermediate local configuration. A generalized dissipation potential can be introduced depending on the generalized Mandel stress tensor:

$$\overline{\underset{\sim}{\boldsymbol{L}}}^p = \frac{\partial \Omega}{\partial (\underset{\sim}{\boldsymbol{M}} + \underset{\sim}{\boldsymbol{X}}^b)} \quad , \quad \dot{\alpha}_I = -\frac{\partial \Omega}{\partial \boldsymbol{A_I}} \tag{2.31}$$

The choice of a convex function $\Omega(\underset{\sim}{\boldsymbol{M}}, \boldsymbol{A_I}, \overline{a}, \overline{\underline{\boldsymbol{b}}})$ ensures identical fulfillment of the positivity of dissipation rate.

2.2.4 Model based on the cumulative plastic strain

The previous formulations are now illustrated in a simple elastoplastic case with the choice of the cumulative plastic strain p as a scalar internal variable controlling isotropic hardening, and of the tensor internal variable $\underset{\sim}{\boldsymbol{\alpha}} \in \{\boldsymbol{\alpha_I}\}$ accounting for kinematic hardening, as done in classical plasticity theory, see *e.g.* [Besson et al., 2009]. The micromorphic variable associated to cumulative plastic strain is denoted by p_χ ($\chi \equiv p_\chi$). The following quadratic form for the free energy potential is adopted

$$\psi_0(\underset{\sim}{\boldsymbol{C}}^e, p, \underset{\sim}{\boldsymbol{\alpha}}, p_\chi, \underline{\boldsymbol{K}}) = \psi^{ref}(\underset{\sim}{\boldsymbol{C}}^e, p, \underset{\sim}{\boldsymbol{\alpha}}) + \frac{1}{2\rho_0}\underline{\boldsymbol{K}} \cdot \underset{\sim}{\boldsymbol{A}} \cdot \underline{\boldsymbol{K}} + \frac{H_\chi}{2\rho_0}(p - p_\chi)^2 \tag{2.32}$$

where H_χ is a coupling modulus (MPa) and $\underset{\sim}{\boldsymbol{A}}$ is a second rank tensor of generalized moduli. For the sake of demonstration, the following expression of the classical specific free energy is adopted

$$\psi^{ref}(\underset{\sim}{\boldsymbol{C}}^e, p, \underset{\sim}{\boldsymbol{\alpha}}) = \frac{1}{2\overline{\rho}}\underset{\sim}{\boldsymbol{E}}^e : \underset{\approx}{\mathbb{C}} : \underset{\sim}{\boldsymbol{E}}^e + \psi^h(p, \underset{\sim}{\boldsymbol{\alpha}}) \tag{2.33}$$

where $\underset{\sim}{\boldsymbol{E}}^e = (\underset{\sim}{\boldsymbol{C}}^e - \underset{\sim}{\boldsymbol{1}})/2$ is the Green–Lagrange strain w.r.t. the intermediate configuration, $\underset{\approx}{\mathbb{C}}$ is the fourth-order tensor of elastic moduli and $\psi^h(p, \alpha_I)$ is the stored energy contribution associated with work-hardening.

The state laws (2.26) become

$$\underset{\sim}{\boldsymbol{\Pi}}^e = \underset{\approx}{\mathbb{C}} : \underset{\sim}{\boldsymbol{E}}^e, \qquad a_0 = -H_\chi\left(p - p_\chi\right) \quad , \quad \underline{\boldsymbol{b}}_0 = \underset{\sim}{\boldsymbol{A}}.\underline{\boldsymbol{K}}, \qquad R(p) = \overline{\rho}\frac{\partial \psi_0}{\partial p} \tag{2.34}$$

The first equation is called Saint-Venant-Kirchhoff hyperelasticity law w.r.t. the local intermediate configuration. The yield function is then taken of the form

$$f(\underset{\sim}{\boldsymbol{M}}, \underset{\sim}{\boldsymbol{X}}_m) = \left[\underset{\sim}{\boldsymbol{M}} - \underset{\sim}{\boldsymbol{X}}^{ref}\right]_{eq} - R_0 - R(p) \tag{2.35}$$

involving the Mandel stress tensor. The scalar functions $[\diamond]_{eq}$ and R_0 denote the equivalent stress and the initial yield stress, respectively. The back-stress $\underset{\sim}{\boldsymbol{X}}^{ref}$ and the isotropic hardening R^{ref} are related to internal variables $\underset{\sim}{\alpha}$ and p by

$$\underset{\sim}{\boldsymbol{X}}^{ref} = \bar{\rho}\frac{\partial \psi^{ref}}{\partial \underset{\sim}{\alpha}}, \qquad R^{ref} = \bar{\rho}\frac{\partial \psi^{ref}}{\partial p} \tag{2.36}$$

By combining the second balance equation in Eq. (2.11) and Eq. (2.34), we get the following regularization operator

$$p = p_\chi - \frac{1}{H_\chi}\mathrm{Div}(\underset{\sim}{\boldsymbol{A}} \cdot \underline{\boldsymbol{K}}) \tag{2.37}$$

In isotropic and homogeneous case, *i.e.* $\underset{\sim}{\boldsymbol{A}} = A\underset{\sim}{\boldsymbol{1}}$, Eq. (2.37) reduces to

$$p = p_\chi - \frac{A}{H_\chi}\Delta_0 p_\chi \tag{2.38}$$

which involves the Laplacian operator Δ_0 w.r.t. Lagrangian coordinates. The constitutive choices of specific free energy potential for different formulations are summarized in Table 2.1. For the sake of comparison, the regularization equations are all expressed in terms of Lagrangian operators.

	Eulerian	Lagrangian	intermediate
Specific free energy	$\psi = \psi^{ref} + \frac{1}{2\rho}\underline{\boldsymbol{k}}.\underset{\sim}{\boldsymbol{A}}.\underline{\boldsymbol{k}} + \frac{H_\chi}{2\rho}(p-p_\chi)^2$	$\psi_0 = \psi^{ref} + \frac{1}{2\rho_0}\underline{\boldsymbol{K}}.\underset{\sim}{\boldsymbol{A}}.\underline{\boldsymbol{K}} + \frac{H_\chi}{2\rho_0}(p-p_\chi)^2$	$\overline{\psi} = \psi^{ref} + \frac{1}{2\overline{\rho}}\overline{\underline{\boldsymbol{K}}}.\underset{\sim}{\boldsymbol{A}}.\overline{\underline{\boldsymbol{K}}} + \frac{H_\chi}{2\overline{\rho}}(p-p_\chi)^2$
Yield function f	$\left[\underset{\sim}{\boldsymbol{M}} - \underset{\sim}{\boldsymbol{X}}^{ref}\right]_{eq} - (R^{ref} - J_e a)$	$\left[\underset{\sim}{\boldsymbol{M}} - \underset{\sim}{\boldsymbol{X}}^{ref}\right]_{eq} - \left(R^{ref} - J_p^{-1}a_0\right)$	$\left[\underset{\sim}{\boldsymbol{M}} - \underset{\sim}{\boldsymbol{X}}^{ref} + \underset{\sim}{\boldsymbol{X}}^{b}\right]_{eq} - (R^{ref} - \overline{a})$ $\underset{\sim}{\boldsymbol{X}}^{b} = \overline{\underline{\boldsymbol{K}}} \otimes \overline{\underline{\boldsymbol{b}}}$
Generalized stresses	$a = -H_\chi\,(p-p_\chi)$ $\underline{\boldsymbol{b}} = \underset{\sim}{\boldsymbol{A}}.\underline{\boldsymbol{k}}$	$a_0 = -H_\chi\,(p-p_\chi)$ $\underline{\boldsymbol{b}}_0 = \underset{\sim}{\boldsymbol{A}}.\underline{\boldsymbol{K}}$	$\overline{a} = -H_\chi\,(p-p_\chi)$ $\overline{\underline{\boldsymbol{b}}} = \underset{\sim}{\boldsymbol{A}}.\overline{\underline{\boldsymbol{K}}}$
Regularization operator	$p = p_\chi - \frac{1}{H_\chi}\mathrm{Div}\left(J(\underset{\sim}{\boldsymbol{F}}^{-1}\underset{\sim}{\boldsymbol{A}}\underset{\sim}{\boldsymbol{F}}^{-T})\cdot\underline{\boldsymbol{K}}\right)$	$p = p_\chi - \frac{1}{H_\chi}\mathrm{Div}(\underset{\sim}{\boldsymbol{A}}\cdot\underline{\boldsymbol{K}})$	$p = p_\chi - \frac{1}{H_\chi}\mathrm{Div}\left(J_p(\underset{\sim}{\boldsymbol{F}}^{p-1}\underset{\sim}{\boldsymbol{A}}\underset{\sim}{\boldsymbol{F}}^{p-T})\cdot\underline{\boldsymbol{K}}\right)$

Table 2.1: *A summary of constitutive choices and regularization operators for different formulations.*

Remark 2. *To illustrate the difference between different formulations while assuming the same form of free energy potentials, we derive a Lagrangian formulation based on a quadratic potential ψ expressed in terms of Eulerian gradient $\underline{\boldsymbol{k}}$. In the isotropic case, the conversion (2.18) shows that a quadratic potential of Eulerian arguments results in a non-quadratic potential in terms of Lagrangian arguments. As shown in Table 2.1, the regularisation operators provided by the three formulations are quite different for a given form of free energy potential and the same material parameters.*

Remark 3. *The last equation (2.35) implies that the isotropic hardening variable can be written as*

$$\begin{aligned} R(p) &= \overline{\rho}\frac{\partial \psi^{ref}}{\partial p} + \frac{\overline{\rho}}{\rho_0}H_\chi(p-p_\chi) \\ &= \overline{\rho}\frac{\partial \psi^{ref}}{\partial p} - a_0 = \overline{\rho}\frac{\partial \psi^{ref}}{\partial p} - Div\ \underline{\boldsymbol{b}}_0 \\ &= R^{ref}(p) - A\Delta_0 p_\chi \end{aligned} \tag{2.39}$$

where plastic incompressibility condition and isotropic tensor $\underset{\sim}{\boldsymbol{A}}$ have been implemented. The constraint $p_\chi \equiv p$ can be enforced by adopting a sufficiently large value of the penalty modulus H_χ. The hardening law is then enhanced by a Laplace term and the model coincides accordingly with the Aifantis theory of strain gradient plasticity, see [Aifantis, 1984; Forest and Aifantis, 2010].

2.2.5 Model based on the equivalent plastic strain

The model based on the cumulative plastic strain will be shown to lead to a size-dependent isotropic hardening. In contrast, an alternative scalar model has been proposed in [Jebahi and Forest, 2021], in the small strain framework, in order to model size-dependent kinematic hardening without using the full plastic strain tensor as done previously in [Poh et al., 2011] which is believed to be computationally expensive. Here, we present an extension of that model to finite strains by considering the norm of $(\underset{\sim}{\boldsymbol{B}}^{p} - \underset{\sim}{\boldsymbol{1}})$ where

$\underset{\sim}{\boldsymbol{B}}^p = \underset{\sim}{\boldsymbol{F}}^p \underset{\sim}{\boldsymbol{F}}^{pT}$ is the plastic left Cauchy-Green tensor. Accordingly, the micromorphic variable is associated to the equivalent measure of plastic strain B^p_{eq} defined by

$$B^p_{eq} = \sqrt{\frac{1}{6}\left(\underset{\sim}{\boldsymbol{B}}^p - \underset{\sim}{\boldsymbol{1}}\right) : \left(\underset{\sim}{\boldsymbol{B}}^p - \underset{\sim}{\boldsymbol{1}}\right)} \tag{2.40}$$

In what follows, the derivation of constitutive equations and flow rules for a Lagrangian formulation are presented. Similarly, as shown in the section 2.2.1, other formulations are possible by considering gradients of micromorphic variables defined w.r.t. Eulerian and intermediate configurations. The free energy potential per unit mass, assumed to be a function

$$\psi_0 = \psi_0(\underset{\sim}{\boldsymbol{C}}^e, \alpha_I, \underset{\sim}{\boldsymbol{B}}^p, \chi, \underline{\boldsymbol{K}}) \tag{2.41}$$

The Clausius-Duhem inequality becomes[2]

$$\left(\frac{J_p}{2}\underset{\sim}{\boldsymbol{\Pi}}^e - \rho_0 \frac{\partial \psi_0}{\partial \underset{\sim}{\boldsymbol{C}}^e}\right) : \dot{\underset{\sim}{\boldsymbol{C}}}^e + \left(J_p \underset{\sim}{\boldsymbol{M}} - 2\rho_0 \frac{\partial \psi_0}{\partial \underset{\sim}{\boldsymbol{B}}^p}\underset{\sim}{\boldsymbol{B}}^p\right) : \underset{\sim}{\overline{\boldsymbol{L}}}^p + \left(a_0 - \rho_0 \frac{\partial \psi_0}{\partial \chi}\right)\dot{\chi} + \left(\underline{\boldsymbol{b}}_0 - \rho_0 \frac{\partial \psi_0}{\partial \underline{\boldsymbol{K}}}\right).\dot{\underline{\boldsymbol{K}}} - \rho_0 \frac{\partial \psi_0}{\partial \boldsymbol{\alpha}_I}\dot{\boldsymbol{\alpha}}_I \geq 0 \tag{2.42}$$

The state laws follow as

$$\underset{\sim}{\boldsymbol{\Pi}}^e = 2\overline{\rho}\frac{\partial \psi_0}{\partial \underset{\sim}{\boldsymbol{C}}^e}, \qquad a_0 = \rho_0 \frac{\partial \psi_0}{\partial \chi}, \qquad \underline{\boldsymbol{b}}_0 = \rho_0 \frac{\partial \psi_0}{\partial \underline{\boldsymbol{K}}}, \qquad \boldsymbol{A}_I = \bar{\rho}\frac{\partial \psi_0}{\partial \boldsymbol{\alpha}_I} \tag{2.43}$$

The residual dissipation becomes

$$\left(J_p \underset{\sim}{\boldsymbol{M}} - 2\rho_0 \frac{\partial \psi_0}{\partial \underset{\sim}{\boldsymbol{B}}^p}\underset{\sim}{\boldsymbol{B}}^p\right) : \underset{\sim}{\overline{\boldsymbol{L}}}^p - \boldsymbol{A_I}\dot{\boldsymbol{\alpha}}_I \geq 0 \tag{2.44}$$

By assuming the existence of a convex potential $\Omega(\underset{\sim}{\boldsymbol{M}}, A_I)$, the flow rule reads

$$\underset{\sim}{\overline{\boldsymbol{L}}}^p = \dot{\lambda}\frac{\partial \Omega}{\partial\left(\underset{\sim}{\boldsymbol{M}} - \underset{\sim}{\boldsymbol{X}}_m\right)} \tag{2.45}$$

where a back-stress arises given by

$$\underset{\sim}{\boldsymbol{X}}_m = 2\overline{\rho}\frac{\partial \psi_0}{\partial \underset{\sim}{\boldsymbol{B}}^p}\underset{\sim}{\boldsymbol{B}}^p \tag{2.46}$$

The particular choice of a partly quadratic potential as

$$\psi_0(\underset{\sim}{\boldsymbol{C}}^e, \underset{\sim}{\boldsymbol{B}}^p, p, \chi, \underline{\boldsymbol{K}}) = \psi^{ref} + \frac{H_\chi}{2\rho_0}(B^p_{eq} - \chi)^2 + \frac{1}{2\rho_0}\underline{\boldsymbol{K}}.\underset{\sim}{\boldsymbol{A}}.\underline{\boldsymbol{K}} \tag{2.47}$$

leads to the following constitutive equations

$$\underset{\sim}{\boldsymbol{\Pi}}^e = \underset{\approx}{\mathbb{C}} : \underset{\sim}{\boldsymbol{E}}^e, \qquad R(p) = \bar{\rho}\frac{\partial \psi_0}{\partial p}, \qquad a_0 = -H_\chi(B^p_{eq} - \chi), \qquad \underline{\boldsymbol{b}}_0 = \underset{\sim}{\boldsymbol{A}}\underline{\boldsymbol{K}} \tag{2.48}$$

and

$$\underset{\sim}{\boldsymbol{X}}_m = \frac{H_\chi}{3J_p}\frac{\left(\underset{\sim}{\boldsymbol{B}}^p - \underset{\sim}{\boldsymbol{1}}\right)\underset{\sim}{\boldsymbol{B}}^p}{B^p_{eq}}(B^p_{eq} - \chi) \tag{2.49}$$

---

[2] It can be checked that

$$\frac{\partial \psi_0}{\partial \underset{\sim}{\boldsymbol{B}}^p} : \dot{\underset{\sim}{\boldsymbol{B}}}^p = \frac{\partial \psi_0}{\partial \underset{\sim}{\boldsymbol{B}}^p} : (\underset{\sim}{\overline{\boldsymbol{L}}}^p \underset{\sim}{\boldsymbol{B}}^p + \underset{\sim}{\boldsymbol{B}}^p \underset{\sim}{\overline{\boldsymbol{L}}}^{pT}) = 2\frac{\partial \psi_0}{\partial \underset{\sim}{\boldsymbol{B}}^p} : (\underset{\sim}{\overline{\boldsymbol{L}}}^p \underset{\sim}{\boldsymbol{B}}^p) = 2\left(\frac{\partial \psi_0}{\partial \underset{\sim}{\boldsymbol{B}}^p}\underset{\sim}{\boldsymbol{B}}^p\right) : \underset{\sim}{\overline{\boldsymbol{L}}}^p$$

assuming that $\frac{\partial \psi_0}{\partial \underset{\sim}{\boldsymbol{B}}^p}$ is symmetric.

The proposed yield function is given by

$$f(\underset{\sim}{M}, \underset{\sim}{X}_m) = \left[\underset{\sim}{M} - \underset{\sim}{X}_m\right]_{eq} - R_0 - R(p) \tag{2.50}$$

The size-dependent character of the enhanced kinematic hardening component $\underset{\sim}{X}_m$ is apparent in Eq. (2.49) by noting that the term $H_\chi(B^p_{eq} - \chi) = -a_0 = -\text{Div}\ \underline{b}_0$ thus involving higher order derivatives.

2.2.6 Implementation scheme

The general implementation of constitutive and balance laws of scalar micromorphic models is briefly described in this section (one can refer to [Ling et al., 2018] for more details on the FEM implementation). The present approach is implemented in the Finite Element code Z-set [2022].

The principle of virtual power in Eq. (2.10) is discretized as

$$\sum_{e=1}^{n} \int_{D_0^e} \mathscr{P}^{(i)} dV = \sum_{e=1}^{n_s} \int_{\partial D_0^e} (\underline{T}.\dot{\underline{u}} + a_0^c \dot{\chi})\, dS \quad , \quad \forall D_0 \subset \Omega_0 \tag{2.51}$$

Here, the sub-domain D_0^e corresponds to the space occupied by the individual element e. The boundary ∂D_0 is discretized into n_s surface elements ∂D_0^e for the application of surface tractions. Within each individual element, u_i is interpolated from the displacement values of m nodes and χ from the values of q nodes as

$$u_i = \sum_{k=1}^{m} {}^uN^k \tilde{u}_i^k, \qquad \chi = \sum_{k=1}^{q} {}^\chi N^k \tilde{\chi}^k \tag{2.52}$$

${}^uN^k$ and ${}^\chi N^k$ are shape functions for u_i and χ, respectively. The deformation gradient $\underset{\sim}{F}$ and the Lagrangian gradient of χ denoted by $\underline{K}$ are given by

$$F_{ij} = \sum_{k=1}^{m} {}^uB_j^k \tilde{u}_i^k, \qquad K_i = \sum_{k=1}^{q} {}^\chi B_i^k \tilde{\chi}^k \tag{2.53}$$

with ${}^uB_j^k = \dfrac{\partial\, {}^uN^k}{\partial X_j}$ and ${}^uB_i^k = \dfrac{\partial\, {}^\chi N^k}{\partial X_i}$. Finally, by substituting equations (2.52) and (2.53) into Eq. (2.51), one gets

$$\begin{aligned}
&\sum_{e=1}^{n}\sum_{k=1}^{m}\left[\int_{D_0^e} (P_{ij}\,{}^uB_j^k)\, dV_0\right] \dot{\tilde{u}}_i^k + \sum_{e=1}^{n}\sum_{k=1}^{q}\left[\int_{D_0^e} (a_0\,{}^\chi N^k + b_{0,i}\,{}^\chi B_i^k)\, dV_0\right] \dot{\tilde{\chi}}^k \\
&= \sum_{e=1}^{n_s}\sum_{k=1}^{m}\left[\int_{\partial D_0^e} \left(T_i\,{}^uN^k\right) dS_0\right] \dot{\tilde{u}}_i^k + \sum_{e=1}^{n_s}\sum_{k=1}^{q}\left[\int_{\partial D_0^e} \left(a_0^c\ {}^\chi N^k\right) dS_0\right] \dot{\tilde{\chi}}^k
\end{aligned} \tag{2.54}$$

According to Eq. (2.54), an internal (resp. external) reaction is associated with each degree of freedom. The FE problem will be solved by a monolithic iterative method, using a Newton algorithm. The consistent tangent matrix as shown in [Ling et al., 2018; Scherer et al., 2020] is given

$$[\underline{K}] = \frac{\partial \Delta \mathscr{V}_{OUT}}{\partial \Delta \mathscr{V}_{IN}} - \frac{\partial \Delta \mathscr{V}_{OUT}}{\partial \Delta \mathscr{V}_{int}} \left(\frac{\partial \mathscr{R}}{\partial \Delta \mathscr{V}_{int}}\right)^{-1} \frac{\partial \mathscr{R}}{\partial \Delta \mathscr{V}_{IN}} \tag{2.55}$$

where $\mathscr{V}_{OUT}$, $\mathscr{V}_{IN}$ and $\mathscr{V}_{int}$ denote output, input and integrated variables, respectively. The output variables are the Boussinesq stress $\underset{\sim}{P}$ and generalized stresses a and $\underline{b}$. The input variables are $\underset{\sim}{F}$, χ, $\underline{K}$. For the sake of demonstration, we consider $\underset{\sim}{F}^e$ and the cumulative plastic strain p as integrated variables. Additional internal variables related to isotropic/kinematic hardening are readily incorporated in this framework.

The residuals $\underset{\sim}{\mathscr{R}}(\Delta\mathscr{V}_{int},\Delta\mathscr{V}_{IN})$ for the evolution equation for $\underset{\sim}{\boldsymbol{F}}^e$ and the yield conditions, are given by

$$\begin{cases} \mathscr{R}_e = & \Delta\underset{\sim}{\boldsymbol{F}}^e - \underset{\sim}{\boldsymbol{L}}\,\underset{\sim}{\boldsymbol{F}}^e + \Delta p\,\underset{\sim}{\boldsymbol{F}}^e \dfrac{\partial f}{\partial \underset{\sim}{\boldsymbol{M}}} = 0 \\ \mathscr{R}_p = & \dfrac{f}{H_\chi} = 0 \quad \text{(plastic)}, \qquad \text{or} \qquad \mathscr{R}_p = \Delta p - \Delta t \dfrac{\partial \Omega}{\partial f} = 0 \quad \text{(viscoplastic)} \end{cases} \tag{2.56}$$

Supplementary equations can be added in order to integrate internal variables (*e.g.* associated to isotropic and kinematic hardening). In order to satisfy the plastic incompressibility condition ($\det\{\underset{\sim}{\boldsymbol{F}}^p\} = 1$), $\underset{\sim}{\boldsymbol{F}}^e$ is replaced in Eq. (2.56) by $\left(\dfrac{\det\{\underset{\sim}{\boldsymbol{F}}\}}{\det\{\underset{\sim}{\boldsymbol{F}}^e\}}\right)^{1/3}\underset{\sim}{\boldsymbol{F}}^e$. The normalization of $\mathscr{R}_p$ by H_χ parameter is carried out to improve the numerical efficiency by avoiding ill-conditioned Jacobian matrices $\mathscr{J} = \dfrac{\partial \mathscr{R}}{\partial \Delta\mathscr{V}_{int}}$, especially in case of rate-independent plasticity. The calculation of the tangent matrix $[\boldsymbol{K}]$ is detailed in C.3.

2.2.7 Limit case of Aifantis plasticity

Following the Remark 3, we present here an implementation of Aifantis strain gradient plasticity relying upon Lagrange multipliers added to the micromorphic model. This method has been applied for plasticity and damage models [Lorentz and Benallal, 2005; Zhang et al., 2018; Scherer et al., 2020]. A Lagrange multiplier is introduced to enforce the internal constraint $p_\chi \equiv p$ at each material point. The enhanced free energy potential, interpreted as a Lagrangian function, is given by

$$\psi_0^{\mathscr{L}}(\underset{\sim}{\boldsymbol{C}}^e, p, p_\chi, \underline{\boldsymbol{K}}) = \psi^{ref}(\underset{\sim}{\boldsymbol{C}}^e, p) + \frac{1}{2\rho}\underline{\boldsymbol{K}}.\underset{\sim}{\boldsymbol{A}}.\underline{\boldsymbol{K}} + \frac{\lambda}{\rho_0}(p_\chi - p) + \frac{\mu_\chi}{2\rho_0}(p_\chi - p)^2 \tag{2.57}$$

where λ is a Lagrange multiplier and μ_χ is a penalization modulus. The Lagrange multiplier λ is introduced to weakly enforce the equality between p_χ and p. The augmented Lagrangian term $\mu_\chi(p_\chi - p)^2$ provides an additional coercivity so as to avoid potential oscillation of the cumulative plasticity (see *e.g.* [Lorentz and Benallal, 2005; Scherer et al., 2020]). By substituting Eq. (2.57) in the Clausius–Duhem inequality and assuming that a_0 and $\underline{\boldsymbol{b}}_0$ are non-dissipative generalized stresses, the following constitutive laws are obtained:

$$\underset{\sim}{\boldsymbol{\Pi}}^e = 2\frac{\partial \psi}{\partial \underset{\sim}{\boldsymbol{C}}^e}, \qquad a_0 = \rho_0 \frac{\partial \psi}{\partial \chi}, \qquad \underline{\boldsymbol{b}}_0 = \rho_0 \frac{\partial \psi}{\partial \underline{\boldsymbol{K}}} \tag{2.58}$$

When the constraint $p = p_\chi$ is met, one has

$$\frac{\partial \psi_0^{\mathscr{L}}}{\partial \lambda}\dot{\lambda} = \frac{\dot{\lambda}}{\rho_0}(p_\chi - p) = 0 \tag{2.59}$$

Similarly, formulations w.r.t. Eulerian and intermediate configurations are readily developed. The numerical implementation of this approach is detailed thoroughly in [Scherer et al., 2020].

2.3 Size effects in confined plasticity

In the following, we illustrate the ability of the present approach to model size effects through several examples. For convenience, in this section we consider only the model presented in 2.2.4 based on cumulative plastic strain. Confined plasticity conditions are applied to a unit cell in order to get non-vanishing plasticity gradients. Cyclic loadings are performed in order to compare the three finite strain formulations previously discussed. Throughout the rest of the document, the material parameters for isotropic elasticity are: Young modulus $E = 78$ GPa and Poisson ratio $\nu = 0.3$. The plasticity related coefficients and the higher order parameters H_χ (unit MPa) and A (unit N) are varied.

2.3.1 Confined plasticity under shear loading

A strip of length $2h$ is considered in Fig. 2.1a. A macroscopic shear deformation $\underset{\sim}{\overline{\boldsymbol{F}}} = \underset{\sim}{\boldsymbol{1}} + \overline{F}_{12}\underline{\boldsymbol{e}}_x \otimes \underline{\boldsymbol{e}}_y$ is applied such that the displacement field takes the form

$$\underline{\boldsymbol{u}} = (\underset{\sim}{\overline{\boldsymbol{F}}} - \underset{\sim}{\boldsymbol{1}}) \cdot \underline{\boldsymbol{X}} + \underline{\boldsymbol{v}}(\underline{\boldsymbol{X}}) \tag{2.60}$$

Periodic boundary conditions are imposed on the displacement fluctuation $\underline{\boldsymbol{v}}$. Dirichlet conditions for the micromorphic variable are prescribed: $p_\chi = 0$ at $x = \pm h$. Periodicity conditions are enforced between top and bottom surfaces for p_χ. As a consequence, the fields are invariant along $\underline{\boldsymbol{e}}_y$, except the linear distribution $u_x(y)$. Plane strain conditions are adopted.

A time-independent von Mises plasticity model is considered. The hardening free energy $\overline{\rho}\psi^h(p) = \dfrac{1}{2}Hp^2$ corresponding to linear hardening/softening leads to the following yield function for classical models

$$f(\underset{\sim}{\boldsymbol{M}}) = \sqrt{\frac{3}{2}\underset{\sim}{\boldsymbol{M}}' : \underset{\sim}{\boldsymbol{M}}'} - (R_0 + Hp) \tag{2.61}$$

where $\underset{\sim}{\boldsymbol{M}}'$ is the deviatoric part of $\underset{\sim}{\boldsymbol{M}}$. The hardening law is modified in the micromorphic model such that the enhanced yield function becomes

$$f(\underset{\sim}{\boldsymbol{M}}) = \sqrt{\frac{3}{2}\underset{\sim}{\boldsymbol{M}}' : \underset{\sim}{\boldsymbol{M}}'} - (R_0 + R) \qquad \text{with} \qquad R = Hp + H_\chi(p - p_\chi) \tag{2.62}$$

Analytical solutions of this one-dimensional boundary value problem can be derived in the small strain limit. They are provided in 2.8 for $H \geq 0$. An important relation is derived therein, namely the characteristic length $2\pi/\omega$ given by Eq. (2.89) which emerges from the analysis as a function of hardening modulus H and generalized moduli H_χ and A. As shown in Fig. 2.2b ($H = 0$), by increasing the value of the parameter H_χ, the difference between p and p_χ becomes smaller for a given value of higher order modulus A. Meanwhile, the generalized stress $a_0 = -H_\chi(p - p_\chi)$ increases with H_χ. It means that, enforcing equality between p and p_χ induces a very high yield stress in the vicinity of $x = \pm h$ given by

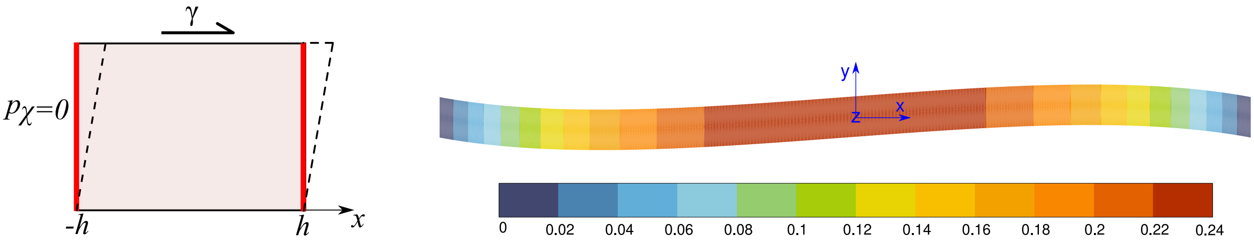

(a) (b)

Figure 2.1: *(a) Simple glide test with imposed microplastic boundary conditions; (b) the deformed shape and the distribution of microplastic strain p_χ for $\overline{F}_{12} = 1$, $R_0 = 20$ MPa, $H = 0$ (Lagrangian formulation).*

$$\sigma_Y = R_0 + R = R_0 + H_\chi(p - p_\chi) \tag{2.63}$$

The analytical solution for $H \geq 0$, detailed in 2.8 in the small strain framework, predicts that the profile of cumulative plastic plasticity is given by a hyperbolic (exponential) function. Fig. 2.3 shows such profiles of microplastic variable p_χ for several values of the parameter A. These curves can be shown to agree well with the predicted profiles at small strains but more complex distributions are found at large shear amounts. Fig. 2.4a depicts the stress-strain curves for different values of the parameter A in the absence of classical hardening ($H = 0$). A progressive stiffening is observed when increasing the value of parameter A or, equivalently, the intrinsic length scale. The same phenomenon is observed when the size of the unit cell gets smaller for a fixed value of A according to Fig. 2.4b. This leads to significant stiffening of the overall

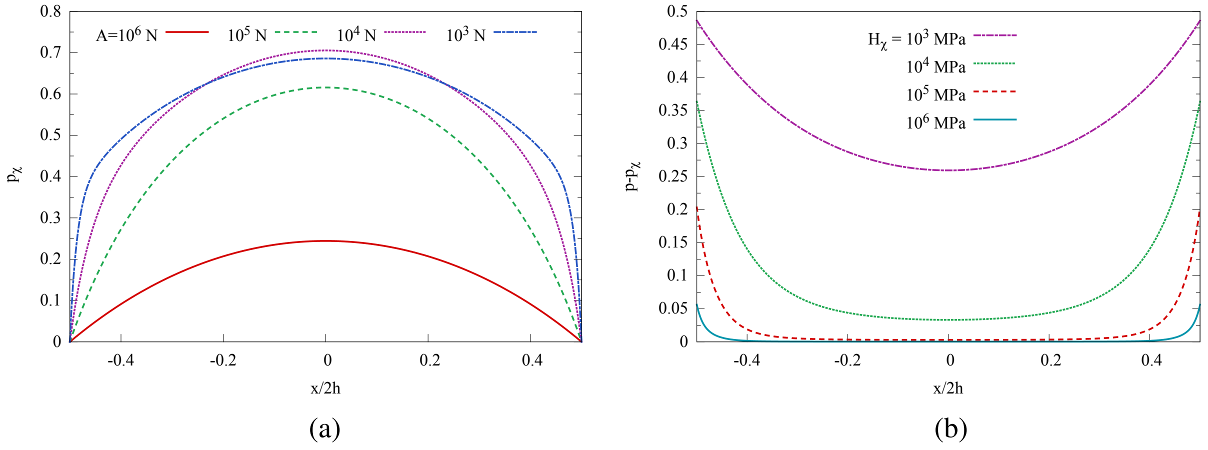

(a) (b)

Figure 2.2: *(a) The profile of the microplastic variable p_χ for different values of A ($H_\chi = 10^5$ MPa); (b) the difference $(p - p_\chi)$ for different values of H_χ ($A = 10^4$ N). The applied macroscopic strain is $\overline{F}_{12} = 1$, $R_0 = 20$ MPa, $H = 0$ (Lagrangian formulation).*

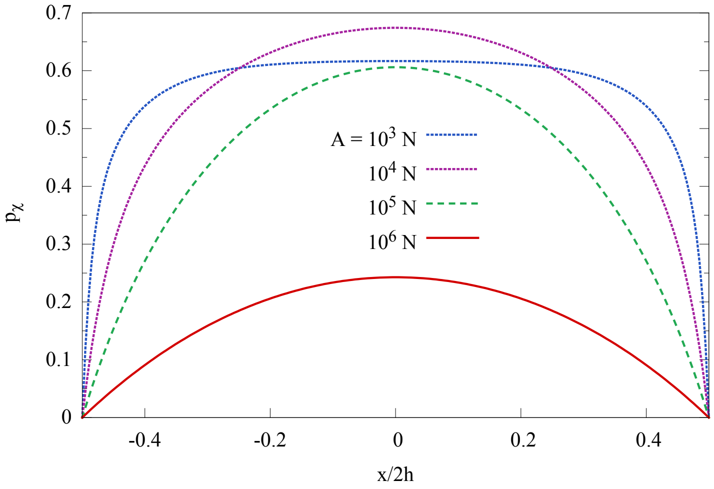

Figure 2.3: *The profile of microplastic variable p_χ for different values of A ($H_\chi = 10^5$ MPa). The applied macroscopic strain is $\overline{F}_{12} = 1$, $R_0 = 20$ MPa, $H = 1000$ MPa (Lagrangian formulation).*

response when increasing the higher modulus A or, equivalently reducing the strip width. This corresponds to the well-known effect: *smaller is harder*. This is directly related to the fact that gradients of plastic variables are higher at small scales for the same loading conditions.

The results of a cyclic simple glide loading, with similar boundary conditions as in Fig. 2.1a, are provided in Fig. 2.5a for different finite deformation formulations. In this cyclic test, strain values remain moderate so that the differences between Eulerian and Lagrangian formulations are negligible. Meanwhile, a kinematic hardening effect is induced by the formulation w.r.t. the intermediate configuration. Over cycles, the gradient of microplastic variable p_χ increases, hence $\underset{\sim}{\boldsymbol{X}}^b$, given by Eq. (2.30), increases as well. The sign of $\underset{\sim}{\boldsymbol{X}}^b$ components remains the same while shearing in both directions. The kinematic hardening $\underset{\sim}{\boldsymbol{X}}^b$ becomes more significant after few cycles. It remains that the effect of the finite deformation formulation remains rather limited for the components σ_{12} and X^b_{12}. The effect is much more pronounced for the components σ_{11}, σ_{22} and σ_{33} which are not negligible due to the Poynting effect, see Fig. 2.5b. The reason is that X^b_{11} is the component having the highest value.

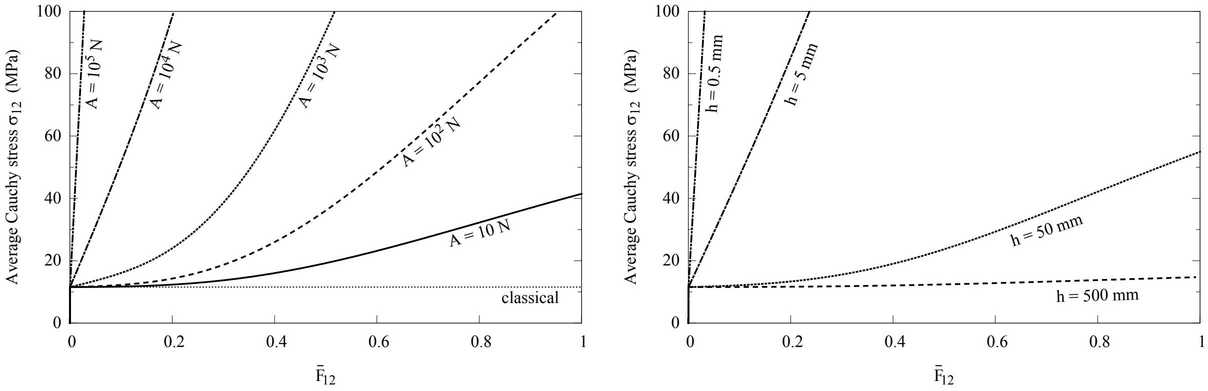

(a) (b)

Figure 2.4: *The macroscopic stress-strain curves for different values of (a) the parameter A, $h = 5$ mm; (b) length of the unit cell h, $A = 10^4$ N. Material parameters: $R_0 = 20$ MPa, $H = 0$ and $H_\chi = 10^5$ MPa (Lagrangian formulation).*

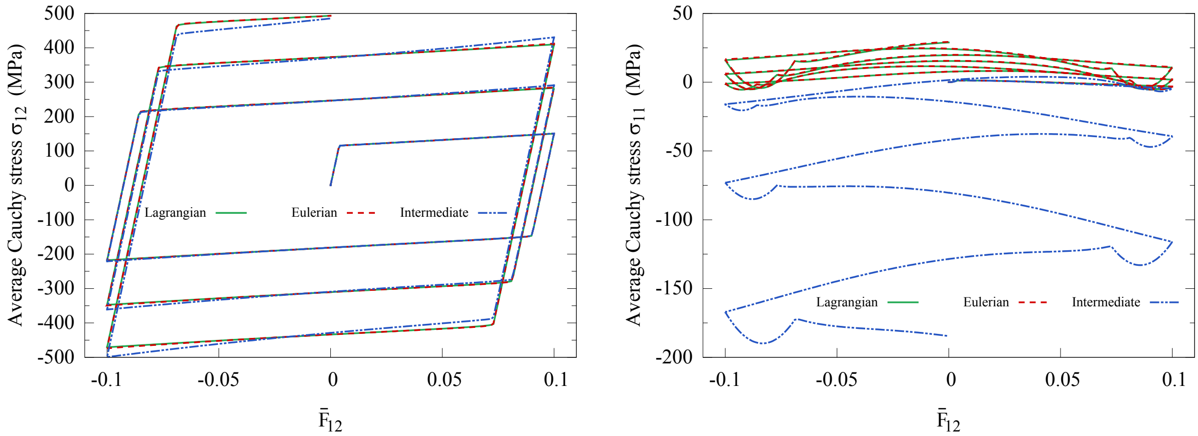

Figure 2.5: *Cyclic simple glide test with confined plasticity for different finite strain formulations. Material parameters: $R_0 = 200$ MPa, $H = 0$ MPa, $H_\chi = 10^4$ MPa, $A = 10^4$ N.*

2.3.2 Confined plasticity under tensile loading

A simple tension test is considered with confined plasticity boundary conditions (passivation). The unit cell of width $2h$ is subjected to a uniform displacement u_x at $x = h$, u_y being constrained to be uniform at the top and bottom lines, see insert in Fig. 2.6a. Plane strain conditions are adopted. The microplastic variable p_χ is set to zero at $x = \pm h$. Fig. 2.6a depicts the stress-strain curves for several values of material parameter A and the size of unit cell h. It shows that the induced isotropic hardening increases with higher values of the ratio A/h.

The stress-strain curves for a cyclic loading (tension+compression) are shown in Fig. 2.7a for the three finite deformation formulations. Small differences are noticed between Lagrangian and Eulerian formulations. In contrast, the formulation w.r.t. the intermediate configuration differs significantly from the two others. Note that the stress response drifts away towards negative values. This is due to kinematic hardening contribution by $\underset{\sim}{\boldsymbol{X}}^b$ having the same sign in tension (points 1 and 2 on the curves) and compression (point 1' and 2'). The gradient of cumulative plastic strain increases over cycles, so does $\underset{\sim}{\boldsymbol{X}}^b$ (see results for X^b_{11} component in Fig. 2.7a. In fact, the quantity $\underset{\sim}{\boldsymbol{X}}^b$ grows proportionally to the square of gradient $\underline{\boldsymbol{b}}$ according to Eq. (2.30). This indicates that this back-stress is a second order contribution at small strains but becomes dominant at large strains.

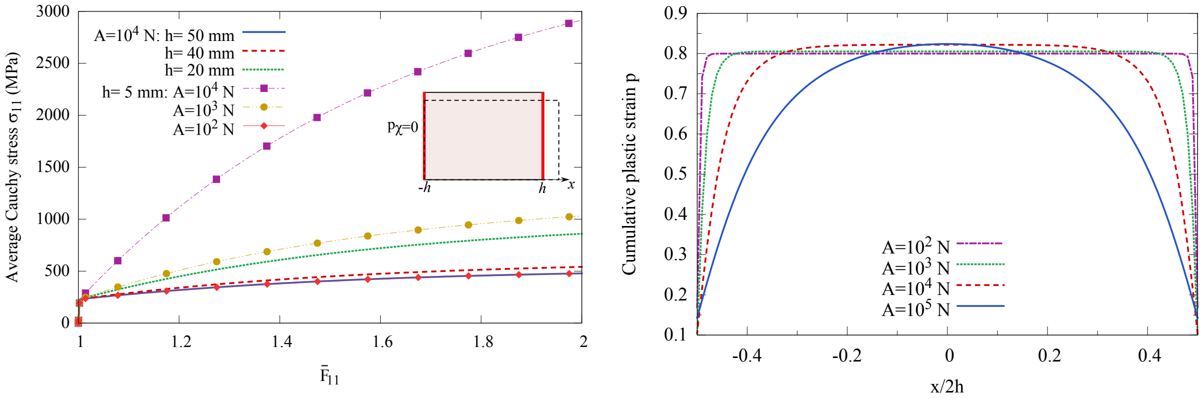

(a) (b)

Figure 2.6: *Monotonic tensile loading: (a) overall stress-strain curves; (b) profiles of cumulative plastic strain p for* $\overline{F}_{11} = 2$. *Material parameters are* $H_\chi = 10^5$ *MPa,* $R_0 = 200$ *MPa,* $H = 0$ *(Lagrangian formulation).*

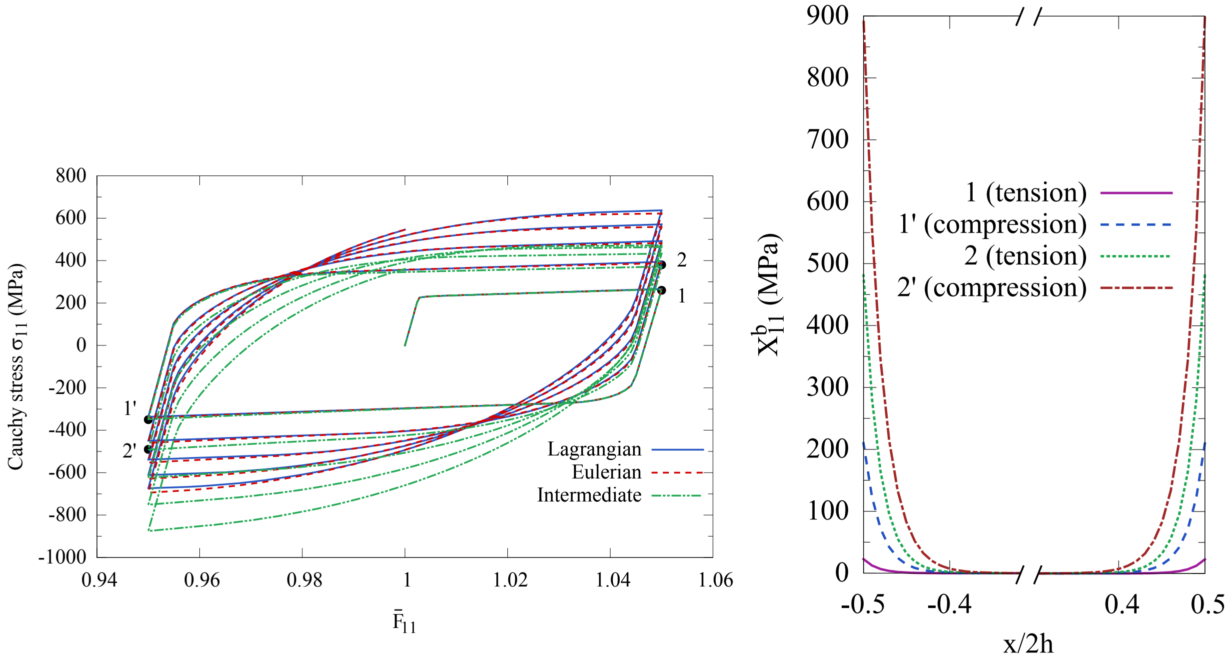

(a) (b)

Figure 2.7: *Cyclic tensile loading with confined plasticity: (a) Comparison of stress-strain curves for different finite strain formulations; (b) evolution of back-stress* X^b_{11}. *Material parameters:* $H_\chi = 10^5$ *MPa,* $A = 10000$ *N,* $R_0 = 200$ *MPa,* $H = 0$. *Unit cell length* $h = 5$ *mm.*

2.4 Size effects in bending and torsion

At this stage, the scale effect was studied in cases where plastic strain gradients are caused by applying particular boundary conditions (confined plasticity). In this section, another type of loading conditions naturally inducing plastic strain gradients is addressed. Bending and torsion loadings were investigated thoroughly in the past to point out size effects in the plasticity of metals, as discussed in [Fleck and Hutchinson, 1997]. They represent crucial benchmark tests to analyze the pros and the cons of various gradient approaches. In the following, the bending of a two-dimensional foil and the torsion of a cylinder are investigated at finite strains.

2.4.1 Bending

The problem of thin foil bending is widely studied in the computational mechanics literature in the small strain framework [Peerlings, 2007; Poh et al., 2011; Jebahi and Forest, 2021]. As pointed out by these authors, the cumulative plastic strain is shown to be non smooth at the neutral axis when plasticity has invaded the whole beam. The fact the cumulative plastic strain distribution is not differentiable on the neutral axis is challenging for most strain gradient plasticity approaches. This difficulty can be overcome using the micromorphic approach since the plastic strain is not required to be smooth. On the other hand, the micromorphic model relying on the cumulative plastic strain was shown in [Poh et al., 2011] to induce spurious negative yield stress.

The present section aims to investigate this bending problem at finite strain. The plane-strain bending of a 2D-foil of width $2w$, around z-axis is considered. Due to mirror symmetry about $y-$axis, only the right half of the foil is simulated. Four-point bending is applied to the sample, as shown in Fig. 2.8. The curvature is approximately given by $\kappa = (F_{11}(x=0, y=w)-1)/w$ which will be used as loading parameter in the analysis. The material is assumed to be perfectly plastic ($H = 0$ MPa in Eq. 2.62). The micromorphic formulation given in Sec. 2.2.4 where $\chi \equiv p$ is adopted. The FE mesh is made of 3232 P2P1 elements (quadratic for displacement and linear for the micromorphic variable) with reduced integration (C2D8R) and 9963 nodes.

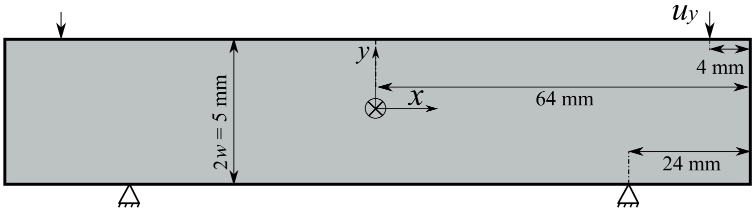

Figure 2.8: *Schematic of two-dimensional foil subjected to four points bending.*

The distribution of cumulative plastic strain is shown in Fig. 2.9. The profiles of p and p_χ are plotted for two different values of parameter A in Fig. 2.10a. Contrary to small strain case, the profile of cumulative plastic strain is not symmetric, due to tension-compression asymmetry at finite deformations. Besides, one can notice that the distribution of cumulative plastic strain p is not smooth in the vicinity of the neutral axis for small values of A. This is in contrast to the microdeformation p_χ distribution exhibiting a horizontal tangent at the neutral axis where p vanishes and p_χ is finite. Due to nonlinear geometric effects, the neutral axis is shifted. A gap between p and p_χ occurs around $y = \pm w$ and at the neutral axis. The generalized stress $\underline{\boldsymbol{b}}_0$ vanishes at $y = \pm w$, so does the gradient $\underline{\boldsymbol{K}}$ (see Fig. 2.10b). As a consequence, the curve of p_χ shows a horizontal asymptote at $y = \pm w$. By increasing A, the gap between p and p_χ becomes larger. The negative contribution of $(p - p_\chi)$ in the vicinity of the neutral axis leads to a decrease of the radius of the yield surface (see Fig. 2.11a). As the parameter A (or H_χ) increases, this negative term becomes stronger. To satisfy consistency conditions, the radius of the yield surface must remain positive. Beyond a certain stage of deformation, $H_\chi(p - p_\chi)$ tends to become higher than R_0, hence a negative radius σ_Y. Since the equivalent von Mises stress is positive as well, the condition $f = 0$ cannot be satisfied when σ_Y is negative and the numerical simulation will diverge accordingly. It is the case for $A = 2000$ N in Fig. 2.11b in which the simulation diverges at a curvature of $\kappa = 0.024$ mm^{-1}. In the work of Poh et al. [2011], a negative yield radius is reported. This is due the fact that the provided analytical solution does not satisfy the consistency condition. Note also that considering a viscoplastic model will delay to some extent the occurrence of the aforementioned issue due to the overstress. Further discussion about this limitation is postponed to section 2.6.4.

The curves of bending moment w.r.t. current coordinates vs. curvature are depicted in Fig. 2.11b. A size-dependent hardening effect can be shown clearly while increasing the parameter A. A comparison between formulations w.r.t. Eulerian, Lagrangian and intermediate configurations (see Table 2.1) has been carried out. Accordingly, no significant differences was noticed between different formulations. This is due mainly to the fact that the applied loading does not induce sufficiently large values of plastic strain to reveal

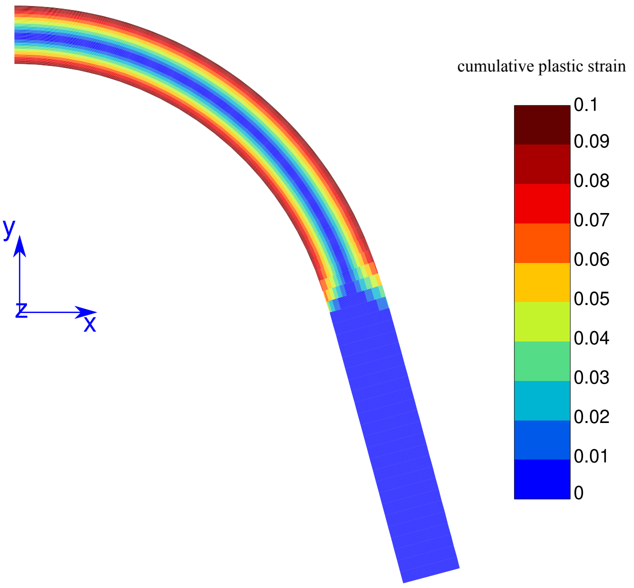

Figure 2.9: *The distribution of cumulative plastic strain in the foil. Material parameters* $R_0 = 100$ *MPa,* $H = 0$, $H_\chi = 10^4$ *MPa,* $A = 500$ *N. Applied curvature* $\kappa = 0.0348$ mm^{-1}.

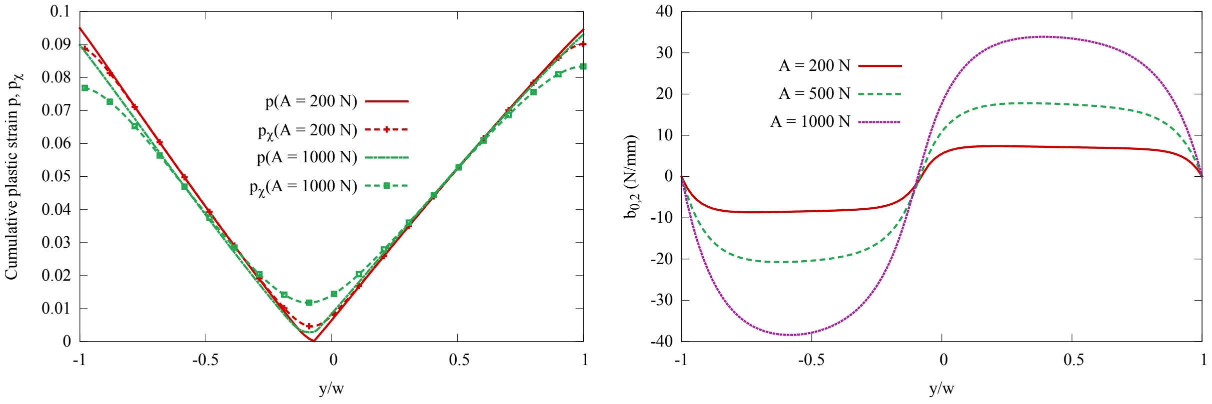

(a) (b)

Figure 2.10: *(a) Cumulative plastic strain and associated micromorphic variable along the cross section at* $x = 0$*; (b) the generalized stress component* $b_{0,2}$ *along the cross section at* $x = 0$*. Material parameters:* $R_0 = 100$ *MPa,* $H_\chi = 10^4$ *MPa,* $H = 0$*. Applied curvature* $\kappa = 0.0348$ mm^{-1}.

potential deviation. Note that when the plastic strain becomes higher, its gradient increases as well leading to a negative yield radius σ_Y and accordingly the simulation does not converge. That holds true for both monotonic and cyclic loadings.

2.4.2 Torsion

The torsion of a cylinder bar with circular cross-section of diameter $d = 2r$ and length L is considered, see Fig. 2.12a for the FE mesh and the dimensions used. The cylinder is twisted along z-axis by applying a rotation angle θ on the top surface ($z = L$) and fixing the bottom surface ($z = 0$). Studies carried out in literature, particularly on single crystal plasticity [Nouailhas and Cailletaud, 1995] have shown the existence of plastic gradients along the outer circumference in addition to radial gradients due to the anisotropic activation of slip systems. In the present application, a von Mises time-independent perfectly plastic model is adopted as in Eq. (2.61). Accordingly, only radial plastic gradients are present, see Fig. 2.12b. The torsion test is used here as a benchmark for 3D finite element simulations at large strains.

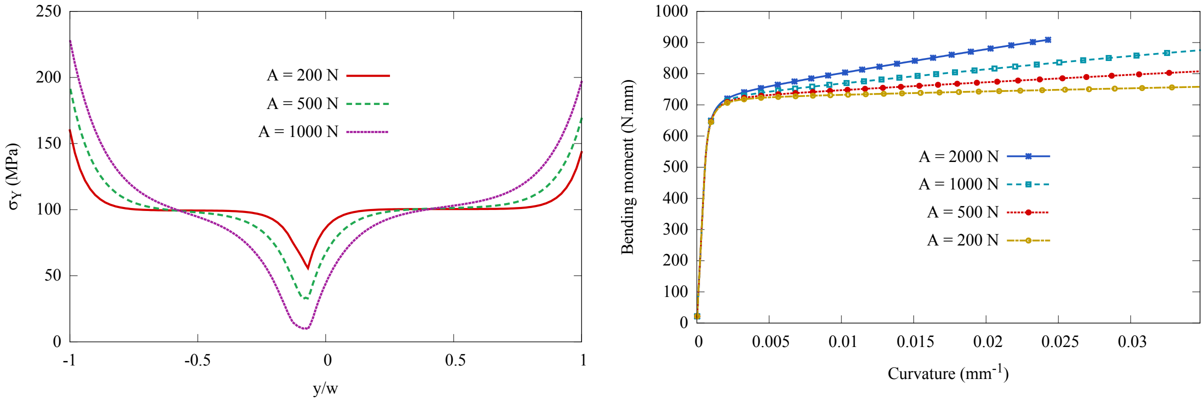

(a) (b)

Figure 2.11: *(a) The radius of yield surface* $\sigma_Y = R_0 + H_\chi(p - p_\chi)$ *captured at* $\kappa = 0.0348\ mm^{-1}$*; (b) the bending moment-curvature curve. Material parameters:* $H_\chi = 10^4$ *MPa,* $R_0 = 100$ *MPa,* $H = 0$*.*

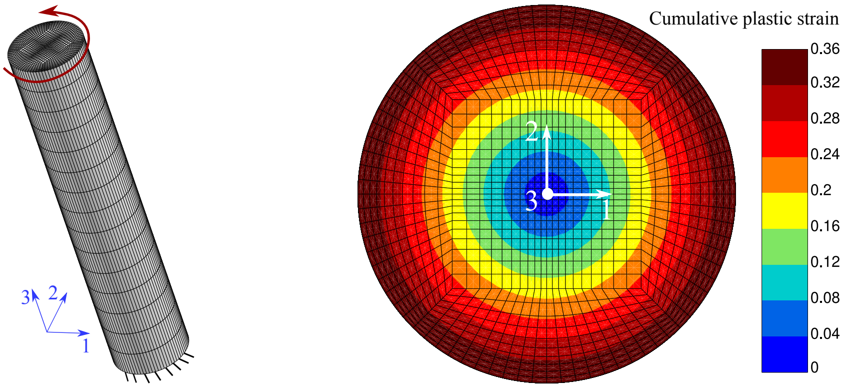

(a) (b)

Figure 2.12: *Torsion of a cylinder bar: (a) geometry and boundary conditions. The mesh contains 77511 nodes;* $r = 1$ *mm and* $L = 10$ *mm; (b) cumulative plastic strain contours obtained for* $r\theta/L = 0.628$ $(\theta = 2\pi)$*.*

The fields of cumulative plastic strain in Fig. 2.13a are found to be similar to the ones obtained in bending case, except that no asymmetry is observed. The cumulative plastic strain is not smooth along the cylinder axis in contrast to p_χ which does not vanish at the center and displays a horizontal tangent near the circumference. The difference $(p - p_\chi)$ is negative in the middle of the cylinder. As this term decreases, the cylinder's core undergoes a softening. In contrast, the outer region is subjected to hardening since p is larger than p_χ. The resulting size effect is shown by the torque-twist curves of Fig. 2.13b. The model induces a size-dependent isotropic hardening given by $A\Delta_0 p_\chi$. Again, divergence occurs when the yield stress $\sigma_Y = R_0 + R$ vanishes.

2.5 Regularization of strain localization simulations

The micromorphic model used for the modeling of size effects in hardening materials can also be used for the regularization of spurious mesh-dependence in the simulation of plastic strain localization phenomena for softening materials. Two benchmarks are considered for that purpose. The first case is the simulation of one-dimensional shear banding, for which an analytical solution can be worked out for the micromorphic model at small strains. The second case deals with a two-dimensional plate undergoing anisotropic shear banding. The attention is focused on finite strain effects on plastic strain localization which has rarely been tackled in the literature.

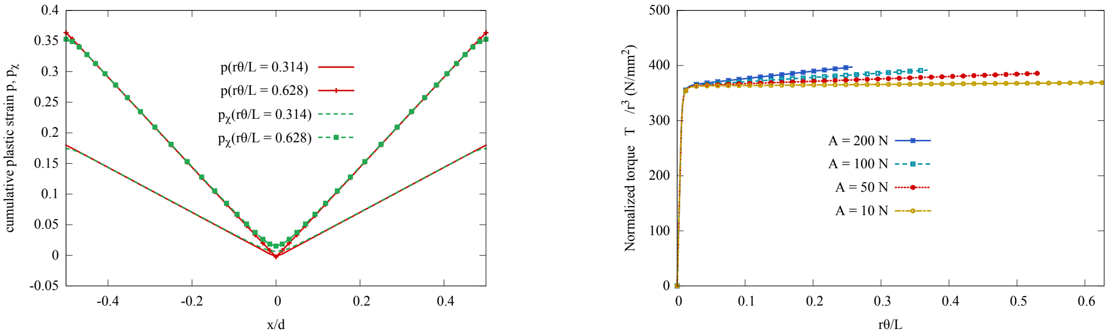

(a) (b)

Figure 2.13: *(a) Profiles of cumulative plastic strain and microplastic variable for $H_\chi = 10^4$ MPa, $A = 10$ N, $R_0 = 300$ MPa, $H = 0$ MPa; (b) the normalized torque (w.r.t deformed configuration) vs. surface strain curves.*

2.5.1 One-dimensional shear banding

A macroscopic shear deformation $\underset{\sim}{\overline{\boldsymbol{F}}} = \underset{\sim}{\boldsymbol{1}} + \overline{F}_{12}\, \underline{\boldsymbol{e}}_x \otimes \underline{\boldsymbol{e}}_y$ is applied on a strip of length $2h$. The displacement field is given by $\underline{\boldsymbol{u}} = (\underset{\sim}{\overline{\boldsymbol{F}}} - \underset{\sim}{\boldsymbol{1}}) \cdot \underline{\boldsymbol{X}} + \underline{\boldsymbol{v}}(\underline{\boldsymbol{X}})$. Periodic boundary conditions are imposed on the displacement fluctuation $\underline{\boldsymbol{v}}$ and the microplastic variable p_χ. A defect is introduced in the middle of the strip (one element with an initial yield stress of $\approx 0.99\, R_0$) in order to trigger strain localization at a precise location. The Fig. 2.14 shows the development of the shear localizing zone in the strip, see also Fig. 2.28 from section 2.8.3. A new complete analytical solution for a linear softening model ($H < 0$ in Eq. (2.62)) for the micromorphic model at small strains is derived and detailed in section 2.8.3. The following intrinsic length emerges from the analysis:

$$\ell_c = 2\pi \sqrt{A \frac{H_\chi + H}{H_\chi |H|}} \tag{2.64}$$

When H_χ is sufficiently large, ℓ_c in Eq. (2.64) tends to $2\pi\sqrt{A/|H|}$ which corresponds to the characteristic length for the Aifantis model (see Remark 3).

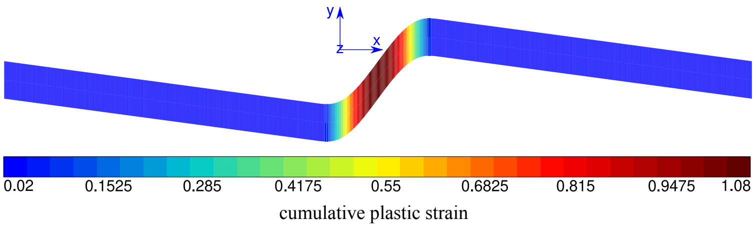

Figure 2.14: *Localization band in a periodic strip under simple glide conditions ($\overline{F}_{12} = 0.12$); $R_0 = 20$ MPa, $H = -20$ MPa, $H_\chi = 10^5$ MPa, $A = 1$ N, $h = 5$ mm.*

The curves in Fig. 2.15a show that the overall response of the softening material without micromorphic enhancement pathologically depends on the mesh size since the plastic strain is localized in only one single element. However, by considering a micromorphic model, the simulations will converge to one well–defined response as soon as the mesh is sufficiently refined, see Fig. 2.15b. The yield stress evolves according to the equation

$$\sigma_Y = R_0 + R = R_0 + Hp - a_0 = R_0 + Hp + H_\chi(p - p_\chi) \tag{2.65}$$

The two softening/hardening contribution are depicted in Fig. 2.16. The generalized stress $a_0 = -H_\chi(p - p_\chi)$ is negative in the middle of the strip. This contribution therefore counteracts the softening term Hp ($H < 0$) in Eq. (2.65). Fig. 2.17 shows the profiles of cumulative plastic strain and the generalized stress a_0

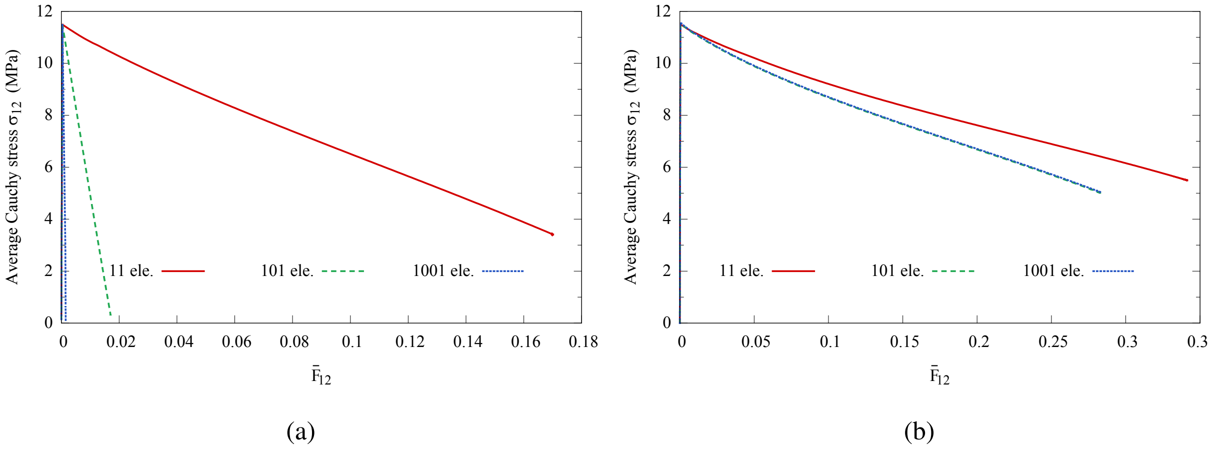

(a) (b)

Figure 2.15: *Mesh dependency for (a) the classical plasticity model, (b) the micromorphic enhanced model. The corresponding material parameters are indicated in the caption of Fig. 2.14*

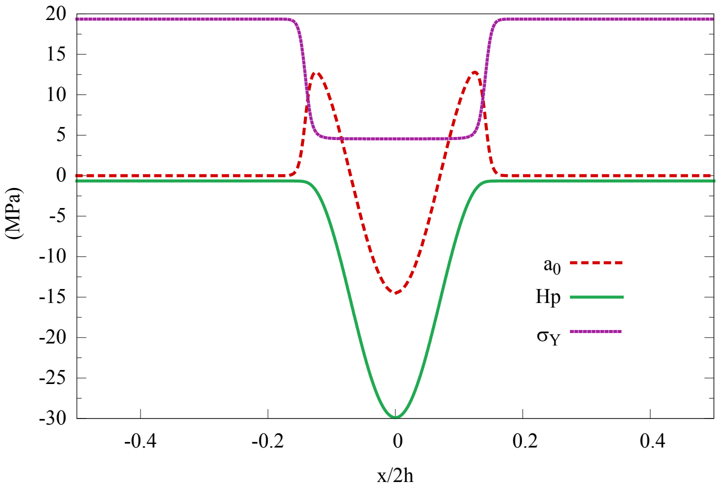

Figure 2.16: *Radius σ_Y of the yield surface, the generalized stress a_0 and the contribution of the linear softening term Hp along the strip length ($\overline{F}_{12} = 0.12$); $R_0 = 20$ MPa, $H = -20$ MPa, $H_\chi = 10^5$ MPa, $A = 4$ N, $h = 5$ mm.*

for different values of the parameter A. By increasing A, hence the characteristic length ℓ_c, the magnitude of plastic strain and of a_0 becomes smaller and the band width is larger.

The distribution of plastic strain and stress-strain curves given by the three proposed finite strain formulations are plotted in Fig. 2.18. For a value of imposed macroscopic shear $\overline{F}_{12} = 0.4$, one can notice that the cumulative plastic strain given by the Lagrangian formulation is slightly higher compared to the two other formulations (see Fig. 2.18a). Accordingly, the average Cauchy stress σ_{12} tends to be lower. Formulations w.r.t. Eulerian and intermediate configurations yield similar profile of cumulative plastic strain. Meanwhile, deviations are noticed between corresponding stress-strain curves at large strain due to kinematic hardening term $\underset{\sim}{\boldsymbol{X}}^b$.

In the case of linear softening ($H < 0$), the bandwidth is bounded and takes a finite and fixed value, as shown by Fig. 2.19a. Now, consider an exponential softening law by replacing the linear hardening term (Hp) in Eq. (2.62) by R_{sat} given by

$$R_{sat} = Q(1 - \exp(-cp)) \tag{2.66}$$

where Q and c are material parameters. Softening is obtained for $Q < 0$, c being always taken positive. In that case, R_{sat} will decrease from 0 at $p = 0$ to the limit Q for $p \to \infty$. Fig. 2.19b reveals a widening of

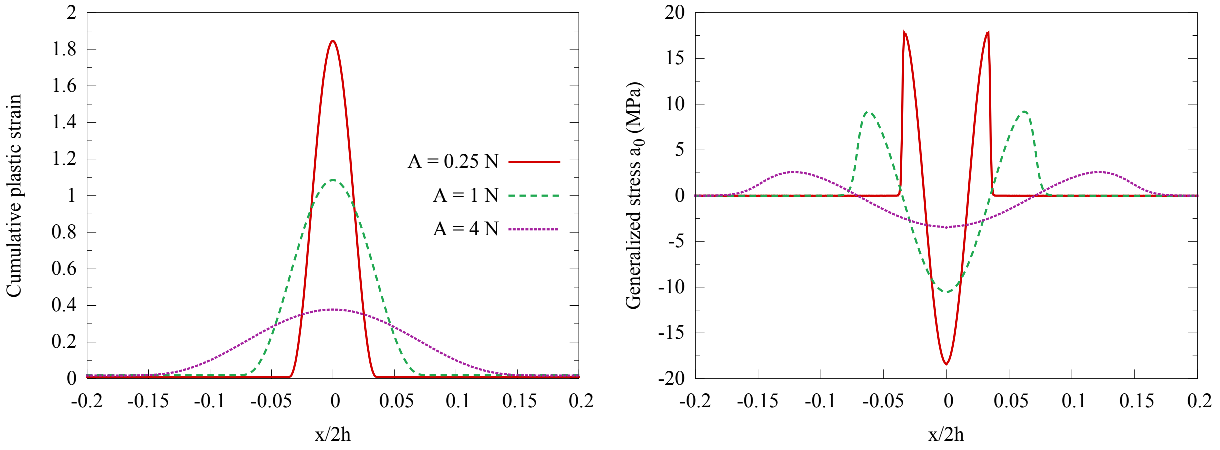

Figure 2.17: *The distribution of cumulative plastic strain and the generalized stress* $a_0 = A\Delta_0 p_\chi$ *for different values of generalized modulus* A*;* $\overline{F}_{12} = 0.12$*.*

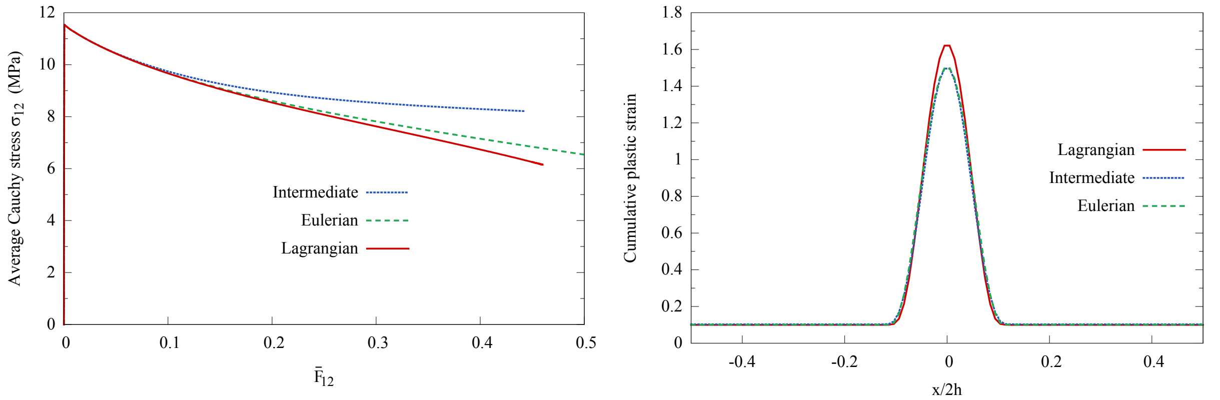

(a)*stress-strain curves*

(b)*profiles of* p, $\overline{F}_{12} = 0.4$

Figure 2.18: *Shear banding for the three finite strain formulations. Material parameters:* $R_0 = 20$ *MPa,* $H_\chi = 10^4$ *MPa,* $A = 2$ *N.*

the localization band for continuing applied shear. This can be explained as follows. For a nonlinear law, the instantaneous softening modulus is $H_\varepsilon = \overline{\rho}\dfrac{\partial^2 \psi^h}{\partial p^2}$. When the softening law $\dfrac{\partial \psi}{\partial p}$ saturates (*e.g.* R_{sat}), H_ε tends to zero. Therefore, the intrinsic length given in Eq. (2.64) (replace H par H_ε) tends to infinity as plastic strain increases.

The band broadening is observed for all formulations. The band widening can be an undesirable feature of strain localization simulations. It will happen in case of localization of plastic strain much larger than the saturating softening strain. This feature of the model has been recognized by [Scherer et al., 2019]. A remedy was proposed to ensure that the band remains in a bounded region for ever increasing strain values. It consists in considering that the material parameter A is not constant any more but depends on plastic strain level. That is to say that the width of the localization band is bounded by adjusting properly the value of $A(p)$. It is noteworthy to mention that for nonlinear softening laws at finite strains, only approximate evolutions of A can be derived. By doing that, $A(p)$ tends to decrease for further straining $\overline{F}_{12}$. Consequently, continuing plastic flow was found in [Scherer et al., 2019] to localize in a narrower band until it reaches the size of a single element. At the end, the classical model behavior is retrieved.

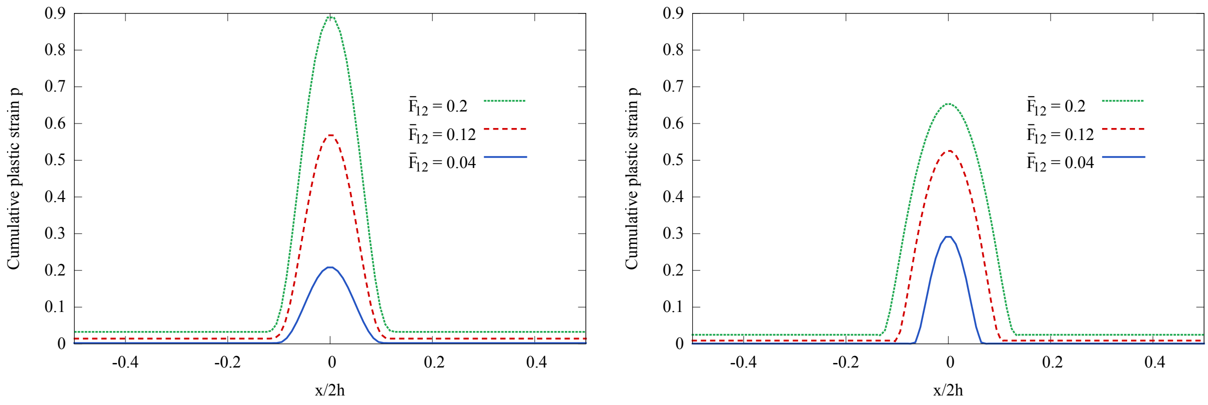

(a) *Linear softening ($H = -20$ MPa)* (b) *Exponential softening ($Q = -15$ MPa, $c = 10$)*

Figure 2.19: *The exponential softening behaviour induces widening of the localization band. Material parameters: $R_0 = 20$ MPa, $A = 2$ N, $H_\chi = 10^5$ MPa.*

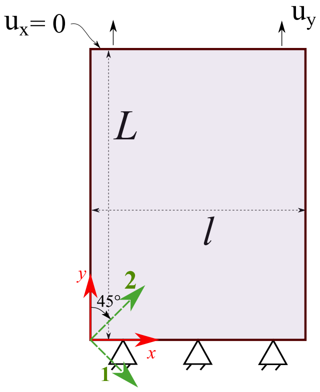

Figure 2.20: *Schematic of the geometry and boundary conditions for the plane-strain tension problem. The material frame is rotated by -45°. Geometry: $2L = 3l$.*

2.5.2 Anisotropic shear banding in a plate in tension

The shear band formation in a plate in tension is studied in this section in the case of an anisotropic contribution of the micromorphic model represented by the symmetric second order tensor $\underset{\sim}{A}$, see Eq. (2.32). The orthotropic class symmetry for $\underset{\sim}{A}$ is associated with 3 distinct eigenvalues A_1, A_2, A_3 and orthogonal 3 eigenvectors characterizing the material anisotropy axes. The two-dimensional plate of width $l = 400$ mm and length $L = 3l/2$ is shown in Fig. 2.20 where the red axes denote the Cartesian coordinate system of the mesh whereas the green axes represent the material anisotropy axes. The simulations are limited to plane-strain conditions, so that only the eigenvalues $A_1 \neq A_2$ play a role in the simulation. Regarding boundary conditions, the nodes along the bottom edge are prescribed to have displacement component $u_x = 0$ and $u_y = 0$, while the nodes along the top part are prescribed to have $u_x = 0$ and a non-zero u_y displacement is applied. The remaining edges are taken to be traction-free. Due to the fact that top and bottom edges are clamped, *i.e.* not allowed to contract, localization bands emerge automatically in this simulation. Hence, no imperfection is introduced to trigger shear bands at a specific location. This example has been studied previously in [Anand et al., 2012], also using the micromorphic approach at large deformations (Lagrangian formulation), but the analysis was limited to an isotropic gradient contribution. Quadratic elements with eight nodes and nine integration points C2D8R (reduced integration) are employed, meaning that the same quadratic interpolation is used for displacement and micromorphic degrees of freedom. Fig. 2.21 shows the localization bands at tensile displacements u_y/L of 0.02 and 0.14 for isotropic and anisotropic generalized moduli $\underset{\sim}{A}$. The material frame is rotated by an angle of $-45°$ so that the anisotropy axes are parallel to the localization bands. A perfect plasticity model is used for this simulation. For isotropic generalized moduli $\underset{\sim}{A} = A\underset{\sim}{1}$ ($A_1 = A_2$), the resulting bands are strictly symmetric w.r.t. the y and $x-$axes. In the anisotropic

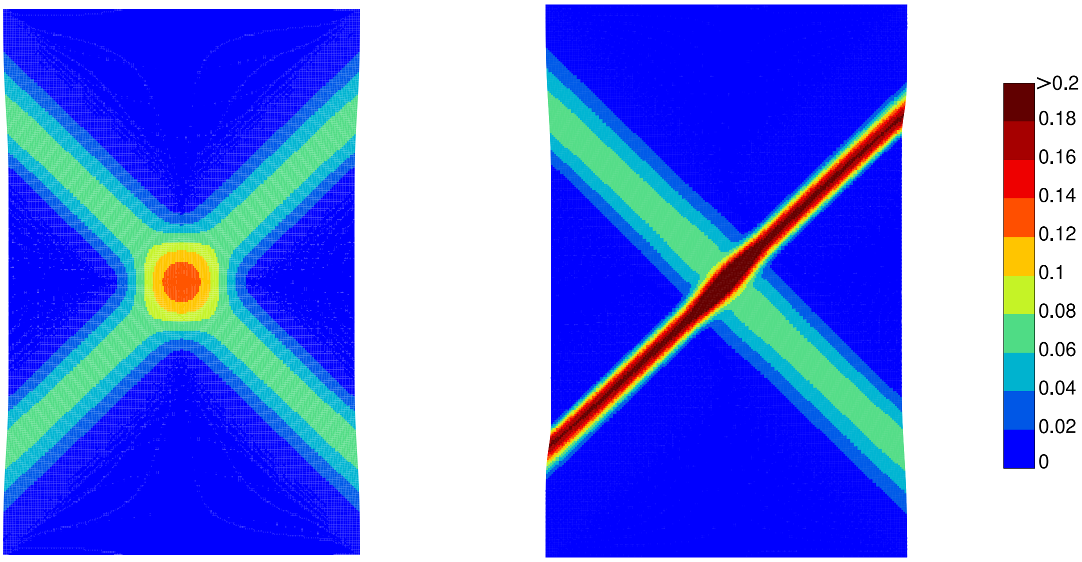

(a)$A_1 = A_2 = 10000\ N$ (b)$A_1 = 1000\ N$, $A_2 = 10000\ N$

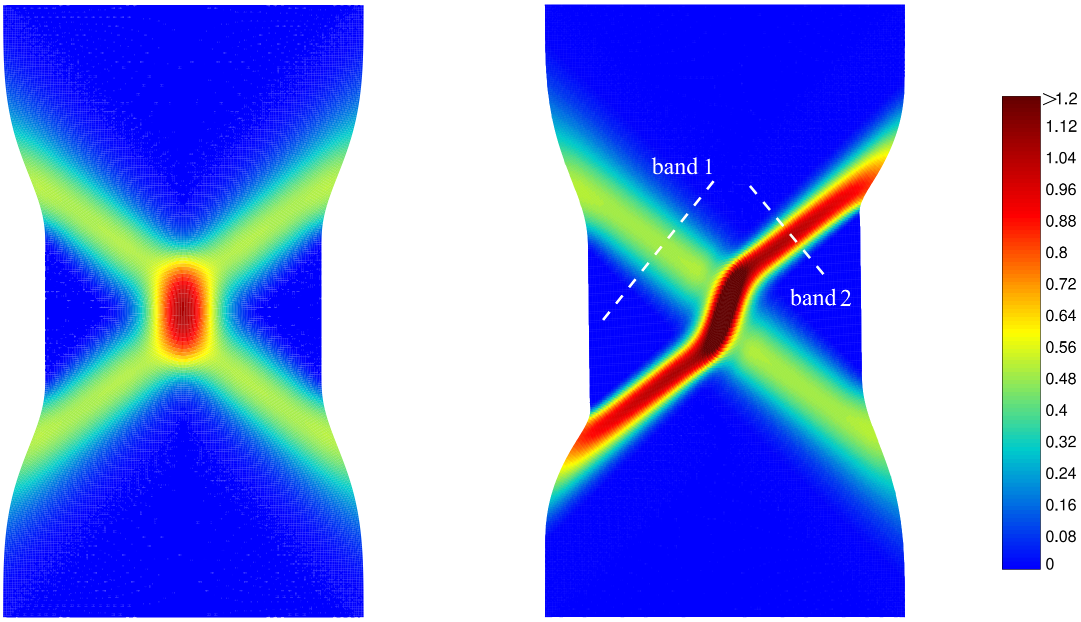

(c)$A_1 = A_2 = 10000\ N$ (d)$A_1 = 1000\ N$, $A_2 = 10000\ N$

Figure 2.21: *The localization of cumulative plastic strain in a plate under tension. Results obtained for applied displacement of: (a)-(b)* $u_y/L = 0.02$*, (c)-(d)* $u_y/L = 0.14$*. Material parameters* $R_0 = 100$ *MPa,* $H = -20$ *MPa,* $H_\chi = 10^5$ *MPa. The left (resp. right) pictures correspond to isotropic (resp. anisotropic) gradient contribution in the model.*

case, the localization band that is parallel to the A_1 eigenvector, *i.e.* the smallest value, is wider, more diffuse and has a lower peak value than the second one. Anisotropy therefore breaks the symmetry of the geometry and loading conditions. The plastic strain profiles along two lines perpendicular to the localization bands are plotted in Fig. 2.22 in the anisotropic case at 5 loading stages. The two lines are indicated in Fig. 2.21d. At small plastic strain levels (levels 1 and 2), the width of the two bands is correctly estimated by means of the formula

$$\ell_c^1 = 2\pi\sqrt{A_1\frac{(H_\chi + H)}{|H|H_\chi}} \approx 44.4, \qquad \ell_c^2 = 2\pi\sqrt{A_2\frac{(H_\chi + H)}{|H|H_\chi}} \approx 140.5 \tag{2.67}$$

which correspond to independent characteristic lengths induced by A_1 and A_2, respectively. Band 1 is initially significantly wider than band 2. This is due to the fact the gradient of plastic strain in the direction perpendicular to the band is the dominant gradient component, as can be seen from the fields for Fig. 2.21b-d. Only one constant A_1 (resp. A_2) then plays a role in the constitutive equations inside band 2 (resp. band 1). After further straining, gradients of plastic strain parallel to the bands also become significant, leading to a broadening of the bands towards a finite width which is essentially the same for both bands due to the combined influence of parameters A_1 and A_2. However the plastic strain inside the bands remains different due to the localization history of each band.

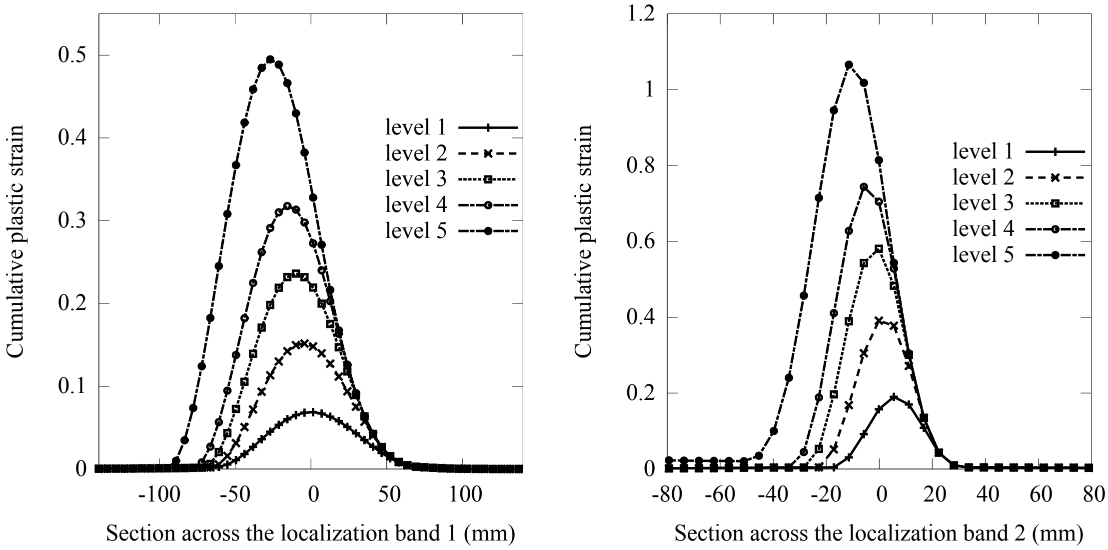

Figure 2.22: *The evolution of two localization bands for anisotropic generalized moduli with* $A_1 = 10000$ *N,* $A_2 = 1000$ *N. Levels 1,2,3,4 and 5 correspond to nominal applied displacement* u_y/L *of* 0.02, 0.04, 0.06, 0.08 *and* 0.14*, respectively.*

2.6 Discussion

Several aspects of the previous simulations are discussed in this section, including limitations of the scalar gradient micromorphic approach and possible remedies. Computational aspects are addressed for an efficient use of gradient plasticity models in practical applications.

2.6.1 Choice of interpolation

The computation of the generalized stress $a = -H_\chi(p - p_\chi)$ involves two quantities p and p_χ. The cumulative plastic strain p is calculated incrementally by integrating the usual elastoplasticity constitutive equations. Accordingly, p is related to the deformation gradient $\underset{\sim}{F}$ which is computed as a function of the gradient of shape functions selected for displacement interpolation. If these shape functions are quadratic, the interpolation degree for the deformation gradient is mainly linear. Hence, p_χ should have the same interpolation degree, *i.e.* linear shape functions. On the other hand, the proposed micromorphic model is a first gradient theory meaning that only the first gradient of the degrees of freedom is evaluated. Accordingly, the same degree of interpolation can be used for displacement and micromorphic deformation degrees of freedom. Two interpolation schemes are evaluated in this section, namely P2P1 elements for which displacement and micromorphic deformation interpolation functions are respectively quadratic and linear, and

P2P2 elements involving quadratic Lagrange polynomials for both types of degrees of freedom. Elements with linear shape functions for displacement (P1P1-type elements) are excluded here because they are subject to hour-glass arising in the early stage of plasticity and leading to strong oscillations in the displacement and micromorphic variable fields.

On the one hand, the use of P2P1 elements is advantageous because it involves a smaller number of degrees of freedom in the finite element simulation. On the other hand, the use of the same interpolation functions may be useful for practical reasons. In applications where boundary conditions on displacement and micromorphic variables are to be applied, using different interpolation degrees requires the duplication of lines and surfaces forming the boundaries for considering the proper nodes involved. Indeed, handling such issues is necessary to conduct systematic enhancement of classical models in finite element codes. This somewhat cumbersome treatment of boundaries is seen as a drawback of P2P1.

The performance of these elements is evaluated in the case of torsion of the 3D cylinder bar of Fig. 2.12 up to an applied angle $\theta = \pi$. The FE mesh is made of 18000 quadratic elements with reduced integration (C3D20R) and 77511 nodes. Brick elements with 20 nodes and reduced integration possessing 8 Gauss points (instead of 27 for full integration) are employed. Reduced integration is preferred in incompressible plasticity in order to limit fluctuations of the hydrostatic stress. The performance of P2P1-type and P2P2-type elements is compared in Table 2.2 which provides the number of degrees of freedom (DOFs), the total number of Newton iterations to solve the entire problem with the same given precision and the total CPU time on a single node with 24 processors whose characteristics are given in the caption. The use of P2P2-type element leads to 30% higher computational time due mainly to a 23% larger number of DOFs. Besides that, no significant differences between stress and plastic strain fields are noticed.

type of elements	number of DOFs	total number of iterations	total CPU time (s)
P2P1	252389	602	3.24×10^5
P2P2	310044	602	4.41×10^5

Table 2.2: *Computational cost for different element types. Simulations of a cylinder torsion, meshed with 18000 C3D20R elements, run on 24 processors of type Intel(R) Xeon(R) CPU E5-2650 v4 @2.20 GHz.* $R_0 = 300$ *MPa,* $H = 0$, $H_\chi = 10^4$ *MPa,* $A = 10$ *N.*

2.6.2 Micromorphic vs. strain gradient plasticity

In the following, a comparison between Lagrange multiplier based strain gradient plasticity (see section 2.2.7) with the micromorphic approach is carried out. The strain gradient plasticity model can be seen as the limit of the micromorphic model when increasing the penalty modulus H_χ, as discussed in Remark 3 and section 2.2.7. In the micromorphic approach, increasing the penalty parameter reduces the gap between the micromorphic variable p_χ and the macro-variable p. The main drawback of the Lagrange based strain gradient plasticity element is that it involves 5 DOFs per node (namely $u_1, u_2, u_3, p_\chi, \lambda$) versus 4 in the micromorphic element. The additional DOF is the Lagrange multiplier λ for which linear interpolation is used (P2P1P1 element). In contrast, the drawback of the micromorphic approach is related to possible numerical problems induced by ill-conditioned matrices in case of high values of the parameter H_χ. These aspects are investigated in the sequel.

The performance of micromorphic and strain gradient plasticity elements is evaluated in the case of torsion of a cylinder bar, *i.e.* the same boundary value problem as in the previous section. Table 2.3 summarizes the results obtained for torsion of a cylinder meshed with 18000 C3D20R elements of type P2P1 (total number of DOFs: 252389). A von Mises perfectly plastic model enhanced by the micromorphic approach is considered. The maximum gap between p and p_χ is observed in the vicinity of the neutral axis (see Fig. 2.13a). This gap decreases as the parameter H_χ increases. If H_χ is not sufficiently large, the gap between p and p_χ becomes very large (61%). In fact, by multiplying H_χ by 100, the maximum gap decreases by a ratio of 4, 18 and 77 consecutively. This means that the isotropic hardening $H_\chi(p - p_\chi)$ induced by the enhanced model increases rapidly with H_χ for smaller values of H_χ and tends to saturate for larger values

	Micromorphic					Lagrange multiplier
	$H_\chi = 10$	$H_\chi = 10^3$	$H_\chi = 10^5$	$H_\chi = 10^7$	$H_\chi = 10^9$	
Max of $\lvert p - p_\chi \rvert / p_{ref}$	0.61	0.13	0.007	9×10^{-5}	9×10^{-7}	-
Total number of iterations	766	605	600	612	673	601
Total CPU time (s)	4.118×10^5	3.26×10^5	3.22×10^5	3.29×10^5	3.61×10^5	3.99×10^5

Table 2.3: *The maximum gap between micro- and macro-variables and the computational cost for various values of H_χ (unit MPa). The maximum value of cumulative plastic strain, regarded as a reference value, is $p_{ref} = 0.19$ obtained for $r\theta/L = 0.314$. Simulations of a cylinder torsion, meshed with 18000 C3D20R elements (P2P1-type element and 252389 DOFs for the micromorphic model, P2P1P1-type elements and 272245 DOFs for the Lagrange multiplier based approach). Material parameters: $R_0 = 300$ MPa, $A = 10$ N, $H = 0$ MPa.*

	Micromorphic			Lagrange multiplier
	$H_\chi = 10^3$	$H_\chi = 10^5$	$H_\chi = 10^7$	
Max of $\lvert p - p_\chi \rvert / p_{ref}$	2.64×10^{-2}	8.26×10^{-4}	9.1×10^{-6}	-
Total number of iterations	749	719	1395	700
Total CPU time (s)	7.61×10^4	7.3×10^4	1.53×10^5	1.03×10^5

Table 2.4: *The maximum gap between micro- and macro-variables and the computational cost for various values of H_χ (unit MPa). The maximum value of cumulative plastic strain, regarded as a reference value, is $p_{ref} = 0.65$ obtained for $u_y = 1/12$ mm (level 4). Simulations are performed using the rectangular plate under tension meshed with 60000 C2D8R elements. P2P1-type element and 422503 DOFs for the micromorphic model, P2P1P1-type elements and 483004 DOFs for the Lagrange multiplier based approach. Material parameters $R_0 = 100$ MPa, $H = -20$ MPa, $A = 10000$ N. The plate geometry 400×600 mm.*

of H_χ. The computational cost of simulations using different H_χ remains almost the same. Indeed, for the same number of loading increments, the total number of iterations of Newton-algorithm required to resolve the global problem is relatively constant for $H_\chi = 10^3, 10^5, 10^7$ MPa. Conversely, when H_χ is either very smaller or larger than elasticity moduli, the simulation requires higher number of iterations to converge.

On the other hand, the approach based on Lagrange multipliers enforces weakly the equality of local and non-local variables. Meanwhile, this cannot be achieved without numerical difficulties. The augmented Lagrangian term, which is similar to the micromorphic contribution in free energy potential is known to provide more coercivity, hence attenuate the oscillations of plastic fields [Zhang et al., 2018; Scherer et al., 2020]. For a given value of μ_χ in Eq. (2.57), a finer mesh leads to a smoother profile of the Laplacian term $\Delta_\chi = \lambda + \mu_\chi p_\chi$. In other words, increasing the discretization reduces the value of μ_χ required to obtain a smooth profile of Δ_χ. Moreover, the value of an optimal μ_χ depends also on the intrinsic length. In fact, larger values of intrinsic length, or, equivalently, parameter A, require a larger value of μ_χ to smoothen the profile of plastic strain.

Table 2.4 summarizes the computational performance of micromorphic and Lagrange multiplier approaches in case of the plane-strain tension of a plate discussed in section 2.5.2. A softening case is studied inducing shear band localization as in Fig. 2.21a-c, for an isotropic gradient contribution. For moderate penalty modulus H_χ, the micromorphic approach performs relatively better compared to the Lagrange multiplier approach. This can be explained mainly by the fact that the Lagrange multiplier based approach involves a larger number of DOFs. Meanwhile, in the case of large values of $H_\chi = 10^7$ MPa, the micromorphic model requires a larger number of iterations to converge. In the presence of localization, high values of H_χ are required to obtained small gaps $\lvert p - p_\chi \rvert$ inside the band. This is associated with more numerous iterations for the micromorphic model than in the Lagrange multiplier based approach. A compromise is to be found on the tolerance for the gap $\lvert p - p_\chi \rvert$ in various situations, noting that a relative gap of less than 0.1% may be acceptable and both models perform similarly in that case.

2.6.3 Choice of scalar micromorphic variables

In previous sections, the model based on a micromorphic scalar variable associated with cumulative plastic strain was discussed. However, it has been shown that this model gives rise to several issues:

- The radius of elastic domain is shown to depend on the gap between cumulative plastic strain p and the microplastic variable p_χ, or equivalently, on the Laplacian of the micromorphic variable according to eq. (2.38). When p is smaller than p_χ, a material softening occurs as illustrated in the core of a beam under bending. But when the generalized stress $a = -H_\chi(p - p_\chi)$ tends to be larger than the radius given by the classical model (initial yield stress R_0 and isotropic hardening), a conceptual problem arises. This problem is more relevant in case of time-independent plasticity where consistency condition needs to be satisfied.

- A conceptual problem of some gradient plasticity formulations has been pointed out in [Wulfinghoff et al., 2014]. Since scalar variables generally contain no information on the direction of the plastic flow, an arbitrary small perturbation in the boundary conditions can determine the direction of the plastic deformation in many scalar-based gradient formulations. Accordingly, the solution remains unstable w.r.t. boundary conditions. This problem arises in the case of the model with cumulative plastic strain. Meanwhile, a scalar model developed in [Jebahi and Forest, 2021] has been shown to overcome this conceptual problem. An extension of this model to finite strain was presented in 2.2.5.

- The cumulative plastic strain is by definition a non-saturating variable and can only increase. Moreover, its gradient may then also become higher and higher, as illustrated in Sec. 2.3. Indeed, the gap between p and p_χ becomes more significant. This will induce a higher value of isotropic hardening. For cyclic loadings, this issue becomes more crucial. One could enforce the equality between p and p_χ by setting H_χ to large values. Nevertheless, the term $H_\chi|p - p_\chi|$ increases with H_χ, *i.e.* the induced isotropic hardening (or softening according to the sign of $p - p_\chi$) increases.

In the following, the main results obtained for the model proposed in section 2.2.5 are presented. Note that the resulting back-stress $\underset{\sim}{\boldsymbol{X}}_m$ in Eq. (2.49) is indeterminate at zero plastic strain. This particular case is regularized numerically as follows. At each iteration, $\underset{\sim}{\boldsymbol{X}}_m$ is computed as

$$\underset{\sim}{\boldsymbol{X}}_m = \frac{H_\chi}{3J_p} \frac{\left(\underset{\sim}{\boldsymbol{B}}^p - \underset{\sim}{\boldsymbol{1}}\right) \underset{\sim}{\boldsymbol{B}}^p}{B^p_{eq} + \varepsilon} \left(B^p_{eq} - \chi\right) \tag{2.68}$$

where ε is a small real number taken as $\varepsilon = 10^{-6}$ in the following simulations. Fig. 2.23 depicts the stress-strain curves obtained for a cyclic glide loading with confined plasticity. This test was considered in 2.3.1 for the gradient of cumulative plastic strain model. The results given by classical and two micromorphic models based on the cumulative plastic strain p and the equivalent plastic strain B^p_{eq} are compared. The classical case is that of an elastic perfectly plastic solid. The model based on B^p_{eq} leads to kinematic hardening with a strong Bauschinger effect. Since the back-stress $\underset{\sim}{\boldsymbol{X}}_m$ depends only on the plastic strain tensor, its components remain bounded from one cycle to another. In contrast, the model with p induces an isotropic hardening that grows and grows over cycles. It can be noted that the slopes of stress-strain curves after yielding, during the first cycle ($\overline{F}_{12}$ ∈[0,0.1]), given by both micromorphic models overlap. That is to say that both models are equivalent for monotonic loadings, in particular for one-dimensional problems. Differences arise in the next cycles.

Now consider the case of the bending example investigated in section 2.4.1. A cyclic loading is applied and monitored by the displacement u_y at the top part of the foil (see Fig. 2.8). Fig. 2.24 depicts the bending moment vs. curvature curves for the two models based on cumulative and equivalent plastic strain, respectively. Contrary to the model relying upon cumulative plastic strain that leads to isotropic overall hardening, the B^p_{eq}-model induces kinematic hardening.

Recall that the formulation of this model in the intermediate configuration will result in a supplementary back-stress $\underset{\sim}{\boldsymbol{X}}^b$. In case of cyclic loading with moderate imposed strains, $\underset{\sim}{\boldsymbol{X}}^b$ remains negligible since it is

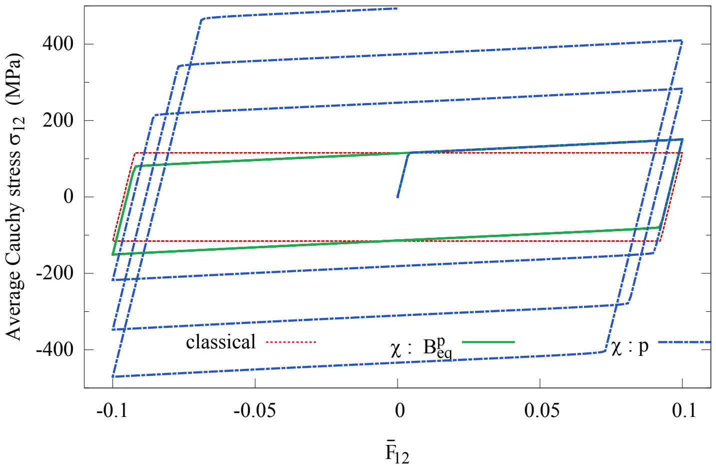

Figure 2.23: *Cyclic simple glide with confined plasticity for two micromorphic variables associated with p and* B^p_{eq}.

a second order contribution. In contrast, the model with cumulative plastic strain induces a significant value of $\underset{\sim}{\boldsymbol{X}}^b$ for the same loading case (not shown here).

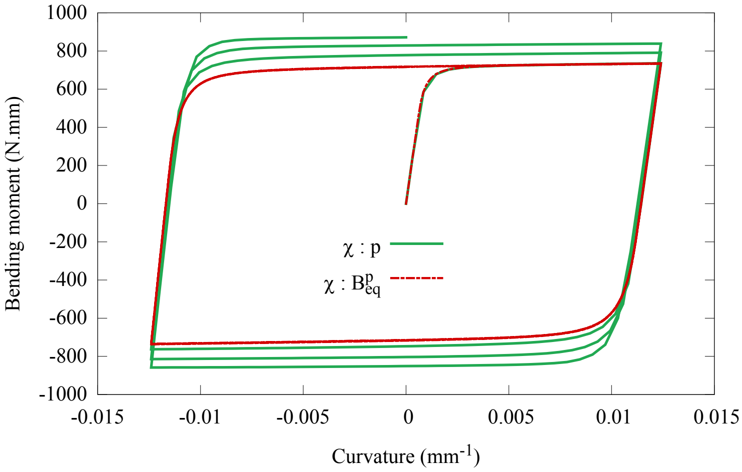

Figure 2.24: *Bending moment vs. curvature curves for a foil under cyclic loading for two micromorphic variables associated with cumulative plastic variable p and equivalent plastic strain* B^p_{eq}. *Quadratic Lagrangian formulation of the gradient term.*

Although this model is based on the gradient of a scalar field variable B^p_{eq}, it takes into account the direction of the plastic strain, making the solution stable with respect to the boundary conditions. Indeed, the back-stress $\underset{\sim}{\boldsymbol{X}}_m$ resulting from the higher-order term is a function of the direction of the plastic strain tensor. In order to illustrate that, consider a von Mises viscoplastic model. For instance, a Norton-type viscoplastic potential is $\Omega = \dfrac{K}{n+1}\left\langle \dfrac{\partial f}{\partial K} \right\rangle^n$ where K and n are material parameters. Using the model with cumulative plastic strain, the flow rule and the yield criterion are given by

$$\underset{\sim}{\boldsymbol{L}}^p = \frac{\partial \Omega}{\partial \underset{\sim}{\boldsymbol{M}}} = \frac{\partial \Omega}{\partial f}\frac{\partial f(\underset{\sim}{\boldsymbol{M}})}{\partial \underset{\sim}{\boldsymbol{M}}} = \frac{3}{2}\frac{\underset{\sim}{\boldsymbol{M}}'}{J(\underset{\sim}{\boldsymbol{M}})}\left\langle \frac{f}{K} \right\rangle^n \tag{2.69}$$

$$f(\underset{\sim}{\boldsymbol{M}}) = [\underset{\sim}{\boldsymbol{M}}]_{eq} - R_0 - R(p) \tag{2.70}$$

where the von Mises equivalent stress is $[\diamond]_{eq} = \sqrt{\frac{3}{2}\underset{\sim}{\diamond}' : \underset{\sim}{\diamond}'}$ and $\underset{\sim}{\diamond}'$ is the deviatoric part of $\underset{\sim}{\diamond}$. It has been shown that the yield stress $\sigma_Y = R_0 + R$ may vanish in some situations, *e.g.* strong strain gradients. The deviatoric Mandel stress may also vanish (or Cauchy stress $\underset{\sim}{\boldsymbol{\sigma}}$) so that the flow rule in Eq. (2.69) cannot provide the direction of plastic flow $\underset{\sim}{\overline{\boldsymbol{L}}}^p$. In contrast, the flow rule and the yield criterion for the model with B^p_{eq} write

$$\underset{\sim}{\overline{\boldsymbol{L}}}^p = \frac{\partial \Omega}{\partial \underset{\sim}{\boldsymbol{M}}} = \frac{\partial \Omega}{\partial f} \frac{\partial f(\underset{\sim}{\boldsymbol{M}})}{\partial (\underset{\sim}{\boldsymbol{M}} - \underset{\sim}{\boldsymbol{X}}_m)} = \frac{3}{2} \frac{\underset{\sim}{\boldsymbol{M}}' - \underset{\sim}{\boldsymbol{X}}_m}{J(\underset{\sim}{\boldsymbol{M}} - \underset{\sim}{\boldsymbol{X}})} \left\langle \frac{f}{K} \right\rangle^n \tag{2.71}$$

$$f(\underset{\sim}{\boldsymbol{M}}) = [\underset{\sim}{\boldsymbol{M}} - \underset{\sim}{\boldsymbol{X}}_m]_{eq} - R_0 - R(p) \tag{2.72}$$

In the case of vanishing yield stress σ_Y, satisfaction of the yield criterion means that $(\underset{\sim}{\boldsymbol{M}}' - \underset{\sim}{\boldsymbol{X}}_m) \neq 0$. Therefore, the flow direction is always defined by Eq. (2.71).

2.6.4 Limitations of the model due to negative yield radius and remedies

As shown in the previous examples, the model based on the cumulative plastic strain may induce negative yield radius in the presence of high positive values of the Laplacian $\Delta_0 p_\chi$. A remedy has been proposed in the viscoplastic micromorphic model in [Poh et al., 2011] by substituting the yield radius by zero whenever it is negative, *i.e.* substitute $R_0 + R(p)$ in Eq. (2.50) by its positive part $\langle R_0 + R(p) \rangle$. Meanwhile, this remedy is not effective in the case of time-independent plasticity considered in the present work. When the radius of elastic domain is set to zero, the equivalent stress must vanish as well. Numerically, the carried out simulations diverge when the radius of yield surface tends to be negative with and without this modification. For viscoplastic models, due to overstress, the radius can be set to zero while the stress does not vanish. Nevertheless, by doing so the classical model is retrieved insofar as gradient terms are cancelled.

The model relying upon equivalent plastic strain B^p_{eq} can be a plausible alternative. The hardening induced by this model manifests itself as a back-stress that can be either positive or negative. For instance, in bending and torsion examples shown previously, the components of the back-stress $\underset{\sim}{\boldsymbol{X}}_m$ go abruptly from large positive values to large negative values across the neutral axis (see Fig. 2.25). However, a drawback of the model is the indeterminacy of the back-stress $\underset{\sim}{\boldsymbol{X}}_m$ when the plastic strain vanishes which may lead to some numerical difficulties. A regularized formulation was used here, see Eq. (2.68).

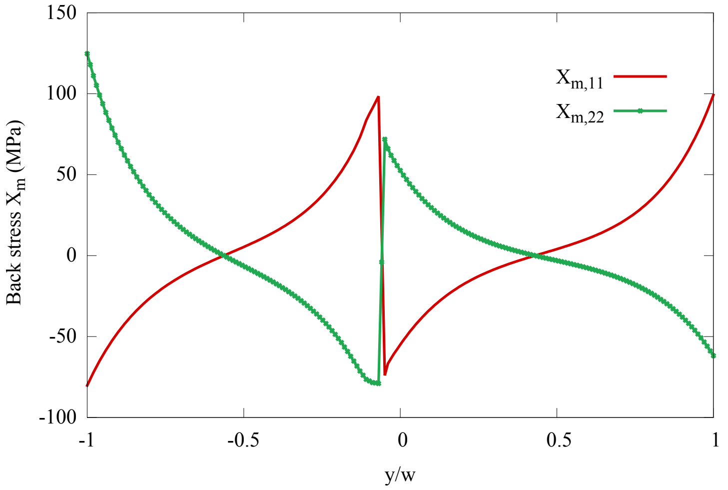

Figure 2.25: *Back-stress plotted at the cross section $x = 0$ for the bending example in section 2.4.1. Material parameters $R_0 = 100$ MPa, $H = 0$, $A = 2000$ N, $H_\chi = 10^4$ MPa. Results obtained for $\kappa = 0.0348$ mm^{-1}.*

2.7 Conclusion

The major outcomes of the present work can be stated as follows:

1. A generic approach for micromorphic strain gradient plasticity at finite strains was presented. The finite element implementation is detailed with a particular focus on scalar micromorphic variables. Models were assessed for a variety of benchmarks involving monotonic and cyclic loading conditions.

2. Two main features of micromorphic elastoplastic models are emphasized. First, size effects can be predicted by varying two additional material parameters (A and H_χ contrarily to Aifantis-like models with only one parameter referred to as intrinsic length). Second, the same models allow regularizing finite element simulations of plastic strain localization by cancelling the spurious mesh-dependency linked to classical continua without intrinsic length.

3. Three finite strain formulations are discussed based on quadratic function of the gradient terms w.r.t. either Eulerian, Lagrangian or intermediate configurations. Eulerian and Lagrangian formulations of the gradient of cumulative plastic strain enhance classical elastoplastic models by a supplementary size-dependent isotropic hardening. The formulation defined in the intermediate configuration leads to both isotropic and kinematic size-dependent hardening. The supplementary back-stress is a second-order contribution that vanishes within the small strain limit. Significant differences between the formulations are therefore observed under cyclic loading. Decision on the best framework eventually remains material-dependent.

4. The choice of the micromorphic variable and free energy potentials leads to a wide range of constitutive models. Indeed, the model based on the cumulative plastic strain is shown to induce a size-dependent isotropic hardening whereas the model with equivalent plastic strain results in a size-dependent kinematic hardening. For the sake of demonstration, only quadratic potentials w.r.t. gradient terms were investigated. More general gradient contributions such as power laws can be implemented [Jebahi et al., 2020].

5. The model based on cumulative plastic strain leads to a material softening and possibly vanishing or negative yield radius in regions where the plastic strain profile is non-smooth. This feature is related to possible divergence of the integration scheme. To overcome this limitation, an alternative model relying upon gradient of equivalent plastic strain was suggested. Meanwhile, the indeterminate back-stress at zero plastic strain may lead to numerical difficulties under cyclic loading and in regions where the plastic strain vanishes (in the neutral axis in torsion and bending).

6. Numerical comparison between micromorphic approach and Lagrange-multiplier based strain gradient plasticity was carried out. The computational cost of both approaches is shown to be similar. Meanwhile, in the case of applications that involve some instabilities like strain localization modes, the micromorphic approach may perform poorly for very large values of the penalty modulus H_χ since the model becomes stiffer. On the other hand, such large values may not be necessary to obtain satisfactory accordance between micro and macro-variables. A drawback of the presented FE implementation for the Lagrange-multiplier model is that continuity of the Lagrange multiplier λ is enforced by the chosen shape function although this is a too strong requirement [Scherer et al., 2020]. Discontinuous Galerkin methods could be used to overcome this limitation.

The choice of the micromorphic variable was shown to play a key role in the present work which was however limited to plasticity. The present work will be completed in the future by studying other scalar variables, *e.g.* a saturating variable [Kocks and Mecking, 2003; Ren et al., 2017] and the equivalent total strain proposed in [Forest, 2016]. Moreover, further investigations on micromorphic models accounting for tensor micromorphic variables [Forest, 2009; Aslan et al., 2011; Saanouni and Hamed, 2013] will be carried out in future works. Dissipative contributions of gradient terms should also be considered according to Jebahi et al. [2020]. Enhancements of damage models for simulation of crack initiation and propagation have been proposed recently based on the micromorphic approach, see [Fassin et al., 2019; Langenfeld and Mosler, 2020; Sprave and Menzel, 2020; Holthusen et al., 2022]. The micromorphic approach can also be useful to ease numerical implementation of phase field models as demonstrated recently for twinning plasticity in [Rezaee-Hajidehi et al., 2022]. Note finally that the micromorphic approach is also suitable for explicit finite element simulation schemes used in metal forming as recently shown in [Davaze et al., 2020; Russo et al., 2022].

2.8 Complement: analytical solutions for simple glide at small strains

Consider the boundary value problem of Fig. 2.1a and introduced in section 2.3.1. The strip is $2h$-wide and infinite in the y-direction (invariant solution in this direction). In the case of a hardening plate (*i.e.*, H $\geq$ 0), the microplastic variable p_χ is set to zero at $x = \pm h$ (Dirichlet higher order boundary conditions). In the case of a softening plate (*i.e.*, H $<$ 0), p_χ is free at $x = \pm h$ far from the localization zone (Neumann higher order conditions).The first balance equation reads

$$\text{div}\ \underset{\sim}{\sigma} = 0 \tag{2.73}$$

which yields

$$\sigma_{12,2} = 0 \text{ and } \sigma_{12,1} = 0 \tag{2.74}$$

Therefore, $\sigma_{12} = \tau$, taken positive without loss of generality, is uniform in the plate. The second balance equation is

$$\text{div}\ \underline{b} = \text{a} \tag{2.75}$$

where the constitutive equations for generalized stresses are given by

$$a = -H_\chi(p - p_\chi), \qquad \underline{b} = A\nabla p_\chi \tag{2.76}$$

The differential equation governing the microplastic variable p_χ reads

$$\Delta p_\chi - \frac{H_\chi}{A}(p_\chi - p) = 0 \tag{2.77}$$

The yield function is given by

$$f(\underset{\sim}{\sigma}, p) = \sigma_{eq} - \big(R_0 + Hp + H_\chi\left(p - p_\chi\right)\big) = 0 \tag{2.78}$$

with $\sigma_{eq} = \sqrt{3}\ \tau$ is the von Mises stress. By combining Eqs. (2.77) and (2.78), the following partial differential equation for p_χ is obtained

$$\Delta p_\chi - \frac{HH_\chi}{A(H + H_\chi)} p_\chi + \frac{H_\chi}{A(H + H_\chi)}(\sigma_{eq} - R_0) = 0 \tag{2.79}$$

Three different cases can be distinguished: perfect plasticity ($H = 0$), hardening ($H > 0$) and softening ($H < 0$) behavior.

2.8.1 Case 1: perfect plasticity ($H = 0$)

In this case, the equation (2.79) reduces to

$$\Delta p_\chi + \frac{1}{A}(\sigma_{eq} - R_0) = 0 \tag{2.80}$$

whose solution is

$$p_\chi(x) = -\frac{\sqrt{3}\tau - R_0}{2A}x^2 + C_1 x + C_2 \tag{2.81}$$

where C_1 and C_2 are integration constants to be determined from boundary conditions:

$$p_\chi(x = \pm h) = 0 \implies C_1 = 0 \quad \text{and} \quad C_2 = \frac{\sqrt{3}\tau - R_0}{2A}h^2 \tag{2.82}$$

Finally, the fields of micromorphic deformation and cumulative plastic strain are

$$p_\chi(x) = -\frac{\sqrt{3}\tau - R_0}{2A}(x^2 - h^2) \tag{2.83}$$

$$p(x) = p_\chi(x) + \frac{\sqrt{3}\tau - R_0}{H_\chi} \tag{2.84}$$

Further, the expression of the uniform stress τ in the plate is

$$\tau = 2\mu\varepsilon_{12}^e = \frac{\mu}{h}\int_{-h}^{h}(\varepsilon_{12} - \varepsilon_{12}^p)dx = \mu\bar{\gamma} - \frac{\sqrt{3}\mu}{2h}\int_{-h}^{h}p(x)dx \tag{2.85}$$

Using Eq. (2.84), Eq. (2.85) reduces to

$$\tau = \frac{\bar{\gamma} + \dfrac{R_0}{\sqrt{3}}\left(\dfrac{3}{H_\chi} + \dfrac{h^2}{A}\right)}{\dfrac{1}{\mu} + \dfrac{3}{H_\chi} + \dfrac{h^2}{A}} \tag{2.86}$$

The parabolic profiles $p(x)$ et $p_\chi(x)$ are illustrated by Fig. 2.26 and used for the validation of the FE implementation of the model. It is apparent in Fig. 2.26a that the value $H_\chi = 10^5$ MPa ensures a very small difference $|p - p_\chi|$. It follows that the presented solution is almost identical to the solution of the same problem using the Aifantis strain gradient plasticity model. Increasing the parameter A flattens the profiles indicating that plastic deformation is more difficult to develop and higher stresses are reached. The limit $H_\chi \to \infty$ in Eq. (2.86) provides the shear stress level for the Aifantis model:

$$\tau = \frac{\mu}{A + \mu h^2}\left(A\bar{\gamma} + R_0 h^2/\sqrt{3}\right) \tag{2.87}$$

The limit $A \to \infty$ shows that deformation is then purely elastic: $\tau = \mu\bar{\gamma}$. Plastic strain gradient would be too high to develop. In contrast, setting $A = 0$ provides the classical elastic-perfectly plastic solution. The previous formula also reveals the apparent hardening modulus depending on A and the width h.

2.8.2 Case 2: hardening ($H > 0$)

For a strictly positive linear hardening modulus, the solution of Eq. (2.79) reads

$$p_\chi(x) = C_3\cosh(\omega x) + C_4\sinh(\omega x) + \frac{\sigma_{eq} - R_0}{H} \tag{2.88}$$

where

$$\omega^2 = \frac{HH_\chi}{A(H + H_\chi)} \tag{2.89}$$

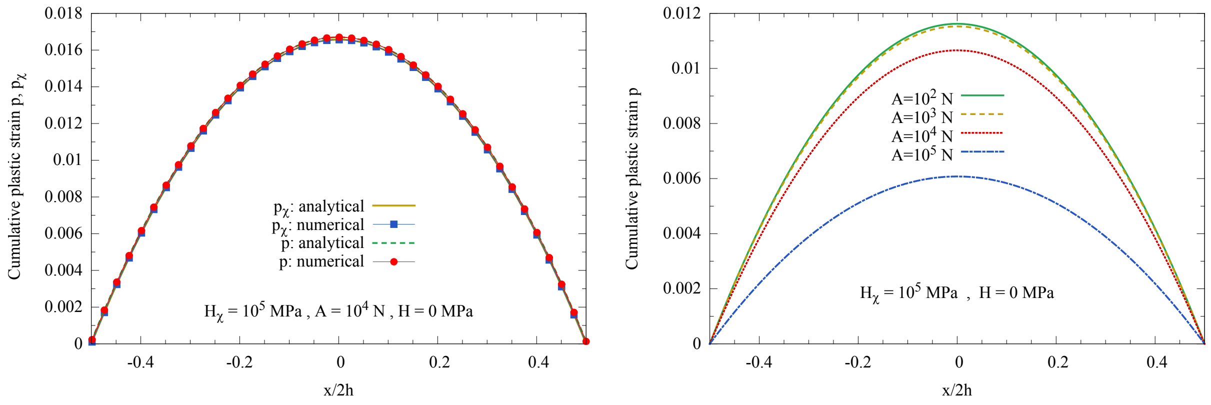

(a) (b)

Figure 2.26: *(a) Analytical vs. numerical fields of cumulative plastic strain p and micromorphic variable* p_χ *for confined simple glide; (b) distribution of cumulative plastic strain for different values of the generalized modulus A. The profiles are given for the prescribed overall shear value* $\bar{\gamma} = 0.2$.

This formula defines the inverse characteristic length ω as a function of the plastic hardening modulus and higher order parameters. The integration constants C_3 and C_4 are obtained by applying boundary conditions:

$$p_\chi(x = \pm h) = 0 \implies C_3 = -\frac{\sigma_{eq} - R_0}{H\cosh(\omega h)} \text{ and } C_4 = 0 \tag{2.90}$$

It follows that

$$p_\chi(x) = \frac{\sqrt{3}\tau - R_0}{H}\left(1 - \frac{\cosh(\omega x)}{\cosh(\omega h)}\right) \tag{2.91}$$

and

$$p(x) = p_\chi(x) + \frac{\sqrt{3}\tau - R_0}{H + H_\chi}\frac{\cosh(\omega x)}{\cosh(\omega h)} = \frac{\sqrt{3}\tau - R_0}{H}\left(1 - \frac{H_\chi}{H + H_\chi}\frac{\cosh(\omega x)}{\cosh(\omega h)}\right) \tag{2.92}$$

The value of τ is given by

$$\tau = \frac{\bar{\gamma} + R_0 Z_h}{\dfrac{1}{\mu} + \sqrt{3}Z_h} \tag{2.93}$$

where $Z_h = \dfrac{\sqrt{3}}{H}\left(1 - \sqrt{\dfrac{AH_\chi}{H(H + H_\chi)}}\dfrac{\tanh(\omega h)}{h}\right)$.

These results are illustrated by Fig. 2.27. A clear difference $|p - p_\chi|$ is visible in Fig. 2.27a for a low value of the penalty modulus $H_\chi = 10^3$ MPa. This difference almost vanished in Fig. 2.27b when H_χ is sufficiently high. This indicates again that the gradient plasticity model by Aifantis [1984] is a limit case of the micromorphic model as H_χ tends to infinity. The hyperbolic profiles can be recognized in Fig. 2.27c and 2.27d. Low values of the higher order modulus A lead to flat distribution of plastic strain where high curvatures are reached for high values of A.

2.8.3 Case 3: softening ($H < 0$)

The development of a shear localization band in a homogeneous matrix strip is studied. The strip has a thickness of $2h$ in the x–direction and is infinite in the y–direction of the 2D shear plane. The stress state is homogeneous with

$$\underset{\sim}{\sigma} = \tau(\underline{e}_x \otimes \underline{e}_y + \underline{e}_y \otimes \underline{e}_x)$$

The localization band of finite width $2x_c < 2h$ is entirely contained in the material strip. It is assumed that no plastic flow takes place outside the localization band so that the following zones can be defined:

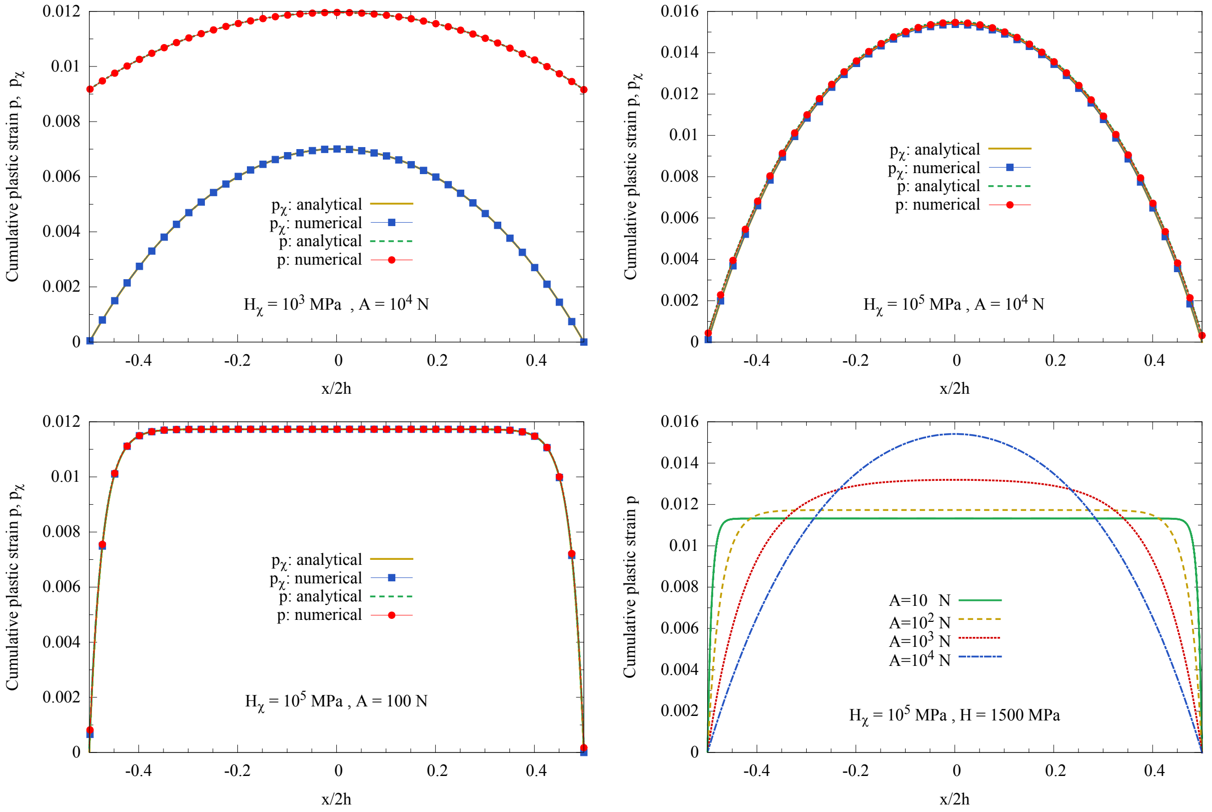

Figure 2.27: *The distribution of cumulative plastic strain for confined simple glide for various values of A and* H_χ. *Material parameters:* $R_0 = 20$ *MPa,* $H = 1500$ *MPa. The profiles are given for the prescribed overall shear value* $\bar{\gamma} = 0.2$.

- $-h \leq x \leq -x_c$: elastic domain, labelled with "-" superscript;
- $|x| \leq x_c$: plastic domain, without any label;
- $x_c \leq x \leq h$: elastic domain, labelled with "+" superscript.

Periodicity boundary conditions are applied at the boundaries $x = \pm h$. Solutions are derived for the micromorphic plasticity model in the small deformation framework, using the standard von Mises plasticity yield function and softening modulus $H < 0$. The limit case of the Aifantis strain gradient plasticity model is also obtained. The cumulative plastic strain field $p(x)$ and the plastic microstrain $p_\chi(x)$ are functions of the sole variable x. The displacement field takes the following form:

$$u_x = \bar{\gamma} y, \qquad u_y = u(x) \tag{2.94}$$

where $\bar{\gamma}$ is the applied mean glide amount and $u(x)$ is the unknown displacement fluctuation. The shear strain component is

$$\varepsilon_{12} = \frac{1}{2}(\bar{\gamma} + u') = \varepsilon^e_{12} + \varepsilon^p_{12} = \varepsilon^e_{12} + \frac{\sqrt{3}}{2} p \tag{2.95}$$

where $u'(x) = du/dx$.

The material is described by a linear hardening law with initial yield stress R_0 and negative hardening modulus $H < 0$.

Solution in the elastic domain

In the elastic domain, the micro–plastic strain $p_\chi^{\pm}(x)$ is the solution of the following differential equation:

$$p_\chi^{\pm\prime\prime} - \omega_\chi^2 p_\chi^{\pm} = 0 \qquad \text{with} \qquad \omega_\chi = \sqrt{\frac{H_\chi}{A}} \tag{2.96}$$

This equation admits solutions of exponential type with wave number ω_χ. For symmetry reasons, assuming localization at the center of the plastic zone, the plastic microstrain and higher order stress $b_x = Ap'_\chi(x)$ are respectively even and odd functions. Since b_x is periodic, it must vanish at the boundary (flat profile of microstrain):

$$p_\chi^{-\prime}(-h) = p_\chi^{+\prime}(h) = 0 \tag{2.97}$$

It follows that

$$p_\chi^-(x) = \alpha^- \cosh\big(\omega_\chi(h+x)\big), \qquad p_\chi^+(x) = \alpha^+ \cosh\big(\omega_\chi(h-x)\big) \tag{2.98}$$

where $\alpha^{\pm}$ are integration constants to be determined from boundary conditions.

Solution in the plastic domain

The yield conditions reads

$$\sqrt{3}\tau = R_0 + Hp - Ap''_\chi = R_0 + Hp_\chi - \frac{A(H+H_\chi)}{H_\chi} p''_\chi \tag{2.99}$$

As a consequence of equilibrium, the shear stress τ is uniform. Due to the linear softening law $H < 0$, the previous equation admits harmonic solutions with the wave number

$$\omega_{\chi p} = \sqrt{\frac{|H| H_\chi}{A(H+H_\chi)}} \tag{2.100}$$

assuming $H + H_\chi > 0$. This defines the inverse intrinsic length $\omega_{\chi p}$ in the plastic zone. The plastic microstrain profile takes the form

$$p_\chi(x) = \frac{\sqrt{3}\tau - R_0}{H} + C\cos\big(\omega_{\chi p} x\big) \tag{2.101}$$

The plastic strain is obtained from the plastic microstrain field by the following equation, valid for $|x| \leq x_c$:

$$p = p_\chi - \frac{A}{H_\chi} p''_\chi = \frac{\sqrt{3}\tau - R_0}{H} + C\frac{H_\chi}{H+H_\chi}\cos\big(\omega_{\chi p} x\big) = \frac{\sqrt{3}\tau - R_0}{H} + C\left(1 - \frac{\omega_{\chi p}^2}{\omega_\chi^2}\right)\cos\big(\omega_{\chi p} x\big) \tag{2.102}$$

The definition of the location x_c is given by

$$p(\pm x_c) = 0 = \frac{\sqrt{3}\tau - R_0}{H} + C\frac{H_\chi}{H+H_\chi}\cos\big(\omega_{\chi p} x_c\big) \tag{2.103}$$

Four unknowns remain: $\alpha^+, \alpha^-, C, x_c$ to be determined from left-over continuity requirements.

Continuity conditions

The interface conditions to be enforced are the following

- Continuity of microstrain at $x = x_c$: $p_\chi(x_c) = p_\chi^+(x_c)$

$$\alpha^+ \cosh\big(\omega_\chi(h - x_c)\big) = \frac{\sqrt{3}\tau - R_0}{H} + C\cos\big(\omega_{\chi p} x_c\big) \tag{2.104}$$

- Continuity of microstrain at $x=-x_c$: $p_\chi(x_c) = p_\chi^-(-x_c)$

  $$\alpha^- \cosh\big(\omega_\chi(h-x_c)\big) = \frac{\sqrt{3}\tau - R_0}{H} + C\cos\big(\omega_{\chi p} x_c\big) \tag{2.105}$$

  It follows from the two previous equations that

  $$\alpha^+ = \alpha^- = \alpha \tag{2.106}$$

- Continuity of the higher order stress component at x_c: $b_x(x_c) = b_x^+(x_c) \Longrightarrow p'_\chi(x_c) = p_\chi^{+\prime}(x_c)$

  $$\alpha^+ \omega_\chi \sinh\big(\omega_\chi(h-x_c)\big) = C\omega_{\chi p} \sin\big(\omega_{\chi p} x_c\big) \tag{2.107}$$

- Continuity of the higher order stress component at $-x_c$:
  $b_x(-x_c) = b_x^-(-x_c) \Longrightarrow p'_\chi(-x_c) = p_\chi^{-\prime}(-x_c)$
  This condition turns out to be automatically fulfilled once the result (2.106) is taken into account.

Only three unknowns remain, namely α, C, x_c, which are determined from the three equations (2.103), (2.104) and (2.107).

Transcendental equation for the plastic zone boundary

The equation to be solved for x_c is obtained by computing the ratio of Eq. (2.107) by (2.104):

$$\begin{aligned}
\tanh\big(\omega_\chi(h-x_c)\big) &= \frac{\omega_{\chi p}}{\omega_\chi} \frac{C\sin\big(\omega_{\chi p} x_c\big)}{\frac{\sqrt{3}\tau - R_0}{H} + C\cos\big(\omega_{\chi p} x_c\big)} \\
&= \frac{\omega_{\chi p}}{\omega_\chi} \frac{C\cos\big(\omega_{\chi p} x_c\big)}{\frac{\sqrt{3}\tau - R_0}{H} + C\cos\big(\omega_{\chi p} x_c\big)} \tan\big(\omega_{\chi p} x_c\big) \\
&= \frac{\omega_{\chi p}}{\omega_\chi} \frac{H + H_\chi}{H} \tan\big(\omega_{\chi p} x_c\big)
\end{aligned} \tag{2.108}$$

after elimination of $C\cos\big(\omega_{\chi p} x_c\big)$ term by means of (2.103).

The location x_c is therefore a zero of the function

$$f(y) = \tanh\big(\omega_\chi(h-y)\big) - \frac{\omega_{\chi p}}{\omega_\chi}\left(1 + \frac{H_\chi}{H}\right)\tan\big(\omega_{\chi p} y\big) \tag{2.109}$$

which results in the announced transcendental equation.

Once x_c is determined, the constant C and α are computed from (2.103) and (2.107):

$$C = \frac{(R_0 - \sqrt{3}\tau)(H + H_\chi)}{HH_\chi \cos\big(\omega_{\chi p} x_c\big)}, \qquad \alpha = C\frac{\omega_{\chi p}\sin\big(\omega_{\chi p} x_c\big)}{\omega_\chi \sinh\big(\omega_\chi(h-x_c)\big)} \tag{2.110}$$

It remains to derive the relation between $\bar{\gamma}$ and τ. This is done by means of the elasticity law:

$$\frac{\tau}{\mu} = \bar{\gamma} + u' - \sqrt{3}p \tag{2.111}$$

Integration of this equation over the interval $[-h,h]$, after accounting for the periodicity of u, provides the relation between shear stress and applied shear strain:

$$\frac{\tau}{\mu} = \bar{\gamma} - \frac{1}{h}\left(\frac{\sqrt{3}\tau - R_0}{H} x_c - \sqrt{3}h\bar{p}\right) \tag{2.112}$$

where the average plasic strain is

$$
\begin{aligned}
\bar{p} &= \frac{1}{2h}\int_{-x_c}^{x_c} p(x)dx \\
&= \frac{1}{h}\left(\frac{\sqrt{3}\tau - R_0}{H}x_c + C\left(1 - \frac{\omega_{\chi p}^2}{\omega_\chi^2}\right)\sin\left(\omega_{\chi p}x_c\right)\right) \\
&= \frac{\sqrt{3}\tau - R_0}{hH}\left(x_c - \frac{\tan\left(\omega_{\chi p}x_c\right)}{\omega_{\chi p}}\right)
\end{aligned}
\tag{2.113}
$$

Finally

$$
\bar{\gamma} = \frac{\tau}{\mu} + \sqrt{3}\frac{\sqrt{3}\tau - R_0}{hH}\left(x_c - \frac{\tan\left(\omega_{\chi p}x_c\right)}{\omega_{\chi p}}\right) \tag{2.114}
$$

The problem can therefore be solved for each given value of the shear stress τ. The corresponding applied shear is computed from Eq. (2.114). Conversely, for prescribed shear $\bar{\gamma}$, the unknowns τ and x_c are determined by solving the nonlinear system (2.109) an (2.114).

Limit case: strain gradient plasticity

The solution is straightforwardly found in the case of Aifantis strain gradient plasticity, either directly from the strain gradient plasticity equations or as a limit case of the previous micromorphic solution. The plastic field $p(x)$ is the solution of the yield condition

$$
\sqrt{3}\tau = R_0 + Hp - Ap'' \tag{2.115}
$$

in the whole plastic domain $|x| \leq x_c$. The negative hardening modulus $H < 0$ is responsible for the localization phenomenon. A harmonic solution with wave number

$$
\omega_p = \sqrt{\frac{|H|}{A}} = \lim_{H_\chi \to \infty} \omega_{\chi p} \tag{2.116}
$$

is found. It is the limit of the micromorphic wave number (2.100) by increasing the penalty on the difference between the cumulative plastic strain p and the plastic microstrain p_χ. The boundary of the plastic zone is defined by the condition

$$
p(x_c) = 0 \qquad \Longrightarrow \qquad x_c = \frac{\pi}{\omega_p} \tag{2.117}
$$

Finally, the localization band can be described by the following sinus branch:

$$
p(x) = \frac{\sqrt{3}\tau - R_0}{H}(1 + \cos(\omega_p x)) \tag{2.118}
$$

with maximum plastic strain $2(\sqrt{3}\tau - R_0)/H$ at $x = 0$. Using Hooke's law (2.111) and periodicity of displacement, the relation between shear stress and shear strain is obtained:

$$
\tau\left(\frac{1}{\mu} + \frac{3}{H}\frac{x_c}{h}\right) = \bar{\gamma} + \frac{\sqrt{3}R_0}{H}\frac{x_c}{h} \tag{2.119}
$$

This relation is also obtained from the micromorphic solution (2.114) in the limit $H_\chi \to \infty$, which leads to $\tan\left(\omega_{\chi p}x_c\right) \to 0$.

Half-strip width	$h = 5$ mm
Prescribed shear strain	$\bar{\gamma} = 0.2$
Young's modulus	$E = 78000$ MPa
Poisson ratio	$\nu = 0.3$
Initial yield stress	$R_0 = 20$ MPa
Softening modulus	$H = -20$ MPa
Strain gradient modulus	$A = 5$ N
Micromorphic penalty modulus	$H_\chi = 100$ MPa

Table 2.5: *Geometrical, loading and material parameters for the simulation of shear localization in a strip.*

Example and discussion of multiple solutions

The previous solutions are illustrated in a specific case characterized by the parameters given in Table 2.5. The analytical solutions are compared to finite element simulations based on the micromorphic plasticity model at small deformations. The finite element simulation is illustrated by the deformed states of the strip and plastic microstrain fields of Fig. 2.28.

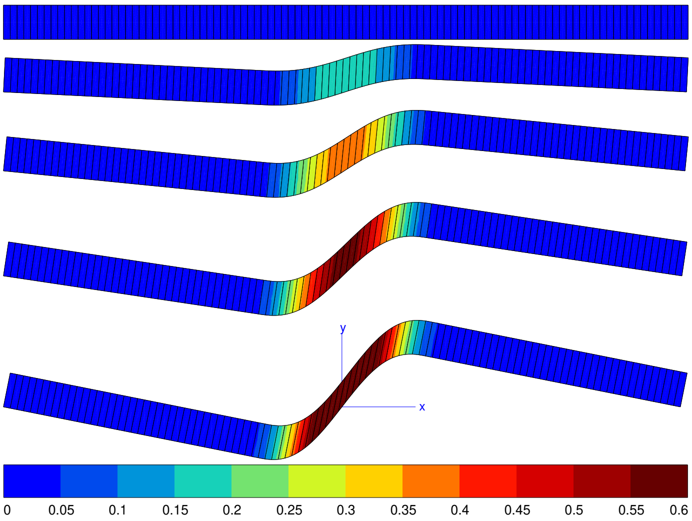

Figure 2.28: *Finite element simulation of shear localization in a micromorphic strip. Deformed states* $\bar{\gamma} = 0.; 0.05; 0.1; 0.15; 0.2$, *from top to bottom, respectively. The fields of plastic microstrain* p_χ *are also given. The parameters of the simulation are given in Table 2.5.*

The limit case of strain gradient plasticity is illustrated by Fig. 2.29 where the analytical solution is compared to the FE simulations using the micromorphic model with the penalty parameter $H_\chi = 10^5$ MPa. The same excellent agreement is observed using the Lagrange multiplier based model.

Fig. 2.30 shows that the transcendental equation $f(x) = 0$, see Eq. (2.109), admits three solutions for x_c in the interval $[0, h]$, namely $x_c \simeq 1.198, 2.604, 4.012$ mm.

Fig. 2.31 shows perfect agreement between the analytical and FE solutions, for the lowest value of x_c. The regularity of the $p_\chi(x)$ profile is clearly visible with vanishing tangents around $x = \pm 2$ mm. In contrast, the $p(x)$ function is not differentiable at $\pm x_c$ and reaches higher peak value than the smoother microplastic strain $p_\chi(x)$.

Fig. 2.32 show the solutions obtained for the other possible values of x_c. They correspond to the existence of 2 or 3 coexisting bands. However these solutions cannot be accepted because it is apparent that the cumulative plastic strain variable takes negative values at some places, which is forbidden. This means that these solutions must be reconsidered by taking possible elastic unloading into account. This explains why these two or three-branch solutions are not found in the FE analysis. Note also that the number of finite width localization bands is limited by the size $2h$ of the strip element.

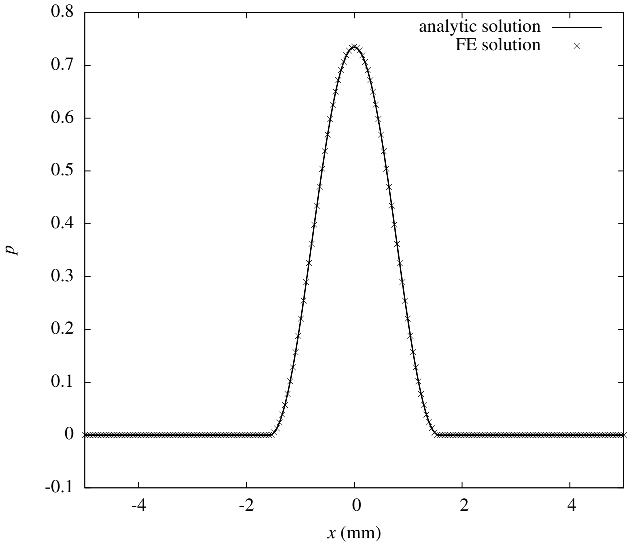

Figure 2.29: *Strain gradient plasticity solution of the shear localization problem with parameters listed in Table 2.5.*

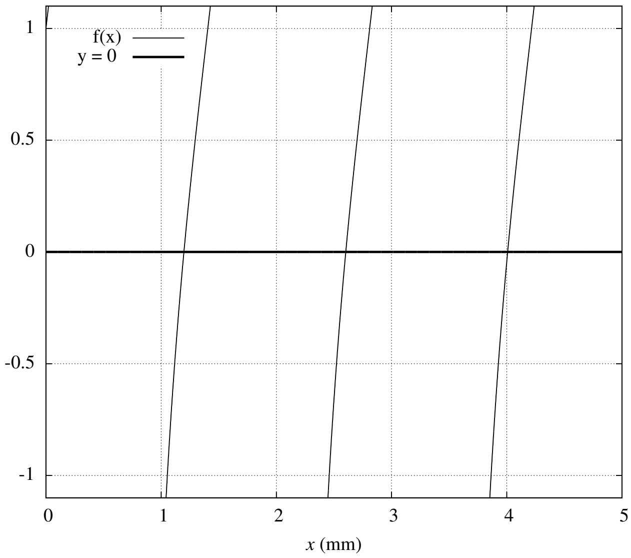

Figure 2.30: *Roots of the transcendental equation $f(x) = 0$ given by Eq. (2.109), with parameters listed in Table 2.5.*

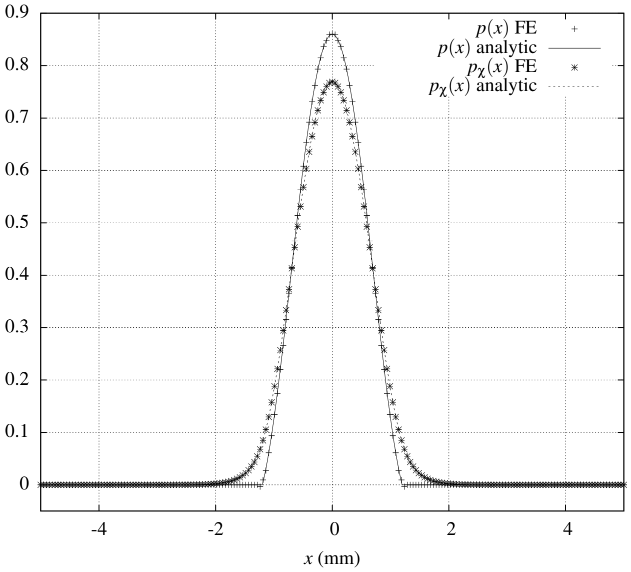

Figure 2.31: *Comparison between analytical and FE solutions of the shear localization problem for the micromorphic plasticity model and the smallest positive solution of the transcendental equation, with parameters listed in Table 2.5.*

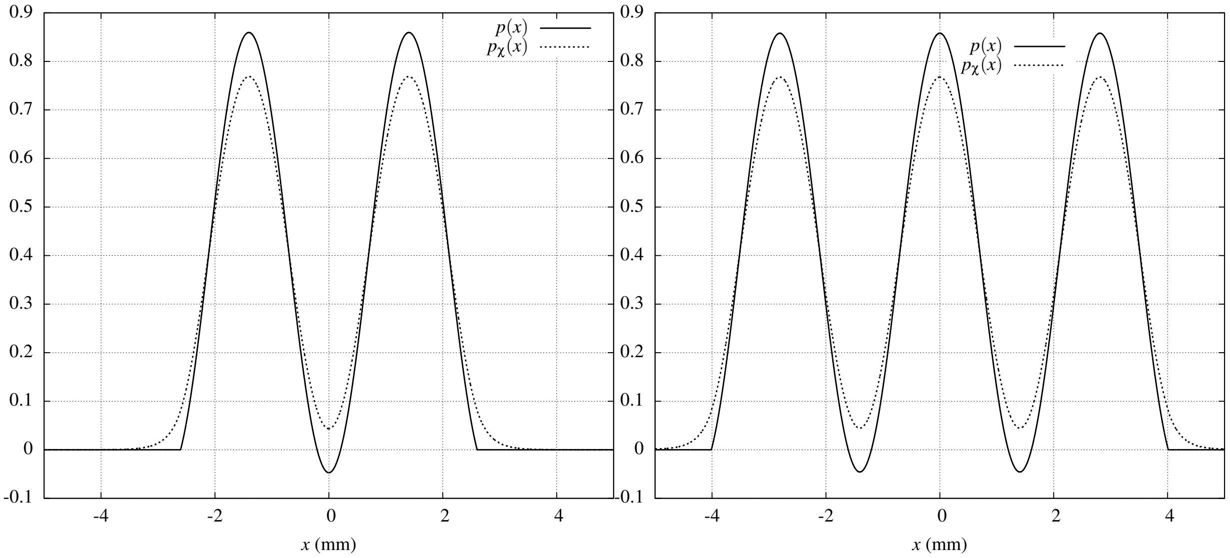

Figure 2.32: *Analytical solution of the shear localization problem using the second and the third smallest positive value of x_c, with parameters listed in Table 2.5.*

Chapter 3

Tensorial elastoplastic micromorphic continua

Abstract This chapter addresses micromorphic models associated to tensor variables. Two models based on the symmetric total and plastic strain tensors are treated in the framework of small strains. The first model is based on the total deformation and allows to model size effects in elasticity and plasticity. The micromorphic contribution modifies the elasticity law and the yield criterion as a kinematic hardening term. The second model predicts a kinematic hardening term without modifying the elasticity law. The extension of these models to finite strains is carried out by making choices of appropriate tensorial total or plastic strain measures. For the applications, however, we limit ourselves to the framework of small strains. Analytical solutions have been worked out in elasticity for simple extension and simple glide loading. In elastoplasticity, analytical solutions are provided for simple glide loading in the softening and hardening cases. These models represent an alternative to the scalar models. In particular, the proposed tensorial models introduce a back stress term that can take theoretically any value in contrast to the model based on the cumulative plastic strain. For the latter model, the induced isotropic hardening is limited to positive values. This is illustrated in the case of a 2D-foil bending and a cylinder torsion.

Résumé Ce chapitre est consacré à l'étude des modèles micromorphes associés à des variables tensorielles. Deux modèles basés sur le tenseur symétrique de la déformation totale et la déformation plastique sont traités dans le cadre des petites perturbations. Le premier modèle se base sur la déformation totale permettant de modéliser les effets d'échelle en élasticité et en plasticité. La contribution micromorphe intervient dans la loi d'élasticité et dans le critère de plasticité comme étant un écrouissage cinématique. Le deuxième modèle introduit un terme d'écrouissage cinématique sans modifier la loi d'élasticité. L'extension de ces modèles en grandes déformations est proposée en effectuant des choix de mesures adéquates de la déformation totale et plastique. Pour les applications, on se limite toutefois au cadre des petites déformations. Les solutions analytiques ont été élaborées en élasticité pour un chargement d'extension simple et de glissement simple. En élastoplasticité, les solutions analytiques sont fournies pour un chargement de glissement simple dans les cas adoucissant et durcissant. Ces modèles tensoriels représentent une alternative aux modèles scalaires. En particulier, ils introduisent un terme d'écrouissage cinématique qui peut prendre théoriquement n'importe quelle valeur, contrairement au modèle basé sur la déformation plastique cumulée. Des illustrations sont présentées dans le cas d'une poutre en flexion et d'un cylindre en torsion.

Contents

3.1 Introduction

The softening due to thermal, damage or any other microstructure-dependent phenomena, using classical theories leads to ill-posed boundary value problems (BVP). Hence, BVPs based on local constitutive laws lead to solutions sensitive to space and time discretization. In addition, these classical theories are not able, by construction, to model size effects. In fact, it is due to the fact that constitutive laws do not contain any internal length scale. The local action assumption postulates that the neighbourhood of each material point has no influence on state variables and on the mechanical state at that point. To overcome this limitation, it is required to account for an appropriate neighbourhood of each material point by introducing some characteristic lengths, representative of the local material's microstructure, into constitutive equations. Several theories have been proposed and widely studied since the 1960s. First, the method relying on non-local integral operators [Eringen and Edelen, 1972; Bažant and Jirásek, 2002] assumes that the constitutive law at a point of a continuum involves weighted averages of a state variable over a certain neighbourhood of that point. Second, strain gradient theories, or higher grade generalized continua [Truesdell and Noll, 1965], for which the constitutive laws are defined as higher spatial derivatives of the displacement field. Gradient formulations, while adhering to the principle of local action, take the field in the immediate vicinity of the material point into account by enriching the local constitutive laws with the first or higher gradients of some state variables. In addition, another way is suggested by higher-order theories that enrich the classical continuum with additional degrees of freedom [Eringen and Suhubi, 1964; Germain, 1973].

A microcontinuum can be perceived as a higher-order theory since it involves internal variables as additional degrees of freedom. To represent the notion of the deformation of the underlying microstructure at a material point, deformable *microvectors* are associated with it. This amounts to saying that the micro-continuum is a classical continuum endowed with extra-degrees of freedom, namely the deformable *microvectors*. The macro and the microdeformation are related through constitutive laws. Several microcontinua can be distinguished as follows:

- *Micropolar* continuum (Cosserat): the motion of microvectors, which are orthonormal, is represented as a rigid body rotation. The rotation tensor is represented by its axial vector (3 supplementary degrees of freedom). Note that the macro-rotation and the micro-rotation are different and that induces extra stress fields.

- *Microstretch* continuum is subjected to microrotation and microstretch (microvolume change) without micro-shearing. It means that the microvectors undergo only expansion and contraction.
- *Microdilatation* continuum accounts for microvolume changes only. This model introduces only one additional degree of freedom.
- *Microstrain* continuum [Forest and Sievert, 2003, 2006]: it considers only the change of the shape of the volume delimited by the triad of microvectors. If the rotation of that volume is considered as well, the micromorphic continuum is retrieved. The microstrain model introduces six additional degrees of freedom.
- The micromorphic continuum [Eringen and Suhubi, 1964; Mindlin, 1964] is endowed with 9 microdeformation degrees of freedom represented by a second-order tensor, called the microdeformation tensor which is in general non-symmetric and non-compatible.

As noticed, the choice of the proper higher-order continuum depends on the relevant microscopic deformation mechanisms observed in the material. Further, a more accurate description of the kinematics and the constitutive behavior of the material implies a higher number of degrees of freedom which comes at a computational cost. In the microcontinuum theories, the material behavior is assumed generally to be affected only by the first gradient of all degrees of freedom.

The aforementioned micro-continua are used to address elasto-viscoplasticity at small and finite strains [Forest and Sievert, 2003, 2006; Hirschberger and Steinmann, 2009]. A classification of higher order models for elasto-viscoplasticity is made by Forest and Sievert [2006]. The micromorphic contribution can be either dissipative Forest and Sievert [2003]; Anand et al. [2012] or energetic Forest [2009, 2016]. The gradient of the microdeformation can be decomposed additively into *elastic* and *inelastic* parts. An evolution equation is required for the *inelastic* part.

In addition to these models, there exist several reduced micromorphic models that are physically motivated to model size effects or cancel the spurious mesh dependency. The methodology proposed by Forest [2009] illustrates how to enhance local models that involve damage, plastic strain, and isotropic and kinematic hardening variables. The strain gradient enhancement can be achieved using one or more variables at once [Geers et al., 1998; Forest, 2009; Saanouni and Hamed, 2013]. For crystal plasticity, instead of considering micromorphic variables associated with the cumulative plastic strain at each slip system, which is computationally expensive, the formulation is often reduced such that the micromorphic variable is related only to the total cumulative plastic strain [Wulfinghoff and Böhlke, 2012; Scherer et al., 2019]. The scalar micromorphic variable is very convenient to enhance classical models at a low computational cost. However, many conceptual issues arise, *e.g.* yield radius that tends to be negative [Poh et al., 2011], unstable solutions w.r.t. boundary conditions because scalar micromorphic variable contains no information on the direction of the plastic flow. These issues are illustrated through several examples in the previous chapter 2.

The main objective of this chapter is to revisit the micromorphic formulation based on symmetric second-order tensors to enhance elastoplasticity models. It allows to solve the aforementioned conceptual problems induced by scalar strain gradient models. The model relying on total strain tensor was already proposed by Dillard et al. [2006] for elasticity and its extension to finite strain by Forest [2016]. The novelty of this chapter is to reinvestigate these models for elastoplasticity by giving explicit expressions of yield functions and normality rules. The model based on the plastic strain tensor was proposed in the small strain framework by Forest [2009]; Poh et al. [2011]. An extension to finite strain is proposed based on a proper plastic strain measure. The multiplicative decomposition of the deformation gradient is adopted. The comparison between different micromorphic models is carried out for different loading cases.

This chapter addresses the formulation and implementation of micromorphic models based on symmetric second-order tensors. The first model is based on the total strain tensor and the second one relies upon the plastic strain tensor. The extension of these models to finite strain is presented. Analytical solutions for different micromorphic models are derived at small strains for different loading cases which are used as a validation of the FEM implementation. For instance, The model based on total strain is studied in the case of elasticity and elastoplasticity whereas the second model is applied only in the case of elastoplasticity. The size effect is illustrated through simple glide loading with confined plasticity, the bending of a 2D foil, and the cyclic torsion of a cylinder bar. The strain localization in the case of simple glide loading is studied for both micromorphic models.

3.2 Micromorphic continuum based on the total strain tensor

This model is a reduced micromorphic model (microstrain) since Eringen's microdeformation tensor is assumed here to be symmetric. In the following, the micromorphic model is elaborated first in the small strains framework. An extension to finite strains of this model that has already been proposed by Forest [2016] is revisited. Explicit expressions of the yield surface and normality rules are provided for elasto-viscoplasticity.

3.2.1 Small strain formulation

Balance equations and kinematics

The total strain is additively decomposed into elastic and inelastic parts as

$$\underset{\sim}{\varepsilon} = \underset{\sim}{\varepsilon}^e + \underset{\sim}{\varepsilon}^p \tag{3.1}$$

In the small strain framework, the power density of internal forces is taken as

$$\mathscr{P}^{(i)} = \underset{\sim}{\sigma} : \dot{\underset{\sim}{\varepsilon}} + \underset{\sim}{a} : \dot{\underset{\sim}{\chi}} + \underset{\approx}{b} \,\vdots\, \nabla \dot{\underset{\sim}{\chi}} \tag{3.2}$$

$\underset{\sim}{a}$ and $\underset{\approx}{b}$ denote generalized stresses associated to generalized strains $\underset{\sim}{\chi}$ and $\nabla\underset{\sim}{\chi}$. The units of $\underset{\sim}{a}$ and $\underset{\approx}{b}$ are MPa and N/mm, respectively. The principle of virtual power, with negligible volume forces, in a domain $D \in \Omega$ writes

$$\int_D \mathscr{P}^{(i)} dV = \int_{\partial D} \left(\underline{t} \cdot \dot{\underline{u}} + \underset{\sim}{m} : \dot{\underset{\sim}{\chi}} \right) dS \tag{3.3}$$

The balance of momentum equations for this micromorphic continuum, as deduced from the application of the principle of virtual power, reads

$$\begin{cases} \operatorname{div} \underset{\sim}{\sigma} & = \underset{\sim}{0} \\ \operatorname{div} \underset{\approx}{b} & = \underset{\sim}{a} \end{cases} \quad \forall \underline{x} \in \Omega \qquad \begin{cases} \underline{t} & = \underset{\sim}{\sigma} \cdot \underline{n} \\ \underset{\sim}{m} & = \underset{\approx}{b} \cdot \underline{n} \end{cases} \quad \forall \underline{x} \in \partial\Omega \tag{3.4}$$

where $\underline{n}$ is the outward surface normal, $\underline{t}$ and $\underset{\sim}{m}$ are the surface tractions.

Exploitation of the entropy principle

The free energy is assumed to depend on elastic strain $\underset{\sim}{\varepsilon}^e$, internal variables α_I, total strain $\underset{\sim}{\varepsilon}$, microstrain $\underset{\sim}{\chi}$ and its gradient[1] $\underset{\approx}{k} = \underset{\sim}{\chi} \otimes \nabla$:

$$\psi(\underset{\sim}{\varepsilon}^e, \alpha_I, \underset{\sim}{\varepsilon}, \underset{\sim}{\chi}, \underset{\approx}{k}) = \psi^{ref}(\underset{\sim}{\varepsilon}^e, \alpha_I) + \psi^{\chi}(\underset{\sim}{\varepsilon}, \underset{\sim}{\chi}, \underset{\approx}{k}) \tag{3.5}$$

where ψ^{ref} refers to any classical mechanical model and ψ^{χ} to the micromorphic contribution. The generalized stresses $\underset{\sim}{a}$ and $\underset{\approx}{b}$ are assumed non-dissipative.
The Clausius-Duhem inequality in the isothermal case is given by

$$\mathscr{P}^{(i)} - \rho\dot{\psi} \geq 0 \tag{3.6}$$

---

[1] $k_{ijk} = \chi_{ij,k}$

where

$$\dot{\psi} = \frac{\partial\psi}{\partial\underset{\sim}{\varepsilon}^e} : \dot{\underset{\sim}{\varepsilon}}^e + \frac{\partial\psi}{\partial\underset{\sim}{\varepsilon}} : \left(\dot{\underset{\sim}{\varepsilon}}^e + \dot{\underset{\sim}{\varepsilon}}^p\right) + \frac{\partial\psi}{\partial\underset{\sim}{\chi}} : \dot{\underset{\sim}{\chi}} + \frac{\partial\psi}{\partial\underset{\simeq}{\boldsymbol{k}}} \vdots \dot{\underset{\simeq}{\boldsymbol{k}}} + \frac{\partial\psi}{\partial\alpha_I}\dot{\alpha}_I \tag{3.7}$$

and $\mathscr{P}^{(i)} = \underset{\sim}{\sigma} : (\dot{\underset{\sim}{\varepsilon}}^e + \dot{\underset{\sim}{\varepsilon}}^p) + \underset{\sim}{\boldsymbol{a}} : \dot{\underset{\sim}{\chi}} + \underset{\simeq}{\boldsymbol{b}} \vdots \nabla\dot{\underset{\sim}{\chi}}$

Using the previous equations, the dissipation inequality becomes

$$\left(\underset{\sim}{\sigma} - \rho\frac{\partial\psi}{\partial\underset{\sim}{\varepsilon}^e} - \rho\frac{\partial\psi}{\partial\underset{\sim}{\varepsilon}}\right) : \dot{\underset{\sim}{\varepsilon}}^e + \left(\underset{\sim}{\boldsymbol{a}} - \rho\frac{\partial\psi}{\partial\underset{\sim}{\chi}}\right) : \dot{\underset{\sim}{\chi}} + \left(\underset{\simeq}{\boldsymbol{b}} - \rho\frac{\partial\psi}{\partial\underset{\simeq}{\boldsymbol{k}}}\right) \vdots \dot{\underset{\simeq}{\boldsymbol{k}}} + \left(\underset{\sim}{\sigma} - \rho\frac{\partial\psi}{\partial\underset{\sim}{\varepsilon}}\right) : \dot{\underset{\sim}{\varepsilon}}^p - \rho\frac{\partial\psi}{\partial\alpha_I}\dot{\alpha}_I \geq 0 \tag{3.8}$$

We assume that the three first terms are non dissipative

$$\underset{\sim}{\sigma} = \rho\frac{\partial\psi}{\partial\underset{\sim}{\varepsilon}^e} + \rho\frac{\partial\psi}{\partial\underset{\sim}{\varepsilon}}, \qquad \underset{\sim}{\boldsymbol{a}} = \rho\frac{\partial\psi}{\partial\underset{\sim}{\chi}}, \qquad \underset{\simeq}{\boldsymbol{b}} = \rho\frac{\partial\psi}{\partial\underset{\simeq}{\boldsymbol{k}}} \tag{3.9}$$

The specific free energy potential of the following quadratic form

$$\rho\psi(\underset{\sim}{\varepsilon}^e, \alpha_I, \underset{\sim}{\varepsilon}, \underset{\sim}{\chi}, \underset{\simeq}{\boldsymbol{k}}) = \frac{1}{2}\underset{\sim}{\varepsilon}^e : \underset{\approx}{\mathbb{C}} : \underset{\sim}{\varepsilon}^e + \rho\psi^h(\alpha_I) + \frac{1}{2}(\underset{\sim}{\varepsilon} - \underset{\sim}{\chi}) : \underset{\approx}{\boldsymbol{H}}_\chi : (\underset{\sim}{\varepsilon} - \underset{\sim}{\chi}) + \frac{1}{2}\underset{\simeq}{\boldsymbol{k}} \vdots \underset{\approx\approx}{\boldsymbol{A}} \vdots \underset{\simeq}{\boldsymbol{k}} \tag{3.10}$$

is adopted in the sequel. The fourth-order tensor $\underset{\approx}{\boldsymbol{H}}_\chi$ allows the application of internal constraints. The sixth order tensor $\underset{\approx\approx}{\boldsymbol{A}}$ denotes the elastic stiffness tensor at higher orders.

The state laws are then linear stress-strain relations:

$$\underset{\sim}{\sigma} = \underset{\approx}{\mathbb{C}} : (\underset{\sim}{\varepsilon} - \underset{\sim}{\varepsilon}^p) + \underset{\approx}{\boldsymbol{H}}_\chi : (\underset{\sim}{\varepsilon} - \underset{\sim}{\chi}), \qquad \underset{\sim}{\boldsymbol{a}} = -\underset{\approx}{\boldsymbol{H}}_\chi : \left(\underset{\sim}{\varepsilon} - \underset{\sim}{\chi}\right), \qquad \underset{\simeq}{\boldsymbol{b}} = \underset{\approx\approx}{\boldsymbol{A}} \vdots \underset{\simeq}{\boldsymbol{k}} \tag{3.11}$$

In the following, the set of internal variables consists of the cumulative plastic strain p and $\underset{\sim}{\alpha}$ related to kinematic hardening. Therefore, the yield function writes

$$f(\underset{\sim}{\sigma}, R) = \left[\underset{\sim}{\sigma} - \underset{\sim}{\boldsymbol{X}}^{ref} - \underset{\sim}{\boldsymbol{X}}_\varepsilon\right]_{eq} - R_0 - R(p) \tag{3.12}$$

where $R(p) = \rho\dfrac{\partial\psi^h}{\partial p}$ refers to the isotropic hardening, $\underset{\sim}{\boldsymbol{X}} = \rho\dfrac{\partial\psi^h}{\partial\underset{\sim}{\alpha}}$ is the classical back stress, and $\underset{\sim}{\boldsymbol{X}}_\varepsilon = \rho\dfrac{\partial\psi}{\partial\underset{\sim}{\varepsilon}}$ is a back stress that emerges from the micromorphic model. According to Eq. (3.9), the yield function can be further simplified since

$$\underset{\sim}{\sigma} - \underset{\sim}{\boldsymbol{X}}_\varepsilon = \rho\frac{\partial\psi}{\partial\underset{\sim}{\varepsilon}^e} \tag{3.13}$$

Therefore, the yield function (3.12) has a form identically similar to the yield function of the classical model. However, it is worth noting that the Cauchy stress in Eq. (3.9) contains in fact a micromorphic (non-local) contribution. The flow rule is given by

$$\dot{\underset{\sim}{\varepsilon}}^p = \dot{\lambda}\frac{\partial f}{\partial\underset{\sim}{\sigma}} = \dot{p}\frac{\partial f}{\partial\underset{\sim}{\sigma}} = \dot{p}\,\underset{\sim}{\boldsymbol{n}}, \qquad \text{with} \quad \underset{\sim}{\boldsymbol{n}} = \frac{\partial f}{\partial\underset{\sim}{\sigma}} \tag{3.14}$$

and the loading-unloading conditions $\dot{\lambda} \geq 0, f \leq 0, \dot{\lambda} f = 0$. The intrinsic dissipation

$$\left(\underset{\sim}{\sigma} - \rho\frac{\partial\psi}{\partial\underset{\sim}{\varepsilon}}\right) : \dot{\underset{\sim}{\varepsilon}}^p - \rho\frac{\partial\psi}{\partial\underset{\sim}{\alpha}}\dot{\underset{\sim}{\alpha}} = f\dot{p} + R_0\dot{p} - \underset{\sim}{\boldsymbol{X}} : \dot{\underset{\sim}{\alpha}} \tag{3.15}$$

is always positive if there exists a potential $\Omega(\underset{\sim}{\sigma}, R, \underset{\sim}{\boldsymbol{X}})$ (convex w.r.t $\underset{\sim}{\sigma}$ and concave w.r.t. R and $\underset{\sim}{\boldsymbol{X}}$) such that

$$\dot{p} = -\frac{\partial \Omega}{\partial R} = \frac{\partial \Omega}{\partial f}, \qquad \text{and} \quad \underset{\sim}{\dot{\boldsymbol{\alpha}}} = -\frac{\partial \Omega}{\partial \underset{\sim}{\boldsymbol{X}}} \tag{3.16}$$

During plastic yielding, the yield function must remain equal to zero, and so in the case of rate-independent plasticity, the plastic multiplier $\dot{p}$ must satisfy $\dot{f} = 0$, called consistency condition, which provides the expression of the plastic multiplier:

$$\dot{p} = \frac{\left\langle \underset{\sim}{\boldsymbol{n}} : \underset{\approx}{\mathbb{C}} : \dot{\varepsilon} \right\rangle}{\underset{\sim}{\boldsymbol{n}} : \underset{\approx}{\mathbb{C}} : \underset{\sim}{\boldsymbol{n}} + \dfrac{\partial R}{\partial p} + \dfrac{\partial \underset{\sim}{\boldsymbol{X}}}{\partial p}} \tag{3.17}$$

where $< \cdot >$ denotes the positive part.

3.2.2 Finite strain formulation

The general framework to treat elasto-viscoplasticity for micromorphic continua was proposed by Forest and Sievert [2003, 2006]. The model that we present in what follows is a particular case of the microstrain model proposed in Forest and Sievert [2006]. The generalized stresses are considered non-dissipative. Therefore, no decomposition of the micromorphic variable is adopted in this section.

In the following, we present a Lagrangian formulation of a microstrain medium for elastoplasticity at finite strains. The deformation gradient is decomposed multiplicatively into elastic and plastic parts. The micromorphic variable denoted by $\underset{\sim}{\boldsymbol{\chi}}_C$ is associated to the total right Cauchy-Green strain tensor $\underset{\sim}{\boldsymbol{C}} = \underset{\sim}{\boldsymbol{F}}^T \underset{\sim}{\boldsymbol{F}}$. The Eulerian gradient of additional degrees of freedom is denoted by $\underset{\simeq}{\boldsymbol{k}} = \underset{\sim}{\boldsymbol{\chi}} \otimes \nabla$. The power density of internal forces expressed w.r.t. the current configuration, $\mathscr{P}^{(i)}$, is given by

$$\mathscr{P}^{(i)} = \underset{\sim}{\boldsymbol{\sigma}} : \underset{\sim}{\boldsymbol{D}} + \underset{\sim}{\boldsymbol{a}} : \underset{\sim}{\dot{\boldsymbol{\chi}}} + \underset{\simeq}{\boldsymbol{b}} \,\vdots\, \underset{\simeq}{\dot{\boldsymbol{k}}}, \qquad \forall \underline{\boldsymbol{x}} \in \Omega \tag{3.18}$$

where $\underset{\sim}{\boldsymbol{a}}$ and $\underset{\simeq}{\boldsymbol{b}}$ are generalized stresses associated with the micromorphic variable $\underset{\sim}{\boldsymbol{\chi}}$ and its first gradient $\underset{\simeq}{\boldsymbol{k}}$. By neglecting volume forces for the sake of simplicity, the principle of virtual power is written w.r.t. the current configuration as follows

$$\int_D \mathscr{P}^{(i)} dV = \int_{\partial D} \left(\underline{\boldsymbol{t}} . \dot{\underline{\boldsymbol{u}}} + \underset{\sim}{\boldsymbol{m}} \dot{\chi} \right) dS \quad , \quad \forall\, D \subset \Omega \tag{3.19}$$

where D is a sub-domain of the current configuration Ω of the body. External forces arise from macroscopic surface traction $\underline{\boldsymbol{t}}$ and the generalized surface traction $\underset{\sim}{\boldsymbol{m}}$ related to the micromorphic variable. The application of the virtual power principle, w.r.t. the generalized set of independent degrees of freedom, leads to the static balance laws in the current configuration in the form

$$\begin{cases} \operatorname{div} \underset{\sim}{\boldsymbol{\sigma}} & = \underline{\boldsymbol{0}} \\ \operatorname{div} \underset{\simeq}{\boldsymbol{b}} & = \underset{\sim}{\boldsymbol{a}} \end{cases} \quad \forall \underline{\boldsymbol{x}} \in \Omega \qquad \begin{cases} \underline{\boldsymbol{t}} & = \underset{\sim}{\boldsymbol{\sigma}} \cdot \underline{\boldsymbol{n}} \\ \underset{\sim}{\boldsymbol{m}} & = \underset{\simeq}{\boldsymbol{b}} \cdot \underline{\boldsymbol{n}} \end{cases} \quad \forall \underline{\boldsymbol{x}} \in \partial\Omega \tag{3.20}$$

where $\underline{\boldsymbol{n}}$ denotes the outward surface unit normal in the current configuration. The corresponding Lagrangian forms of the balance equations are

$$\operatorname{Div} \underset{\sim}{\boldsymbol{P}} = 0 \qquad \text{and} \qquad \operatorname{Div} \underset{\simeq}{\boldsymbol{b}}_0 = \underset{\sim}{\boldsymbol{a}}_0 \tag{3.21}$$

where $\underset{\sim}{\boldsymbol{P}}$ is the Boussinesq stress, $\underset{\sim}{\boldsymbol{a}}_0$ and $\underset{\simeq}{\boldsymbol{b}}_0$ are generalized stresses. The relations between the Lagrangian and Eulerian generalized stresses are

$$\underset{\sim}{\boldsymbol{a}}_0 = J \underset{\sim}{\boldsymbol{a}} \qquad \text{and} \qquad \underset{\simeq}{\boldsymbol{b}}_0 = J \underset{\simeq}{\boldsymbol{b}} \cdot \underset{\sim}{\boldsymbol{F}}^{-T} \tag{3.22}$$

We assume that the free energy is a function of the elastic right Cauchy-Green strain tensor $\underset{\sim}{\boldsymbol{C}}^e$, internal variables $\boldsymbol{\alpha}_I$, the right Cauchy-Green strain tensor $\underset{\sim}{\boldsymbol{C}}$, $\underset{\sim}{\chi}$ and $\underset{\simeq}{\boldsymbol{K}} = \underset{\sim}{\chi}_C \otimes \nabla$:

$$\psi_0(\underset{\sim}{\boldsymbol{C}}^e, \boldsymbol{\alpha}_I, \underset{\sim}{\boldsymbol{C}}, \underset{\sim}{\chi}_C, \underset{\simeq}{\boldsymbol{K}}) = \psi_0^{ref}(\underset{\sim}{\boldsymbol{C}}^e, \boldsymbol{\alpha}_I) + \psi_0^{\chi}(\underset{\sim}{\boldsymbol{C}}, \underset{\sim}{\chi}_C, \underset{\simeq}{\boldsymbol{K}}) \tag{3.23}$$

The rate of the total Cauchy-Green strain tensor is related to the plastic velocity gradient $\underset{\sim}{\overline{\boldsymbol{L}}}^p$ by

$$\dot{\underset{\sim}{\boldsymbol{C}}} = \underset{\sim}{\boldsymbol{F}}^{pT}\left(\dot{\underset{\sim}{\boldsymbol{C}}}^e + \underset{\sim}{\overline{\boldsymbol{L}}}^{pT}\underset{\sim}{\boldsymbol{C}}^e + \underset{\sim}{\boldsymbol{C}}^e\underset{\sim}{\overline{\boldsymbol{L}}}^p\right)\underset{\sim}{\boldsymbol{F}}^p = \underset{\sim}{\boldsymbol{F}}^{pT}\left(\dot{\underset{\sim}{\boldsymbol{C}}}^e + 2\left(\underset{\sim}{\boldsymbol{C}}^e\underset{\sim}{\overline{\boldsymbol{L}}}^p\right)_{sym}\right)\underset{\sim}{\boldsymbol{F}}^p \tag{3.24}$$

The Clausius-Duhem inequality is obtained [2]

$$\left(\frac{J_p}{2}\underset{\sim}{\boldsymbol{\Pi}}^e - \rho_0\frac{\partial\psi_0}{\partial\underset{\sim}{\boldsymbol{C}}^e} - \rho_0\underset{\sim}{\boldsymbol{F}}^p\frac{\partial\psi_0}{\partial\underset{\sim}{\boldsymbol{C}}}\underset{\sim}{\boldsymbol{F}}^{pT}\right) : \dot{\underset{\sim}{\boldsymbol{C}}}^e + \left(\underset{\sim}{\boldsymbol{a}}_0 - \rho_0\frac{\partial\psi_0}{\partial\underset{\sim}{\chi}}\right)\dot{\underset{\sim}{\chi}} + \left(\underset{\simeq}{\boldsymbol{b}}_0 - \rho_0\frac{\partial\psi_0}{\partial\underset{\simeq}{\boldsymbol{K}}}\right) \vdots \dot{\underset{\simeq}{\boldsymbol{K}}}$$
$$+\left(J_p\underset{\sim}{\boldsymbol{M}} - 2\rho_0\underset{\sim}{\boldsymbol{C}}^e\underset{\sim}{\boldsymbol{F}}^p\frac{\partial\psi_0}{\partial\underset{\sim}{\boldsymbol{C}}}\underset{\sim}{\boldsymbol{F}}^{pT}\right) : \underset{\sim}{\overline{\boldsymbol{L}}}^p - \rho_0\frac{\partial\psi_0}{\partial\boldsymbol{\alpha}_I}\dot{\boldsymbol{\alpha}}_I \geq 0 \tag{3.25}$$

The constitutive equations are given by

$$\underset{\sim}{\boldsymbol{\Pi}}^e = 2\overline{\rho}\frac{\partial\psi_0}{\partial\underset{\sim}{\boldsymbol{C}}^e} + 2\overline{\rho}\underset{\sim}{\boldsymbol{F}}^p\frac{\partial\psi_0}{\partial\underset{\sim}{\boldsymbol{C}}}\underset{\sim}{\boldsymbol{F}}^{pT}, \qquad \underset{\sim}{\boldsymbol{a}}_0 = \rho_0\frac{\partial\psi_0}{\partial\underset{\sim}{\chi}}, \qquad \underset{\simeq}{\boldsymbol{b}}_0 = \rho_0\frac{\partial\psi_0}{\partial\underset{\simeq}{\boldsymbol{K}}} \tag{3.26}$$

The positiveness of the residual intrinsic dissipation rate

$$\left(\underset{\sim}{\boldsymbol{M}} - 2\overline{\rho}\underset{\sim}{\boldsymbol{C}}^e\underset{\sim}{\boldsymbol{F}}^p\frac{\partial\psi_0}{\partial\underset{\sim}{\boldsymbol{C}}}\underset{\sim}{\boldsymbol{F}}^{pT}\right) : \underset{\sim}{\overline{\boldsymbol{L}}}^p - \overline{\rho}\frac{\partial\psi_0}{\partial\boldsymbol{\alpha}_I}\dot{\boldsymbol{\alpha}}_I \geq 0 \tag{3.27}$$

is satisfied if there exist a convex potential $\Omega(\underset{\sim}{\boldsymbol{M}} - \underset{\sim}{\boldsymbol{X}}_C, \boldsymbol{A_I})$ w.r.t. its arguments. The flow rule is given by

$$\underset{\sim}{\overline{\boldsymbol{L}}}^p = \frac{\partial\Omega(\underset{\sim}{\boldsymbol{M}} - \underset{\sim}{\boldsymbol{X}}_C, \boldsymbol{A_I})}{\partial(\underset{\sim}{\boldsymbol{M}} - \underset{\sim}{\boldsymbol{X}}_C)}, \qquad \boldsymbol{\alpha_I} = -\frac{\partial\Omega}{\partial\boldsymbol{A_I}} \tag{3.28}$$

where $\underset{\sim}{\boldsymbol{X}}_C = 2\overline{\rho}\underset{\sim}{\boldsymbol{C}}^e\left(\underset{\sim}{\boldsymbol{F}}^p\frac{\partial\psi_0}{\partial\underset{\sim}{\boldsymbol{C}}}\underset{\sim}{\boldsymbol{F}}^{pT}\right)$ is a back stress that arises from the micromorphic formulation. Thermodynamic forces $\boldsymbol{A_I}$ are related to internal variables $\boldsymbol{\alpha_I}$ by $\boldsymbol{A_I} = \overline{\rho}\dfrac{\partial\psi_0}{\partial\boldsymbol{\alpha_I}}$. The yield function is assumed of the form

$$f(\underset{\sim}{\boldsymbol{M}}, \boldsymbol{A_I}) = \left[\underset{\sim}{\boldsymbol{M}} - \underset{\sim}{\boldsymbol{X}}_C - \underset{\sim}{\boldsymbol{X}}\right]_{eq} - R_0 - R(p) \tag{3.29}$$

where $R(p) = \overline{\rho}\dfrac{\partial\psi}{\partial p}$ and $\underset{\sim}{\boldsymbol{X}} = \overline{\rho}\dfrac{\partial\psi}{\partial\underset{\sim}{\boldsymbol{\alpha}}}$ are thermodynamic forces associated to isotropic and kinematic hardening, respectively. In a similar way as for the small strain model, the expression of the yield function (3.29) can be simplified since

$$\underset{\sim}{\boldsymbol{M}} - \underset{\sim}{\boldsymbol{X}}_C = 2\overline{\rho}\frac{\partial\psi_0}{\partial\underset{\sim}{\boldsymbol{C}}^e} \tag{3.30}$$

which means that the micromorphic contribution appears only in the expression of the hyperelastic law for the Mandel stress tensor. For instance, if you choose a quadratic free energy potential

$$\psi_0(\underset{\sim}{\boldsymbol{C}}^e, \boldsymbol{\alpha}_I, \underset{\sim}{\boldsymbol{C}}, \underset{\sim}{\chi}, \underset{\simeq}{\boldsymbol{K}}) = \frac{1}{2\overline{\rho}}\underset{\sim}{\boldsymbol{E}}^e : \underset{\approx}{\mathbb{C}} : \underset{\sim}{\boldsymbol{E}}^e + \psi^h(\boldsymbol{\alpha_I}) + \frac{1}{2\rho_0}(\underset{\sim}{\boldsymbol{C}} - \underset{\sim}{\chi}_C) : \underset{\approx}{\boldsymbol{H}}_\chi : (\underset{\sim}{\boldsymbol{C}} - \underset{\sim}{\chi}_C) + \frac{1}{2\rho_0}\underset{\simeq}{\boldsymbol{K}} \vdots \underset{\approx}{\boldsymbol{A}} \vdots \underset{\simeq}{\boldsymbol{K}} \tag{3.31}$$

---

[2] We assume that $\dfrac{\partial\psi_0}{\partial\underset{\sim}{\boldsymbol{C}}}$ is symmetric.

the constitutive equations are written

$$\underset{\sim}{\boldsymbol{\Pi}}^e = \underset{\approx}{\mathbb{C}} : \underset{\sim}{\boldsymbol{E}}^e + \frac{2}{J_p}\underset{\sim}{\boldsymbol{F}}^p \left(\underset{\approx}{\boldsymbol{H}}_\chi : \left(\underset{\sim}{\boldsymbol{C}} - \underset{\sim}{\boldsymbol{\chi}}_C\right)\right)\underset{\sim}{\boldsymbol{F}}^{pT}, \qquad \underset{\sim}{\boldsymbol{a}}_0 = -\underset{\approx}{\boldsymbol{H}}_\chi : \left(\underset{\sim}{\boldsymbol{C}} - \underset{\sim}{\boldsymbol{\chi}}_C\right), \qquad \underset{\simeq}{\boldsymbol{b}}_0 = \underset{\approx}{\underset{\approx}{\boldsymbol{A}}} \,\vdots\, \underset{\simeq}{\boldsymbol{K}} \tag{3.32}$$

3.3 Micromorphic continuum based on the plastic strain tensor

As discussed previously in section 2.6.4, the model based on the cumulative plastic strain suffers from several drawbacks. First, it induces a radius of isotropic hardening that tends toward a negative value. This issue arises when the profile of cumulative plastic strain is non-smooth. Further, as shown in section 2.6.3, the flow rule cannot be defined in some cases. It is due mainly to the fact that scalar cumulative variables do not contain information about flow direction [Wulfinghoff et al., 2014]. The model based on the equivalent plastic strain was shown in [Jebahi and Forest, 2021] to solve partially these two issues since the micromorphic contribution appears as a kinematic hardening and the flow rule is always defined. Meanwhile, the back stress is not defined for vanishing plastic strain. As shown in section 2.2.5, the extension of this model to finite strain exhibits the same limitations. It is shown in particular that such indeterminacy can lead to numerical difficulties in the case of cyclic loading and also near the neutral axis in bending and torsion. Instead, a model based on the plastic strain tensor has been proposed by Forest [2009]; Poh et al. [2011] in the small strain framework. An extension to finite strain is proposed with a proper choice of the plastic strain measure.

3.3.1 Small strain formulation

This model has been proposed by Forest [2009] and revisited by Poh et al. [2011]. It was suggested in order to circumvent issues related to the fact that scalar gradient models do not take into account the direction of the plastic flow [Wulfinghoff et al., 2014]. This issue is more relevant for problems where the cumulative plastic strain does not have a smooth profile. It was also shown that tensorial models allow solving the issue of non-physical negative yield radius [Poh et al., 2011].

The micromorphic variable is associated with the plastic strain tensor $\boldsymbol{\varepsilon}^p$. The free energy potential is assumed to be a function of $\underset{\sim}{\boldsymbol{\varepsilon}}^e$, $\boldsymbol{\alpha}_I$, $\underset{\sim}{\boldsymbol{\varepsilon}}^p$,$\underset{\sim}{\boldsymbol{\chi}}^p$ and $\underset{\simeq}{\boldsymbol{k}} = \underset{\sim}{\boldsymbol{\chi}}^p \otimes \nabla$:

$$\psi(\underset{\sim}{\boldsymbol{\varepsilon}}^e, \boldsymbol{\alpha}_I, \underset{\sim}{\boldsymbol{\varepsilon}}^p, \underset{\sim}{\boldsymbol{\chi}}^p, \underset{\simeq}{\boldsymbol{k}}) = \psi^{ref}(\underset{\sim}{\boldsymbol{\varepsilon}}^e, \boldsymbol{\alpha}_I) + \psi^{\chi}(\underset{\sim}{\boldsymbol{\varepsilon}}^p, \underset{\sim}{\boldsymbol{\chi}}^p, \underset{\simeq}{\boldsymbol{k}}) \tag{3.33}$$

This model combines both isotropic and kinematic hardening effects due to the choice of both cumulative plastic strain $p \in \boldsymbol{\alpha_I}$ and plastic strain tensor as arguments of the free energy potential contrary to models proposed by Forest [2009] and Poh et al. [2011] which involve only one type of hardening law. Assuming isothermal conditions, the Clausius-Duhem inequality in Eq. (3.6) reads

$$\left(\underset{\sim}{\boldsymbol{\sigma}} - \rho\frac{\partial\psi}{\partial\underset{\sim}{\boldsymbol{\varepsilon}}^e}\right) : \dot{\underset{\sim}{\boldsymbol{\varepsilon}}}^e + \left(\underset{\sim}{\boldsymbol{a}} - \rho\frac{\partial\psi}{\partial\underset{\sim}{\boldsymbol{\chi}}^p}\right) : \dot{\underset{\sim}{\boldsymbol{\chi}}}^p + \left(\underset{\simeq}{\boldsymbol{b}} - \rho\frac{\partial\psi}{\partial\underset{\simeq}{\boldsymbol{k}}}\right) \,\vdots\, \dot{\underset{\simeq}{\boldsymbol{k}}}^p + \left(\underset{\sim}{\boldsymbol{\sigma}} - \rho\frac{\partial\psi}{\partial\underset{\sim}{\boldsymbol{\varepsilon}}^p}\right) : \dot{\underset{\sim}{\boldsymbol{\varepsilon}}}^p - \rho\frac{\partial\psi}{\partial\boldsymbol{\alpha}_I}\dot{\boldsymbol{\alpha}}_I \geq 0 \tag{3.34}$$

The constitutive equations are given by

$$\underset{\sim}{\boldsymbol{\sigma}} = \rho\frac{\partial\psi}{\partial\underset{\sim}{\boldsymbol{\varepsilon}}^e}, \qquad \underset{\sim}{\boldsymbol{a}} = \rho\frac{\partial\psi}{\partial\underset{\sim}{\boldsymbol{\chi}}^p}, \qquad \underset{\simeq}{\boldsymbol{b}} = \rho\frac{\partial\psi}{\partial\underset{\simeq}{\boldsymbol{k}}} \tag{3.35}$$

The set of integrated variables is $\boldsymbol{\alpha}_I = \{p, \underset{\sim}{\boldsymbol{\alpha}}\}$. Accordingly, the yield function is

$$f(\underset{\sim}{\boldsymbol{\sigma}}, R) = \left[\underset{\sim}{\boldsymbol{\sigma}} - \underset{\sim}{\boldsymbol{X}}^{ref} - \underset{\sim}{\boldsymbol{X}}^p\right]_{eq} - R_0 - R(p) \tag{3.36}$$

where

$$\underset{\sim}{\boldsymbol{X}}^p = \rho\frac{\partial\psi}{\partial\underset{\sim}{\boldsymbol{\varepsilon}}^p}, \qquad R(p) = \rho\frac{\partial\psi}{\partial p}, \qquad \underset{\sim}{\boldsymbol{X}}^{ref} = \rho\frac{\partial\psi}{\partial\underset{\sim}{\boldsymbol{\alpha}}} \tag{3.37}$$

The plastic flow rule is taken as

$$\dot{\underset{\sim}{\varepsilon}}^p = \dot{\lambda}\frac{\partial f}{\partial \underset{\sim}{\boldsymbol{\sigma}}} \tag{3.38}$$

The particular choice of a quadratic free energy potential

$$\rho\psi(\underset{\sim}{\varepsilon}^e, \alpha_I, \underset{\sim}{\varepsilon}^p, \underset{\sim}{\chi}^p, \underset{\simeq}{\boldsymbol{k}}) = \frac{1}{2}\underset{\sim}{\varepsilon}^e : \underset{\approx}{\mathbb{C}} : \underset{\sim}{\varepsilon}^e + \rho\psi^h(\alpha_I) + \frac{1}{2}(\underset{\sim}{\varepsilon}^p - \underset{\sim}{\chi}^p) : \underset{\approx}{\boldsymbol{H}}_\chi : (\underset{\sim}{\varepsilon}^p - \underset{\sim}{\chi}^p) + \frac{1}{2}\underset{\simeq}{\boldsymbol{k}} \vdots \underset{\approx}{\underset{\sim}{\boldsymbol{A}}} \vdots \underset{\simeq}{\boldsymbol{k}} \tag{3.39}$$

leads to the following constitutive equations

$$\underset{\sim}{\boldsymbol{\sigma}} = \underset{\approx}{\mathbb{C}} : \underset{\sim}{\varepsilon}^e, \qquad \underset{\sim}{\boldsymbol{a}} = -\underset{\approx}{\boldsymbol{H}}_\chi : \left(\underset{\sim}{\varepsilon}^p - \underset{\sim}{\chi}^p\right), \qquad \underset{\simeq}{\boldsymbol{b}} = \underset{\approx}{\underset{\sim}{\boldsymbol{A}}} \vdots \underset{\simeq}{\boldsymbol{k}} \tag{3.40}$$

Note that the model based on plastic strain tensor is in principle similar to the one based on total strain for negligible elastic strain. Furthermore, the model with plastic strain does not modify the elasticity law and affects only the definition of the yield function. Using consistency condition, the plastic multiplier is obtained as

$$\dot{p} = \frac{\left\langle \underset{\sim}{\boldsymbol{n}} : \underset{\approx}{\mathbb{C}} : \dot{\underset{\sim}{\varepsilon}} + \underset{\sim}{\boldsymbol{n}} : \mathbb{C} : \dot{\underset{\sim}{\chi}}^p \right\rangle}{\underset{\sim}{\boldsymbol{n}} : \left(\underset{\approx}{\mathbb{C}} + \underset{\approx}{\boldsymbol{H}}_\chi\right) : \underset{\sim}{\boldsymbol{n}} + \underset{\sim}{\boldsymbol{n}} : \dfrac{\partial \underset{\sim}{\boldsymbol{X}}^{ref}}{\partial p} + \dfrac{\partial R}{\partial p}} \tag{3.41}$$

where $\underset{\sim}{\boldsymbol{n}} = \dfrac{\partial f}{\partial \underset{\sim}{\boldsymbol{\sigma}}}$ is the normal to the yield surface.

3.3.2 Finite strain formulation

The extension of the previous model to finite strain requires choosing an appropriate plastic strain tensor. Several formulations are therefore possible. In the following, we present a Lagrangian formulation based on a plastic strain measure that lies in the reference configuration. The deformation gradient is decomposed multiplicatively into elastic and plastic parts. The micromorphic variable denoted by $\underset{\sim}{\chi}^p_C$ is associated to the plastic Cauchy-Green strain tensor $\underset{\sim}{\boldsymbol{C}}^p = \underset{\sim}{\boldsymbol{F}}^{pT}\underset{\sim}{\boldsymbol{F}}^p$. The free energy potential is assumed to be a function of $\underset{\sim}{\boldsymbol{C}}^e$, internal variables $\boldsymbol{\alpha_I}$, $\underset{\sim}{\boldsymbol{C}}^p$, $\underset{\sim}{\chi}^p_C$ and $\underset{\simeq}{\boldsymbol{K}} = \underset{\sim}{\chi}^p_C \otimes \nabla$

$$\psi_0(\underset{\sim}{\boldsymbol{C}}^e, \boldsymbol{\alpha_I}, \underset{\sim}{\boldsymbol{C}}^p, \underset{\sim}{\chi}^p_C, \underset{\simeq}{\boldsymbol{K}}) = \psi_0^{ref}(\underset{\sim}{\boldsymbol{C}}^e, \boldsymbol{\alpha_I}) + \psi_0^\chi(\underset{\sim}{\boldsymbol{C}}^p, \underset{\sim}{\chi}^p_C, \underset{\simeq}{\boldsymbol{K}}) \tag{3.42}$$

The Lagrangian version of the Clausius-Duhem inequality reads

$$\left(\frac{J_p}{2}\underset{\sim}{\boldsymbol{\Pi}}^e - \rho_0\frac{\partial\psi_0}{\partial \underset{\sim}{\boldsymbol{C}}^e}\right) : \dot{\underset{\sim}{\boldsymbol{C}}}^e + J_p\underset{\sim}{\boldsymbol{M}} : \underset{\sim}{\overline{\boldsymbol{L}}}^p - \rho_0\frac{\partial\psi_0}{\partial \underset{\sim}{\boldsymbol{C}}^p}\dot{\underset{\sim}{\boldsymbol{C}}}^p + \left(\underset{\sim}{\boldsymbol{a}}_0 - \rho_0\frac{\partial\psi_0}{\partial \underset{\sim}{\chi}^p_C}\right) : \dot{\underset{\sim}{\chi}}^p_C + \left(\underset{\simeq}{\boldsymbol{b}}_0 - \rho_0\frac{\partial\psi_0}{\partial \underset{\simeq}{\boldsymbol{K}}}\right) \vdots \dot{\underset{\simeq}{\boldsymbol{K}}} - \rho_0\frac{\partial\psi_0}{\partial\alpha_I}\dot{\alpha}_I \geq 0 \tag{3.43}$$

The constitutive equations are derived as follows

$$\underset{\sim}{\boldsymbol{\Pi}}^e = 2\overline{\rho}\frac{\partial\psi_0}{\partial \underset{\sim}{\boldsymbol{C}}^e}, \qquad \underset{\sim}{\boldsymbol{a}}_0 = \rho_0\frac{\partial\psi_0}{\partial \underset{\sim}{\chi}^p_C}, \qquad \underset{\simeq}{\boldsymbol{b}}_0 = \rho_0\frac{\partial\psi_0}{\partial \underset{\simeq}{\boldsymbol{K}}}, \qquad \boldsymbol{A_I} = \overline{\rho}\frac{\partial\psi_0}{\partial\alpha_I} \tag{3.44}$$

The intrinsic dissipation rate is

$$\underset{\sim}{\boldsymbol{M}} : \underset{\sim}{\overline{\boldsymbol{L}}}^p - \overline{\rho}\frac{\partial\psi}{\partial \underset{\sim}{\boldsymbol{C}}^p}\dot{\underset{\sim}{\boldsymbol{C}}}^p - \overline{\rho}\frac{\partial\psi_0}{\partial\alpha_I}\dot{\alpha}_I \geq 0 \tag{3.45}$$

The rate of plastic right Cauchy-Green strain tensor is

$$\dot{\underset{\sim}{\boldsymbol{C}}}^p = \underset{\sim}{\boldsymbol{F}}^{pT}\left(\underset{\sim}{\overline{\boldsymbol{L}}}^{pT} + \underset{\sim}{\overline{\boldsymbol{L}}}^p\right)\underset{\sim}{\boldsymbol{F}}^p \tag{3.46}$$

Hence, the dissipation rate is simplified[3] to obtain

$$\left(\underset{\sim}{\boldsymbol{M}} - 2\overline{\rho}\,\underset{\sim}{\boldsymbol{F}}^p \frac{\partial \psi}{\partial \underset{\sim}{\boldsymbol{C}}^p} \underset{\sim}{\boldsymbol{F}}^{pT}\right) : \underset{\sim}{\overline{\boldsymbol{L}}}^p - \overline{\rho}\frac{\partial\psi_0}{\partial\boldsymbol{\alpha_I}}\dot{\boldsymbol{\alpha}}_{\boldsymbol{I}} \geq 0 \tag{3.47}$$

The intrinsic dissipation is always positive if there exists a potential $\Omega(\underset{\sim}{\boldsymbol{M}}, \boldsymbol{A_I})$, convex w.r.t. $\underset{\sim}{\boldsymbol{M}}$ and concave w.r.t. $\boldsymbol{A_I}$ such that

$$\underset{\sim}{\overline{\boldsymbol{L}}}^p = \frac{\partial\Omega}{\partial\left(\underset{\sim}{\boldsymbol{M}} - \underset{\sim}{\boldsymbol{X}}^p_C\right)}, \qquad \dot{\boldsymbol{\alpha}}_{\boldsymbol{I}} = -\frac{\partial\Omega}{\partial\boldsymbol{A_I}} \tag{3.48}$$

where $\underset{\sim}{\boldsymbol{X}}^p_C = 2\overline{\rho}\,\underset{\sim}{\boldsymbol{F}}^p \dfrac{\partial \psi}{\partial \underset{\sim}{\boldsymbol{C}}^p} \underset{\sim}{\boldsymbol{F}}^{pT}$. We consider the set of internal variables $\boldsymbol{\alpha_I} = \{p, \underset{\sim}{\boldsymbol{\alpha}}\}$. Accordingly, the set of thermodynamic forces $\boldsymbol{A}_I = \{R^{ref}, \underset{\sim}{\boldsymbol{X}}^{ref}\}$ are given by

$$\underset{\sim}{\boldsymbol{X}}^{ref} = \overline{\rho}\frac{\partial\psi}{\partial\underset{\sim}{\boldsymbol{\alpha}}}, \quad \text{and} \quad R^{ref} = \overline{\rho}\frac{\partial\psi}{\partial p} \tag{3.49}$$

The yield function is postulated as

$$f(\underset{\sim}{\boldsymbol{M}}, R^{ref}, \underset{\sim}{\boldsymbol{X}}^{ref}) = \left[\underset{\sim}{\boldsymbol{M}} - \underset{\sim}{\boldsymbol{X}}^{ref} - \underset{\sim}{\boldsymbol{X}}^p_C\right]_{eq} - R_0 - R^{ref}(p) \tag{3.50}$$

For instance, if a quadratic free energy potential is chosen

$$\psi_0(\underset{\sim}{\boldsymbol{C}}^e, \boldsymbol{\alpha}_I, \underset{\sim}{\boldsymbol{C}}, \underset{\sim}{\boldsymbol{\chi}}^p_C, \underset{\simeq}{\boldsymbol{K}}) = \frac{1}{2\overline{\rho}}\underset{\sim}{\boldsymbol{E}}^e : \underset{\approx}{\mathbb{C}} : \underset{\sim}{\boldsymbol{E}}^e + \psi^h(\boldsymbol{\alpha_I}) + \frac{1}{2\rho_0}(\underset{\sim}{\boldsymbol{C}} - \underset{\sim}{\boldsymbol{\chi}}^p_C) : \underset{\approx}{\boldsymbol{H}}_\chi : (\underset{\sim}{\boldsymbol{C}} - \underset{\sim}{\boldsymbol{\chi}}^p_C) + \frac{1}{2\rho_0}\underset{\simeq}{\boldsymbol{K}} \vdots \underset{\approx}{\underset{\sim}{\boldsymbol{A}}} \vdots \underset{\simeq}{\boldsymbol{K}} \tag{3.51}$$

the state laws are given by

$$\underset{\sim}{\boldsymbol{\Pi}}^e = \underset{\approx}{\mathbb{C}} : \underset{\sim}{\boldsymbol{E}}^e, \qquad \underset{\sim}{\boldsymbol{a}}_0 = -\underset{\approx}{\boldsymbol{H}}_\chi : \left(\underset{\sim}{\boldsymbol{C}} - \underset{\sim}{\boldsymbol{\chi}}^p_C\right), \qquad \underset{\simeq}{\boldsymbol{b}}_0 = \underset{\approx}{\underset{\sim}{\boldsymbol{A}}} \vdots \underset{\simeq}{\boldsymbol{K}} \tag{3.52}$$

3.4 Finite element implementation

In the following, the finite element implementation of micromorphic models based on symmetric second-order tensors is detailed in the small strain framework. The principle of virtual power in (3.3) is discretized as

$$\sum_{e=0}^{n}\int_{D^e}(\underset{\sim}{\boldsymbol{\sigma}} : \underset{\sim}{\dot{\boldsymbol{\varepsilon}}} + \underset{\sim}{\boldsymbol{a}} : \underset{\sim}{\dot{\boldsymbol{\chi}}} + \underset{\simeq}{\boldsymbol{b}} \vdots \underset{\simeq}{\dot{\boldsymbol{k}}})dV = \sum_{e=0}^{n_s}\int_{\partial D^e}(\underline{\boldsymbol{t}} \cdot \underline{\boldsymbol{u}} + \underset{\sim}{\boldsymbol{m}} : \underset{\sim}{\dot{\boldsymbol{\chi}}})dS \tag{3.53}$$

where the sub-domain D^e corresponds to the space occupied by the element e and ∂D^e is the element surface. The total number of elements and surface elements are denoted by n and n_s, respectively. For each individual element, u_i and χ_{ij} are interpolated from nodal values at p nodes and q, respectively as

$$u_i = \sum_{k=1}^{p} {}^{u}N^k \tilde{u}_i^k, \qquad \chi_{ij} = \sum_{k=1}^{q} {}^{\chi}N^k \tilde{\chi}_{ij}^k \tag{3.54}$$

Thus, the gradients of displacement and micromorphic variable are derived as

$$\varepsilon_{ij} = \sum_{k=1}^{p} {}^{u}B_j^k \tilde{u}_i^k, \qquad k_{ijl} = \sum_{k=1}^{q} {}^{\chi}B_l^k \tilde{\chi}_{ij}^k \tag{3.55}$$

---

[3] Assuming that $\dfrac{\partial\psi_0}{\partial\underset{\sim}{\boldsymbol{C}}^p}$ is symmetric

where

$$ {}^{u}B_j^k = \frac{\partial {}^{u}N^k}{\partial x_j}, \qquad {}^{\chi}B_l^k = \frac{\partial {}^{\chi}N^k}{\partial x_l} \tag{3.56} $$

are the discrete symmetric gradient operators for $\underline{\boldsymbol{u}}$ and $\underset{\sim}{\chi}$ fields. Finally, Eq. (3.53) becomes

$$ \begin{aligned} \sum_{e=0}^{n}\sum_{k=1}^{p}\left[\int_{D^e} \sigma_{ij}\,{}^{u}B_j^k\, dV\right]\dot{u}_i^k + \sum_{e=0}^{n_s}\sum_{k=1}^{q}\left[\int_{D^e}\left(a_{ij}\,{}^{\chi}N^k + b_{ijl}\,{}^{\chi}B_l^k\right) dV\right]\dot{\chi}_{ij}^k \\ = \sum_{e=0}^{n_s}\sum_{k=1}^{q}\left[\int_{\partial D^e} t_i\,{}^{u}N^k dS\right]\dot{u}_i^k + \sum_{e=0}^{n_s}\sum_{k=1}^{p}\left[m_{ij}\,{}^{\chi}N^k dS\right]\dot{\chi}_{ij}^k \end{aligned} \tag{3.57} $$

Practically, this equation is written in a matrix form for FEM implementation. The expression of stresses and strains vectors are given in appendix B.2. The nonlinear system (3.57) is solved by means of Newton algorithms. The computation of the tangent matrix for both models relying on total and plastic strain tensors is detailed in appendix C.4.

3.5 Application to strain gradient elasticity

The model based on total strain can be used to enhance elasticity laws. In this section, analytical solutions are provided for the simple extension and glide problems at small strains in order to investigate size effects in elastic materials. The material model is assumed to be isotropic elastic with $E = 78$ GPa and $\nu = 0.3$. The fourth-order tensor $\underset{\approx}{\boldsymbol{H}}_\chi$, allows imposing internal constraints. For the sake of simplicity, it is used here as a penalization parameter without any coupling between components of the difference $(\underset{\sim}{\varepsilon} - \underset{\sim}{\chi})$, *i.e.* $\underset{\approx}{\boldsymbol{H}}_\chi = H_\chi \underset{\approx}{\boldsymbol{1}}$. If H_χ is sufficiently large, the micromorphic model tends to the limit of the strain gradient continuum model. The reader is referred to the works of Mindlin [1964] and Auffray et al. [2009], among others, for the matrix representation of $\underset{\approx}{\boldsymbol{A}}$ for different material symmetries in the case of strain gradient elasticity. For the sake of demonstration, we assume that $\underset{\approx}{\boldsymbol{A}} = A\underset{\approx}{\boldsymbol{1}}$.

3.5.1 Simple extension

We consider the simple extension of a strip of width $2h$ and infinite in the y-direction. The strip is subjected to prescribed displacement $u_x(x=-h) = 0$ and $u_x(x=h) = \bar{u}$. The top and bottom parts are subjected to zero displacement in the y-direction, *i.e.* $u_y(y) = 0$. Plane strain conditions are imposed, *i.e.* $u_z = 0$. The clamping boundary conditions $\chi_{11}(x \pm h) = 0$ are prescribed. The stress and strain states are defined by

$$ \underset{\sim}{\sigma} = \sigma_{11}\,\underline{e}_x \otimes \underline{e}_x + \sigma_{22}\,\underline{e}_y \otimes \underline{e}_y + \sigma_{33}\,\underline{e}_z \otimes \underline{e}_z, \quad \text{and} \quad \underset{\sim}{\varepsilon} = \varepsilon_{11}\,\underline{e}_x \otimes \underline{e}_x \tag{3.58} $$

We consider the isotropic Hooke's law such that

$$ \begin{cases} \sigma_{11} = (\lambda + 2\mu)\varepsilon_{11}(x) + H_\chi\left(\varepsilon_{11}(x) - \chi_{11}(x)\right) \\ \sigma_{22}(x) = \lambda\varepsilon_{11}(x) \\ \sigma_{33}(x) = \lambda\varepsilon_{11}(x) \end{cases} \tag{3.59} $$

where λ and μ are Lamé constants. Cauchy stress component σ_{11} is homogeneous in the strip, *i.e.* $\sigma_{11,1} = 0$. Therefore,

$$ \varepsilon_{11,1} = \frac{H_\chi \chi_{11,1}}{\lambda + 2\mu + H_\chi} \tag{3.60} $$

The second balance equation suggests that

$$ A\chi_{11,11} + H_\chi(\varepsilon_{11} - \chi_{11}) = 0 \tag{3.61} $$

leading to the following differential equation for $\chi_{11,1}$:

$$\chi_{11,111} - \frac{H_\chi(\lambda+2\mu)}{A(\lambda+2\mu+H_\chi)}\chi_{11,1} = 0 \tag{3.62}$$

Its solution is given by

$$\chi_{11} = C_1\cosh(\omega_\varepsilon x) + C_2\sinh(\omega_\varepsilon x) + C_3 \tag{3.63}$$

where C_1 and C_2 are integration constants and

$$\omega_\varepsilon^2 = \frac{H_\chi(\lambda+2\mu)}{A(\lambda+2\mu+H_\chi)} \tag{3.64}$$

since $\chi_{11}(x=\pm h)=0$, the constant C_2 vanishes and $C_3 = -C_1\cosh(\omega_\varepsilon h)$. Using Eq. (3.61), we get

$$\varepsilon_{11} = C_1\left(\frac{H_\chi}{\lambda+2\mu+H_\chi}\cosh(\omega_\varepsilon x) - \cosh(\omega_\varepsilon h)\right) \tag{3.65}$$

Using the fact that $\varepsilon_{11} = \dfrac{\partial u_x}{\partial x}$ and considering boundary conditions $u_x(-h)=0$ and $u_x(h)=\bar{u}$ we obtain

$$C_1 = \frac{\bar{u}/2h}{\cosh(\omega_\varepsilon h)\left(\dfrac{H_\chi}{\lambda+2\mu+H_\chi}\dfrac{\tanh(\omega_\varepsilon h)}{\omega_\varepsilon h} - 1\right)} \tag{3.66}$$

Hence, the displacement u_1 is given by

$$u_x(x) = C_1\left(\frac{H_\chi}{\lambda+2\mu+H_\chi}\frac{\sinh(\omega_\varepsilon x)+\sinh(\omega_\varepsilon h)}{\omega_\varepsilon} - (x+h)\cosh(\omega_\varepsilon h)\right) \tag{3.67}$$

Finally, the Cauchy stress component σ_{11} is obtained as

$$\sigma_{11} = -C_1(\lambda+2\mu)\cosh(\omega_\varepsilon h) = \frac{(\lambda+2\mu)}{1 - \dfrac{H_\chi}{\lambda+2\mu+H_\chi}\dfrac{\tanh(\omega_\varepsilon h)}{\omega_\varepsilon h}}\bar{u}/2h \tag{3.68}$$

Note that the apparent extension modulus is size-dependent. In the limit case of $A \rightarrow 0$, the classical extension modulus $\lambda+2\mu$ is retrieved. If $A \rightarrow \infty$, *i.e.* at infinitely small scale, the extension modulus reads $\lambda+2\mu+H_\chi$. That means that the size effect obtained for the micromorphic model is bounded at very small scales [Cordero et al., 2016]. The solution of this problem for strain gradient elasticity is obtained as $H_\chi \rightarrow \infty$. At an infinitely small scale, the solution for strain gradient elasticity is however not bounded. Fig. 3.1 depicts the analytical solutions u_x, ε_{11} and χ_{11} fields. The numerical results (not shown here) given by finite elements agree perfectly with the analytical solution detailed previously. In the classical case (*i.e.* $A \rightarrow 0$), the displacement u_x increases linearly between 0 at $x=-h$ and the prescribed value $\bar{u}$ at $x=h$. The profile of χ_{11} exhibits a boundary layer that depends on the wave number ω_ε related to Lamé constants and micromorphic parameters.

3.5.2 Simple glide

The simple glide problem of a strip of width $2h$ and infinite in the y-direction, under plane strain condition is discussed herein for an elastic micromorphic model based on the total strain tensor. The analytical solution is provided in the small strain case. The displacement fields are given by $u_x = \bar{\gamma}y$ and $u_y = u_y(x)$ where $\bar{\gamma}$ is the applied shear and u_y is the resulting fluctuation. Periodic boundary conditions are applied on u_y. The component χ_{12} is set to zero at $x=\pm h$. The Cauchy stress writes $\underset{\sim}{\sigma} = \tau(\underline{e}_x\otimes\underline{e}_y + \underline{e}_y\otimes\underline{e}_x)$. The

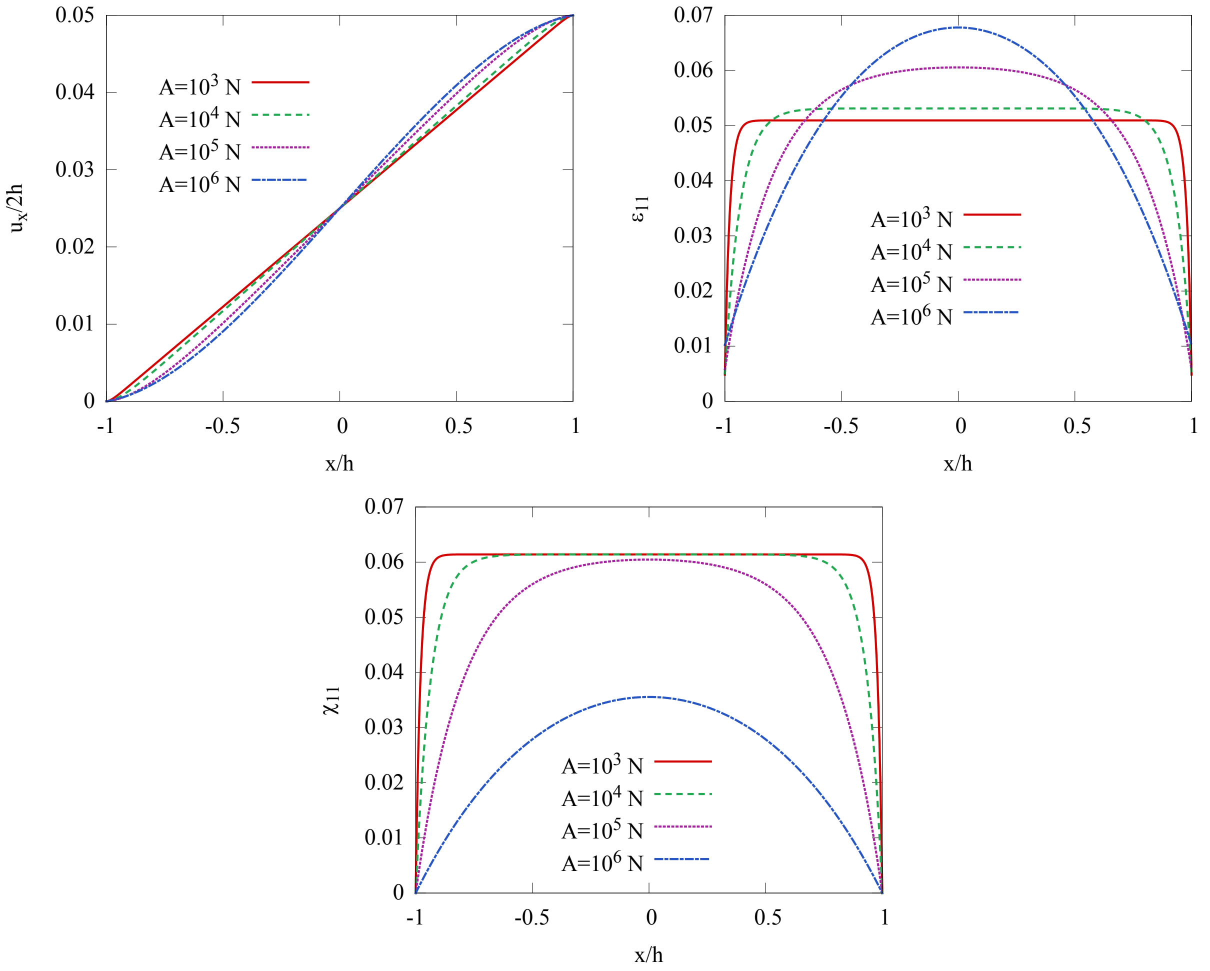

Figure 3.1: *Analytical solutions to the simple extension problem. Material parameters:* $\lambda = 45000$ *MPa,* $\mu = 30000$ *MPa,* $H_\chi = 10^5$ *MPa.*

first balance equation in (3.4) gives that

$$\tau = 2\mu\varepsilon_{12} + H_\chi(\varepsilon_{12} - \chi_{12}) \tag{3.69}$$

is homogeneous in the strip. It follows that

$$2\mu\varepsilon_{12,1} + H_\chi(\varepsilon_{12,1} - \chi_{12,1}) = 0 \tag{3.70}$$

Therefore, the gradient of shear strain ε_{12} writes

$$\varepsilon_{12,1}(x) = \frac{H_\chi}{2\mu + H_\chi}\chi_{12,1} \tag{3.71}$$

The second balance equation in (3.4) is rewritten as

$$A\Delta\chi_{12} + H_\chi(\varepsilon_{12} - \chi_{12}) = 0 \tag{3.72}$$

The previous equation is differentiated once again to obtain

$$\chi_{12,111} - \frac{2\mu H_\chi}{A(2\mu + H_\chi)}\chi_{12,1} = 0 \tag{3.73}$$

The solution of the previous equation is of exponential form as

$$\chi_{12}(x) = C_1 \cosh\big(\omega_\gamma x\big) + C_2 \sinh\big(\omega_\gamma x\big) + C_3 \tag{3.74}$$

where

$$\omega_\gamma^2 = \frac{2\mu H_\chi}{A(2\mu + H_\chi)} \tag{3.75}$$

and C_1, C_2 and C_3 are integration constants. Using the prescribed boundary condition $\chi_{12}(x = \pm h) = 0$, it follows that

$$\chi_{12}(x) = C_1 \left(\cosh\big(\omega_\gamma x\big) - \cosh\big(\omega_\gamma h\big)\right) \tag{3.76}$$

Now, this solution is substituted in Eq. (3.72) such that

$$\varepsilon_{12}(x) = C_1 \left(\frac{H_\chi}{2\mu + H_\chi} \cosh\big(\omega_\gamma x\big) - \cosh\big(\omega_\gamma h\big) \right) \tag{3.77}$$

The expression of shear strain can also be written as

$$\varepsilon_{12} = \frac{1}{2}\left(\frac{\partial u_x}{\partial y} + \frac{\partial u_y}{\partial x} \right) = \frac{1}{2}\left(\bar{\gamma} + \frac{\partial u_y}{\partial x} \right) \tag{3.78}$$

such that

$$\frac{\partial u_y}{\partial x} = 2\varepsilon_{12} - \bar{\gamma} \tag{3.79}$$

By integrating the previous equation, the expression of the fluctuation $u_y(x)$ is obtained:

$$u_y(x) = \frac{2C_1 H_\chi}{2\mu + H_\chi} \frac{\sinh\big(\omega_\gamma x\big)}{\omega_\gamma} - \big(2C_1 \cosh\big(\omega_\gamma h\big) + \bar{\gamma}\big)\, x + C_4 \tag{3.80}$$

where C_4 is a integration constant that vanishes since $u_2(x = \pm h) = 0$. Further, we have

$$C_1 = \frac{\bar{\gamma}/2}{\dfrac{H_\chi}{2\mu + H_\chi} \dfrac{\sinh\big(\omega_\gamma h\big)}{\omega_\gamma h} - \cosh\big(\omega_\gamma h\big)} \tag{3.81}$$

Finally, the expression of shear stress is obtained

$$\tau = -2\mu C_1 \cosh\big(\omega_\gamma h\big) = \mu^{app} \bar{\gamma} \tag{3.82}$$

where μ^{app} denotes the apparent shear modulus given by

$$\mu^{app} = \frac{\mu}{1 - \dfrac{H_\chi}{2\mu + H_\chi} \dfrac{\tanh\big(\omega_\gamma h\big)}{\omega_\gamma h}} \tag{3.83}$$

Note that the apparent shear modulus μ^{app} is size-dependent. Its value is plotted for different values of the generalized moduli A and H_χ in Fig. 3.2-c. For instance, for a given value of H_χ the size effect increases rapidly for small values of A and tends to the value of $(2\mu + H_\chi)/2$ as A goes to infinity. That is to say that the size effect saturates for very small values of h. By increasing the value of the parameter H_χ, the saturation value of the apparent modulus increases. When $H_\chi \to \infty$, the apparent modulus tends to the limit value of

$$\mu^{app}|_{H_\chi \to \infty} = \frac{\mu}{1 - \sqrt{\dfrac{A}{2\mu h^2}} \tanh\left(\sqrt{\dfrac{2\mu}{A}} h \right)} \tag{3.84}$$

This corresponds to the solution of strain gradient elasticity. In the latter case, if $A \to \infty$, the apparent shear modulus $\mu^{app} \to \infty$. That means that the solution provided by the micromorphic model saturates at small scales whereas the strain gradient solution is not bounded. Fig. 3.2-a shows that the numerical solutions of

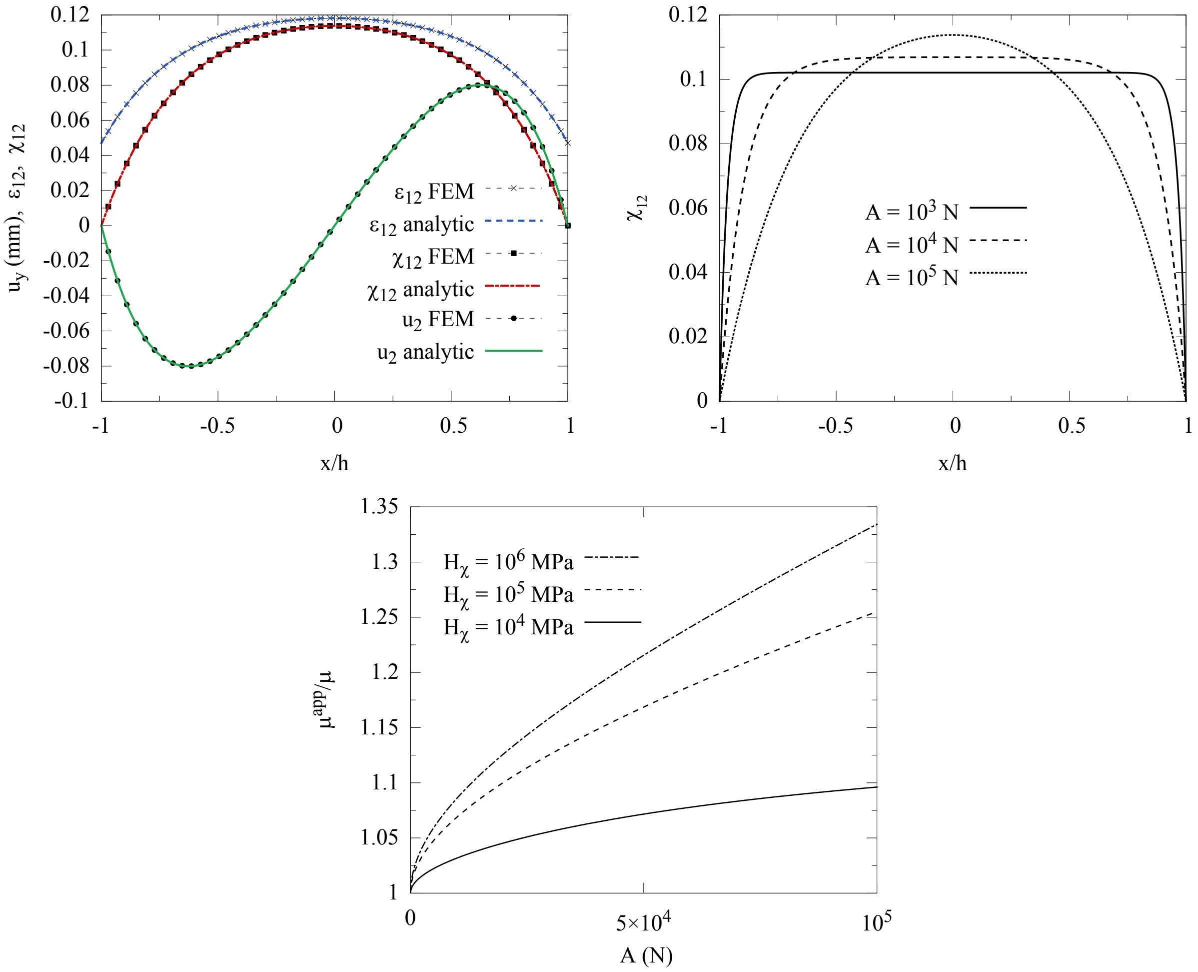

Figure 3.2: *(a) Analytical vs. finite element solutions of the simple glide problem with the total strain-based model (b) The profile of* χ_{12} *for several values of A,* $H_\chi = 10^5$ *MPa (c) Apparent shear modulus for several values of parameters A and* H_χ*. Unit cell size* $2h = 10$ *mm.*

the simple glide problem fit perfectly with the analytical solutions. The limit case of classical model, *i.e.* $A \to 0$ leads to $\mu^{app} = \mu$.

3.6 Application to strain gradient plasticity

In the following, micromorphic models relying on total and plastic strain tensors are applied for elasto-plastic problems. First, analytical solutions are given for the simple glide problem. Three types of solutions are obtained depending on the hardening law: perfect plasticity, linear hardening, and linear softening. These solutions are compared to the model based on the cumulative plastic strain. Second, the bending of a 2D foil and the torsion of a cylinder are studied for tensorial micromorphic models.

3.6.1 Simple glide: total strain-based model

Re-consider the example of simple glide in section 2.8. The first balance equation in section 3.4 leads to only one non-vanishing stress component σ_{12} that is homogeneous in the strip. Its expression writes

$$\sigma_{12} = \tau = 2\mu\varepsilon^e_{12} + H_\chi(\varepsilon_{12} - \chi_{12}) \tag{3.85}$$

The second balance equation in 3.4 gives that

$$A\chi_{12,11} + H_\chi(\varepsilon_{12} - \chi_{12}) = 0 \tag{3.86}$$

The yield function

$$f(\underset{\sim}{\sigma}, R) = [\underset{\sim}{\sigma} - \underset{\sim}{X}_\varepsilon]_{eq} - R_0 - R(p) \tag{3.87}$$

Note that

$$[\underset{\sim}{\sigma} - \underset{\sim}{X}_\varepsilon]_{eq} = 2\sqrt{3}\mu|\varepsilon^e_{12}| = \sqrt{3}\left|\tau - H_\chi(\varepsilon_{12} - \chi_{12})\right| \tag{3.88}$$

For the sake of demonstration, a linear isotropic hardening plasticity law is adopted. Without loss of generality, the elastic deformation ε^e_{12} is considered to be positive. Accordingly, the yield function is given by

$$f(\underset{\sim}{\sigma}, R) = \sqrt{3}\left(\tau - H_\chi(\varepsilon_{12} - \chi_{12})\right) - R_0 - Hp \tag{3.89}$$

On the other hand, using Eq. (3.85) one has

$$\varepsilon^p_{12} = \varepsilon_{12} - \frac{\tau - H_\chi(\varepsilon_{12} - \chi_{12})}{2\mu} \tag{3.90}$$

At yielding, the yield function vanishes and

$$\sqrt{3}\left(\tau - H_\chi(\varepsilon_{12} - \chi_{12})\right) = R_0 + Hp = R_0 + \frac{2H}{\sqrt{3}}\varepsilon^p_{12} \tag{3.91}$$

By substituting the expression of ε_{12} obtained from Eq. (3.91) and (3.90), the differential equation governing χ_{12} is given by

$$\chi_{12,11} - \frac{2\mu H H_\chi}{A\left(H_\chi(3\mu + H) + 2\mu H\right)}\chi_{12} + \frac{H_\chi\left((3\mu + H)\tau - \sqrt{3}\mu R_0\right)}{A\left(H_\chi(3\mu + H) + 2\mu H\right)} = 0 \tag{3.92}$$

The solution of this equation is obtained for three different cases:

Case 1: perfect plasticity (H = 0) Eq. (3.92) reduces to

$$\chi_{12,11} + \frac{\tau - R_0/\sqrt{3}}{A} = 0 \tag{3.93}$$

By solving the differential equation in Eq. (3.93), we get

$$\chi_{12}(x) = -\frac{\tau - R_0/\sqrt{3}}{2A}x^2 + C_1 x + C_2 \tag{3.94}$$

where C_1 and C_2 are integration constants to be determined from boundary conditions:

$$\chi_{12}(x = \pm h) = 0 \implies C_1 = 0 \quad \text{and} \quad C_2 = \frac{\tau - R_0/\sqrt{3}}{2A}h^2 \tag{3.95}$$

It follows that

$$\chi_{12}(x) = -\frac{\tau - R_0/\sqrt{3}}{2A}(x^2 - h^2) \tag{3.96}$$

$$\varepsilon_{12}(x) = \chi_{12}(x) + \frac{\tau - R_0/\sqrt{3}}{H_\chi} \tag{3.97}$$

Finally, using

$$\frac{1}{2h}\int_{-h}^{h} \varepsilon_{12}(x)\,dx = \frac{\bar{\gamma}}{2} = \frac{1}{2h}\int_{-h}^{h} \chi_{12}(x)dx + \frac{\tau - R_0/\sqrt{3}}{H_\chi} \tag{3.98}$$

we get

$$\tau = \frac{\bar{\gamma}}{Z_h} + \frac{R_0}{\sqrt{3}}, \qquad \text{with} \quad Z_h = \frac{2}{H_\chi} + \frac{2h^2}{3A} \tag{3.99}$$

Before yielding, the shear stress is given by Eq. (3.82). Fig. 3.3 shows that the numerical solution agrees perfectly with the analytical solution. The gap between ε_{12} and χ_{12} decreases for large values of the penalty parameter H_χ.

Fig. 3.4a depicts the shear stress-strain curves for different values of the parameter A. Several effects of the parameter A on the stress-strain curves are noticed. First, the apparent shear modulus increases with the parameter A. In addition, the plastic yield occurs at $\bar{\gamma} = \bar{\gamma}_{yield}$ which depends on micromorphic parameters (see Fig. 3.4b). The yielding occurs when $\bar{\gamma}$ satisfies both Eq. (3.82) and (3.99) such that

$$\bar{\gamma}_{yield} = \frac{Z_h}{\mu^{app}Z_h - 1}\frac{R_0}{\sqrt{3}} \tag{3.100}$$

When $A \to 0$ or $A \to \infty$, $\bar{\gamma}_{yield} = R_0/(\sqrt{3}\mu)$, which is the classical shear yield strain. The shear yield stress is given by

$$\tau_{yield} = \frac{R_0}{\sqrt{3}}\frac{\mu^{app}Z_h}{\mu^{app}Z_h - 1} \tag{3.101}$$

Indeed, the value $\tau_{yield} = R_0/\sqrt{3}$ for $A = 0$ and tends towards $\dfrac{R_0}{\sqrt{3}}\dfrac{\mu^{app}}{\mu}$ for large values of A. Further, the hardening slope increases with the parameter A, or equivalently for small values of unit cell size h.

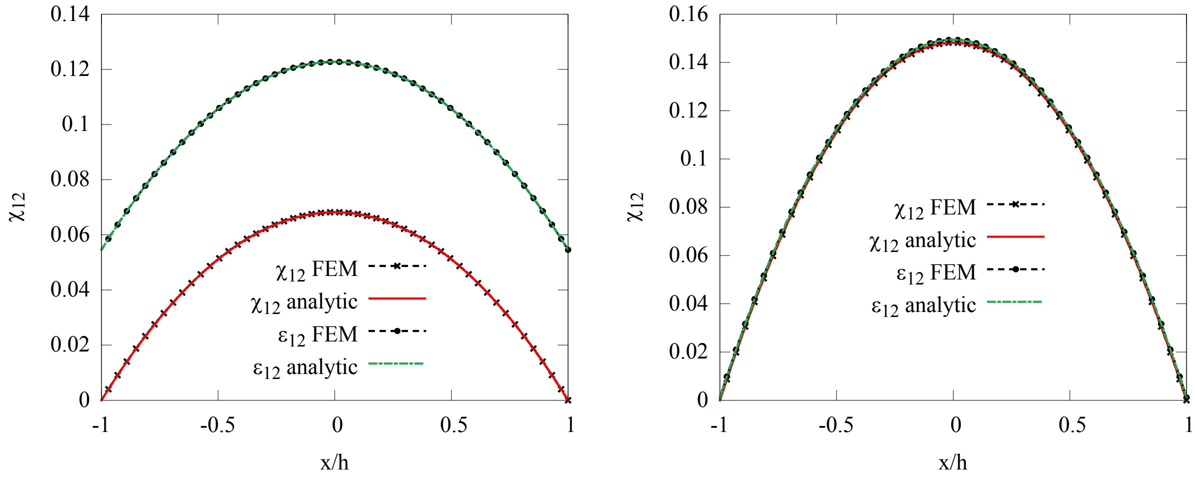

Figure 3.3: *The profiles of* ε_{12} *and* χ_{12} *for (left)* $H_\chi = 10^2$ *MPa (right)* $H_\chi = 10^4$ *MPa for simple glide loading. Material parameters* $R_0 = 100$ *MPa,* $\mu = 30000$ *MPa,* $H = 0$ *MPa,* $A = 1000$ *N (total strain-based model).*

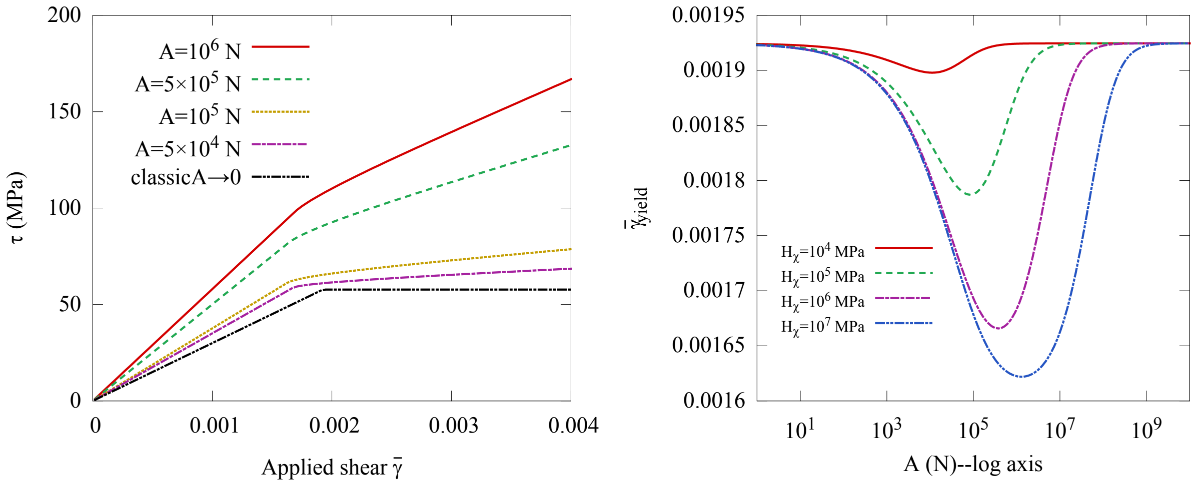

(a) *Shear stress vs. applied shear curves for different value of the parameter A* ($H_\chi = 10^5$ *MPa*)

(b) *The evolution of* $\bar{\gamma}_{yield}$ *for different values of parameters A and* H_χ

Figure 3.4: *Simple glide loading. Material parameters* $R_0 = 100$ *MPa,* $\mu = 30000$ *MPa,* $H = 0$ *MPa (total strain-based model).*

Case 2: Hardening (H > 0) The solution of Eq. (3.92) is given by

$$\chi_{12}(x) = C_1 \cosh(\omega_1 x) + C_2 \sinh(\omega_1 x) + \frac{(3\mu + H)\tau - \sqrt{3}\mu R_0}{2\mu H} \tag{3.102}$$

where C_1 and C_2 are integration constants and

$$\omega_1^2 = \frac{2\mu H H_\chi}{A\left(H_\chi(3\mu + H) + 2\mu H\right)} \tag{3.103}$$

By applying the boundary conditions, one gets

$$\chi_{12}(x \pm h) = 0 \implies C_1 = \frac{\sqrt{3}\mu R_0 - (3\mu + H)\tau}{2\mu H \cosh(\omega_1 h)} \quad \text{and} \quad C_2 = 0 \tag{3.104}$$

Therefore, the solution of Eq. (3.102) is

$$\chi_{12}(x) = \frac{(3\mu + H)\tau - \sqrt{3}\mu R_0}{2\mu H} \left(1 - \frac{\cosh(\omega_1 x)}{\cosh(\omega_1 h)}\right) \tag{3.105}$$

The shear strain component ε_{12} is obtained from Eq. (3.86) as

$$\varepsilon_{12}(x) = \frac{(3\mu + H)\tau - \sqrt{3}\mu R_0}{2\mu H} \left(1 - \frac{(3\mu + H)H_\chi}{(3\mu + H)H_\chi + 2\mu H} \frac{\cosh(\omega_1 x)}{\cosh(\omega_1 h)}\right) \tag{3.106}$$

When $H_\chi \to \infty$, χ_{12} and ε_{12} fields are identical. The value of uniform shear stress τ is obtained through Eq. (3.98) as

$$\tau = \frac{\bar{\gamma}\mu H}{(3\mu + H)\left(1 - \dfrac{(3\mu + H)H_\chi}{(3\mu + H)H_\chi + 2\mu H} \dfrac{\tanh(\omega_1 h)}{\omega_1 h}\right)} + \frac{\sqrt{3}\mu R_0}{3\mu + H} \tag{3.107}$$

The limit case of strain gradient plasticity, *i.e.* $H_\chi \to \infty$ leads to $\omega_1 \to \sqrt{\dfrac{2\mu H}{A(3\mu+H)}}$ and

$$\tau = \frac{\bar{\gamma}\mu H}{(3\mu+H)\left(1-\dfrac{\tanh(\omega_1 h)}{\omega_1 h}\right)} + \frac{\sqrt{3}\mu R_0}{3\mu+H} = H^{app}\bar{\gamma} + \frac{\sqrt{3}\mu R_0}{3\mu+H} \tag{3.108}$$

where $H^{app} = \dfrac{\mu H}{(3\mu+H)\left(1-\dfrac{\tanh(\omega_1 h)}{\omega_1 h}\right)}$ is the effective hardening modulus. Fig. 3.5 illustrates the profile of χ_{12} for various values of the parameter A. In fact, the boundary layer thickness, which is related to the characteristic length $1/\omega_1$, increases with the parameter A.

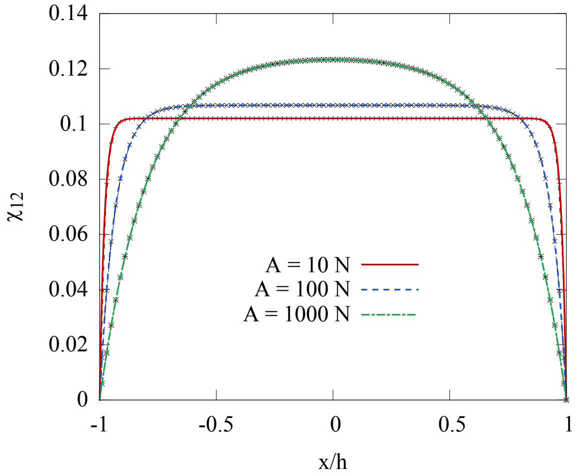

Figure 3.5: *The profile of χ_{12} for several values of A. Dashed black lines with crosses correspond to FEM solutions. $R_0 = 100$ MPa, $H = 1500$ MPa, $H_\chi = 10^5$ MPa, and $h = 5$ mm.*

Case 3: Softening (H < 0) The plastic strain is assumed to not reach the edges of the strip. Therefore, the analytical solution is given for elastic and plastic zones, delimited by $\pm x_c$ are

- In the plastic region ($|x| \le x_c$), the solution of Eq. (3.92) is

$$\chi_{12}(x) = C_1 \cos(\omega_1 x) + \frac{(3\mu+H)\tau - \sqrt{3}\mu R_0}{2\mu H} \tag{3.109}$$

  where

$$\omega_1^2 = \frac{2\mu|H|H_\chi}{A\left(H_\chi(3\mu+H)+2\mu H\right)}, \qquad \text{with} \quad H_\chi(3\mu+H)+2\mu H > 0 \tag{3.110}$$

  and

$$\varepsilon_{12}(x) = C_1 \frac{(3\mu+H)H_\chi}{(3\mu+H)H_\chi+2\mu H}\cos(\omega_1 x) + \frac{(3\mu+H)\tau - \sqrt{3}\mu R_0}{2\mu H} \tag{3.111}$$

$$\varepsilon^p_{12}(x) = C_1 \frac{3\mu H_\chi}{(3\mu+H)H_\chi+2\mu H}\cos(\omega_1 x) + \frac{3\tau - \sqrt{3}R_0}{2H} \tag{3.112}$$

- In the elastic region, the differential equation governing the evolution of χ_{12} is given by

$$\Delta\chi_{12} - \frac{2\mu H_\chi}{A(2\mu+H_\chi)}\chi_{12} + \frac{H_\chi}{A(2\mu+H_\chi)}\tau = 0 \tag{3.113}$$

Its solution is given by

$$\chi_{12}(x) = \begin{cases} C_2 \cosh\left(\omega_2(h-x)\right) + \dfrac{\tau}{2\mu}, & x_c \le x \le h \\ C_2 \cosh\left(\omega_2(h+x)\right) + \dfrac{\tau}{2\mu}, & -h \le x \le -x_c \end{cases} \tag{3.114}$$

and

$$\varepsilon_{12}(x) = C_2 \frac{H_\chi}{2\mu + H_\chi} \cosh\left(\omega_2(h-x)\right) + \frac{\tau}{2\mu} \tag{3.115}$$

where $\omega_2^2 = \dfrac{2\mu H_\chi}{A(2\mu + H_\chi)}$.

After considering the continuity of χ_{12} and of the generalized stress component b_{121} at the elastic/plastic zone boundary, x_c is, therefore, the zero of the function

$$f(y) = \tanh(\omega_2(h-y)) - \frac{\omega_1}{\omega_2} \frac{(3\mu + H)H_\chi + 2\mu H}{H(2\mu + H_\chi)} \tan(\omega_1 y) \tag{3.116}$$

The integration constants C_1 and C_2 are obtained as

$$C_1 = \frac{H_\chi(3\mu + H) + 2\mu H}{\cos(\omega_1 x_c)} \frac{\sqrt{3}R_0 - 3\tau}{6\mu H H_\chi} \tag{3.117}$$

$$C_2 = C_1 \frac{\omega_1 \sin(\omega_1 x_c)}{\omega_2 \sinh(\omega_2(h - x_c))} = \frac{(2\mu + H_\chi)(R_0/\sqrt{3} - \tau)}{2\mu H_\chi \cosh(\omega_2(h - x_c))} \tag{3.118}$$

The shear stress is obtained

$$\tau = \frac{\overline{\gamma} + R_0 Z_s}{1/\mu + \sqrt{3} Z_s} \tag{3.119}$$

with $Z_s = \dfrac{\sqrt{3}}{hH}\left(x_c - \dfrac{\tan(\omega_1 x_c)}{\omega_1}\right)$.

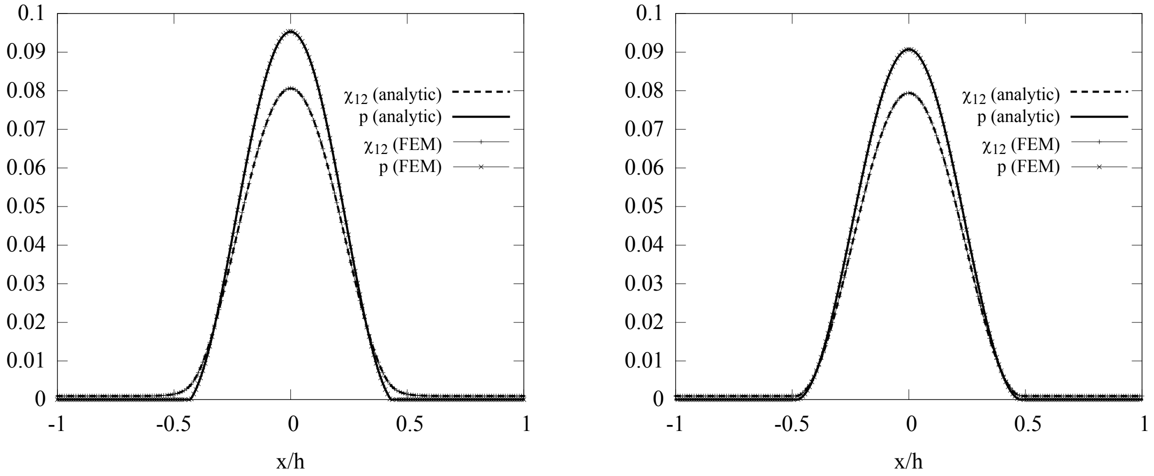

Figure 3.6: *The profiles of χ_{12} and the cumulative plastic strain for (left) $H_\chi = 10^3$ MPa, $x_c = 2.158$ (right) $H_\chi = 10^5$ MPa, $x_c = 2.379$. $R_0 = 100$ MPa, $H = -100$ MPa, $A = 40$ N, $h = 5$ mm. Applied shear $\overline{\gamma} = 0.04$ (total strain-based model).*

Fig. 3.6 depicts the profile of the micromorphic variable and the cumulative plastic strain for two values of the parameter H_χ and for the first root of Eq. (3.116). It shows that the analytical solutions agree perfectly with the FEM solution. The Equation (3.116) admits several solutions. Nevertheless, the obtained solutions are not admissible (except one) since the obtained value of the cumulative plastic strain is negative in some regions. Notice that the value of χ_{12} (or ε_{12}) is higher than the plastic strain by a value of $\tau/2\mu$ in the elastic region as shown in Eq. (3.115).

3.6.2 Simple glide: plastic strain-based model

Now, the response of the model with a micromorphic variable associated with the plastic strain tensor is investigated. The analytical solutions are derived for the simple glide problem and compared to other micromorphic models. Following the same reasoning, the following differential equation governing the evolution of the component χ^p_{12} is obtained:

$$\chi^p_{12,11} - \frac{2HH_\chi}{A(2H+3H_\chi)}\chi^p_{12} + \frac{H_\chi(3\tau-\sqrt{3}R_0)}{A(2H+3H_\chi)} = 0 \tag{3.120}$$

The solution of the previous equation is obtained for three different cases: perfect plasticity, linear hardening, and linear softening.

Case 1: Perfect plasticity ($H = 0$) The differential equation (3.120) reduces to

$$\chi^p_{12,11} + \frac{\tau - R_0/\sqrt{3}}{A} = 0 \tag{3.121}$$

This differential equation is similar to Eq. (3.93). Solving Eq. (3.121) gives

$$\chi^p_{12}(x) = -\frac{\tau - R_0/\sqrt{3}}{2A}(x^2-h^2) \tag{3.122}$$

The plastic strain is obtained from the second balance equation as

$$\varepsilon^p_{12}(x) = \chi^p_{12}(x) + \frac{\tau - R_0/\sqrt{3}}{H_\chi} \tag{3.123}$$

The shear stress τ is given by

$$\begin{aligned}\tau = \frac{\mu}{h}\int_{-h}^{h}\left(\varepsilon_{12}(x) - \varepsilon^p_{12}(x)\right)dx = \mu\bar{\gamma} - 2\mu\frac{\tau - R_0/\sqrt{3}}{H_\chi} - \frac{\mu}{h}\int_{-h}^{h}\chi^p_{12}(x)dx \\ = \frac{\bar{\gamma} + \dfrac{R_0}{\sqrt{3}}Z^p_0}{1/\mu + Z^p_0}\end{aligned} \tag{3.124}$$

with $Z^p_0 = \dfrac{2}{H_\chi} + \dfrac{2h^2}{3A}$. When H_χ tends to larger values, the previous equation reduces to

$$\tau = \frac{\mu}{\dfrac{3}{2}A + \mu h^2}\left(\frac{3}{2}A\bar{\gamma} + R_0h^2/\sqrt{3}\right) \tag{3.125}$$

which is the strain gradient plasticity limit. The apparent hardening modulus depends on the parameter A and the size of the strip. Using the same material parameters, the value of shear stress obtained for this model is larger than the value of shear stress given by the model relying on cumulative plastic strain in Eq. (2.87). An equivalence between these two models is obtained if the parameter A in the plastic strain tensor based model is divided by a factor of $2/3$.

Case 2: Hardening ($H > 0$) Applying boundary conditions $\chi_{12}(x = \pm h) = 0$, the solution of Eq. (3.120) is given by

$$\chi^p_{12}(x) = \frac{3\tau - \sqrt{3}R_0}{2H}\left(1 - \frac{\cosh(\omega_1 x)}{\cosh(\omega_1 h)}\right) \tag{3.126}$$

where $\omega_1^2 = \dfrac{2HH_\chi}{A(2H+3H_\chi)}$. The plastic strain is obtained from the second balance equation as

$$\varepsilon^p_{12}(x) = \frac{3\tau - \sqrt{3}R_0}{2H}\left(1 - \frac{3H_\chi}{2H+3H_\chi}\frac{\cosh(\omega_1 x)}{\cosh(\omega_1 h)}\right) \tag{3.127}$$

The shear stress is obtained as

$$\tau = \frac{\bar{\gamma} + R_0 Z^p_h}{\dfrac{1}{\mu} + \sqrt{3}Z^p_h} \tag{3.128}$$

where $Z^p_h = \dfrac{\sqrt{3}}{H}\left(1 - \sqrt{\dfrac{9AH_\chi}{2H(2H+3H_\chi)}}\dfrac{\tanh(\omega_1 h)}{h}\right)$. For the same material parameters, the value of shear stress given by this model is higher than the one induced by the model based on cumulative plastic strain. For $H_\chi \to \infty$, the equivalence between both models is obtained if the parameter A in this model is divided by a factor of $2/3$ (see Eq. (2.93)).

Case 3: Softening ($H < 0$) We assume that the plastic strain does not reach the edges of the strip. Therefore, the solution to the problem is given for elastic and plastic zones separately, that is

- Plastic zone ($|x| \leq x_c$): the solution of Eq. (3.120) is

  $$\chi^p_{12}(x) = C_1\cos(\omega_1 x) + \frac{3\tau - \sqrt{3}R_0}{2H} \tag{3.129}$$

  The plastic strain is obtained from the second balance equation as

  $$\varepsilon^p_{12}(x) = C_1\frac{3H_\chi}{2H+3H_\chi}\cos(\omega_1 x) + \frac{3\tau - \sqrt{3}R_0}{2H} \tag{3.130}$$

  where $\omega_1 = \sqrt{\dfrac{2|H|H_\chi}{A(2H+3H_\chi)}}$. The assumption $2H + 3H_\chi > 0$ is made.

- Elastic zone: the plastic strain vanishes and

  $$\begin{cases} \chi^p_{12}(x) &= C_2\cosh(\omega_2(h-x)) \qquad x_c \leq x \leq h \\ \chi^p_{12}(x) &= C_2\cosh(\omega_2(h+x)) \qquad -h \leq x \leq -x_c \end{cases} \tag{3.131}$$

  where $\omega_2 = \sqrt{\dfrac{H_\chi}{A}}$.

Recall that χ_{12} and the generalized stress $b_{121} = A\chi^p_{12,1}$ are continuous at $x = x_c$. Therefore, from Eq. (3.129), (3.130) and (3.131), the position x_c is obtained as the zero of the following function

$$f(y) = \tanh(\omega_2(h-y)) - \frac{\omega_1}{\omega_2}\frac{2H+3H_\chi}{2H}\tan(\omega_1 y) \tag{3.132}$$

After finding the roots of the previous equation, the integration constants are readily obtained

$$C_1 = \frac{(\sqrt{3}R_0 - 3\tau)(2H + 3H_\chi)}{6HH_\chi \cos(\omega_1 x_c)}, \qquad C_2 = C_1 \frac{\omega_1 \sin(\omega_1 x_c)}{\omega_2 \sinh(\omega_2(h - x_c))} = \frac{\sqrt{3}R_0 - 3\tau}{3H_\chi \cosh(\omega_2(h - x_c))} \tag{3.133}$$

The shear stress follows as

$$\begin{aligned} \tau &= \mu\bar{\gamma} - \frac{\mu}{h}\int_{-x_c}^{x_c} \varepsilon^p_{12}(x)dx \\ &= \frac{\bar{\gamma} + R_0 Z^p_s}{1/\mu + \sqrt{3}Z^p_s} \end{aligned} \tag{3.134}$$

where $Z^p_s = \dfrac{\sqrt{3}}{Hh}\left(x_c - \dfrac{\tan(\omega_1 x_c)}{\omega_1}\right)$. Fig. 3.7 depicts the profiles of localized cumulative plastic strain and the micromorphic variable. For small values of the penalty parameter H_χ, the characteristic length gets smaller. By increasing H_χ, the plastic ε^p_{12} and the micromorphic χ^p_{12} variables coincide. The resulting cumulative plastic strain profile is obtained as $p = 2/\sqrt{3}\varepsilon^p_{12}$.

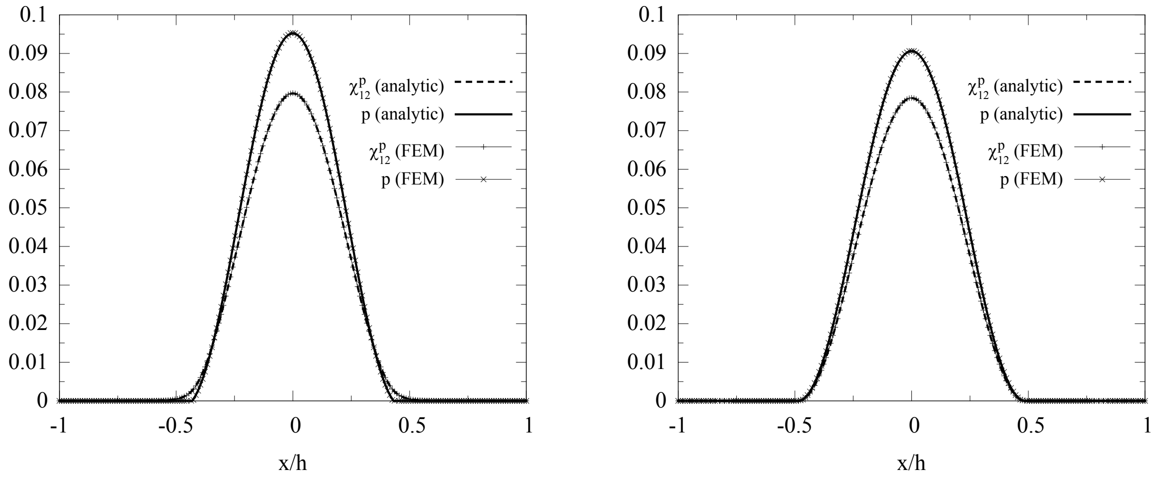

Figure 3.7: *The localization band for (left)* $H_\chi = 10^3$ *MPa, the solution is obtained for the first root of Eq. (3.132)* $x_c = 2.155$ *(right)* $H_\chi = 10^5$ *MPa,* $x_c = 2.412$ *. Material parameters* $R_0 = 100$ *MPa,* $H = -100$ *MPa. Applied shear* $\bar{\gamma} = 0.04$, $h = 5$ *mm (plastic strain-based model).*

Discussion

Table 3.1 summarizes the characteristic length suggested by each model. These are obtained for the simple glide problem with a linear hardening law.

		cumulative plastic strain	total strain tensor	plastic strain tensor
Characteristic length l_c^2	$H = 0$	$\dfrac{A}{H_\chi}$	$\dfrac{A(2\mu + H_\chi)}{2\mu H_\chi}$	$\dfrac{A}{H_\chi}$
	$H \neq 0$	$\dfrac{A(H + H_\chi)}{\lvert H\rvert H_\chi}$	$\dfrac{A\left(H_\chi(3\mu + H) + 2\mu H\right)}{2\mu \lvert H\rvert H_\chi}$	$\dfrac{A(2H + 3H_\chi)}{2\lvert H\rvert H_\chi}$

Table 3.1: *The characteristic length provided by each model and the apparent hardening modulus in the case of simple glide with linear hardening/softening law.*

Remark 4. *The characteristic length scales depend on constitutive equations, geometry, and loading. They emerge from the Helmholtz regularization operators obtained for each problem. The length scales delivered* *throughout this document are given for some simple loading cases. The suggested constitutive models are derived for quadratic free energy potentials.*

The present total and plastic strain-based models exhibit also a broadening of the localization bandwidth for saturating hardening variables, *e.g.* $R(p) = Q(1-e^{-cp})$ where Q is the softening modulus and c is a material parameter that steers the saturation of the softening law (see Fig. 3.8).

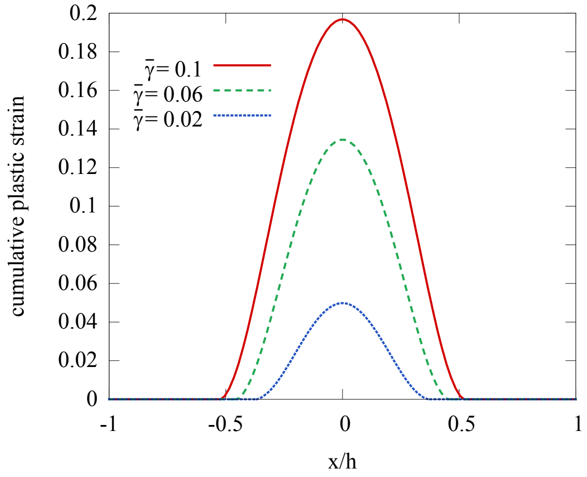

Figure 3.8: *The broadening of the localization band for an exponential softening. Material parameters* $Q = -100$ *MPa,* $c = 10$*,* $R_0 = 100$ *MPa (total strain-based model).*

At this point, it can be seen that the models based on strain tensors are capable of modeling size effects and to regularize constitutive models. Meanwhile, the computational cost of the tensorial models remains a drawback.

3.6.3 Bending

In section 2.4.1, the bending of a 2D foil of thickness $2w$ under plane strain conditions was studied at finite strains. The same problem is revisited using tensorial micromorphic variables but only at small strains. The loading is monitored by the curvature $\kappa = \varepsilon_{11}(y=w)/w$.

Fig. 3.9 shows the bending moment vs. curvature curves for several micromorphic models. The model based on cumulative plastic strain diverges when the radius σ_Y is to become negative. Contrarily, models based on total and plastic strain do not diverge since the micromorphic contribution is a back stress that can take theoretically any value. Furthermore, the hardening induced by the plastic strain-based model is higher than the one obtained with the model relying on the cumulative plastic strain since the generalized moduli in each model have different physical meanings. The model with total strain induces a slightly higher hardening compared to the plastic strain-based model. This difference can be larger if the elastic strain is significantly higher.

Fig. 3.10 depicts the distribution of micromorphic variable $\underset{\sim}{\chi}^p$ and its gradient $\underset{\approx}{k}$ along the cross-section $x = 0$. The gradient of χ^p_{11} and χ^p_{22} vanishes at $y = \pm w$ since it is a traction-free surface. The profiles of the back stress components shows that a gap between the micromorphic variable and the plastic strain occurs near the outer surface $y \pm w$ and also near the neutral axis. It exhibits some kinks near the neutral axis but is still continuous contrary to the model based on equivalent plastic strain shown in section 2.2.5.

3.6.4 Torsion

The torsion of a cylinder bar of radius r and length L is considered for different micromorphic models. A cyclic twist of ±20 degrees is applied on the top surface ($z = L$) while the bottom surface is clamped. The lateral surfaces are traction-free. We consider a von Mises time-independent perfectly plastic model. The

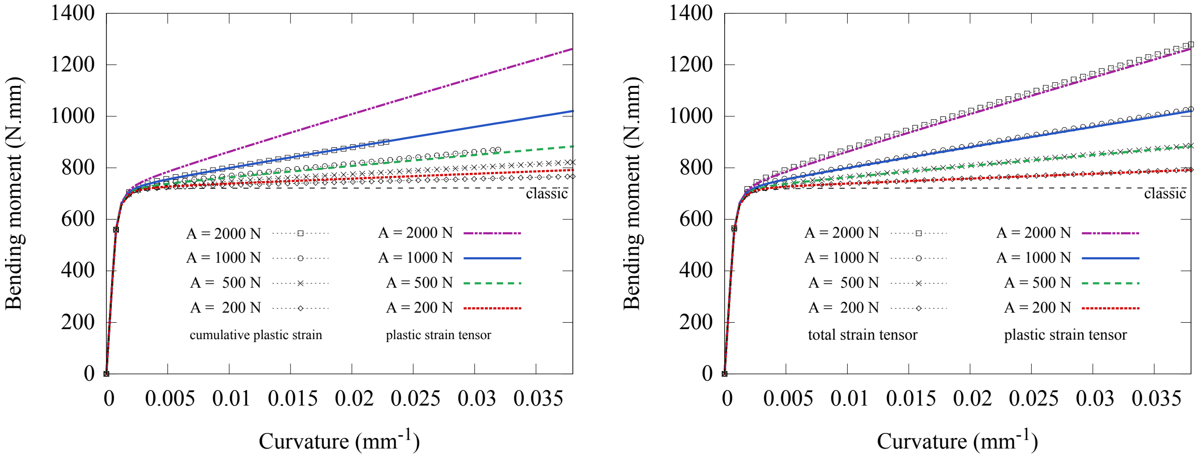

(a)

(b)

Figure 3.9: *Comparison of bending moment vs. applied curvature curves obtained for three micromorphic models using cumulative plastic strain, total strain, and plastic strain tensors. Material parameters:* $R_0 = 100$ *MPa,* $H = 0$ *MPa,* $H_\chi = 10^4$ *MPa.*

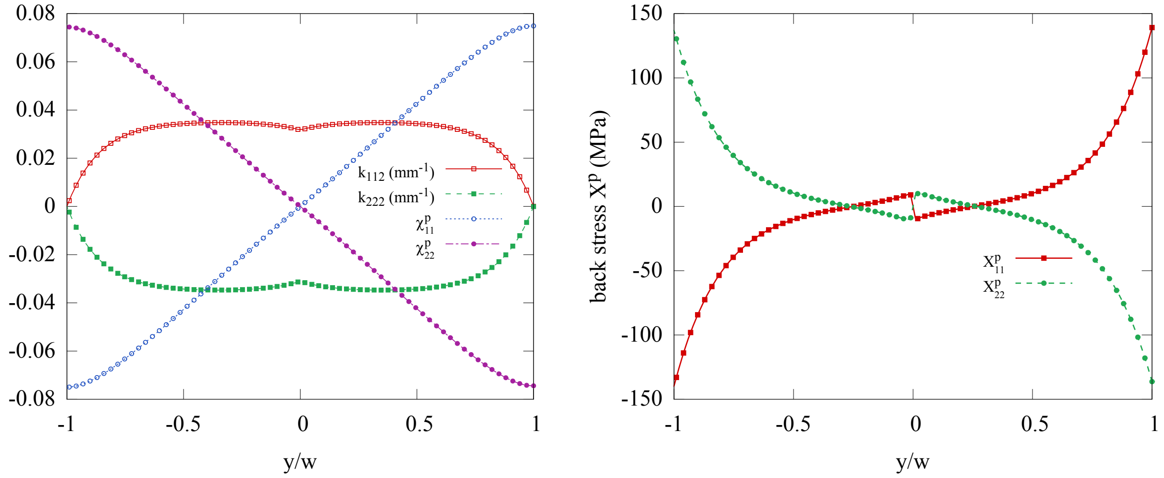

Figure 3.10: *(a) The profiles of the micromorphic variable and its gradient. (b) The back stress is proportional to the difference between the plastic strain and the micromorphic variable.*

FE mesh contains 2160 quadratic elements with reduced integration (C3D20R) and 10355 nodes. The total number of degrees of freedom is 41420 and 93195 for scalar and tensorial models, respectively. Fig. 3.11 depicts the torque-twist curves obtained for different micromorphic models for the same material parameters. The model with cumulative plastic strain induces an isotropic hardening. During the second cycle, the latter model diverges since the radius of elasticity domain vanishes and tends to negative values. In contrast, the tensorial models produce kinematic hardening. The amplitude of the hardening induced by tensorial models is higher since the micromorphic parameters have different meanings.

3.7 Conclusion

The major outcomes of this chapter are:

- Two microstrain models relying on second-order symmetric tensors are presented. They respectively rely on total and plastic strain tensors. They give similar results if the elastic strain is negligible. The

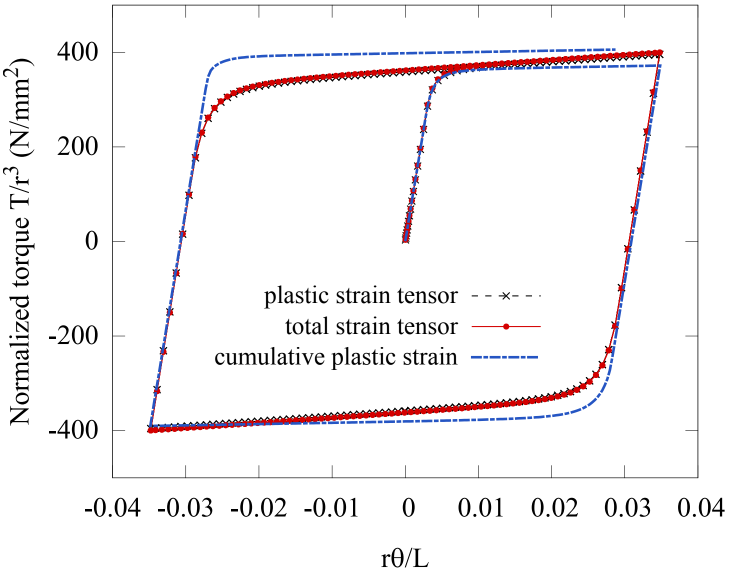

Figure 3.11: *The normalized torque vs surface strain* $r\theta/L$ *for various micromorphic models. Material parameters:* $R_0 = 300$ *MPa,* $H = 0$ *MPa,* $A = 200$ *N,* $H_\chi = 10^4$ *MPa. Geometry:* $r = 1$ *mm and* $L = 10$ *mm.*

first model modifies the elasticity law in addition to the kinematic hardening contribution whereas the second one induces only a supplementary kinematic hardening. The first model predicts size effect in the elastic domain in contrast to the second one.

- The extension of these models to finite strain is presented. Note that many formulations are possible depending on the plastic/total strain measure.

- Models based on strain tensors lead to size-dependent kinematic hardening which solves the non-physical response related to the negative radius of the elasticity domain observed for the model relying on the cumulative plastic strain. This is due to the fact that the kinematic hardening can take theoretically any value.

- The tensorial micromorphic models are shown to be able to regularize elastoplastic constitutive models. For saturating hardening laws, the broadening of the localization band is noticed.

- Tensorial micromorphic models have no downsides at least theoretically. Meanwhile, the number of degrees of freedom is increased threefold compared to the classical model which is a limitation to extensive use for industrial applications.

Throughout this chapter, we assumed that the generalized moduli involved in constitutive laws, for the sake of illustration, are taken as $\underset{\approx}{\boldsymbol{A}} = A\underset{\approx}{\mathbf{1}}$ and $\underset{\approx}{\boldsymbol{H}}_\chi = H_\chi\underset{\approx}{\mathbf{1}}$. In strain gradient elasticity, several works address the representation of the sixth order tensor $\underset{\approx}{\boldsymbol{A}}$ [Mindlin, 1964; Auffray et al., 2009]. These moduli can be determined using homogenization schemes [Auffray et al., 2010; Fergoug et al., 2022]. Meanwhile, to the best of our knowledge, the determination of such moduli in case of plasticity is not addressed yet by the community. The question of how to determine all the material parameters involved in such models from experiments remains relevant.

The issue of localization bands broadening was raised by Scherer et al. [2020]. A solution was proposed therein by assuming that generalized parameters can depend on the plastic strain. Alternatively, the use of proper micromorphic saturating variables will solve this issue as studied in section 4.1.

Chapter 4

Applications

Abstract

This chapter addresses the enhancement of other types of classical models using the micromorphic approach. In particular, two models based on the micromorphic variable associated to the internal variable describing saturating isotropic hardening are presented. The first model induces a size effect that saturates with the cumulative plastic strain while the second one induces a size effect that decreases when the micromorphic variable saturates. These two models allow us to solve the problem of localization band broadening. In addition, the Kocks-Mecking model based on the evolution of the dislocation density is studied. The enhancement of this model with a micromorphic variable associated to the dislocation density introduces a size effect but does not regularize the strain localization in case of softening described by a decreasing dislocation density. An alternative has been proposed based on the cumulative plastic strain.

The micromorphic approach is finally used to model the behavior of a unidirectional fibre-reinforced polymer-matrix composite. This application combines both the modeling of size effects induced by the material microstructure and the localization of the plastic deformation due to the softening exhibited by the matrix. First, a hyperelastoplastic model from the literature has been used to simulate the necking phenomena in a plate under tension. Indeed, the micromorphic model allows to regularize the front of the band throughout the neck propagation. Then, the effect of the volume fraction and the characteristic length scale were studied through the consideration of a composite Representative Volume Element subjected to tension with a single inclusion. Finally, the characteristic length is identified from stress-strain curves for a transverse compression test.

Résumé

Ce chapitre traite l'application de l'approche micromorphe pour enrichir d'autres types de modèles classiques. En particulier, nous proposons deux modèles reposant sur le choix d'une variable micromorphe associée à la variable interne d'écrouissage isotrope saturant. Ils permettent d'obtenir un effet d'échelle qui évolue avec l'histoire du matériau. Le premier modèle induit un effet d'échelle qui sature avec la déformation plastique cumulée tandis que le deuxième entraîne un effet d'échelle qui diminue lorsque la variable micromorphe sature. Ces deux modèles permettent de résoudre le problème de l'élargissement des bandes de localisation. En outre, nous traitons également le cas du modèle de Kocks-Mecking basé sur l'évolution de la densité de dislocation. L'enrichissement de ce modèle avec une variable micromorphe associé à la densité de dislocation introduit un effet d'échelle mais ne permet pas de régulariser la localisation pour un cas adoucissant caractérisé par la diminution de la densité de dislocations. Une alternative est proposée en se basant sur la déformation plastique cumulée.

L'approche micromorphe a été également utilisé pour modéliser le comportement d'un composite à matrice polymère renforcé de fibres unidirectionnelles. Ce cas d'application combine à la fois les effets d'échelle induits par la microstructure du matériau et la localisation de la déformation plastique due au comportement adoucissant de la matrice. Premièrement, un modèle hyperélastoplastique issu de la littérature a été utilisé pour la simulation de la propagation de la striction dans une plaque en traction. En effet, le modèle micromorphe permet de régulariser le front de la bande. Ensuite, l'effet de la fraction volumique et la longueur caractéristique ont été étudiés grâce à un Volume Élémentaire Représentatif d'un composite soumis à une traction avec une seule inclusion. Finalement, la longueur caractéristique est identifiée sur les courbes de contraintes-déformations issues d'un essai de compression transverse.

Contents

4.1 Gradient of saturating variables

The constitutive modelling of plasticity, damage, diffusion, etc. involves bounded or saturating internal variables. For instance, the damage quantity, the dislocation density, the concentration of a chemical element, etc. are frequently used. Local models accommodating such variables relying on the classical framework of continuum mechanics are well established. Meanwhile, the absence of internal length scales makes such formulations not suitable to model size effects or to simulate mesh-objective localization phenomena. In the following non-exhaustive list, theories involving bounded variables and their gradient enhancement are summarized:

- The diffusion of chemical elements is usually modelled by means of the Cahn–Hilliard model. An enhanced Cahn–Hilliard model was proposed by Ubachs et al. [2004]. A micromorphic version of this model, called microdiffusion, was proposed in [Forest et al., 2011] and compared to phase field methods that are widely used for damage, fracture, and diffusion phenomena.
- The damage theory in the framework of classical continuum (see *e.g.* Lemaitre and Chaboche [1994]) is widely accepted. Several theories of damage gradient have been proposed, see *e.g.* Frémond and Nedjar [1996]; Peerlings et al. [1996]. A microdamage model was elaborated in Forest [2009].
- For several materials, the mechanical state is described by the density of dislocations. The presence of geometrically necessary dislocations induced by strong strain gradients gives rise to size effects in the form of higher yield stress and hardening [Fleck and Hutchinson, 1993]. The widely used evolution equation for dislocation density is the Kocks-Mecking model [Mecking and Kocks, 1981]. The original model is modified and tailored to describe the dislocation motion, interactions between different types of dislocations, annihilation, etc. According to crystal plasticity theory, a dislocation density is associated with each slip system. Some theories directly involve the dislocation density tensor which characterizes the incompatibility of plastic deformation. Several enhanced models have been proposed using: strain gradient theories involving either the rotational part of plastic deformation or its full gradient and the micromorphic approach accounting for rotation or full deformation of a triad of crystal directors [Cordero et al., 2010; Ling et al., 2018], etc.

In this section, an alternative class of micromorphic models for elastoplasticity based on saturating variables is proposed. First, a model based on the internal variable related to exponential isotropic hardening is detailed. Analytical solutions are given for the simple glide problem. A generalization to any hardening law is proposed. Next, two enhanced versions of the Kocks-Mecking model are presented. The main features of these models are shown in the small strain framework. The regularization properties of such models are discussed. The extension to finite strain can be readily achieved following the model formulation detailed in 2.2.1.

4.1.1 A model with a saturating micromorphic variable

Consider an internal variable whose evolution equation is given by

$$\dot{r} = (1 - kr)\dot{p} \tag{4.1}$$

where k is a material parameter and $\dot{p}$ is the usual plastic multiplier. By integrating Eq. (4.1), it follows that

$$r = \frac{1 - (1 - kr_0)e^{-kp}}{k} \tag{4.2}$$

where $r_0 = r(p = 0)$ is the initial value of r. The variable r saturates for increasing p towards the limit $1/k$.

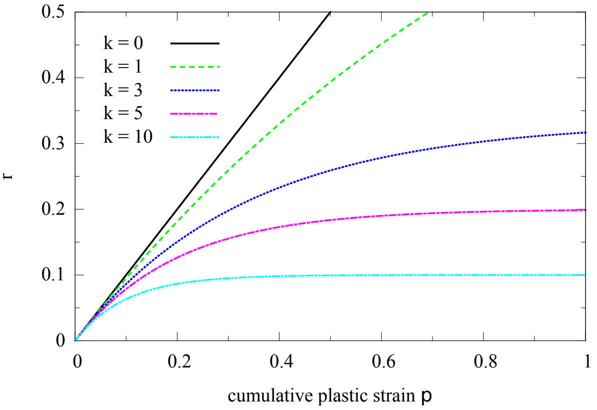

Figure 4.1: *The evolution of the variable r as a function of cumulative plastic strain for several values of the parameter k. The initial value* $r_0 = 0$.

The micromorphic variable, denoted by r_χ, is associated with the variable r. The free energy in terms of elastic deformation $\underset{\sim}{\varepsilon}^e$, internal variables α_I, r, r_χ and ∇r_χ is postulated as

$$\psi(\underset{\sim}{\varepsilon}^e, \alpha_I, r, r_\chi, \nabla r_\chi) = \psi^e(\varepsilon^e) + \frac{1}{2}cQr^2 + \frac{1}{2}H_\chi(r - r_\chi)^2 + \frac{1}{2}\nabla r_\chi \cdot \underset{\sim}{\boldsymbol{A}} \cdot \nabla r_\chi \tag{4.3}$$

where c and Q are material parameters. In case of choosing a micromorphic variable associated with the variable $\phi = kr \in [0,1]$ such that $r_0 = 0$, taking $(\phi - \phi_\chi)$ and $\nabla\phi_\chi$ is equivalent by modifying suitably the constants H_χ and $\underset{\sim}{\boldsymbol{A}}$. The model becomes then similar to the microdamage model [Forest, 2009] in which the variable ϕ is associated with the damage variable. The power of internal forces is defined by

$$\mathscr{P}^{(i)} = \underset{\sim}{\sigma} : \dot{\underset{\sim}{\varepsilon}} + a\dot{r}_\chi + \underline{\boldsymbol{b}} \cdot \nabla\dot{r}_\chi \tag{4.4}$$

The Clausius-Duhem inequality is given by

$$\mathscr{P}^{(i)} - \rho\dot{\psi} \geq 0 \tag{4.5}$$

so that

$$\left(\underset{\sim}{\sigma} - \rho\frac{\partial\psi}{\partial\underset{\sim}{\varepsilon}^e}\right) : \dot{\underset{\sim}{\varepsilon}}^e + \left(a - \rho\frac{\partial\psi}{\partial r_\chi}\right)\dot{r}_\chi + \left(\underline{\boldsymbol{b}} - \rho\frac{\partial\psi}{\partial\nabla r_\chi}\right) \cdot \nabla\dot{r}_\chi + \underset{\sim}{\sigma} : \dot{\underset{\sim}{\varepsilon}}^p - \rho\frac{\partial\psi}{\partial r}\dot{r} \geq 0 \tag{4.6}$$

Constitutive equations are obtained as follows

$$\underset{\sim}{\sigma} = \rho\frac{\partial\psi}{\partial\underset{\sim}{\varepsilon}^e}, \qquad a = \rho\frac{\partial\psi}{\partial r_\chi}, \qquad \underline{\boldsymbol{b}} = \rho\frac{\partial\psi}{\partial\nabla r_\chi} \tag{4.7}$$

We define the yield condition by

$$f = \sigma_{eq} - R_0 - R(r) \tag{4.8}$$

where

$$R(r) = \rho \frac{\partial \psi}{\partial r} = cQr + H_\chi (r - r_\chi) \tag{4.9}$$

and σ_{eq} is any equivalent stress measure. The intrinsic dissipation rate becomes

$$\underset{\sim}{\sigma} : \dot{\underset{\sim}{\varepsilon}}^p - R\dot{r} \geq 0 \tag{4.10}$$

Therefore, with further simplification we get

$$f(\underset{\sim}{\sigma}, R)\dot{p} + (R_0 + krR)\dot{p} \geq 0 \tag{4.11}$$

In the case of rate-independent plasticity, and following the loading–unloading conditions formalised using the Karush–Kuhn–Tucker conditions: $f \leq 0$, $\dot{p} \geq 0$, $f\dot{p} = 0$, the dissipation rate is then positive if

$$\phi R(r) \geq -R_0 \tag{4.12}$$

with $\phi = kr \in [kr_0, 1]$. The flow rule is written as

$$\dot{\varepsilon}^p = \dot{\lambda} \frac{\partial f}{\partial \underset{\sim}{\sigma}} \tag{4.13}$$

For time-independent, the plastic multiplier is obtained from the consistency condition as

$$\dot{p} = \frac{\left\langle \underset{\sim}{n} : \underset{\approx}{\mathbb{C}} : \dot{\underset{\sim}{\varepsilon}} + H_\chi \dot{r}_\chi \right\rangle}{\underset{\sim}{n} : \underset{\approx}{\mathbb{C}} : \underset{\sim}{n} + (cQ + H_\chi)(1 - kr)} \tag{4.14}$$

Analytical solution for the simple glide test

Consider a periodic and infinite plate (in the y-direction) with an initial width of $2h$ (see Fig. 2.1). The first balance equation yields

$$\sigma_{12,2} = 0 \text{ and } \sigma_{12,1} = 0 \tag{4.15}$$

since σ_{12} is the only non-zero stress component. Therefore, $\sigma_{12} = \tau$ is uniform in the plate. The differential equation governing the micromorphic variable r_χ is obtained from the second balance equation as

$$\Delta r_\chi - \frac{H_\chi}{A}(r_\chi - r) = 0 \tag{4.16}$$

where Δ denotes the Laplacian operator. The yield function is given by

$$f = \sigma_{eq} - \left(R_0 + cQr + H_\chi \left(r - r_\chi\right)\right) = 0 \tag{4.17}$$

with $\sigma_{eq} = \sqrt{3}\,\tau$ is the von Mises equivalent stress. By combining Eqs. (2.77) and (2.78), we get

$$\Delta r_\chi - \frac{cQH_\chi}{A(cQ + H_\chi)} r_\chi + \frac{H_\chi}{A(cQ + H_\chi)}(\sigma_{eq} - R_0) = 0 \tag{4.18}$$

Three cases can be distinguished depending on the sign of the modulus Q: perfect plasticity ($Q = 0$), hardening ($Q > 0$), and softening ($Q < 0$).

Case 1: perfect plasticity ($Q = 0$) In this case, the equation (4.18) reduces to

$$\Delta r_\chi + \frac{1}{A}(\sigma_{eq} - R_0) = 0 \tag{4.19}$$

The boundary condition $r_\chi = 0$ is prescribed at $x = \pm h$. By solving the differential equation in Eq. (4.19), we get

$$r_\chi(x) = -\frac{\sqrt{3}\tau - R_0}{2A}(x^2 - h^2) \tag{4.20}$$

and

$$r(x) = r_\chi(x) + \frac{\sqrt{3}\tau - R_0}{H_\chi} \tag{4.21}$$

Therefore, assuming that $r_0 = 0$, the expression of the cumulative plastic strain is given by

$$p(x) = -\frac{\log(1 - k\,r(x))}{k} \tag{4.22}$$

where $\log(\cdot)$ denotes the natural logarithm. The analytical expression of the shear stress τ is

$$\tau = 2\mu\varepsilon^e_{12} = \frac{\mu}{h}\int_{-h}^{h}(\varepsilon_{12} - \varepsilon^p_{12})dx = \mu\bar{\gamma} - \frac{\sqrt{3}\mu}{2h}\int_{-h}^{h}p(x)dx \tag{4.23}$$

Fig. 4.2 shows the profiles of the micromorphic variable r_χ, solution of the differential equation (4.19), the internal variable r and the cumulative plastic strain for three levels of applied shear ($\bar{\gamma} = 0.05$, 0.2 and 0.34). The stress-strain curve in Fig. 4.2d shows a saturating size effect . This is due to the fact that the difference between r and r_χ does not evolve when r saturates. When the value of r tends to the saturating value $1/k$, the value of p in Eq. (4.22) tends to infinity.

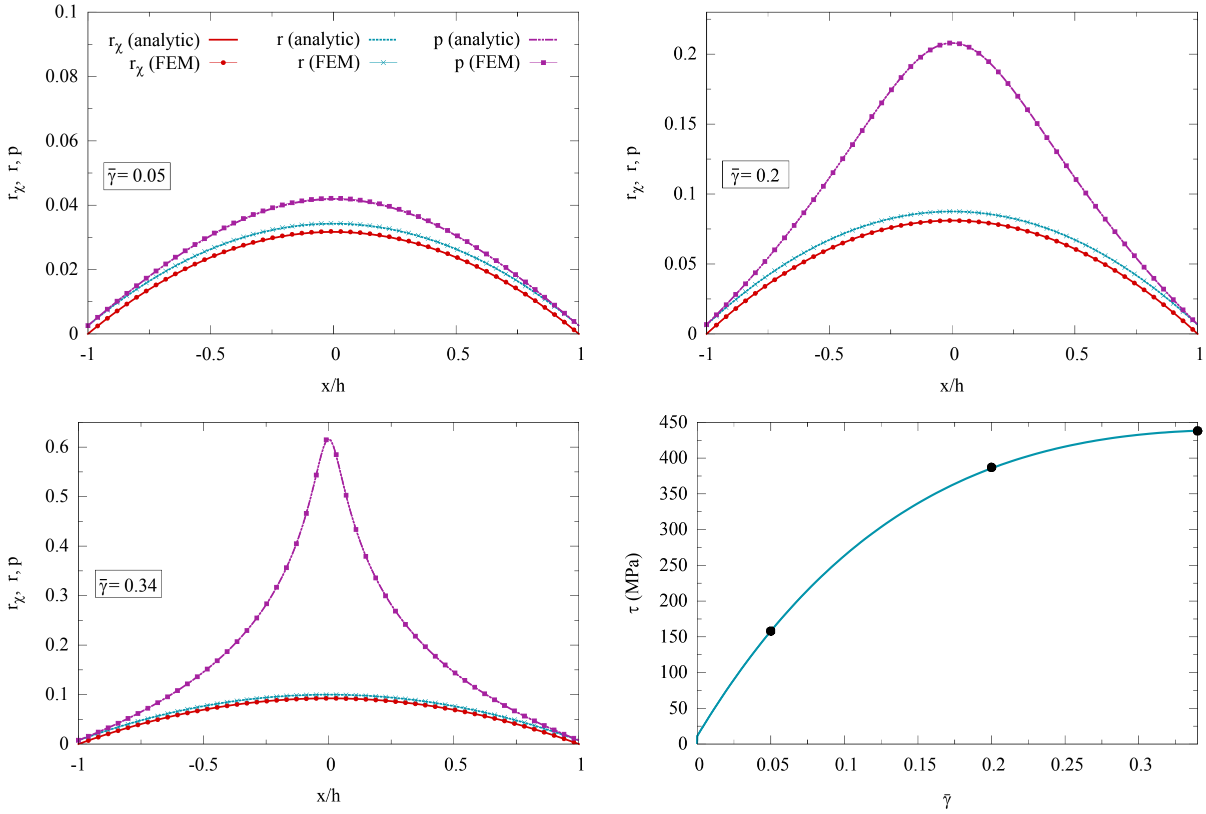

Figure 4.2: *The distribution of cumulative plastic strain p, the saturating variable r and the micromorphic variable r_χ at three levels of applied shear $\bar{\gamma}$. The numerical results are compared to analytical solutions. Material parameters: $R_0 = 20$ MPa, $k = 10$, $Q = 0$ MPa, $H_\chi = 10^5$ MPa and $A = 10^5$ N.*

As shown in Fig. 4.3, the size effect varies in terms of the parameter k. For increasing values of k, the isotropic hardening induced by the micromorphic model saturates rapidly and tends to decrease.

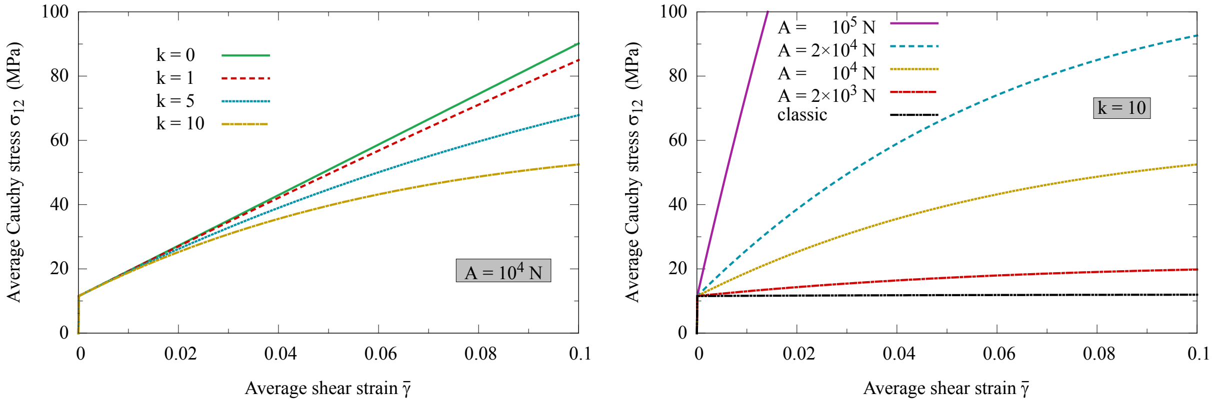

Figure 4.3: *The evolution of shear stress for several values of the parameters k and A. Material parameters* $R_0 = 20$ *MPa,* $Q = 0$ *MPa and* $H_\chi = 10^5$ *MPa. Unit cell size* $2h = 10$ *mm.*

Case 2: hardening ($Q > 0$) The boundary condition $r_\chi = 0$ is prescribed at $x = \pm h$. Therefore, the solution to Eq. (4.18) is given by

$$r_\chi(x) = \frac{\sqrt{3}\tau - R_0}{cQ}\left(1 - \frac{\cosh(\omega_r x)}{\cosh(\omega_r h)}\right) \tag{4.24}$$

Thus,

$$r(x) = r_\chi(x) + \frac{\sqrt{3}\tau - R_0}{cQ + H_\chi}\frac{\cosh(\omega_r x)}{\cosh(\omega_r h)} = \frac{\sqrt{3}\tau - R_0}{cQ}\left(1 - \frac{H_\chi}{cQ + H_\chi}\frac{\cosh(\omega_r x)}{\cosh(\omega_r h)}\right) \tag{4.25}$$

where

$$\omega_r^2 = \frac{cQH_\chi}{A(cQ + H_\chi)} \tag{4.26}$$

Similarly, the shear stress τ is obtained using Eqs. (4.22) and (4.23). The distribution of the variable $r(x)$ is hyperbolic with a boundary layer that depends on the characteristic length $1/\omega_r$. But the profile of plastic strain exhibits large values in the region (middle of the strip) where r gets closer to $1/k$.

Case 3: softening ($Q < 0$) The plastic strain is assumed to not reach the edges of the strip. Therefore, the analytical solution is given for elastic and plastic zones, delimited by $\pm x_c$ are

- Plastic zone ($|x| \leq x_c$): the solution of Eq. (4.18) is

$$r_\chi(x) = \frac{(R_0 - \sqrt{3}\tau)(cQ + H_\chi)}{cQH_\chi \cos(\omega_{rp} x_c)}\cos(\omega_{rp} x) + \frac{\sqrt{3}\tau - R_0}{cQ} \tag{4.27}$$

$$r(x) = \frac{R_0 - \sqrt{3}\tau}{cQ\cos(\omega_{rp} x_c)}\cos(\omega_{rp} x) + \frac{\sqrt{3}\tau - R_0}{cQ} \tag{4.28}$$

where $\omega_{rp}^2 = \dfrac{c|Q|H_\chi}{A(cQ + H_\chi)}$

- Elastic zone: the variable r vanishes and r_χ is governed by the differential equation

$$\Delta r_\chi - \frac{H_\chi}{A} r_\chi = 0 \tag{4.29}$$

The solution of the previous equation for (-) $-h \leq x \leq -x_c$ and (+) $x_c \leq x \leq h$ is given by

$$r_\chi^{\mp}(x) = \frac{R_0 - \sqrt{3}\tau}{H_\chi}\frac{\cosh(\omega_{re}(h \pm x))}{\cosh(\omega_{re}(h - x_c))} \tag{4.30}$$

where $\omega_{re}^2 = \dfrac{H_\chi}{A}$

The elastic/plastic boundary is obtained using the continuity of the micromorphic variable and its gradient at x_c. The expression of shear stress is obtained using Eqs. (4.22) and (4.23). The analytical solution shows that the plastic strain localization band remains bounded. Meanwhile, the cumulative plastic strain $p = -\log(1-kr)/k$ goes to infinity in the localization band when r saturates.

Recall that the broadening of the localization band can also be cancelled by assuming that the generalized parameter A depends on the plastic strain. For instance, for a saturating softening law, the parameter A must saturate at the same rate as the softening modulus. However, the peak of the plastic strain in the localization band is not bounded for finite strains. In the limit case of $H_\chi \to \infty$, the supplementary term introduced as an isotropic hardening is given by $A(p)\Delta p$ is equivalent to $A\Delta r(p)$ for the model based on the saturating variable. The drawback of these models relies on the fact that at large plastic strains, the plastic strain is localized in a band getting narrower until it reaches the size of an element. Hence, the model becomes mesh-dependent at large plastic strains. This may however have physical justification.

Cyclic tension with confined plasticity

Consider a cyclic tension/compression test of a strip of size $2h$ and infinite in the y-direction. The prescribed displacement is $u_x(x=-h) = 0$ and $u_x(x=h) = \bar{u}$. Confined plasticity boundary conditions ($r_\chi = 0$) are applied at $x = \pm h$. Fig. 4.4 shows the average stress vs. average total strain for two values of the parameter k. In the case of $k = 0$, *i.e.* $r = p$, the isotropic hardening induced by the micromorphic model increases over cycles. When the variable r saturates, the induced isotropic hardening saturates as well.

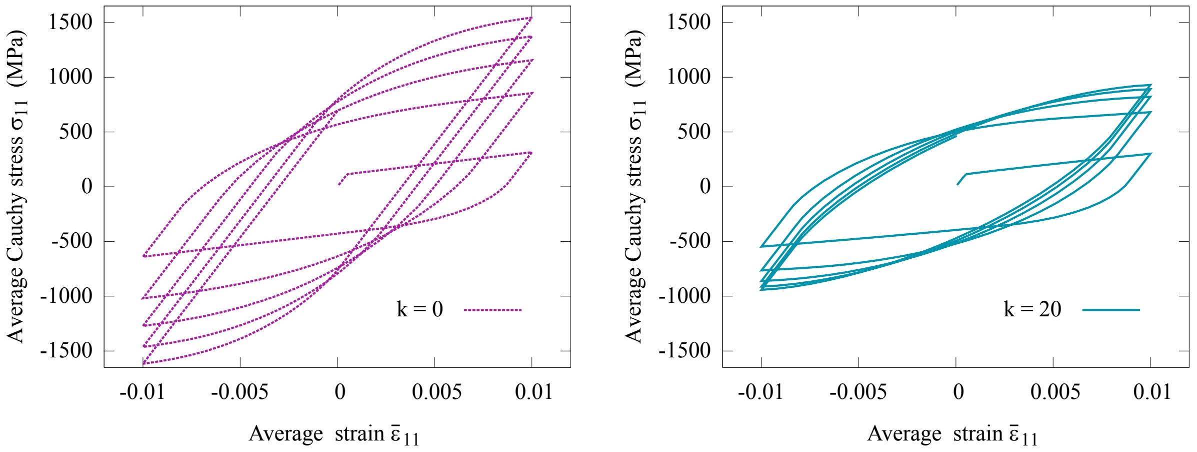

Figure 4.4: *Cyclic tension loading with confined plasticity. Material parameters:* $R_0 = 100$ *MPa,* $Q = 0$ *MPa,* $A = 10^5$ *N,* $H_\chi = 10^5$ *MPa. Unit cell size* $2h = 10$ *mm.*

Localization banding in a plate

Consider the tension of a plate as discussed earlier in section 2.5.2. Using an exponential hardening law (c, Q), a comparison between two models with $k = 0$ and $k = 10$ is carried out. Fig. 4.5 shows that the localization band exhibits a broadening in the case of $k = 0$. In contrast, when $k = c = 10$, the width of the localization band remains unchanged. Further, in Fig. 4.5-e, the model with $k = 10$ shows significant softening since the plastic strain is localized in a narrower band. It can also be noticed that the model with $k = 0$ diverges when the radius $R_0 + cQr + H_\chi(r - r_\chi)$ is to become negative. For $k = 10$, the simulation does not diverge since both terms $(r - r_\chi)$ and cQr ceases to decrease when r tends to $1/k$. When $k \neq c$, we can distinguish two cases:

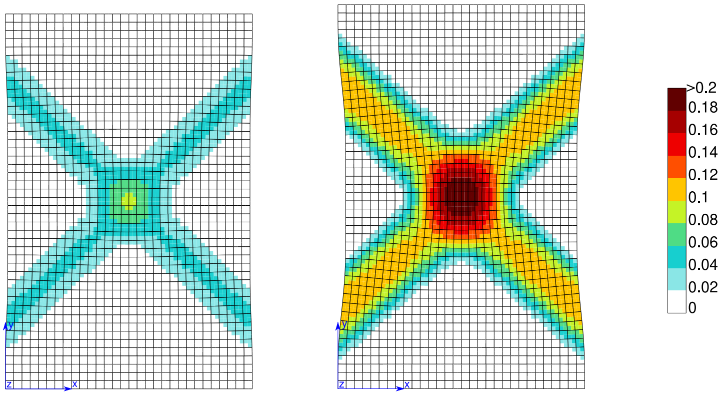

(a) $k = 0$, $u_y/L = 0.012$ (b) $k = 0$, $u_y/L = 0.037$

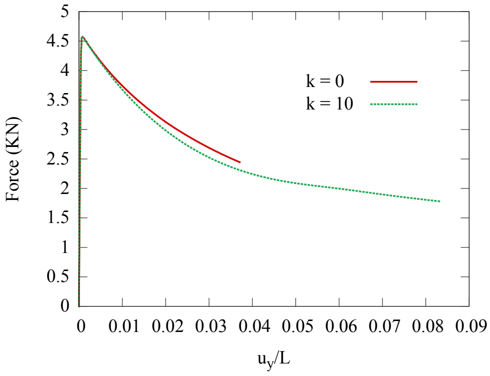

(e) Force vs. applied displacement

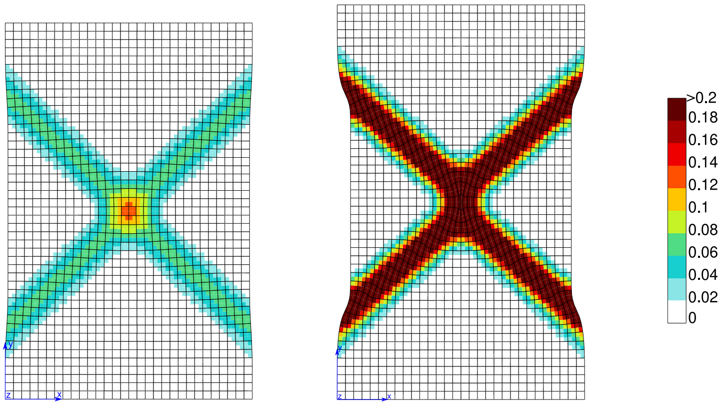

(c) $k = 10$, $u_y/L = 0.014$ (d) $k = 10$, $u_y/L = 0.062$

Figure 4.5: *The broadening of the localization band for* $k = 0$. *Material parameters* $R_0 = 100$ *MPa,* $Q = -100$ *MPa,* $c = 10$*,* $H_\chi = 10^4$ *MPa.*

- $k \geq c$: the localization bandwidth is bounded but the further straining localizes only in a narrower band until the bandwidth reaches the element size.
- $k < c$: the localization band broadens until the variable r, through the parameter k, saturates. Hence, the broadening is more significant when $k \ll c$.

4.1.2 Alternative model: generalization to any hardening law

This model will be formulated relying on the same micromorphic variable r_χ associated with the saturating variable r. However, for this one, the isotropic hardening law of the reference model can be any function of cumulative plastic strain. This formulation will be of use to enhance models that are already implemented in FEM codes, which are often expressed in terms of cumulative plastic strain.
The free energy potential is rewritten as

$$\rho\psi(\underset{\sim}{\varepsilon}^e, p, r_\chi, \nabla r_\chi) = \frac{1}{2}\underset{\sim}{\varepsilon}^e : \underset{\approx}{\mathbb{C}} : \underset{\sim}{\varepsilon}^e + \rho\psi^h(p) + \frac{1}{2}H_\chi\left(r(p) - r_\chi\right)^2 + \frac{1}{2}\nabla r_\chi \cdot \underset{\sim}{\boldsymbol{A}} \cdot \nabla r_\chi \tag{4.31}$$

where $r(p)$ is the solution of Eq. (4.2). The Clausius-Duhem inequality is then given by

$$\left(\underset{\sim}{\sigma} - \rho\frac{\partial\psi}{\partial\underset{\sim}{\varepsilon}^e}\right) : \dot{\underset{\sim}{\varepsilon}}^e + \left(a - \rho\frac{\partial\psi}{\partial r_\chi}\right)\dot{r}_\chi + \left(\underline{\boldsymbol{b}} - \rho\frac{\partial\psi}{\partial\nabla r_\chi}\right)\cdot\nabla\dot{r}_\chi + \underset{\sim}{\sigma} : \dot{\underset{\sim}{\varepsilon}}^p - \rho\frac{\partial\psi}{\partial p}\dot{p} \geq 0 \tag{4.32}$$

Similarly, the constitutive equations are given by Eqs. (4.7). The yield function is

$$f = \sigma_{eq} - R_0 - R(p) \tag{4.33}$$

where

$$R(p) = \rho \frac{\partial \psi}{\partial p} = \rho \frac{\partial \psi^h}{\partial p} + H_\chi (r - r_\chi)(1 - kr) \tag{4.34}$$

Note that the isotropic hardening induced by this model vanishes when $r \to 1/k$ [1]. The intrinsic dissipation rate writes

$$\underset{\sim}{\sigma} : \underset{\sim}{\dot{\varepsilon}}^p - R\dot{p} = (\sigma_{eq} - R_0 - R)\,\dot{p} + R_0 \dot{p} \geq 0 \tag{4.35}$$

By applying the standard Karush–Kuhn–Tucker conditions, the dissipation rate is positive as long as R_0 is positive.

Analytical solution for the simple glide

The differential equation governing the micromorphic variable r_χ writes

$$\Delta r_\chi - \frac{H_\chi}{A}(r_\chi - r) = 0 \tag{4.36}$$

The value of r in the previous equation is obtained through the yield function as

$$f = \sigma_{eq} - \big(R_0 + Hp + H_\chi (r - r_\chi)(1 - kr)\big) = 0 \tag{4.37}$$

with $\sigma_{eq} = \sqrt{3}\,\tau$ is the von Mises equivalent stress and the hardening law of the classical model is given by the linear function Hp.

Remark 5. *In general, one cannot get the explicit expression of the differential equation for r_χ since Eq. (4.37) is nonlinear w.r.t. r_χ. Meanwhile, if the variable r is infinitesimal, Eq. (4.36) reduces to*

$$\Delta r_\chi - \frac{HH_\chi}{A(H + H_\chi)} r_\chi + \frac{H_\chi}{A(H + H_\chi)}(\sigma_{eq} - R_0) = 0 \tag{4.38}$$

This differential equation in Eq. (4.38) suggests a characteristic length scale similar to the one given by the model for which the micromorphic variable is associated with the cumulative plastic strain. For this model, the characteristic length will decrease with the cumulative plastic strain. Numerically, at sufficiently large plastic strains, it leads to localization of further plastic strain in one single element. Consequently, the simulation becomes mesh-dependent at large strains.

Fig. 4.6-(a) shows the stress-strain curves for a simple glide loading, obtained for the model based on the saturating variable r and the linear isotropic hardening law. For $k = 0$, the characteristic length does not evolve and the softening slope is constant. As k increases, the characteristic length becomes smaller for large values of plastic strain (see Fig. 4.6-(b)). Therefore, the plastic strain is localized in a narrower band such that the softening slope decreases exponentially.

4.1.3 An enhanced Kocks-Mecking model

In metals and alloys, the plastic strain is due mainly to the motion of large numbers of dislocations. Besides, dislocations are introduced in materials during solidification. During plastic deformation, the dislocation density increases such that the average distance between adjacent dislocations decreases. Accordingly, the material becomes harder because of the repulsive interaction between dislocations. The density of dislocation in a material is the total dislocation length per unit volume (mm^{-2}). In carefully solidified metal crystals, dislocation densities can be as low as 10^3 mm^{-2}. It can be as high as 10^{10} mm^{-2} for heavily deformed materials. Dislocations are also found in ceramic materials (10^3-10^4 mm^{-2}) and silicon single

---

[1] A slightly different version of this model can be obtained by considering the variable r as an argument of the free energy potential and modifying the definition of the isotropic hardening term in the yield function. This model induces a saturating but non-vanishing isotropic hardening given by $H_\chi(r - r_\chi)$.

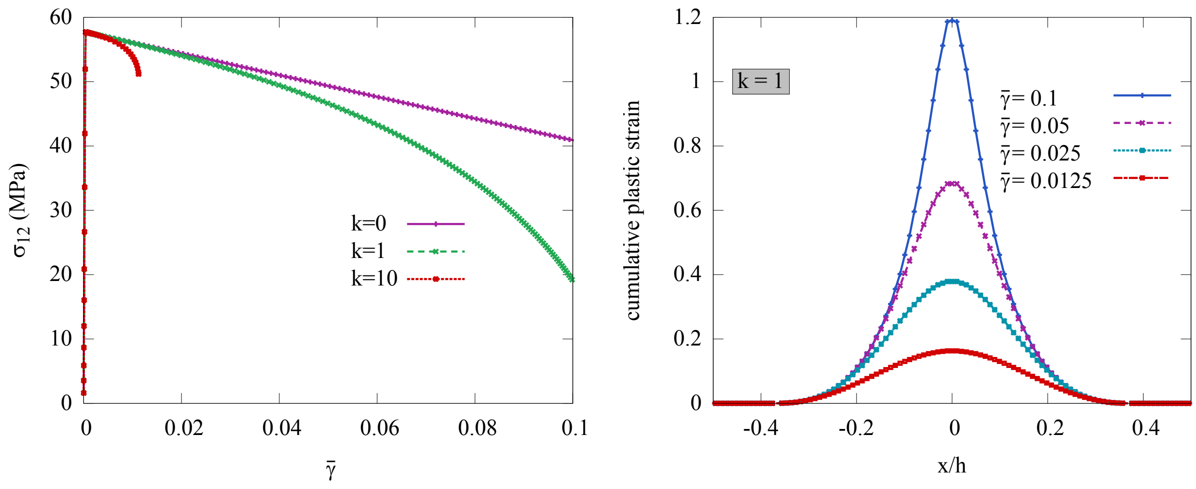

(a) (b)

Figure 4.6: *Simple glide loading. Material parameters* $R_0 = 100$ *MPa,* $H = -100$ *MPa. (model in section 4.1.2)*

crystals (0.1-1 mm^{-2}) [Callister and Rethwisch, 2013]. The dislocation density may diminish under proper heat treatments. A widely used model relating the shear flow stress and the average dislocation density ρ^d has been proposed by *e.g.* Mecking and Kocks [1981]. Accordingly, the yield function is

$$f(\underset{\sim}{\sigma}, \rho^d) = \sigma_{eq} - R_0 - \zeta \mu b \sqrt{\rho^d} \tag{4.39}$$

where b is the magnitude of the Burgers vector (its unit is *mm*), μ is the shear modulus and ζ is a coefficient close to 0.3 which depends partly on the strength of the interaction between dislocations. The evolution equation of the dislocation density ρ^d (its physical unit taken in mm^{-2}) is given by

$$\dot{\rho}^d = (k_1 \sqrt{\rho^d} - k_2\, \rho^d)\dot{p} \tag{4.40}$$

where k_1 and k_2 are positive material parameters. The first term (k_1) corresponds to multiplication of dislocations and the second one (k_2) to dislocation annihilation during dislocation motion ($\dot{p} > 0$). The dislocation density saturates at $\rho^d = (k_1/k_2)^2$.

Fig. 4.7-(a) shows the response of the Kocks-Mecking model for several values of initial dislocation densities. For initial values $\rho^d_0 < (k_1/k_2)^2$, the material behavior exhibits a hardening that saturates when $\rho^d = (k_1/k_2)^2$. In contrast, it becomes a softening model when $\rho^d_0 > (k_1/k_2)^2$. For $\rho^d_0 = (k_1/k_2)^2$, the model reduces to a perfect plasticity model. Regarding the softening case, Fig. (4.7) depicts the stress-strain curves for a simple glide loading. They are obtained for several mesh sizes. It is shown that the softening is very sharp for smaller mesh sizes since the plastic strain is localized on one single element. This issue requires the enhancement of the Kocks-Mecking model to take into account length scales.

Now, we propose a first enhanced Kocks-Mecking model using the micromorphic approach. The micromorphic variable is associated to a dimensionless variable $\varrho = b\sqrt{\rho^d}$. Using Eq.(4.40), the evolution equation for ϱ writes

$$\dot{\varrho} = \frac{1}{2}(k_1 b - k_2 \varrho)\dot{p} \tag{4.41}$$

The initial value of ϱ is denoted by $\varrho_0 = b\sqrt{\rho^d_0}$. The integration of Eq. (4.41) yields

$$\varrho = b\sqrt{\rho^d} = \frac{k_1 b}{k_2} + \left(\varrho_0 - \frac{k_1 b}{k_2}\right) e^{-\frac{k_2}{2} p} \tag{4.42}$$

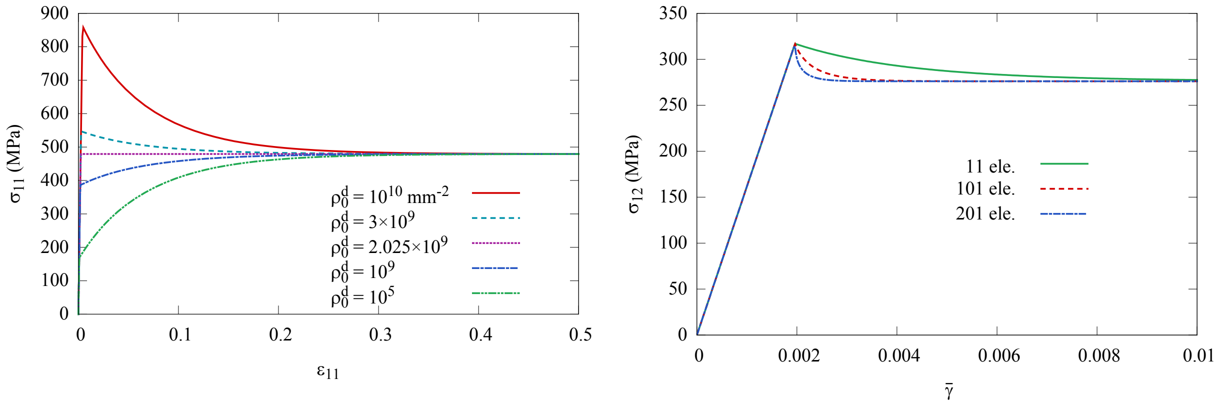

(a) (b)

Figure 4.7: *(a) Stress-strain curves for simple tension loading for various initial values of dislocation density ρ_0^d. (b) Simple glide loading for $\rho_0^d = 3.045\times10^9\ mm^{-2}$ and various mesh sizes. Material parameters [Ren et al., 2017]: $R_0 = 166\ MPa$, $\zeta = 0.3$, $\mu = 80000\ MPa$, $k_1 = 1.44\times10^6\ mm^{-1}$, $k_2 = 32$, $b = 2.9\times10^{-7}$ mm.*

The free energy is assumed to be a quadratic function of $\underset{\sim}{\varepsilon}^e$, ϱ, ϱ_χ and $\nabla\varrho_\chi$ as

$$\rho\psi(\underset{\sim}{\varepsilon}^e,\varrho,\varrho_\chi,\nabla\varrho_\chi)=\frac{1}{2}\underset{\sim}{\varepsilon}^e:\underset{\approx}{\mathbb{C}}:\underset{\sim}{\varepsilon}^e+\frac{1}{2}\zeta\mu\,\varrho^2+\frac{1}{2}H_\chi(\varrho-\varrho_\chi)^2+\frac{1}{2}\nabla\varrho_\chi\cdot\underset{\sim}{\boldsymbol{A}}\cdot\nabla\varrho_\chi \tag{4.43}$$

The power of internal forces is given by

$$\mathscr{P}^{(i)}=\underset{\sim}{\sigma}:\dot{\underset{\sim}{\varepsilon}}^e+a\dot{\varrho}_\chi+\underline{\boldsymbol{b}}\cdot\nabla\dot{\varrho}_\chi \tag{4.44}$$

Thus, the dissipation rate inequality writes

$$\left(\underset{\sim}{\sigma}-\rho\frac{\partial\psi}{\partial\underset{\sim}{\varepsilon}^e}\right):\dot{\underset{\sim}{\varepsilon}}^e+\left(a-\rho\frac{\partial\psi}{\partial\varrho_\chi}\right)\dot{\varrho}_\chi+\left(\underline{\boldsymbol{b}}-\rho\frac{\partial\psi}{\partial\nabla\varrho_\chi}\right)\cdot\nabla\dot{\varrho}_\chi+\underset{\sim}{\sigma}:\dot{\underset{\sim}{\varepsilon}}^p-\rho\frac{\partial\psi}{\partial\varrho}\dot{\varrho}\geq 0 \tag{4.45}$$

Constitutive equations are derived as

$$\underset{\sim}{\sigma}=\rho\frac{\partial\psi}{\partial\underset{\sim}{\varepsilon}^e},\qquad R=\rho\frac{\partial\psi}{\partial\varrho},\qquad a=\rho\frac{\partial\psi}{\partial\varrho_\chi},\qquad \underline{\boldsymbol{b}}=\rho\frac{\partial\psi}{\partial\nabla\varrho_\chi} \tag{4.46}$$

and the intrinsic dissipation rate

$$\underset{\sim}{\sigma}:\dot{\underset{\sim}{\varepsilon}}^p-\rho\frac{\partial\psi}{\partial\varrho}\dot{\varrho}\geq 0 \tag{4.47}$$

The yield condition is given by

$$f(\underset{\sim}{\sigma},R)=\sigma_{eq}-R_0-R(\varrho) \tag{4.48}$$

where

$$R(\varrho)=\zeta\mu\,\varrho+H_\chi(\varrho-\varrho_\chi) \tag{4.49}$$

By rewriting the dissipation rate inequality in (Eq. 4.47), we get

$$\underset{\sim}{\sigma}:\dot{\underset{\sim}{\varepsilon}}^p-\frac{1}{2}(k_1 b-k_2\varrho)R\dot{p}\geq 0 \tag{4.50}$$

or

$$\left(\sigma_{eq}-\frac{1}{2}(k_1 b-k_2\varrho)R\right)\dot{p}\geq 0 \tag{4.51}$$

$$(\sigma_{eq}-R_0-R(\varrho))\dot{p}+\left(R_0+R\left(1-\frac{1}{2}(k_1 b-k_2\varrho)\right)\right)\dot{p}\geq 0 \tag{4.52}$$

If $(k_1 b-k_2\varrho)\leq 0$ (*i.e.*, a softening model), the dissipation rate is always positive. However if $(k_1 b-k_2\varrho)>0$, the dissipation rate is positive only if

$$R\geq\frac{-2R_0}{2-(k_1 b-k_2\varrho)} \tag{4.53}$$

The previous inequality is satisfied for typical values reported in literature, *e.g.* [Ren et al., 2017].

Size effect in the case of simple glide

The second balance equation writes

$$\text{div }\underline{\boldsymbol{b}}=\text{a} \tag{4.54}$$

where the constitutive equations for generalized stresses are given by

$$a=-H_\chi(\varrho-\varrho_\chi),\qquad \underline{\boldsymbol{b}}=A\nabla\varrho_\chi \tag{4.55}$$

The differential equation governing the micromorphic variable ϱ_χ writes

$$\Delta\varrho_\chi-\frac{H_\chi}{A}(\varrho_\chi-\varrho)=0 \tag{4.56}$$

The yield function is given by

$$f(\underset{\sim}{\sigma},R)=\sigma_{eq}-\left(R_0+\zeta\mu\,\varrho+H_\chi\left(\varrho-\varrho_\chi\right)\right)=0 \tag{4.57}$$

with $\sigma_{eq}=\sqrt{3}\,\tau$ is the von Mises stress. By combining Eqs. (4.56) and (4.57), we get

$$\Delta\varrho_\chi-\frac{\zeta\mu H_\chi}{A(\zeta\mu+H_\chi)}\varrho_\chi+\frac{H_\chi}{A(\zeta\mu+H_\chi)}(\sigma_{eq}-R_0)=0 \tag{4.58}$$

The solution of the differential equation in (4.58) is always exponential. It is the case also for the softening case when the dislocation density decreases. Fig. 4.8 shows that this model exhibits a mesh dependency. Moreover, the saturation value of the stress decreases for smaller mesh sizes in contrast the classical model characterized by the same saturation value for different mesh sizes as shown in Fig. 4.7.

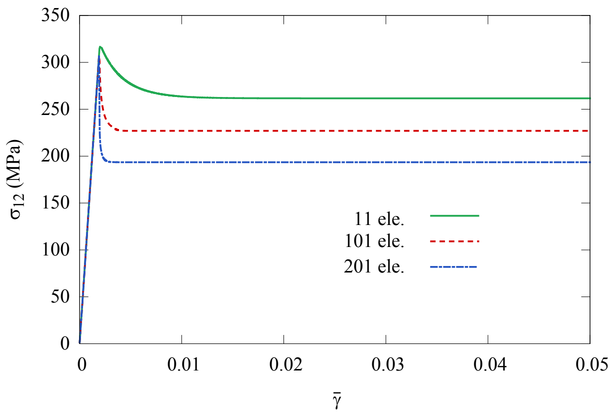

Figure 4.8: *Simple glide loading. Influence of the mesh size on the enhanced Kocks-Mecking model (presented in section 4.1.3). Material parameters are given in the caption of Fig. 4.7. Micromorphic parameters:* $A=80$ *N,* $H_\chi=10^5$ *MPa. Unit cell size* $2h=5$*mm.*

4.1.4 An alternative enhancement of Kocks-Mecking model

In order to regularize simulations using the Kocks-Mecking model, we suggest an alternative enhancement by keeping the same hardening law but the micromorphic variable will be associated with the cumulative plastic strain. The free energy is assumed to be a quadratic function of $\underset{\sim}{\varepsilon}^e$, ϱ, p, p_χ and ∇p_χ as

$$\rho\psi(\underset{\sim}{\varepsilon}^e, p, \varrho, p_\chi, \nabla p_\chi) = \frac{1}{2}\underset{\sim}{\varepsilon}^e : \underset{\approx}{\mathbb{C}} : \underset{\sim}{\varepsilon}^e + \frac{1}{2}\zeta\mu\,\varrho^2 + \frac{1}{2}H_\chi(p - p_\chi)^2 + \frac{1}{2}\nabla p_\chi \cdot \underset{\sim}{\boldsymbol{A}} \cdot \nabla p_\chi \tag{4.59}$$

by considering that p and ϱ are independent variables. Thus, the dissipation rate inequality is given by

$$\left(\underset{\sim}{\sigma} - \rho\frac{\partial\psi}{\partial\underset{\sim}{\varepsilon}^e}\right) : \dot{\underset{\sim}{\varepsilon}}^e + \left(a - \rho\frac{\partial\psi}{\partial p_\chi}\right)\dot{p}_\chi + \left(\underline{\boldsymbol{b}} - \rho\frac{\partial\psi}{\partial\nabla p_\chi}\right) \cdot \nabla\dot{p}_\chi + \underset{\sim}{\sigma} : \dot{\underset{\sim}{\varepsilon}}^p - \rho\frac{\partial\psi}{\partial p}\dot{p} - \rho\frac{\partial\psi}{\partial\varrho}\dot{\varrho} \geq 0 \tag{4.60}$$

Constitutive equations are obtained as

$$\underset{\sim}{\sigma} = \rho\frac{\partial\psi}{\partial\underset{\sim}{\varepsilon}^e}, \qquad a = \rho\frac{\partial\psi}{\partial p_\chi}, \qquad \underline{\boldsymbol{b}} = \rho\frac{\partial\psi}{\partial\nabla p_\chi} \tag{4.61}$$

Further, we define

$$R^p = \rho\frac{\partial\psi}{\partial p}, \qquad R^\varrho = \rho\frac{\partial\psi}{\partial\varrho} \tag{4.62}$$

The yield condition is given by

$$f(\underset{\sim}{\sigma}, R) = \sigma_{eq} - R_0 - R(p, \varrho) \tag{4.63}$$

where $R(p,\varrho) = R^\varrho + R^p = \zeta\mu\,\varrho + H_\chi(p - p_\chi)$. This model provides the same response as the classical model if the plastic strain is homogeneous.
The rate of intrinsic dissipation rate satisfies the following inequality

$$\underset{\sim}{\sigma} : \dot{\underset{\sim}{\varepsilon}}^p - R^p\dot{p} - R^\varrho\dot{\varrho} \geq 0 \tag{4.64}$$

so that

$$f(\underset{\sim}{\sigma}, R)\dot{p} + \left(R_0 + R^\varrho(1 - \frac{1}{2}(k_1 b - k_2\varrho))\right)\dot{p} \geq 0 \tag{4.65}$$

By applying Karush–Kuhn–Tucker conditions, the dissipation rate is positive when

$$R_0 + R^\varrho\left(1 - \frac{1}{2}(k_1 b - k_2\varrho))\right) \geq 0 \tag{4.66}$$

In the case of softening, the term $(k_1 b - k_2\varrho)$ is negative. Accordingly, the dissipation rate is positive. Otherwise, R^ϱ must satisfy the following condition:

$$R^\varrho \geq -\frac{2R_0}{2 - (k_1 b - k_2\varrho)} \tag{4.67}$$

This condition is similar to the one emerged from the previous theory in Eq. (4.53).

Analytical solution for the simple glide

The micromorphic variable p_χ satisfies

$$\Delta p_\chi - \frac{H_\chi}{A}(p_\chi - p) = 0 \tag{4.68}$$

In order to get an approximate solution to this problem, the term R^ϱ can be linearised as

$$R^{\varrho} = \zeta\mu\varrho = \zeta\mu\left(\frac{k_1 b}{k_2} + \left(\varrho_0 - \frac{k_1 b}{k_2}\right)e^{-\frac{k_2}{2}p}\right) \approx R^{\varrho}_0 + \tilde{H}p \tag{4.69}$$

where $R^{\varrho}_0 = \zeta\mu\varrho_0$ and $\tilde{H}(\varrho) = \dfrac{\zeta\mu}{2}(k_1 b - k_2\varrho)$. Notice that the modulus $\tilde{H}$ is positive when the saturating value of ϱ given by $\dfrac{k_1 b}{k_2}$ is higher than the value of the dislocation density ϱ. Otherwise, when the initial value of the dislocation density exceeds the saturation value, $\tilde{H}$ becomes negative. By substituting the value of the cumulative plastic strain p obtained from the yield condition in Eq. (4.63) into the differential equation 4.68, we have

$$\Delta p_{\chi} - \frac{\tilde{H}H_{\chi}}{A(\tilde{H}+H_{\chi})}p_{\chi} + \frac{H_{\chi}}{A(\tilde{H}+H_{\chi})}(\sigma_{eq} - R_0 - R^{\varrho}_0) = 0 \tag{4.70}$$

The differential equation (4.70) is similar to the model presented in 2.8. For instance, in the case of a saturating hardening law, the characteristic length goes to infinity as p increases, *i.e.* the localization band broadens. The profile of the cumulative plastic strain is harmonic (see Fig. 4.9). The localization band broadens since it depends on the modulus $\tilde{H}$ that vanishes when the hardening law saturates. On the other hand, from Eq. (4.42), the dislocation density tends to saturate in the localization band with a non-harmonic profile.

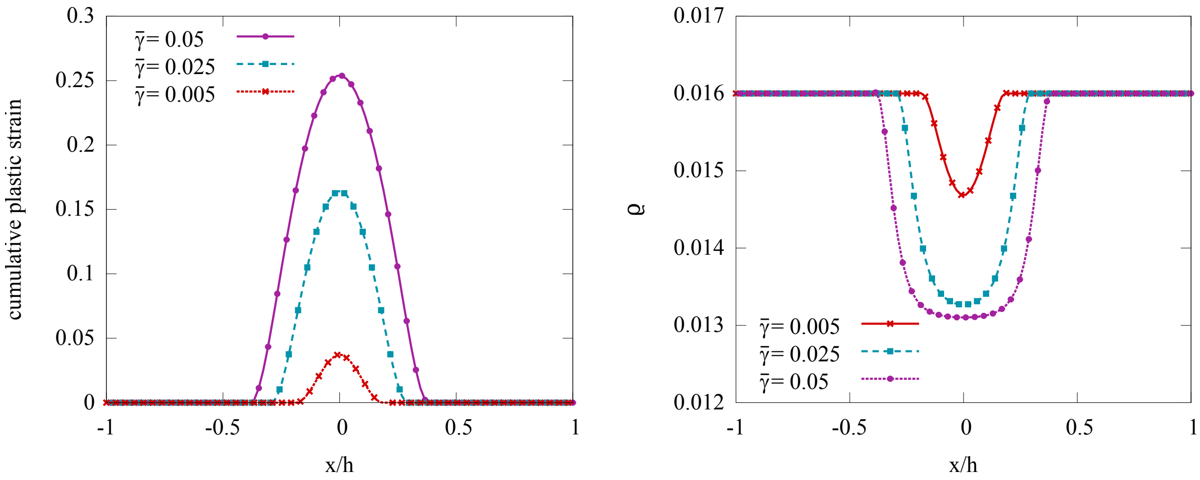

Figure 4.9: *Simple glide loading. Material parameters* $R_0 = 166$ *MPa,* $k_1 = 1.44\times10^6$*,* $k_2 = 32$*,* $b = 2.9\times10^{-7}$*mm,* $\mu = 8000$ *MPa,* $\zeta = 0.3$*,* $\rho^d_0 = 3.045\times10^9$ mm^{-2}*,* $A = 80$ *N and* $H_{\chi} = 10^5$ *MPa. Unit cell size* $2h = 10$*mm.*

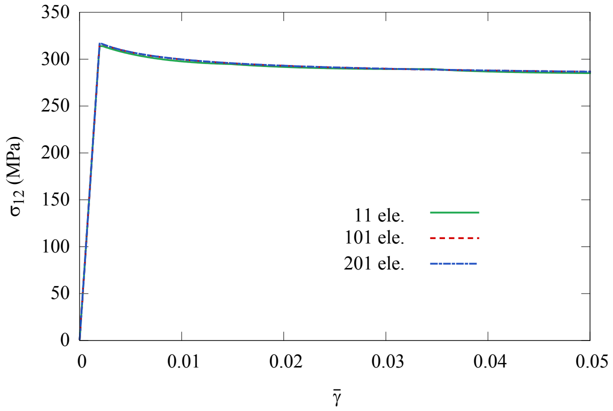

Figure 4.10: *Simple glide loading. Influence of the mesh size on the micromorphic-enhanced model. Material parameters are given in the caption of Fig. 4.7. Micromorphic parameters:* $A = 80$ *N,* $H_\chi = 10^5$ *MPa. Unit cell size* $2h = 5$*mm.*

Fig. 4.10 depicts the shear stress-strain curves for different mesh sizes. It is shown that the enhanced model yields a solution that does not depend on the mesh size.

4.2 Application to polymer composite materials

In this section, a polymer matrix composite reinforced by unidirectional fibers is studied. The hardening law of the matrix is characterized by three stages: hardening → softening → rehardening. The presence of hard inclusions (fibers) induces a plastic strain gradient in the matrix. The softening that occurs in the matrix leads to strain localization. The micromorphic approach is used to address the two following aspects at once: size effects and regularization of strain localization. First, the micromorphic model is employed to study the necking phenomena in a plate under tension. The propagation of Lüders-like bands is investigated. Second, a periodic composite with only one fiber in the unit cell is studied for different volume fractions. Finally, an identification of the characteristic length on a unidirectional composite with random fiber distribution is carried out relying on experimental results from the literature.

4.2.1 Necking phenomenon in polymer materials

Many amorphous and semi-crystalline polymers undergo the so-called necking phenomenon which is a plastic instability. It is also observed for metallic materials. The necking is usually triggered by a section variation or defects coming from manufacturing processes. The occurrence of a neck is affected by several factors such as temperature, pressure and material properties such as the molecular weight, its distribution, and the material history [Halary et al., 2011]. The necking phenomenon is observed mostly in crystalline materials but also in glassy polymers. Understanding the necking is important to predict the material formability and prevent ductile fracture, tearing, etc. during the manufacturing and also for structural analysis.

During tensile tests, the material undergo elastic and viscoplastic deformation. Before the yield point, the section is uniform in the gauge region. Indeed, some inelasticity may occur before yield. At the yield point σ_Y, a small neck is formed within the gauge section of the sample (see Fig. 4.11). In fact, the necking occurs in a section slightly smaller due to geometric imperfections. Within the neck, polymer chain axes become aligned and parallel to the loading direction. As molecular chains reach their extensibility limits, it leads to a localized strengthening which makes further deformation difficult to occur at the same point. Therefore, the neck propagates through the neighbouring regions along the gauge length. The alignment of molecular chains is usually accompanied by a change of mechanical properties (local hardening) and the refractive index (polymer whitening as in Fig. 4.12). The strain becomes uniform when the whole neck propagation is developed, until the sample breaks. The stress at which fracture occurs is denoted by σ_f (see Fig. 4.12 and 4.11a). For some materials, the necking is unstable, and characterized by a fracture during necking (see Fig. 4.11b). For others, the strain is homogeneous until the sample breaks without any necking (see Fig. 4.11c)

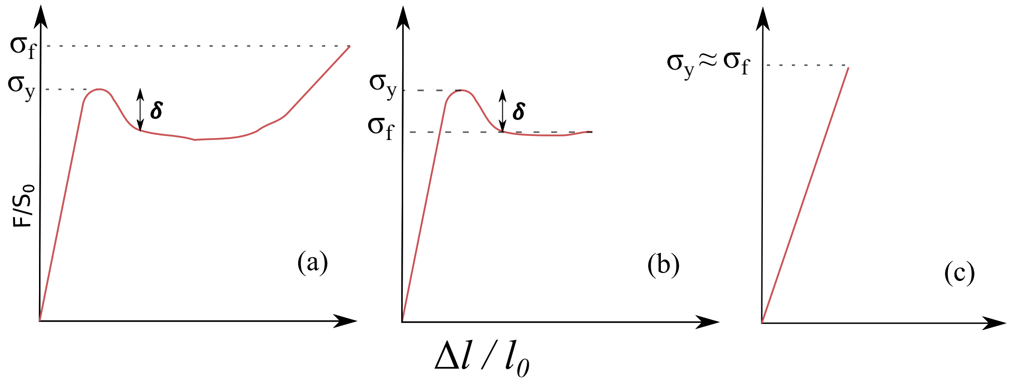

Figure 4.11: *Schematic illustration of necking phenomenon in polymers. For most polymer materials, the curve type (c) (resp. (a)) is obtained for high strain rates or low temperatures (resp. low strain rates or high temperatures).*

The plastic behavior of polymers generally depends on hydrostatic pressure. Under identical conditions, the plastic deformation occurs more easily in tension than in compression loadings. Furthermore, the plastic flow involves molecular motions. For high temperatures or low strain rates, the molecular chains flows easily compared to high strain rates or low temperature. The dependence of yield stress on strain rate and temperature is usually modelled using Ree-Eyring flow equations [Ree et al., 1958].

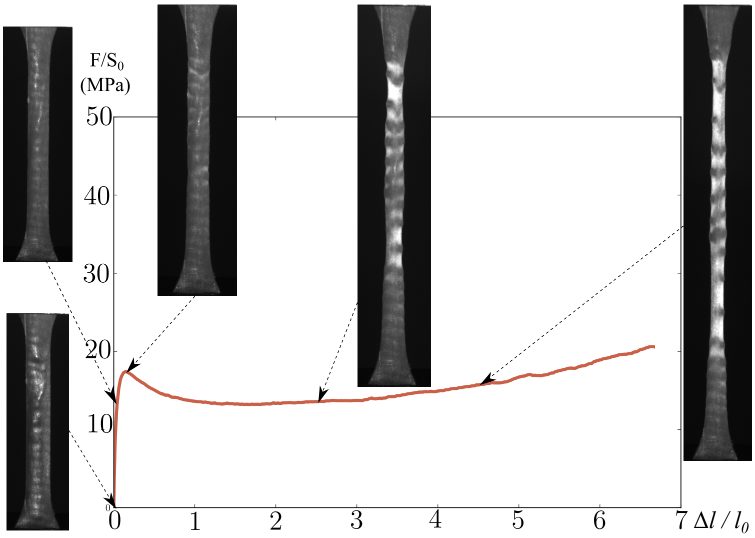

Figure 4.12: *The engineering stress vs strain curve for a tensile test of a UHMW-PE polymer specimen [Abatour, 2019].*

4.2.2 A hyperelastoplastic model for polymer necking

In the following, we consider a highly crosslinked RTM6 epoxy resin [Morelle et al., 2017]. The material behavior is rate and temperature-dependent. This dependency is taken into account by considering material parameters that depend on deformation rate and temperature. A model based on the multiplicative decomposition of the deformation gradient is considered. The elasticity law is isotropic linear. For the sake of illustration, a rate-independent von Mises criterion is adopted for this model. The isotropic hardening law is given by

$$\sigma_Y = R_0 + \sigma_A(1 - e^{-c_A p}) + \sigma_B(1 - e^{-c_B p}) + \sigma_{C_{11}} \tag{4.71}$$

which involves three contributions:

- Pre-peak yield $(R_0 + \sigma_A(1 - e^{-c_A p}))$ where R_0 is the initial yield stress, $\sigma_A > 0$ is the targeted hardening value and c_A is a material parameter driving the hardening rate

- A softening term $\sigma_B(1 - e^{-c_B p})$ where $\sigma_B < 0$ is the targeted yield drop and c_B is a material parameter driving the softening rate.

- Rehardening $\sigma_{C_{11}} > 0$: entropic resistance due to the alignment of the molecular network. The stress $\sigma_{C_{11}}$ is the axial component of the re-hardening stress

$$\underset{\sim}{\sigma}_C = \frac{C_R}{3} \frac{\sqrt{N}}{\lambda_p} \mathscr{L}^{-1}\left(\frac{\lambda_p}{\sqrt{N}}\right) \operatorname{dev}(\underset{\sim}{B}^p) \tag{4.72}$$

  where $\underset{\sim}{B}^p$ is the plastic Left Cauchy-Green tensor, N is the number of links in a chain, C_R is a hardening modulus and $\mathscr{L}^{-1}$ denotes the inverse Langevin function approximated as

$$\mathscr{L}^{-1}(y) = y\frac{3 - y^2}{1 - y^2} \tag{4.73}$$

The plastic stretch λ_p on a chain is defined by $\lambda_p = \sqrt{\mathrm{tr}(\underset{\sim}{B}^{\mathrm{p}})/3}$. In the case of an uniaxial tension and assuming plastic incompressibility, the left Cauchy-Green tensor is given by

$$\underset{\sim}{F}^p = \begin{pmatrix} e^p & 0 & 0 \\ 0 & e^{-0.5p} & 0 \\ 0 & 0 & e^{-0.5p} \end{pmatrix} \rightarrow \underset{\sim}{B}^p = \underset{\sim}{F}^p \underset{\sim}{F}^{pT} = \begin{pmatrix} e^{2p} & 0 & 0 \\ 0 & e^{-p} & 0 \\ 0 & 0 & e^{-p} \end{pmatrix} \quad \text{and} \quad \lambda_p = \sqrt{(e^{2p} + 2e^{-p})/3} \tag{4.74}$$

The material parameters are identified for various strain rates and temperatures in [Morelle et al., 2017]. For this study, only parameters identified for a strain rate $\dot{\varepsilon} = 10^{-3}s^{-1}$ at room temperature will be considered. The same analysis can be readily carried out for other strain rates and temperature conditions. Fig. 4.13 depicts the stress-strain curve obtained for a homogeneous tensile loading using the classical model.

Material parameters	E (MPa)	μ	R_0	σ_A	c_A	σ_B	c_B	C_R	N
values	3180	0.34	62.3	94.24	42.63	-70.44	8	26.6	1

Table 4.1: *Material parameters identified for RTM6 epoxy at room temperature and strain rate $\dot{\varepsilon} = 10^{-3}s^{-1}$ [Morelle et al., 2017].*

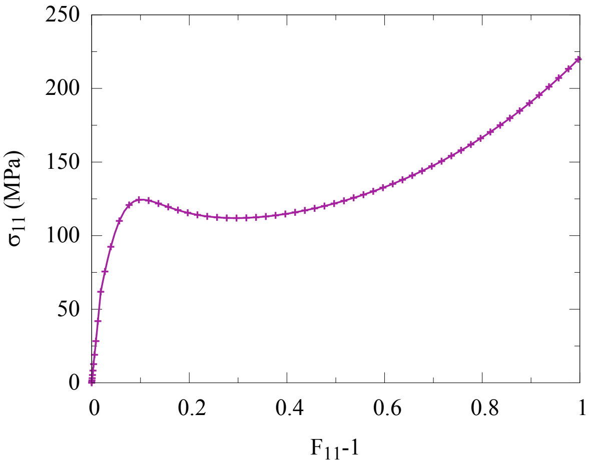

Figure 4.13: *Homogeneous tensile loading. Material parameters are listed in table 4.1.*

The previous model is enhanced using the micromorphic approach. We consider a micromorphic model based on the cumulative plastic strain (see section 2.2.4). The Lagrangian finite strain formulation is adopted. Accordingly, the yield criterion is written as

$$f(\underset{\sim}{M}, \sigma_Y) = \sqrt{\frac{3}{2} \underset{\sim}{M}^{dev} : \underset{\sim}{M}^{dev}} - \sigma_Y - H_\chi (p - p_\chi) \tag{4.75}$$

4.2.3 Propagation of Lüders-like bands

The material model has been used to simulate the propagation of a Lüders-like band in a flat rectangular specimen of width l and length L (see Fig. 4.14). A small defect is introduced in the middle of the structure to trigger the localization. Plane strain conditions are adopted. The response of the classical model is compared to the micromorphic model for several values of the generalized modulus A. Fig. 4.15 illustrates the results obtained for the regularized model ($A = 80$ N, $H_\chi = 10^5$ MPa). The reaction force vs. applied displacement curve in Fig 4.15a is characterized by a hardening until a peak is attained. This peak is followed by a softening corresponding to a 45° localization band (①). The neck is formed when another localization band (−45°) is developed (②). The yield stress increases in the neck region until the cumulative

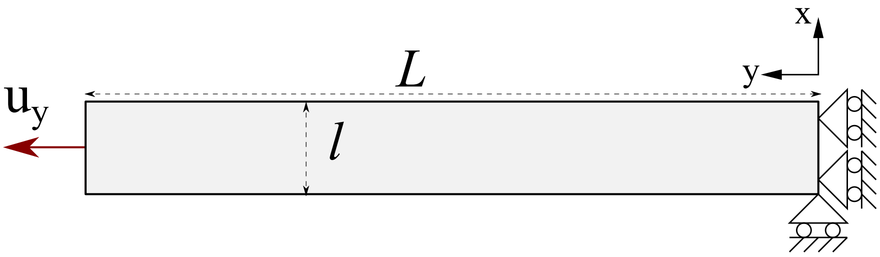

Figure 4.14: *A 2D plate under tension. A small defect is introduced in the middle of the structure to trigger the localization.*

plastic strain reaches, approximatively, a value of 0.5 for which the yield stress becomes greater than the yield peak. Consequently, the neck is propagating to the neighbouring region between (between ② and ⑥). A softening occurs when the band-front reaches either the top or the bottom of the structure (④ and ⑤). This corresponds to the formation of a new neck that merges with the existing one. When the plastic strain is nearly homogeneous in the structure, a re-hardening of the global response is observed.

Fig. 4.15b depicts the profiles of cumulative plastic strain during the propagation of the localization band. The band front can be defined as the region where the hardening modulus is negative and its tail is the region where the rehardening occurs. The band front is defined by the micromorphic parameters A and H_χ and the hardening/softening moduli. An analytical solution for the propagation of Lüders bands is provided in [Mazière and Forest, 2015], obtained for a linear softening/rehardening law at small strains in the case of strain gradient plasticity. This solution is the limit case of the micromorphic model obtained when the value H_χ is high. Note that the stress-strain curves obtained using classical plasticity (not shown here) do not exhibit a significant mesh dependency. This can be explained by the fact that re-hardening part of the constitutive behavior leads to the propagation of the plastic zone in the neighbouring even if the plastic strain is first localized in an element-wide band.

4.2.4 Fiber reinforced polymer

In this section, the material behavior of the matrix identified on the bulk specimens is used to predict the mechanical response of a unidirectional (UD) composite. So far, we studied the size effect and the localization of plastic strain separately. This example allows to study both these phenomena. The size effect is due to the presence of hard particles (fibers in this case). Therefore, local plastic strain gradients are generated in the matrix. In other words, the plastic strain gradients are caused by the microstructure itself. The constitutive behavior of the matrix exhibited a softening leading to plastic strain localization.

Fig. 4.16 depicts the stress-strain curves obtained from transverse compression tests on a cubic specimen of the UD composite. On the surface of the UD composite, several localization bands are observed prior to failure. The classical model is used for FEM simulations with cohesive elements. It is shown that the finite element model is unable to capture the instant of failure initiation even when no damage is assumed to occur in the matrix or cohesive elements. Further, the finite element model underestimates the stress state. In situ digital image correlation (DIC) results do not show the same intensity of strain localization and the experimental deformation seems to accumulate without involving more pronounced localized patterns [Chevalier et al., 2019; Pardoen et al., 2021].

The characterization of the epoxy RTM6 has shown that no damage growth is observed prior to fracture [Morelle et al., 2017]. Further, the stress state does not seem to induce fiber-matrix decohesion prior to fracture. Consequently, the previously described constitutive model including only the plasticity will be used. In an attempt to improve the predictions of the numerical model, the enhanced micromorphic model is adopted.

To understand the effect of the micromorphic enhancement and the fiber volume fraction on the global response of the composite, we start with a simple study case using a periodic unit cell with one single fiber. Consider a 2D periodic square unit cell of side length 2 mm. A fiber of radius r_f is located at the

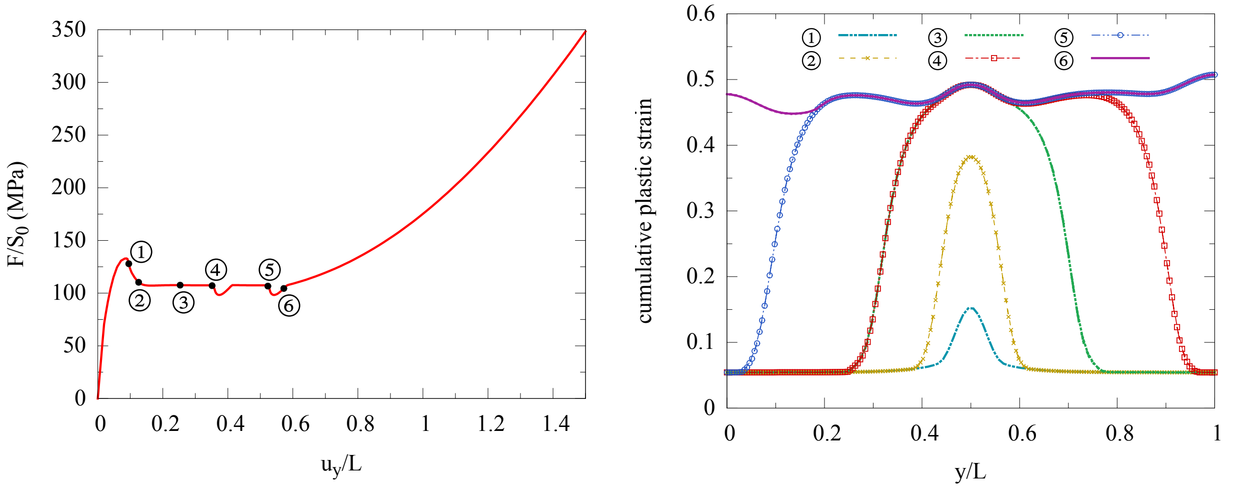

(a) *Reaction force vs. applied displacement* u_y*.*

(b) *Profiles of the cumulative plastic strain plotted along the vertical line* ($x = l/2$) *w.r.t. the reference coordinates.*

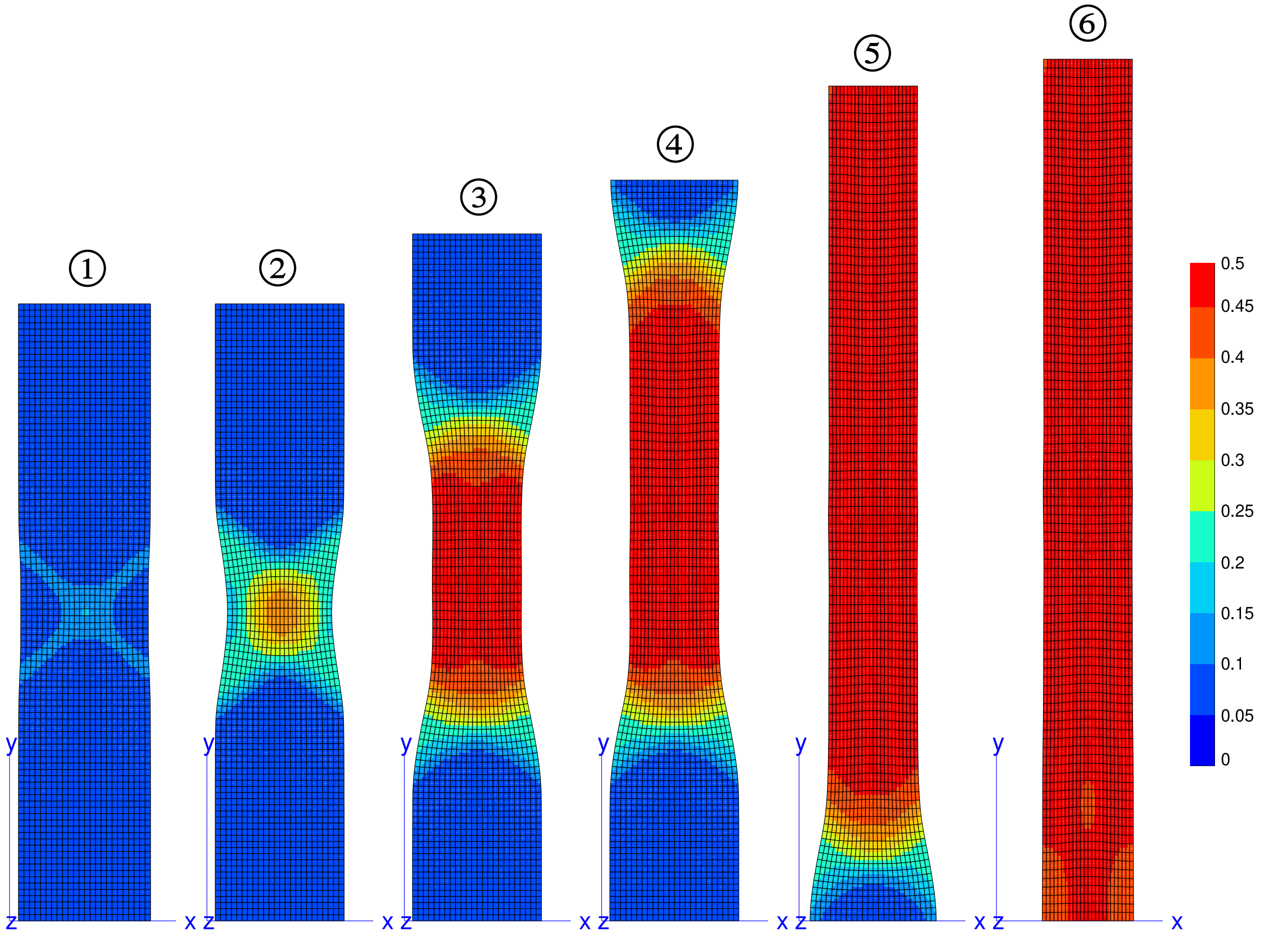

(c) *Maps of the cumulative plastic strain*

Figure 4.15: *The reaction force vs. applied displacement* u_y *and the maps of the cumulative plastic strain* p *at different levels of applied displacement. Micromorphic parameters:* $H_\chi = 10^5$ *MPa,* $A = 80$ *N. Geometry* $L = 48$ *mm,* $l = 12$ *mm.*

center of the unit cell. Different values of the volume fraction V_f are considered. Regular meshes consist of C2D8R elements (reduced integration with four integration points) which are quadratic for displacements $\underline{\boldsymbol{u}}$ and linear for the micromorphic variable p_χ. The integration of constitutive equations is achieved by using

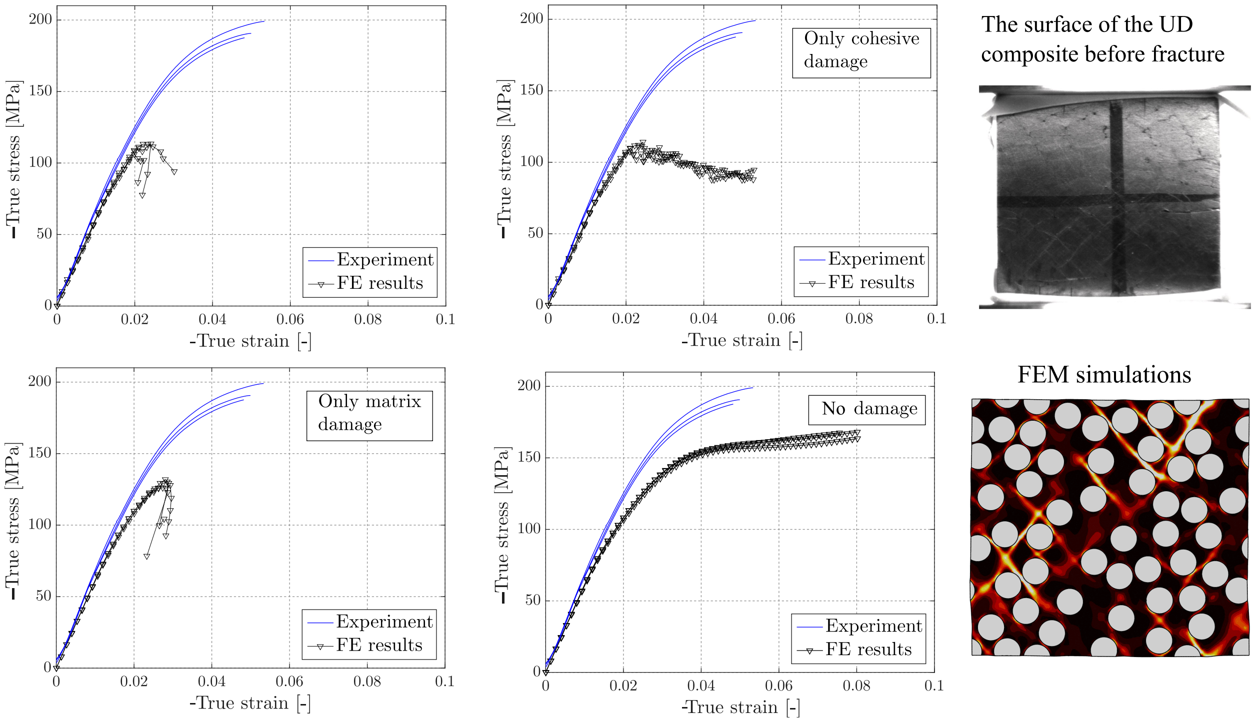

Figure 4.16: *Transverse compression on an RVE of the UD composite. Comparison of finite element simulations using different assumptions with experimental data [Chevalier, 2018; Chevalier et al., 2019]. Plane strain and periodic boundary conditions are applied to the RVE.*

an implicit θ-method integration. Fig. 4.17 shows the mesh used for three different volume fractions. A macroscopic deformation gradient $\overline{F}_{11}$ is prescribed to the unit cell with fully periodic boundary conditions. The micromorphic variable is periodic in the two directions. Plane strain conditions are prescribed. The hardening law for the matrix is given by Eq. (4.71) for the classical model and in Eq. (4.75) for the micromorphic model. The material properties of the fibers, assumed to be orthotropic linear elastic, are given in table 4.2.

E_{11}	E_{22}	E_{33}	ν_{12}	ν_{23}	ν_{31}	G_{12}	G_{23}	G_{31}
238	28	28	0.28	0.33	0.02	24	7.2	24

Table 4.2: *Elastic materials properties of the fibers. Stiffness moduli are given in GPa.*

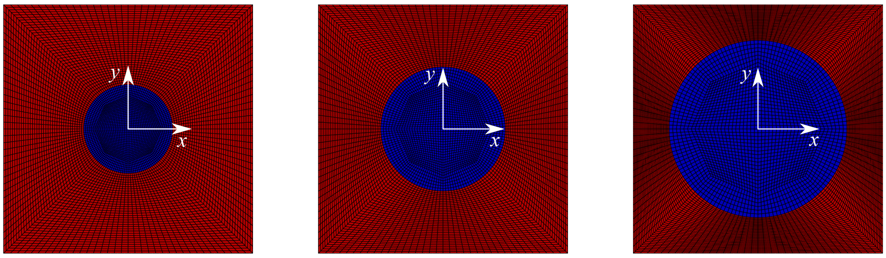

Figure 4.17: *Mesh of a square unit cell with different volume fractions (blue color) $V_f = 0.1$, 0.2 and 0.4. It contains 7344 C2D8R (reduced integration) elements of type P2P1 with 22117 nodes.*

Fig. 4.18 depicts the macroscopic stress-strain curves for different models and volume fractions. The results are compared to the classical model for the same mesh. Regarding the classical model, the width of localization bands depends on the mesh size. For instance, for small mesh sizes, the localization bands are thin. As shown in Fig. 4.19, several bands appear and propagate locally. As long as there is enough space, new bands appear. The nucleation of new bands corresponds to a sharp softening in the global stress-strain response. Numerically, this is accompanied by a bad convergence rate, particularly for finer meshes. Very small increments are then required by the Newton algorithm to converge.

On the other hand, the micromorphic model does not exhibit any mesh dependency (see Fig. 4.20). As depicted in Fig. 4.21, the plastic strain localization bands have a symmetrical distribution around the fiber. The number and the width of bands depend on the micromorphic parameter A. For small values of A, corresponding to small bandwidth, there is enough space in the matrix for new bands to appear. When new bands cannot emerge the plasticity propagates in the matrix because of the re-hardening. For higher values of A, the plastic strain is localized in wider bands. Accordingly, the propagation takes place in a shorter time leading to an earlier re-hardening.

For larger values of the volume fraction, the plastic strain is confined in a narrower region. Consequently, high values of strain gradients occur. The induced size effect is then more significant for large values of the ratio V_f. If the parameter A is sufficiently high, no stress drop is noticed. This means that the plastic strain is localized in wide bands which makes the propagation period shorter or even disappear. The finite element simulations diverge when the radius of the elastic domain σ_Y is to become negative. This issue can be solved using other models that are presented previously such as the equivalent plastic strain-based model, tensorial-based models, etc.

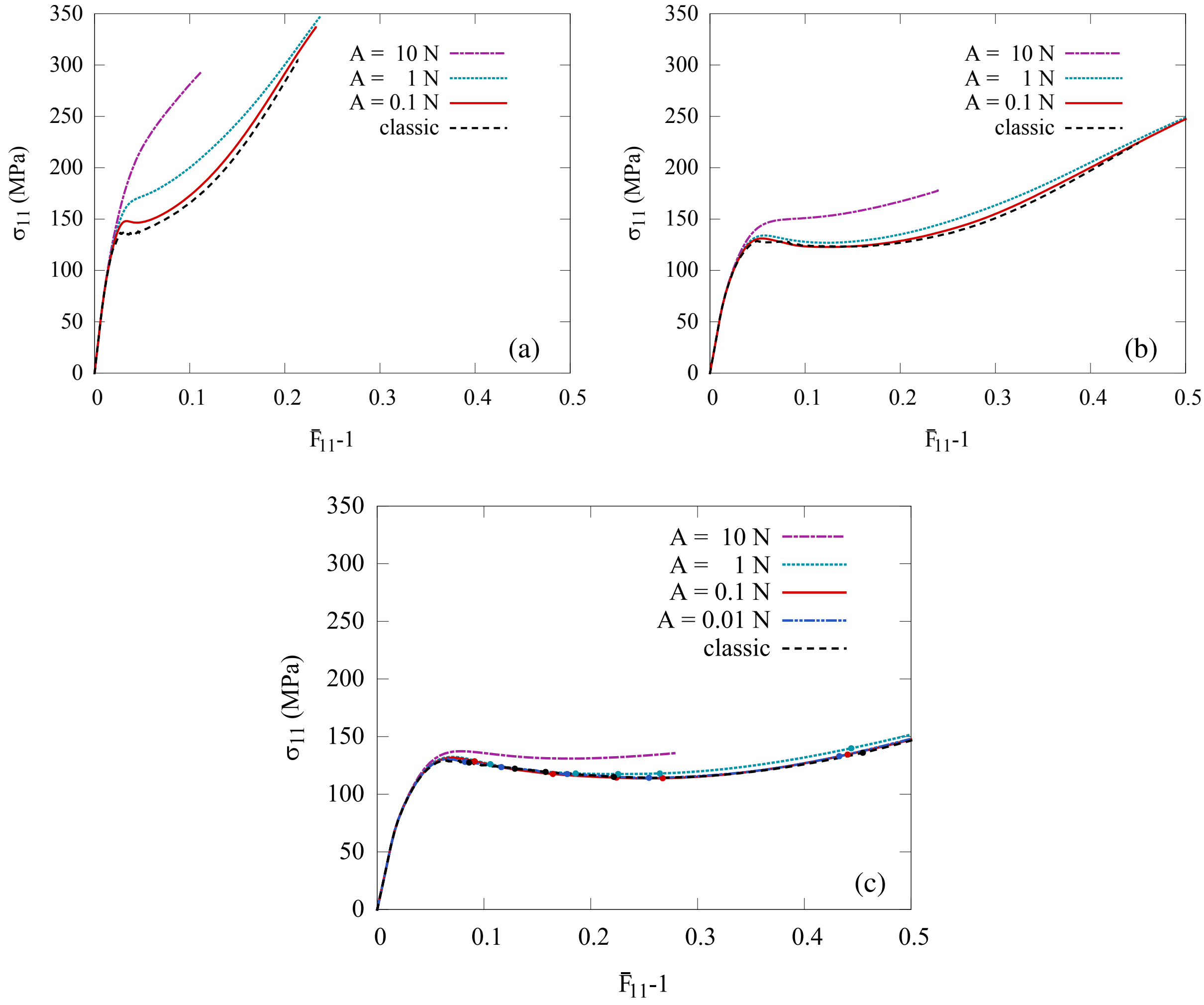

Figure 4.18: *Stress-strain curves for different values of the fiber volume fraction V_f (a) 0.4 (b) 0.2 (c) 0.1; $H_\chi = 10^5$ MPa. Maps of cumulative plastic strain corresponding to loading states identified by markers (dots) are illustrated in Fig. 4.19b and Fig. 4.21.*

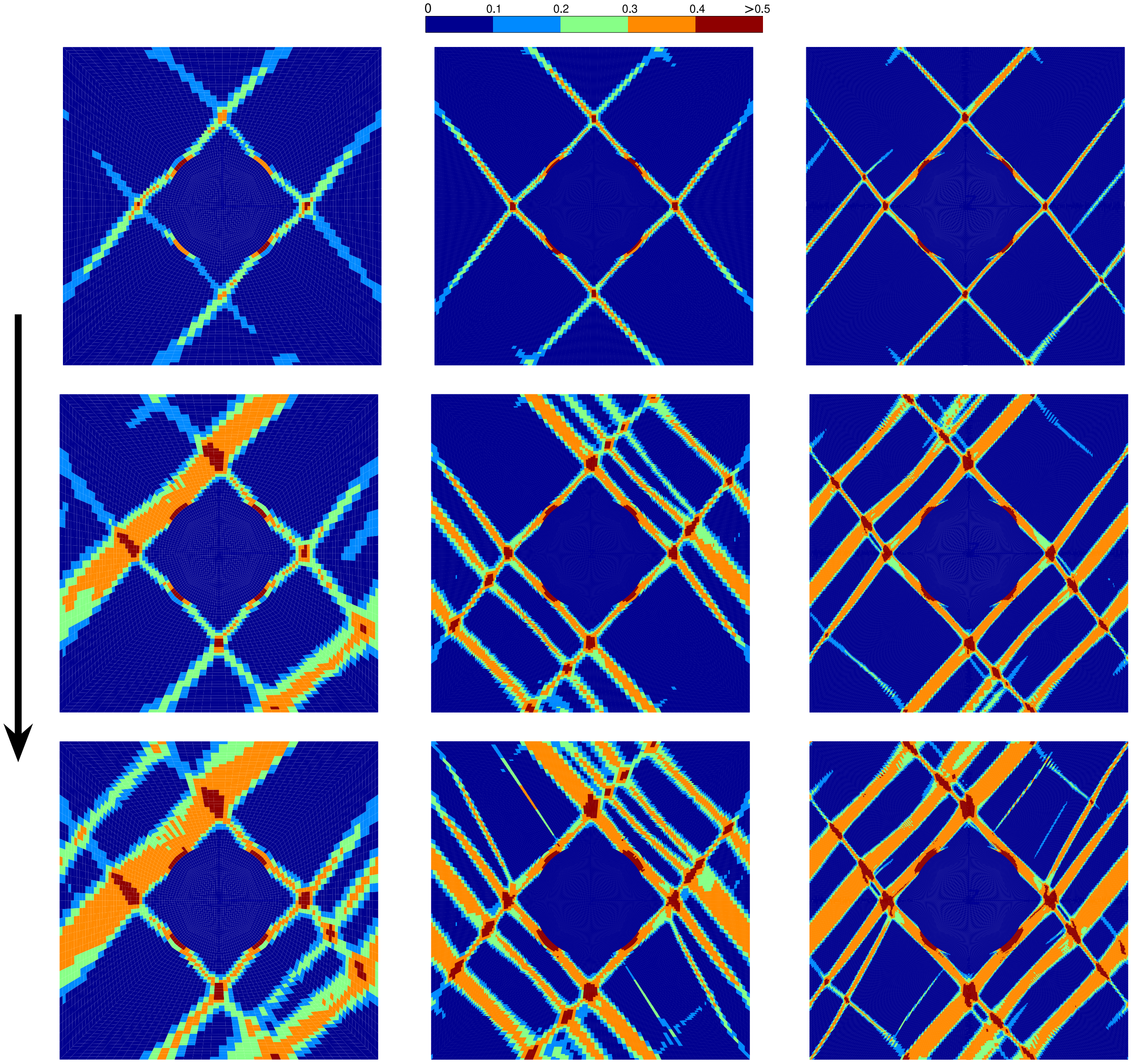

(a) 1896 elements (5581 nodes) (b) 7344 elements (22177 nodes) (c) 29376 elements (88417 nodes)

Figure 4.19: *Maps of the cumulative plastic strain for different meshes obtained at* $\overline{F}_{11} = 1.17,\ 1.258$ *and* 1.315 *using the classical model.*

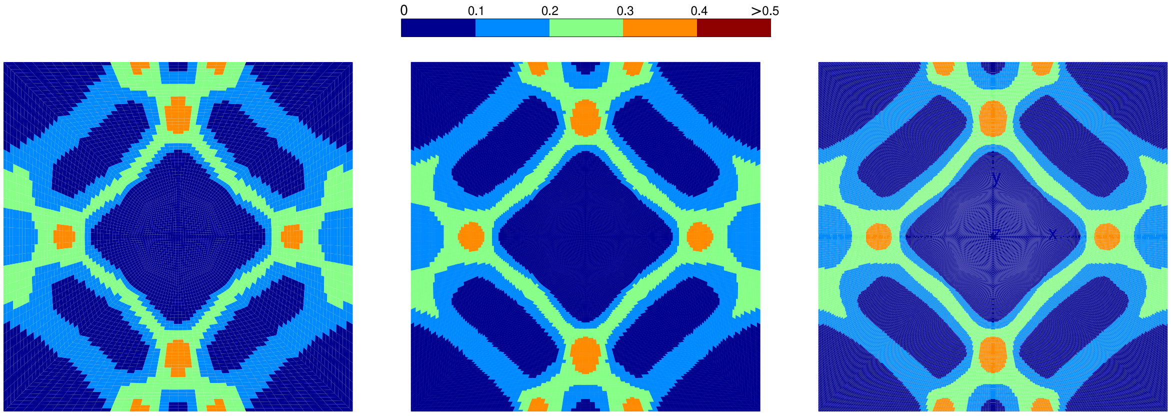

(a) 1896 elements (5581 nodes) (b) 7344 elements (22177 nodes) (c) 29376 elements (88417 nodes)

Figure 4.20: *Maps of the cumulative plastic strain* ($\overline{F}_{11} = 1.28$). *Micromorphic parameters:* $A = 0.1\ N$, $H_\chi = 10^5\ MPa$.

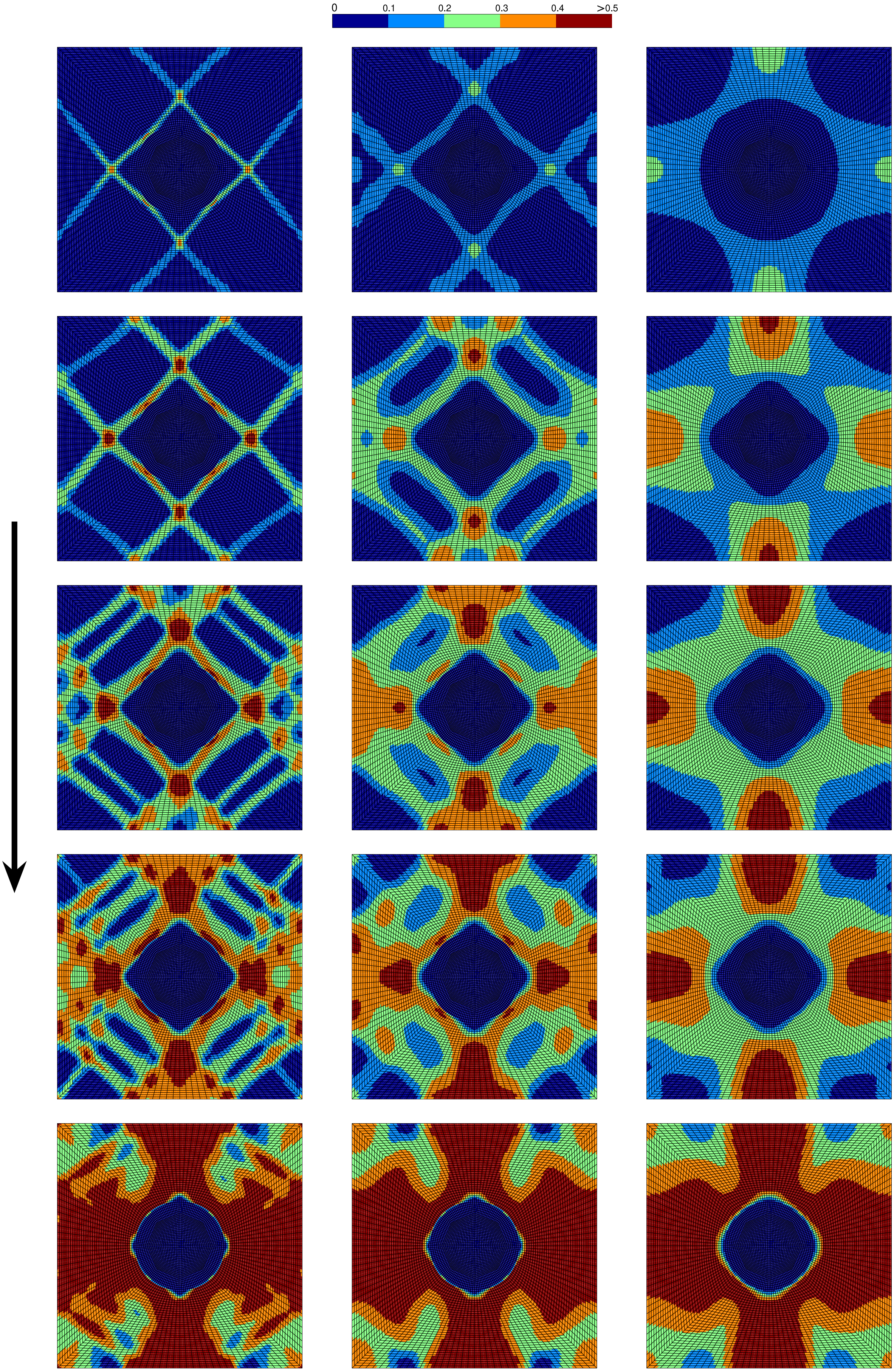

(a) $A = 0.01$ N (b) $A = 0.1$ N (c) $A = 1$ N

Figure 4.21: *Maps of the cumulative plastic strain obtained at different levels of applied macroscopic loadings.*

Now, we consider the compression of a unidirectional composite. The fibers are randomly positioned in the square RVE of side length $S_L = 0.1mm$. They were assumed to have the same radius $r_f = 5\mu m$. Periodic boundary conditions were applied to the edges of the RVE.

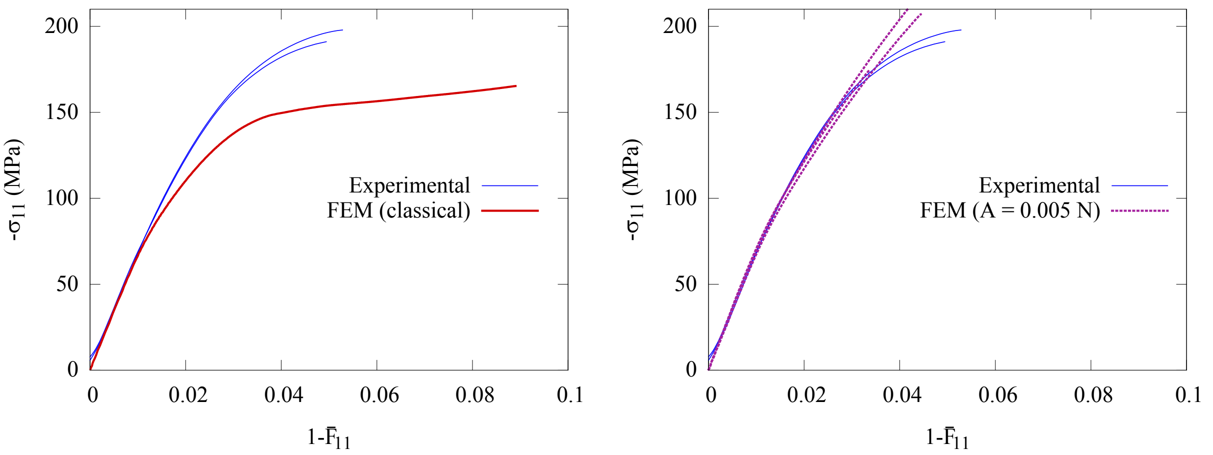

Figure 4.22: *Compression of a UD composite. Comparison of experimental results [Chevalier et al., 2019] and finite elements results obtained for the classical model and the micromorphic enhanced model.*

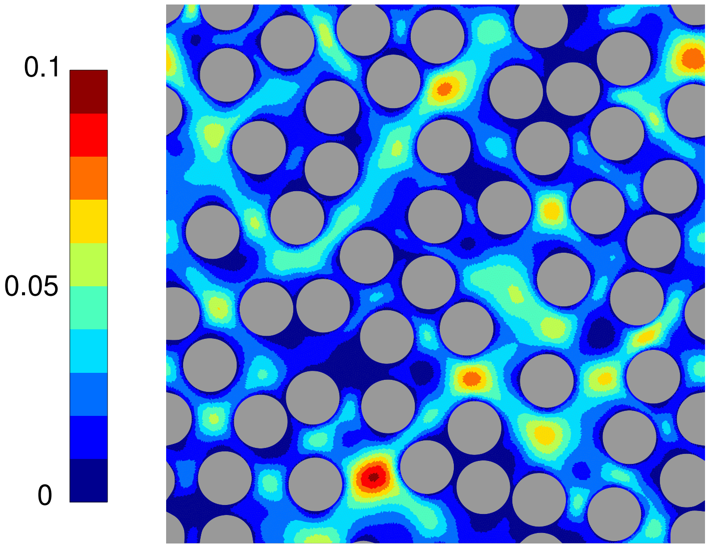

Figure 4.23: *Map of the cumulative plastic strain at* $1 - \overline{F}_{11} = 0.042$

Fig. 4.22 depicts the numerical results obtained for the classical and enhanced model. The classical using the hardening law for the bulk matrix behaviour and properties measured in bulk specimens exhibits more significant strain localization which leads to an underestimation of the stress response compared to the experimental response. The micromorphic parameter A is identified as the one that represents better the material response. The map of cumulative plastic strain is shown in Fig. 4.23. It shows that the plastic strain is localized in wide matrix pockets. If the volume fraction is lower, these pockets becomes wider and lead to more strain localization. If the confined regions of the matrix are broad, the less plastic strain gradient effect is important. For large values of the parameter A, the composite becomes stiffer. The enhanced model yields better predictions until a strain of 4%. This difference can be explained by the fact that this model does not introduce any matrix or cohesive damage which may be responsible for the nonlinearity observed before failure.

Chapter 5

Systematic micromorphic enhancement of constitutive models in FEM codes

Abstract The implementation of a systematic method for the enhancement of constitutive elastoplasticity at finite strains using the micromorphic approach is discussed. The proposed method integrates the micromorphic models discussed previously in chapters 2, 3 and 4. In particular, it has been illustrated for the case of the finite element code Z-set.

Résumé Nous présentons l'implémentation d'une méthode systématique pour pour l'enrichissement des lois de comportements en grandes déformations par l'approche micromorphe. Elle permet d'intégrer les modèles micromorphes présentés dans les chapitres 2, 3 et 4. En particulier, cette méthode a été illustrée pour le cas du code par éléments finis Z-set.

Contents

5.1 Systematic enhancement of constitutive models

The preliminary objective of the thesis is to provide a systematic approach to enhance classical constitutive models for elastoplasticity at small and finite strains. Throughout this document, several micromorphic models were investigated in order to study the properties of the regularization operators suggested by each model. The size effect resulting from each model was studied. Other micromorphic models relying on saturating variables are investigated in section 4.1. Further, micromorphic models can also rely on non-symmetric second-order tensors [Dillard et al., 2006; Cordero et al., 2010].

The micromorphic contribution in all the models that are discussed in this work are assumed to be non-dissipative. However, several works in the literature have advocated the need to consider dissipative contributions [Gudmundson, 2004; Anand et al., 2012; Jebahi et al., 2020].
Practically, the implementation of this approach requires:

- Implementation of finite elements for different types of variables: scalar, symmetric second order tensor, non-symmetric second order tensor [Forest, 2016], third-order tensors [Cordero et al., 2016], etc. The finite element implementation is detailed in 2.2.6 for scalar variables at finite strains and in 3.4 for symmetric second order tensors at small strains. In 3D cases, the total number of degrees of freedom is 3 for classical Cauchy continuum, 4 for scalar-based micromorphic continuum, 9 for symmetric second order tensor-based micromorphic continuum, etc. In 2D cases, the total number of DOFs will be reduced to 2, 3, 6, respectively.
- Enhancement of constitutive laws: the constitutive choice of the micromorphic variable leads to different types of enhancements. For instance,

  - Cumulative plastic strain → size-dependent isotropic hardening and eventually kinematic hardening (in case of the finite strain formulation w.r.t. the intermediate configuration)
  - Equivalent plastic strain → size-dependent kinematic hardening
  - Total strain tensor → size-dependent elasticity law and kinematic hardening
  - Plastic strain tensor → size-dependent kinematic hardening

- Additional evolution equations provided by the micromorphic model. The integration of these equations may be necessary.

- Calculation of consistent tangent matrices

$$[\boldsymbol{K}] = \frac{\partial \Delta \mathscr{V}_{OUT}}{\partial \Delta \mathscr{V}_{IN}} - \frac{\partial \Delta \mathscr{V}_{OUT}}{\partial \Delta \mathscr{V}_{int}} \left(\frac{\partial \mathscr{R}}{\partial \Delta \mathscr{V}_{int}} \right)^{-1} \frac{\partial \mathscr{R}}{\partial \Delta \mathscr{V}_{IN}} \tag{5.1}$$

It requires the calculation of $\frac{\partial \mathscr{V}_{OUT}}{\partial \Delta \mathscr{V}_{IN}}$, $\frac{\partial \Delta \mathscr{V}_{OUT}}{\partial \Delta \mathscr{V}_{int}}$, $\frac{\partial \mathscr{R}}{\partial \Delta \mathscr{V}_{IN}}$ terms in addition to the Jacobian matrix $\mathscr{J} = \frac{\partial \mathscr{R}}{\partial \Delta \mathscr{V}_{int}}$.

5.2 Illustration in the case of Z-set

Fig. 5.1 shows the inheritance diagram of the main classes that permits the integration of constitutive equations. The `MICROMORPHIC` class allows handling all the modifications to be made to the integration scheme of the enhanced model. A `MICROMORPHIC` class has to be implemented for each micromorphic model.

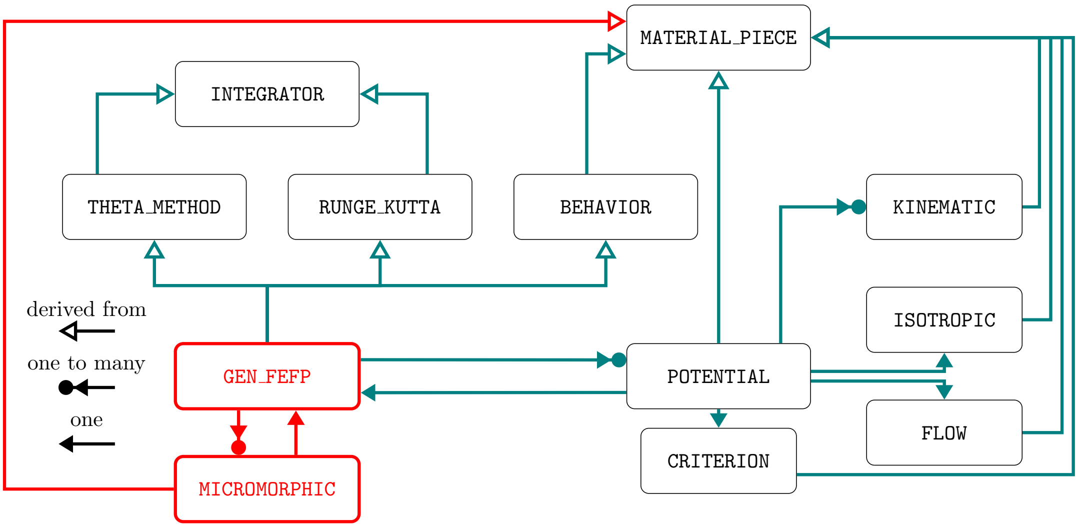

Figure 5.1: *Implementation of a new class to handle systematic enhancement of constitutive models.*

Fig. 5.2 illustrates the integration scheme of constitutive equations enhanced by the micromorphic approach. To solve the global problem, quasi-Newton algorithms are used. At each iteration of the global problem, the integration of constitutive equations is required. This can be achieved using explicit and implicit integration methods, namely Runge-Kutta and θ-methods. For explicit integration, the `derivative` method computes the increment of integrated variables $\mathscr{V}_{int}$. The `MICROMORPHIC` object allows to introduce the micromorphic contribution through the method `enhance_derivative(...)`.

For implicit integration, the increments of integrated variables are found by solving the equation

$$\Delta \mathscr{V}_{int}^{k+1} = \Delta \mathscr{V}_{int}^{k} - [J]^{-1} \mathscr{R}^{k} \tag{5.2}$$

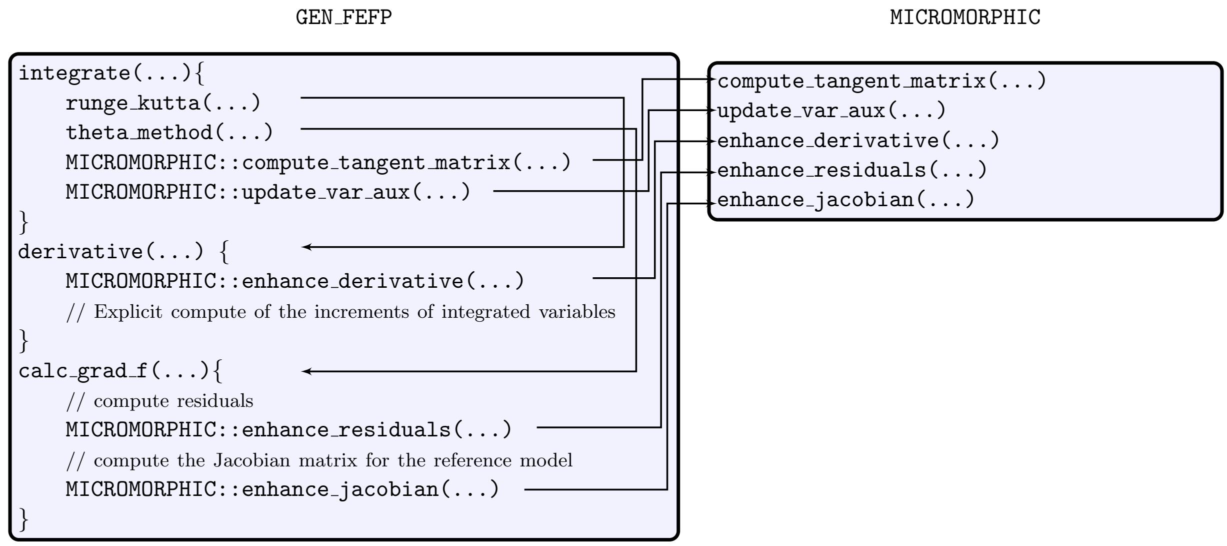

Figure 5.2: *The modification of the integration scheme of constitutive equations.*

where

$$[J] = \left.\frac{\partial \mathscr{R}}{\partial \Delta \mathscr{V}_{int}}\right|_{k+1} \tag{5.3}$$

where is $\mathscr{J}$ the Jacobian matrix (see appendix C) and $\mathscr{R}^k$ denotes the local residual at the k-th iteration. The Jacobian matrix and the residuals of the reference model are computed. The residuals are modified in `enhance_residuals(...)`. Additional terms are introduced to the Jacobian matrix by the micromorphic model via the method `enhance_jacobian(...)`.

Finally, the consistent tangent matrix in Eq. (5.1) is computed via the method `compute_tangent_matrix(...)`. The auxiliary variables (*e.g.* stress) that depends on the micromorphic parameters are updated in `update_var_aux(...)`.

5.3 User interface

This section describes the input file format for the micromorphic generalized behavior. First, a simplified version of the basic input file for a small strain generalized behavior is presented. Fig. 5.3 shows the format of a material file for a generalized constitutive framework of small strain elastoplasticity called `gen_evp` [Foerch et al., 1997]. This framework is available in the material library Z-mat. The material behavior is implemented independently from finite element technologies. For instance, the material behavior `gen_evp` is used in 2D (plane strain, plane stress, axisymmetric, ...) and 3D cases. The material file can be deciphered as follows:

- `**elasticity`: this line creates an `ELASTICITY` object to implement the linear Hooke's law of elasticity. The symmetries of the fourth-order elasticity tensor must be specified using keywords such as `isotropic`, `cubic`, `orthotropic`, etc.

- `**thermal_strain`: it creates an object that handles the computation of the eigenstrain tensor resulting from isotropic or anisotropic thermal expansion.

- `**potential`: this command initiates the creation of a `POTENTIAL` object. This object manages many bricks of viscoplastic models. The flow rule of the viscoplastic model either for time-independent or rate-dependant plasticity is specified after the command `*flow` (*e.g.*, `plasticity, norton`, etc.). The yield criterion is specified using the command `*criterion`. The command `*isotropic` manages the evolution laws of the isotropic hardening. The kinematic hardening rules are specified after the command `*kinematic`. Several kinematic hardening rules are possible. The resulting back stress is obtained as the sum of the back stress yielded by each kinematic hardening rule.

```
***mesh []                % 3D, 2D (plane strain, plane stress, ...)
   ....
   ....
***behavior gen_evp
 **elasticity []          % isotropic, cubic, orthotropic, ...
   ....
 **thermal_strain []      % isotropic, anisotropic
   ....
 **potential [N]          % plastic, viscoplastic
  *flow []                % plasticity, norton, ...
  *criterion []           % mises, hill, ...
  *isotropic []           % linear, nonlinear
   ....
  *kinematic [n]          % linear, nonlinear, ...
   ....
***return
```

Figure 5.3: *The format of a material file for the small strain generalized behavior* `gen_evp`.

As shown in Fig. 5.4, the user input file for the new implementation is kept similar to the previous interface. For classical finite strain elastoplasticity, a new generalized behavior using the multiplicative decomposition `gen_fefp` is implemented. Proper finite element implementations should be selected at finite strains, which are different than the ones used for small strains models. The interpretation of different commands specified in the input file is different for this behavior. The elasticity law is given in the intermediate configuration using different stress and strain measures (e.g. $\underset{\sim}{\boldsymbol{\Pi}}^e = \mathbb{C} : \underset{\sim}{\boldsymbol{E}}^e$). The yield criterion and the flow rules are re-expressed in terms of the Mandel stress tensor instead of the Cauchy stress tensor as shown in chapter 1. This generalized behavior enables the user to add a constitutive equation for the plastic spin after the command `**plastic_spin`.

The regularization of elastoplasticity constitutive equations involves an intrinsic length scale to be provided by the user. Indeed, the refinement of the mesh must be adequate for a given length scale. Practically, the mesh size should be smaller than the length scale. The scalar micromorphic model requires at least two parameters: generalized modulus $\underset{\sim}{\boldsymbol{A}}$ and the penalty parameter H_χ. The parameter H_χ can be used to tune the internal length scale as well. For symmetric tensorial models, the generalized moduli are given by sixth-order tensors $\underset{\approx}{\boldsymbol{A}}$ and fourth order penalization tensor $\underset{\approx}{\boldsymbol{H}}_\chi$. The command `*DXelasticity` creates a tensor for generalized moduli ($\underset{\sim}{\boldsymbol{A}}$, $\underset{\approx}{\boldsymbol{A}}$, etc.). The rank of the tensor is provided by the `MICROMORPHIC` object. The penalty parameters are specified after the command `*Hx`.

Supplementary parameters might be necessary to integrate the new internal (or auxiliary) variables with which micromorphic variables are associated. In the case of dissipative micromorphic models, the micromorphic strain is additively or multiplicatively split to *"elastic"* and *"inelastic"* parts. That means that extra evolution equations (flow rules) are expected.

```
***mesh []               % 3D, 2D (plane strain,axisymmetric), ...
....
***behavior gen_fefp
 **elasticity []         % isotropic, cubic, orthotropic, ...
   ....
 **thermal_strain []     % isotropic, anisotropic
   ....
 **potential [N]         % plastic, viscoplastic
  *flow []               % plasticity, norton, ...
  *criterion []          % mises, hill, ...
  *isotropic []          % linear, nonlinear
   ....
  *kinematic [n]         % linear, nonlinear, ...
   ....

**plastic_spin []
  ....
**micromorphic []
  *DXelasticity []     % isotropic, anisotropic
   ....
  *Hx ....
***return
```

Figure 5.4: *The format of the material file for the extension of the generalized behavior to finite strains and its micromorphic enhancement.*

Finally, it is noteworthy to mention that the user material file for the generalized micromorphic model, illustrated in Fig. 5.4, may evolve in the future. Hopefully, more options will be supported in order to cover a wide range of micromorphic models.

Conclusion

Summary of main results

A systematic and thermodynamically-consistent method to extend thermo-elastoviscoplastic models to finite strain was proposed. The constitutive equations are expressed in the local isoclinic intermediate configuration, in terms of the Mandel stress tensor, which is generally non-symmetric. This method relies upon the multiplicative decomposition of the deformation gradient into thermo-elastic and inelastic parts. This framework combines many deformation mechanisms combining thermo-plasticity, viscosity and possibly damage, with no need for further multiplicative decompositions of the thermo-elastic or inelastic parts. Anisotropy is incorporated by means of material directors and associated structural tensors and the plastic spin concept which are often missing in existing standard formulations. The present framework is illustrated through various models, including isotropic and anisotropic (visco)-plasticity with isotropic and kinematic hardening laws. A nonlinear kinematic hardening rule including dynamic and static recovery terms is considered. In the case of linear kinematic hardening, the models based on the Jaumann rate and the multiplicative decomposition exhibit stress oscillations. However, by including the dynamic recovery term, the finite strain models provide similar predictions if proper material parameters are used.

In general, the expression of the plastic spin is obtained from the normality rule when the anti-symmetric part of the Mandel stress tensor is taken into account in the yield criterion. Meanwhile, a constitutive equation for the plastic spin can always be included in the present framework to model the spin of material directors w.r.t. material lines. The effect of plastic spin was illustrated in the case of anisotropic Hill's criterion and crystal plasticity. This effect is not negligible, particularly for materials characterised by a high degree of anisotropy under large plastic deformation. The comparison between hypo-elastoplastic models applied to crystal plasticity shows that the response depends heavily on the objective stress rate. The multiplicative-based model remains the reference for crystal plasticity as it was successfully validated by experiments, *e.g.* Duchene et al. [2008].

The computational performance of the proposed approach is slightly more expensive compared to hypo-elastoplastic formulation. Meanwhile, it remains a better alternative to model anisotropic plasticity. Further, the use of a thermodynamically consistent formulation of constitutive equations ensures increased reliability of model predictions.

The second part addresses the systematic enhancement of constitutive equations for elastoplasticity at small and finite strains using the micromorphic approach. The micromorphic elastoplastic models are used to model size effects and to regularize finite element simulations of plastic strain localization by cancelling the spurious mesh-dependency linked to classical continua without intrinsic length. The choice of the micromorphic variable and free energy potentials lead to a wide range of constitutive models. Three finite strain formulations are discussed based on quadratic functions of the gradient terms w.r.t. either Eulerian, Lagrangian or intermediate configurations. The choice of an Eulerian or Lagrangian gradient leads to size-dependant phenomena similar to small strain versions. Meanwhile, due the fact that the intermediate configuration is incompatible and is defined only locally, the formulation based on the convected gradient to this configuration induces a supplementary second-order back stress term. Significant differences between different finite strain formulations are observed, particularly for cyclic loadings. Ultimately, the choice of the best formulation remains material-dependent.

Since they introduce only one additional degree of freedom, the scalar micromorphic models are recommended due to their low computational cost. Meanwhile, these models have some drawbacks due to the fact that scalar variables do not contain enough information about the flow direction. Moreover, the cumulative plastic strain based model induces a softening in regions characterised by a non-smooth profile of the plastic field. When the radius of the elastic domain vanishes, numerical difficulties leading to the divergence of the integration scheme are noticed. Another alternative relies on the equivalent plastic strain which induces a size-dependent kinematic hardening. The definition of the back stress is not however determined at zero plastic strains which may lead to numerical difficulties in the case of cyclic loading or in the regions where the plastic strain vanishes. Numerical comparison between micromorphic approach and Lagrange-multiplier based strain gradient plasticity was carried out. Regarding the computational cost, the micromorphic approach is shown to perform slightly better than the Lagrange-multiplier based approach which introduces a supplementary degree of freedom. Meanwhile, the micromorphic approach may perform poorly for very large penalty modulus in the case of strain localization.

To remedy to issues related to scalar micromorphic models, tensorial micromorphic models are proposed. For instance, the model based on the plastic strain tensor induces a size-dependent kinematic hardening. Another model relying on the total strain tensor enhances the constitutive equations of both elasticity and kinematic hardening. Accordingly, this model is convenient to model strain gradient elastoplasticity. The main drawback of tensor-based models is the huge number of degrees of freedom that are introduced.

The characteristic length suggested by each model depends on the boundary value problem. Indeed, its evolution is determined by the constitutive behavior. Explicit expressions of characteristic length are provided for some simple loadings case and linear constitutive equations. In general case, it is not explicitly accessible through simple analysis. Its identification can be achieved by fitting experimental data as it was conducted in the case of a polymer composite.

The width of the localization bands is given by the generalized moduli and the softening modulus. The broadening of the localization band observed for a saturating softening law can be prevented by using saturating micromorphic variables or adjusting the higher order moduli to depend on the plasticity evolution.

Main contributions

Most developments carried-out during the thesis are implemented in the finite element software Z-set. We took advantage of numerous developments that have been already implemented in the software, *e.g.* finite element technologies, micromorphic models at small and finite strain, etc. The main contributions and new developments that I made throughout this work are summarized as follows:

1. **Numerical implementations**: a robust implicit and explicit integration schemes are provided for each model. First, a finite strain multi-mechanism elastoplastic model for the classical framework was implemented. Second, explicit and implicit integration schemes are developed and implemented for scalar micromorphic variables at small and finite strains, associated to the following variables: the cumulative plastic strain, the equivalent total strain, the equivalent plastic strain, the saturating variables presented in section 4.1. Finally, a finite element formulation of symmetric tensor based micromorphic models was implemented in the framework of small strains with both implicit and explicit integration schemes.

2. **Systematic comparison of small/finite strain formulations**: regarding the classical continuum, the proposed formulation based on the multiplicative decomposition is compared systematically to hypoelastic formulations for volume element simulations and structural applications. A comparison of the response of several scalar-based micromorphic models at finite strain was carried out. At small strain, analytical solutions are provided for the simple glide problem in the case of scalar and tensor micromorphic variables. In addition, the response of tensor micromorphic models was compared to scalar micromorphic models for 1D, 2D and 3D problems.

3. **Material modelling**: new micromorphic models were proposed. First, an extension of the micromorphic model relying on the equivalent plastic strain to finite strain was developed in section 2.2.5. A micromorphic model with a saturating micromorphic variable is proposed in section 4.1. The resulting size effect can either saturate or even vanishes at large values of plastic strain. A micromorphic

enhancement of the Kocks-Meckings model is proposed using a variable associated to the cumulative plastic strain.

4. **Industrial applications**: the proposed approach is used for several industrial applications. The classical multiplicative finite strain formulation is applied to deep drawing with anisotropic Hill plasticity and a supplementary plastic spin. Further, the simulation of a single crystal turbine blade is achieved considering two slip system families and thermal strains with material parameters depending on temperature. On the other hand, the micromorphic approach is used to simulate bending and torsion tests. Moreover, the regularization of numerous finite element simulations involving strain localization as in composite materials are studied.

Short-term prospects

The proposed approach is promising and worth further exploration. Most of yield criteria widely used in finite element codes, except for the well-established finite crystal plasticity, are expressed in terms of the symmetric Cauchy stress. Accordingly, the database of material parameters has been identified using this sort of models. The fact that the Mandel stress tensor is not symmetric raises two issues. First, in the event that the elastic strain is not negligible, a re-identification of material parameters may be necessary in order to obtain satisfactory predictions. Second, for anisotropic elasticity, our methodology requires the formulation of yield criteria expressed in terms of the invariants of the non-symmetric Mandel stress tensor [Itskov and Aksel, 2004; Ulz, 2011].

So far, the proposed approach has focused on associated and incompressible elastoplastic models. Meanwhile, it can be readily extended to non-associated and pressure-sensitive models. In Finite element codes, the constitutive modeling of damage is usually coupled with elastoplasticity. In fact, the theoretical and the numerical tools developed herein for plasticity are efficient to deal with this type of models as it has been investigated thoroughly in literature [Forest, 2009; Saanouni and Hamed, 2013; Brepols et al., 2017; Diamantopoulou et al., 2017].

The micromorphic model based on the cumulative plastic strain was shown to induce a vanishing yield radius. The finite element simulations diverge when the consistency condition cannot be satisfied. A robust solution for this issue is the purpose of future developments. In chapter 3, a finite strain formulation of tensor-based micromorphic models is proposed. Its finite element implementation is left to future studies.

The micromorphic approach can also be used to implement strain gradient elasticity. The micromorphic variable can be either associated to scalar (*e.g.* the equivalent total strain) or tensor variables (*e.g.* total strain tensor detailed in section 3.2). In the case of the tensor-based model, the higher-order moduli can be identified through homogenization schemes [Auffray et al., 2010].

Long-term prospects

This work should be considered as a further step towards the systematic use of gradient models for industrial applications. The systematic use of these models will allow to further explore their advantages and disadvantages. However, the appropriate choice of constitutive models is still material-dependent. The identification of material models implies the use of more advanced experimental methods to determine the material parameters. The evolution of the parameters as a function of the temperature, the loading rate, the material history, etc. remains a challenge. Certainly, the understanding of mechanisms behind these aspects will allow to propose more predictive models.

An optimized implementation in commercial packages may require a privileged access to the source code. This need is usually met by the implementation of User subroutines that requires a high-level of expertise. We believe that an easy access to such models through built-in modules will lead to their growing deployment in industry.

In the literature, several gradient-based theories have been developed. A systematic comparison of these approaches is necessary to elucidate the pros and cons of each approach for industrial applications.

Valorization

In this work, several applications are studied at small and finite strains solutions. Benchmarks tests are provided for the community of researchers and the users of the material library of the Z-set suite. Some of the contributions are ready to use in the latest version of Z-set (9.1.4), in particular the developments related to the extension of small strains elastoplasticity models to finite strains in the classical framework.

The first two chapters are the subject of two articles:

- **Abatour, M.**, Ammar, K., Forest, S., Ovalle-Rodas, C., Osipov, N., and Quilici, S. (2021). A generic formulation of anisotropic thermo-elastoviscoplasticity at finite deformations for Finite Element codes. (preprint at `https://hal.archives-ouvertes.fr/hal-03462216`)
- **Abatour, M.**, Forest, S., Ammar, K., Ovalle-Rodas, C., Osipov, N., and Quilici, S. Towards robust finite gradient plasticity modeling and simulation, under review.

The research results of this thesis were communicated in several international conferences:

- 14^{th} World Congress in Computational Mechanics (WCCM) and ECCOMAS Congress 2020 from January 11 to 15, 2021 (Virtual Congress).
- 25^{th} International Congress of Theoretical and Applied Mechanics (ICTAM) from 22 to 27 August 2021 (Virtual Congress).
- 16^{th} International Conference on Computational Plasticity (COMPLAS) held in Barcelona, Spain, from 7 to 9 September 2021.
- 8^{th} European Congress on Computational Methods in Applied Sciences and Engineering (ECCOMAS) held in Oslo, Norway, from 5 to 9 June 2022.
- 11^{th} European Solid Mechanics Conference (ESMC) held in Galway, Ireland, from 4 to 8 July 2022.

Some of the results are also published in a national conference proceedings:

- **Abatour, M.**, Forest, S., Ammar, K., Ovalle, C., Osipov, N., and Quilici, S. (2022). Méthode systématique de régularisation des lois thermo-élastoviscoplastiques en grandes déformations. In 15ème colloque national en calcul des structures, 83400 Hyères-les-Palmiers, France. Université Polytechnique Hauts-de-France [UPHF]. `https://hal.archives-ouvertes.fr/hal-03717640`.

Appendices

Appendix A

Hypo-elastoplastic formulations

In mechanics of materials, the constitutive relations are assumed to be invariant under superposed rigid-body motion. Equivalently, material properties are assumed to be independent of the respective frame of reference (observer). Obviously, constitutive equations expressed in terms of Lagrangian quantities satisfy this principle thanks to their invariance. In Eulerian rate-type formulations, constitutive equations are formulated in terms of objective rates of stress measures. It is therefore essential to derive stress rate measures that are objective. Generally, objective rates may be classified into two different categories, namely corotational and convected rates.

Scalar, vector and tensor fields are called objective if they transform, under a rigid body motion, according to the following equations:

- Scalar field: $f' = f$, *e.g.* temperature T
- Vector field: $\underline{\boldsymbol{u}}' = \underset{\sim}{\boldsymbol{Q}}\underline{\boldsymbol{u}}$, *e.g.* displacement vector
- General second-order tensor: $\underset{\sim}{\boldsymbol{S}}' = \underset{\sim}{\boldsymbol{Q}}\underset{\sim}{\boldsymbol{S}}\underset{\sim}{\boldsymbol{Q}}^T$, *e.g.* Cauchy stress $\underset{\sim}{\boldsymbol{\sigma}}$
- Two-point second-order tensor: $\underset{\sim}{\boldsymbol{P}}' = \underset{\sim}{\boldsymbol{Q}}\underset{\sim}{\boldsymbol{P}}$, *e.g.* the deformation gradient $\underset{\sim}{\boldsymbol{F}}$

The Cauchy stress $\underset{\sim}{\boldsymbol{\sigma}}$ is assumed to be objective. Likewise, we can prove that $\underset{\sim}{\boldsymbol{\tau}}$, $\underset{\sim}{\boldsymbol{P}}$, $\underset{\sim}{\boldsymbol{\Sigma}}$ and $\underset{\sim}{\boldsymbol{M}}$ are objective. Lagrangian quantities like Piola tensor stress $\underset{\sim}{\boldsymbol{\Pi}}$ are invariant. However, the material time derivative of Cauchy stress is not objective

$$\dot{\underset{\sim}{\boldsymbol{\sigma}}}' = \dot{\underset{\sim}{\boldsymbol{Q}}}\underset{\sim}{\boldsymbol{\sigma}}\underset{\sim}{\boldsymbol{Q}}^T + \underset{\sim}{\boldsymbol{Q}}\dot{\underset{\sim}{\boldsymbol{\sigma}}}\underset{\sim}{\boldsymbol{Q}}^T + \underset{\sim}{\boldsymbol{Q}}\underset{\sim}{\boldsymbol{\sigma}}\dot{\underset{\sim}{\boldsymbol{Q}}}^T \tag{A.1}$$

From (A.1), we notice that if $\underset{\sim}{\boldsymbol{\sigma}}$ is constant, $\dot{\underset{\sim}{\boldsymbol{\sigma}}}$ depend on the frame. Therefore, we need other stress rates which are invariant w.r.t. the frame. Two main classes of rates are discussed here. The convected derivative can be attained by the push-forward operation of the material-time differentiation of the quantity pulled back. The corotational derivatives can be captured as the convected derivative taking account only of material element rotation.

A.1 Corotational rates

The corotational rate of any Eulerian second rank $\underset{\sim}{\boldsymbol{T}}$ tensor can be expressed as

$$\underset{\sim}{\boldsymbol{T}} = \dot{\underset{\sim}{\boldsymbol{T}}} + \underset{\sim}{\boldsymbol{T}}\underset{\sim}{\boldsymbol{\Omega}} - \underset{\sim}{\boldsymbol{\Omega}}\underset{\sim}{\boldsymbol{T}} \tag{A.2}$$

with $\dot{\underset{\sim}{\boldsymbol{T}}}$ is the material time derivative of $\underset{\sim}{\boldsymbol{T}}$ and $\underset{\sim}{\boldsymbol{\Omega}}$ is a skew-symmetric second rank tensor called spin tensor. Many corotational rates can be distinguished depending on the spin tensor. For example:

- Jaumann–Zaremba: If we express (A.1) in the non rotating frame, we get

$$\dot{\underset{\sim}{\boldsymbol{\sigma}}}^J = \dot{\underset{\sim}{\boldsymbol{\sigma}}} + \underset{\sim}{\boldsymbol{\sigma}}\underset{\sim}{\boldsymbol{W}} - \underset{\sim}{\boldsymbol{W}}\underset{\sim}{\boldsymbol{\sigma}} \tag{A.3}$$

where $\underset{\sim}{\boldsymbol{W}} = \dot{\underset{\sim}{\boldsymbol{Q}}}\underset{\sim}{\boldsymbol{Q}}^T$ is a skew-symmetric second order tensor. It is also the skew-symmetric part of the spatial velocity gradient $\underset{\sim}{\boldsymbol{L}}$.

- Green-Naghdi:

$$\dot{\underset{\sim}{\boldsymbol{\sigma}}}^{GN} = \underset{\sim}{\boldsymbol{R}} \left[\frac{\mathrm{d}}{\mathrm{d}t} \left(\underset{\sim}{\boldsymbol{R}}^T \underset{\sim}{\boldsymbol{\sigma}} \underset{\sim}{\boldsymbol{R}} \right) \right] \underset{\sim}{\boldsymbol{R}}^T = \dot{\underset{\sim}{\boldsymbol{\sigma}}} + \underset{\sim}{\boldsymbol{\sigma}} \dot{\underset{\sim}{\boldsymbol{R}}} \underset{\sim}{\boldsymbol{R}}^T - \dot{\underset{\sim}{\boldsymbol{R}}} \underset{\sim}{\boldsymbol{R}}^T \underset{\sim}{\boldsymbol{\sigma}} \tag{A.4}$$

In this case, the spin tensor is $\dot{\underset{\sim}{\boldsymbol{R}}}\underset{\sim}{\boldsymbol{R}}^T$. This derivative is defined as the push-forward of the time derivative in the reference configuration after a pull-back operation considering only the polar rotation tensor $\underset{\sim}{\boldsymbol{R}}$ *i.e.* performing the pull-back and push-forward operations as the stretch component of $\underset{\sim}{\boldsymbol{F}}$ is ignored.

$$\underset{\sim}{\boldsymbol{W}} = \dot{\underset{\sim}{\boldsymbol{R}}} \underset{\sim}{\boldsymbol{R}}^T + \frac{1}{2} \underset{\sim}{\boldsymbol{R}} \left(\dot{\underset{\sim}{\boldsymbol{U}}} \underset{\sim}{\boldsymbol{U}}^{-1} - \underset{\sim}{\boldsymbol{U}}^{-1} \dot{\underset{\sim}{\boldsymbol{U}}} \right) \underset{\sim}{\boldsymbol{R}}^T \tag{A.5}$$

From (A.5), we can see that Jaumann and Green-Naghdi derivatives are equivalent if $\underset{\sim}{\boldsymbol{U}}^{-1}$ and $\dot{\underset{\sim}{\boldsymbol{U}}}$ commute.

- Logarithmic:

$$\underset{\sim}{\boldsymbol{\Omega}} = \underset{\sim}{\boldsymbol{W}} + \sum_{i \neq j}^{m} \left[\frac{\lambda_i + \lambda_j}{\lambda_i - \lambda_j} + \frac{2}{\log(\lambda_i) - \log(\lambda_j)} \right] \underset{\sim}{\boldsymbol{P}}_i \underset{\sim}{\boldsymbol{D}} \underset{\sim}{\boldsymbol{P}}_j \tag{A.6}$$

with λ_i denoting the m ($1 \leq m \leq 3$) distinct principal values of $\underset{\sim}{\boldsymbol{B}}$, and $\underset{\sim}{\boldsymbol{P}}_i$ the corresponding eigenprojection tensors.

$$\underset{\sim}{\boldsymbol{P}}_i = \delta_{1m} \underset{\sim}{\boldsymbol{1}} + \prod_{j=1, j \neq i}^{m} \frac{\underset{\sim}{\boldsymbol{B}} - \lambda_j \underset{\sim}{\boldsymbol{1}}}{\lambda_i - \lambda_j} \tag{A.7}$$

It can be shown that [Xiao et al., 1998]:

$$\dot{\underset{\sim}{\boldsymbol{\tau}}}^{log} = 2\mu \underset{\sim}{\boldsymbol{D}} + \lambda (tr \underset{\sim}{\boldsymbol{D}}) \underset{\sim}{\boldsymbol{1}} \Leftrightarrow \underset{\sim}{\boldsymbol{\tau}} = 2\mu \log(\underset{\sim}{\boldsymbol{V}}) + \lambda \left(tr \log(\underset{\sim}{\boldsymbol{V}}) \right) \underset{\sim}{\boldsymbol{1}} \tag{A.8}$$

where the Hencky strain

$$\log \underset{\sim}{\boldsymbol{V}} = \frac{1}{2} \sum_{i=1}^{m} \log(\lambda_i) \underset{\sim}{\boldsymbol{P}}_i \tag{A.9}$$

A.2 Convected rates

- Truesdell: is defined in terms of the Piola transformation[1] of the time derivative of the second Piola–Kirchhoff stress

$$\overset{\circ}{\underset{\sim}{\boldsymbol{\sigma}}} = J^{-1} \underset{\sim}{\boldsymbol{F}} \left[\frac{\mathrm{d}}{\mathrm{d}t} \left(J \underset{\sim}{\boldsymbol{F}}^{-1} \underset{\sim}{\boldsymbol{\sigma}} \underset{\sim}{\boldsymbol{F}}^{-T} \right) \right] \underset{\sim}{\boldsymbol{F}}^T = \dot{\underset{\sim}{\boldsymbol{\sigma}}} - \underset{\sim}{\boldsymbol{L}} \underset{\sim}{\boldsymbol{\sigma}} - \underset{\sim}{\boldsymbol{\sigma}} \underset{\sim}{\boldsymbol{L}}^T + trace(\underset{\sim}{\boldsymbol{D}}) \underset{\sim}{\boldsymbol{\sigma}} \tag{A.10}$$

The Truesdell derivative can also be expressed in terms of Kirchhoff stress $\underset{\sim}{\boldsymbol{\tau}} = J \underset{\sim}{\boldsymbol{\sigma}}$ as

$$\overset{\circ}{\underset{\sim}{\boldsymbol{\tau}}} = \underset{\sim}{\boldsymbol{F}} \left[\frac{\mathrm{d}}{\mathrm{d}t} \left(\underset{\sim}{\boldsymbol{F}}^{-1} \underset{\sim}{\boldsymbol{\tau}} \underset{\sim}{\boldsymbol{F}}^{-T} \right) \right] \underset{\sim}{\boldsymbol{F}}^T = \dot{\underset{\sim}{\boldsymbol{\tau}}} - \underset{\sim}{\boldsymbol{L}} \underset{\sim}{\boldsymbol{\tau}} - \underset{\sim}{\boldsymbol{\tau}} \underset{\sim}{\boldsymbol{L}}^T \tag{A.11}$$

- Oldroyd: The Oldroyd stress rate can be derived in terms of the Lie derivative[2] of the Cauchy stress tensor

$$\dot{\underset{\sim}{\boldsymbol{\sigma}}}^{ol} = \underset{\sim}{\boldsymbol{F}} \left[\frac{\mathrm{d}}{\mathrm{d}t} \left(\underset{\sim}{\boldsymbol{F}}^{-1} \underset{\sim}{\boldsymbol{\sigma}} \underset{\sim}{\boldsymbol{F}}^{-T} \right) \right] \underset{\sim}{\boldsymbol{F}}^T = \dot{\underset{\sim}{\boldsymbol{\sigma}}} - \underset{\sim}{\boldsymbol{L}} \underset{\sim}{\boldsymbol{\sigma}} - \underset{\sim}{\boldsymbol{\sigma}} \underset{\sim}{\boldsymbol{L}}^T \tag{A.12}$$

---

[1] The Piola transformation of a tensor $\underset{\sim}{\boldsymbol{S}}$ is defined as $\phi_*(\underset{\sim}{\boldsymbol{S}}) = \underset{\sim}{\boldsymbol{F}} \underset{\sim}{\boldsymbol{S}} \underset{\sim}{\boldsymbol{F}}^T$

[2] The Lie derivative of a tensor $\underset{\sim}{\boldsymbol{g}}$ over the mapping ϕ is expressed as $\mathscr{L}_\phi[\underset{\sim}{\boldsymbol{g}}] = \phi_*[\frac{\mathrm{d}}{\mathrm{d}t} \phi_*^{-1}[\underset{\sim}{\boldsymbol{g}}]]$

- Cotter–Rivlin

$$\dot{\underset{\sim}{\sigma}}^{cr} = \underset{\sim}{F}^{-T}\left[\frac{\mathrm{d}}{\mathrm{d}t}\left(\underset{\sim}{F}^{T}\underset{\sim}{\sigma}\underset{\sim}{F}\right)\right]\underset{\sim}{F}^{-1} = \dot{\underset{\sim}{\sigma}} + \underset{\sim}{L}^{T}\underset{\sim}{\sigma} + \underset{\sim}{\sigma}\underset{\sim}{L} \tag{A.13}$$

- Other variances

$$\overset{\triangle}{\underset{\sim}{\sigma}} = \underset{\sim}{F}^{-T}\left[\frac{\mathrm{d}}{\mathrm{d}t}\left(\underset{\sim}{F}^{T}\underset{\sim}{\sigma}\underset{\sim}{F}^{-T}\right)\right]\underset{\sim}{F}^{T} = \dot{\underset{\sim}{\sigma}} + \underset{\sim}{L}^{T}\underset{\sim}{\sigma} - \underset{\sim}{\sigma}\underset{\sim}{L}^{T} \tag{A.14}$$

$$\overset{\triangledown}{\underset{\sim}{\sigma}} = \underset{\sim}{F}\left[\frac{\mathrm{d}}{\mathrm{d}t}\left(\underset{\sim}{F}^{-1}\underset{\sim}{\sigma}\underset{\sim}{F}\right)\right]\underset{\sim}{F}^{-1} = \dot{\underset{\sim}{\sigma}} - \underset{\sim}{L}\underset{\sim}{\sigma} + \underset{\sim}{\sigma}\underset{\sim}{L} \tag{A.15}$$

By ignoring the stretch component of $\underset{\sim}{F}$ in (A.13), (A.12) and (A.11), thus performing the pull-back and push-forward operations using only the rotation tensor $\underset{\sim}{R}$, we get the Green-Naghdi rate. Furthermore, the Jaumann rate can be produced as the average of the Oldroyd and the Cotter-Rivlin rates:

$$\dot{\underset{\sim}{\sigma}}^{J} = \frac{1}{2}\left(\dot{\underset{\sim}{\sigma}}^{ol} + \dot{\underset{\sim}{\sigma}}^{cr}\right) \tag{A.16}$$

A.3 Drawbacks: elastic dissipation, spurious oscillations

In this section we will shed the light on some spurious responses of hypoelastic formulations. In the sequel, we will consider two types of loadings: simple shear and cyclic loading (traction and shear combined).

A.3.1 Simple glide problem

Consider a cube subjected to the simple glide kinematics as shown in (A.1)

$$\underset{\sim}{F} = \begin{pmatrix} 1 & \gamma & 0 \\ 0 & 1 & 0 \\ 0 & 0 & 1 \end{pmatrix}$$

with $\gamma = \tan(\theta)$

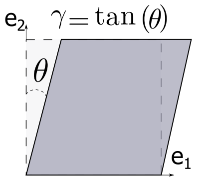

Figure A.1: *Simple glide loading*

In the following, the solution of $\overset{\circ}{\underset{\sim}{\sigma}} = \underset{\sim}{\mathbb{C}} : \underset{\sim}{D}$ for different hypo-elastic rates is detailed.

Zaremba-Jaumann

The system of differential equations to solve writes

$$\begin{cases} \dfrac{d\sigma_{11}}{d\gamma} - \sigma_{12} = 0 \\ \dfrac{d\sigma_{12}}{d\gamma} + \sigma_{11} = \mu \end{cases} \tag{A.17}$$

Combining the two equations leads to the following second order differential equation

$$\frac{d^2\sigma_{11}}{d\gamma^2} + \sigma_{11} = \mu \tag{A.18}$$

The complementary solution is given by

$$\sigma_{11}^{c} = C_1\cos(\gamma) + C_2\sin(\gamma) \quad / \quad C_1, C_2 \in \mathbb{R} \tag{A.19}$$

and the particular solution is

$$\sigma_{11}^{p} = \mu \tag{A.20}$$

Hence

$$\sigma_{11} = \sigma_{11}^c + \sigma_{11}^p = C_1\cos(\gamma) + C_2\sin(\gamma) + \mu \tag{A.21}$$

and

$$\sigma_{12} = -C_1\sin(\gamma) + C_2\cos(\gamma) \tag{A.22}$$

Applying the initial conditions $\sigma_{11}(0) = \sigma_{12}(0) = 0$, we find that $C_1 = -\mu$ and $C_2 = 0$. The final solution is termed as:

$$\begin{cases} \sigma_{11} = \mu\left(1 - \cos(\gamma)\right) \\ \\ \sigma_{12} = \mu\sin(\gamma) \end{cases} \tag{A.23}$$

Green-Naghdi

The set of differential equation to solve is

$$\begin{cases} \dfrac{d\sigma_{11}}{d\gamma} - \dfrac{4}{4+\gamma^2}\sigma_{12} = 0 \\ \dfrac{d\sigma_{12}}{d\gamma} + \dfrac{4}{4+\gamma^2}\sigma_{11} = \mu \end{cases} \tag{A.24}$$

using $\tan(\beta) = \gamma/2$

$$\begin{cases} \dfrac{d\sigma_{11}}{d\beta} - 2\sigma_{12} = 0 \\ \dfrac{d\sigma_{12}}{d\beta} + 2\sigma_{11} = \mu\left(\dfrac{4+\gamma^2}{2}\right) = \dfrac{2\mu}{\cos^2(\beta)} \end{cases} \tag{A.25}$$

$$\frac{d^2\sigma_{11}}{d\beta^2} + 4\sigma_{11} = \mu\left(4+\gamma^2\right) = \frac{4\mu}{\cos^2(\beta)} \tag{A.26}$$

The complementary solution is given by

$$\sigma_{11}^c = C_1\cos(2\beta) + C_2\sin(2\beta) \quad / \quad C_1, C_2 \in \mathbb{R} \tag{A.27}$$

The particular solution can be calculated using the variation of parameters method. First, The Wronskian of $y_1 = \cos(2\beta)$ and $y_2 = \sin(2\beta)$ is evaluated as

$$W = \begin{vmatrix} y_1 & y_2 \\ y_1' & y_2' \end{vmatrix} = \begin{vmatrix} \cos(2\beta) & \sin(2\beta) \\ -2\sin(2\beta) & 2\cos(2\beta) \end{vmatrix} = 2$$

Then, with $g(\beta) = \dfrac{4\mu}{\cos^2(\beta)}$, the particular solution writes

$$\begin{aligned} \sigma_{11}^p &= -y_1 \int \frac{y_2 g(\beta)}{W} d\beta + y_2 \int \frac{y_1 g(\beta)}{W} d\beta && \text{(A.28)} \\ &= -\cos(2\beta) \int \frac{2\mu\sin(2\beta)}{\cos^2(\beta)} d\beta + \sin(2\beta) \int \frac{2\mu\cos(2\beta)}{\cos^2(\beta)} d\beta && \text{(A.29)} \\ &= 4\mu\cos(2\beta)\log|\cos(\beta)| + 2\mu\sin(2\beta)\left[2\beta - \tan(\beta)\right] && \text{(A.30)} \end{aligned}$$

Therefore

$$\begin{aligned} \sigma_{11} &= \sigma_{11}^c + \sigma_{11}^p && \text{(A.31)} \\ &= \left[C_1 + 4\mu\log|\cos(\beta)|\right]\cos(2\beta) + \left[C_2 + 2\mu\left(2\beta - \tan(\beta)\right)\right]\sin(2\beta) && \text{(A.32)} \end{aligned}$$

and

$$\begin{aligned}\sigma_{12} &= \frac{1}{2}\frac{d\sigma_{11}}{d\beta} && \text{(A.33)}\\ &= -\left[C_1 + 4\mu \log|\cos(\beta)|\right]\sin(2\beta) + \left[C_2 + 2\mu\left(2\beta - \tan(\beta)\right)\right]\cos(2\beta) && \text{(A.34)}\end{aligned}$$

Applying the initial conditions $\sigma_{11}(0) = \sigma_{12}(0) = 0$, we find that $C_1 = C_2 = 0$. Using the following equations

$$\cos(\beta) = \frac{2}{\sqrt{4+\gamma^2}} \quad , \quad \sin(\beta) = \frac{\gamma}{\sqrt{4+\gamma^2}} \tag{A.35}$$

$$\cos(2\beta) = \cos^2(\beta) - \sin^2(\beta) = \frac{4-\gamma^2}{4+\gamma^2} \tag{A.36}$$

$$\sin(2\beta) = 2\cos(\beta)\sin(\beta) = \frac{4\gamma}{4+\gamma^2}, \tag{A.37}$$

we can express the solution as

$$\begin{cases} \sigma_{11} = 2\mu\left[\dfrac{\gamma^2-4}{4+\gamma^2}\log\left(\dfrac{4+\gamma^2}{4}\right) + \dfrac{4\gamma}{4+\gamma^2}\left(2\arctan\left(\dfrac{\gamma}{2}\right) - \dfrac{\gamma}{2}\right)\right] \\ \sigma_{12} = 2\mu\left[\dfrac{4\gamma}{4+\gamma^2}\log\left(\dfrac{4+\gamma^2}{4}\right) + \dfrac{4-\gamma^2}{4+\gamma^2}\left(2\arctan\left(\dfrac{\gamma}{2}\right) - \dfrac{\gamma}{2}\right)\right] \end{cases} \tag{A.38}$$

Logarithmic

The applied deformation gradient is

$$\underset{\sim}{\boldsymbol{F}} = \begin{pmatrix} 1 & \gamma & 0 \\ 0 & 1 & 0 \\ 0 & 0 & 1 \end{pmatrix} \tag{A.39}$$

We compute the left Cauchy-Green tensor

$$\underset{\sim}{\boldsymbol{B}} = \underset{\sim}{\boldsymbol{F}}\,\underset{\sim}{\boldsymbol{F}}^T = \begin{pmatrix} 1+\gamma^2 & \gamma & 0 \\ \gamma & 1 & 0 \\ 0 & 0 & 1 \end{pmatrix} \tag{A.40}$$

The eigenvalues of $\underset{\sim}{\boldsymbol{B}}$ are

$$\lambda_{1,2} = \frac{1}{4}\left(\gamma \pm \sqrt{4+\gamma^2}\right)^2 \quad , \quad \lambda_3 = 1 \tag{A.41}$$

The projection tensors are computed as

$$\underset{\sim}{\boldsymbol{P}}_1 = \frac{1}{\lambda_1 - \lambda_2}\begin{pmatrix} \dfrac{\lambda_1\gamma^2}{\lambda_1 - 1} & \gamma & 0 \\ \gamma & \dfrac{\gamma^2}{\lambda_1 - 1} & 0 \\ 0 & 0 & 0 \end{pmatrix}, \quad \underset{\sim}{\boldsymbol{P}}_2 = \frac{1}{\lambda_2 - \lambda_1}\begin{pmatrix} \dfrac{\lambda_2\gamma^2}{\lambda_2 - 1} & \gamma & 0 \\ \gamma & \dfrac{\gamma^2}{\lambda_2 - 1} & 0 \\ 0 & 0 & 0 \end{pmatrix}, \quad \underset{\sim}{\boldsymbol{P}}_3 = \begin{pmatrix} 0 & 0 & 0 \\ 0 & 0 & 0 \\ 0 & 0 & 1 \end{pmatrix} \tag{A.42}$$

Finally, the expression of $\log\left(\underset{\sim}{\boldsymbol{V}}\right)$ is obtained as

$$\log\left(\underset{\sim}{\boldsymbol{V}}\right) = \frac{1}{2}\sum_{i=1}^{m=3}\log(\lambda_i)\underset{\sim}{\boldsymbol{P}}_i = \log\left(\frac{\gamma}{2} + \sqrt{1+\frac{\gamma^2}{4}}\right)\begin{pmatrix} \dfrac{\gamma}{\sqrt{1+\gamma^2/4}} & \dfrac{1}{\sqrt{1+\gamma^2/4}} & 0 \\ \dfrac{1}{\sqrt{1+\gamma^2/4}} & -\dfrac{\gamma}{\sqrt{1+\gamma^2/4}} & 0 \\ 0 & 0 & 0 \end{pmatrix} \tag{A.43}$$

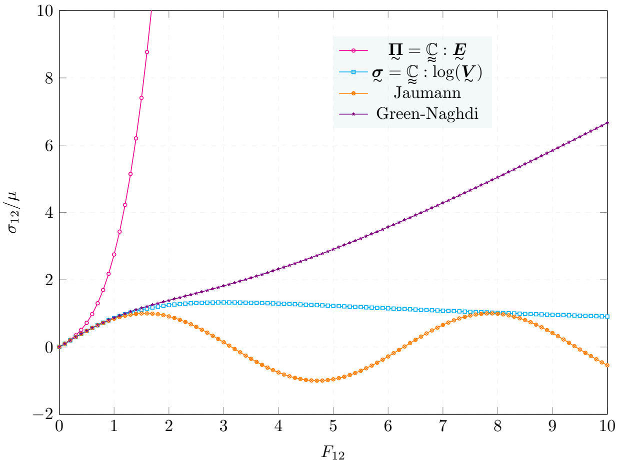

Figure A.2: *Simple glide problem: comparison of various isotropic elasticity formulations at finite strains [Besson et al., 2009].*

A.3.2 Cyclic loading

Case 1: non-proportional loading for a cyclic and non proportional loading. The solution is proposed in [Lin et al., 2003] for various hypoelastic rates.

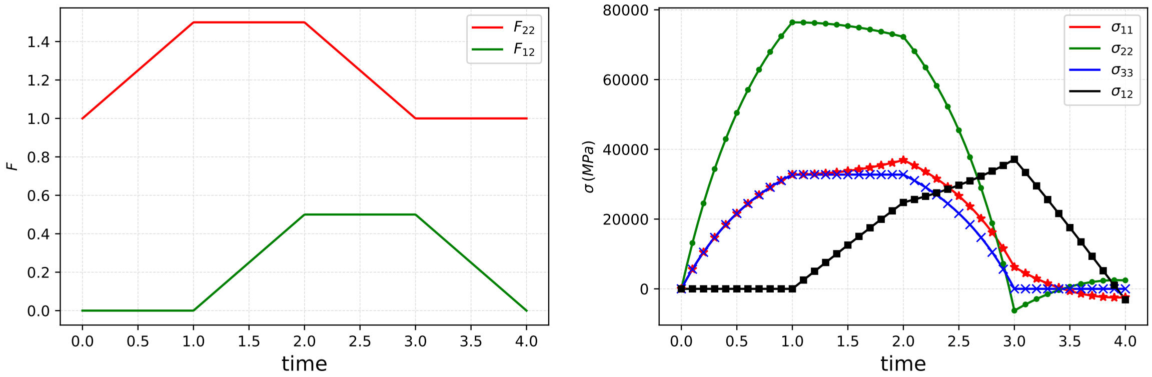

Figure A.3: *Cauchy stress components vs. deformation sequences of a closed strain path computed analytically (lines) and numerically (markers) for Jaumann rate.*

The residual stress at the end of the cycle is given by

$$\begin{cases} \sigma_{11}^{res} = \mu \left[1 + \log(u_m)\cos(\gamma_m) - (1 + \log(u_m)\cos\left(\gamma_m(1 - \dfrac{1}{u_m}) \right) \right] \\ \sigma_{22}^{res} = -\sigma_{11}^{res} \\ \sigma_{12}^{res} = \mu \left[\log(u_m)\sin(\gamma_m) - (1 + \log(u_m)\sin\left(\gamma_m(1 - \dfrac{1}{u_m}) \right) \right] \end{cases} \tag{A.44}$$

We notice that the residual stresses using the Jaumann rate depend on the maximal stretch and shear, γ_m and u_m applied during the cycle. Moreover, it does not depend on λ but only on μ. Therefore, a closed strain path leads to a non-closed stress path as a response *i.e.* the hypoelastic law using the Jaumann rate is not elasticity-consistent. This result is reported by many other authors [Xiao et al., 1999; Kojić and Bathe, 1987; Brepols et al., 2014].

The evolution of residual stresses over cycles depends as well on the hypoelastic rate. For instance, the residual stresses follow a sinusoidal trend for Jaumann rate whereas it have a linear tendency for Green-Naghdi rate (see fig A.4) [Brepols et al., 2014].

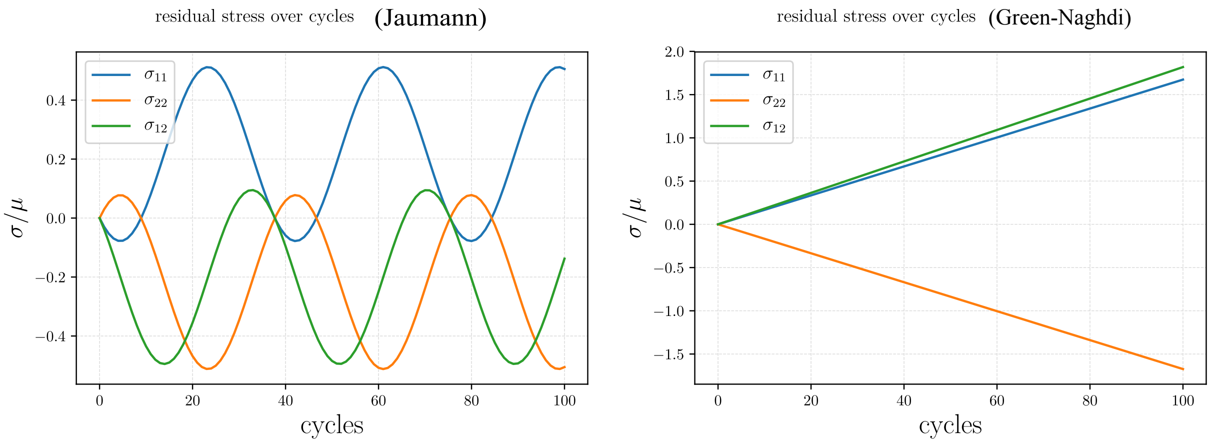

Figure A.4: *Residual stresses for Jaumann and Green-Naghdi rates after each cycle in case of a non-proportional cyclic loading (see Fig. A.3).*

Case 2: proportional loading It has been shown that any hypoelastic law is integrable in the case of proportional loading [Truesdell and Noll, 1965]. Consider a hypoelastic law in the form

$$\dot{\underset{\sim}{\sigma}} + \underset{\sim}{\sigma}\underset{\sim}{W} - \underset{\sim}{W}\underset{\sim}{\sigma} = \mathscr{H}(\underset{\sim}{\sigma}) : \underset{\sim}{D} \tag{A.45}$$

satisfying the initial condition

$$\underset{\sim}{\sigma}(t_0) = \sigma_0 \tag{A.46}$$

If a deformation process depending only on one parameter $\alpha(t)$ is applied

$$\underset{\sim}{F} = \hat{\underset{\sim}{F}}(\alpha(t)) \quad , \quad \alpha(t_0) = 0 \quad , \quad t \geq t_0 \tag{A.47}$$

the strain rate and spin tensors can be therefore expressed as

$$\underset{\sim}{D}(t) = \dot{\alpha}(t)\hat{\underset{\sim}{D}}(\alpha(t)) \quad , \quad \underset{\sim}{W}(t) = \dot{\alpha}(t)\hat{\underset{\sim}{W}}(\alpha(t)) \tag{A.48}$$

Likewise, the time derivative of stress tensor is defined

$$\underset{\sim}{\sigma}(t) = \hat{\underset{\sim}{\sigma}}(\alpha(t)) \implies \dot{\underset{\sim}{\sigma}}(t) = \dot{\alpha}(t)\frac{d\hat{\underset{\sim}{\sigma}}(\alpha)}{d\alpha} \tag{A.49}$$

We can show that $\hat{\underset{\sim}{\sigma}}$ satisfy both (A.45) and (A.46). Hence, a hypoelastic material is always integrable if the loading is proportional.

A.3.3 Integrability conditions

It has been proved that hypoelastic formulations are not generally integrable to hyperelastic laws. Bernstein [1960] has given the necessary conditions to ensure that a hypoelastic law is integrable. However, any hyperelastic law can be put in rate form meaning that is hypoelastic. After the works of Xiao et al. [1998], the hypoelastic law with logarithmic rate is the only one that is elastic-consistent *i.e.* the elastic work depends only on initial and final states. Nevertheless, a recent study by Jiao and Fish [2018] has shown that logarithmic-based hypoelastic law is not integrable after plastic yielding.

Appendix B

FEM implementation

B.1 Finite strain elastoplasticity

The nodal displacements are written in vector form as

$$\{\underline{\boldsymbol{u}}^e\} = \left\{u_1^1 \;\; u_2^1 \;\; u_3^1 \;\; \cdots \;\; u_1^p \;\; u_2^p \;\; u_3^p\right\}^T \tag{B.1}$$

u_j^i denotes the j-th ($1 \leq j \leq 3$) component of the nodal displacement at node i. p is the total number of nodes. The shape functions can be written as

$$[\boldsymbol{N}] = \begin{bmatrix} N^1 & 0 & 0 & \cdots & N^p & 0 & 0 \\ 0 & N^1 & 0 & \cdots & 0 & N^p & 0 \\ 0 & 0 & N^1 & \cdots & 0 & 0 & N^p \end{bmatrix} \tag{B.2}$$

and

$$\{\underline{\boldsymbol{u}}\} = [\boldsymbol{N}]\{\underline{\boldsymbol{u}}^e\} \tag{B.3}$$

It follows that

$$\{\underset{\sim}{\boldsymbol{F}}\} = \{F_{11} \;\; F_{22} \;\; F_{33} \;\; F_{12} \;\; F_{23} \;\; F_{31} \;\; F_{21} \;\; F_{32} \;\; F_{13}\}^T = [\boldsymbol{B}]\{\underline{\boldsymbol{u}}^e\} \tag{B.4}$$

where

$$[\boldsymbol{B}] = \begin{bmatrix} \dfrac{\partial N^1}{\partial X_1} & 0 & 0 & \cdots & \dfrac{\partial N^p}{\partial X_1} & 0 & 0 \\ 0 & \dfrac{\partial N^1}{\partial X_2} & 0 & \cdots & 0 & \dfrac{\partial N^p}{\partial X_2} & 0 \\ 0 & 0 & \dfrac{\partial N^1}{\partial X_3} & \cdots & 0 & 0 & \dfrac{\partial N^p}{\partial X_3} \\ \dfrac{\partial N^1}{\partial X_2} & 0 & 0 & \cdots & \dfrac{\partial N^p}{\partial X_2} & 0 & 0 \\ 0 & \dfrac{\partial N^1}{\partial X_3} & 0 & \cdots & 0 & \dfrac{\partial N^p}{\partial X_3} & 0 \\ 0 & 0 & \dfrac{\partial N^1}{\partial X_1} & \cdots & 0 & 0 & \dfrac{\partial N^p}{\partial X_1} \\ 0 & \dfrac{\partial N^1}{\partial X_1} & 0 & \cdots & 0 & \dfrac{\partial N^p}{\partial X_1} & 0 \\ 0 & 0 & \dfrac{\partial N^1}{\partial X_2} & \cdots & 0 & 0 & \dfrac{\partial N^p}{\partial X_2} \\ \dfrac{\partial N^1}{\partial X_3} & 0 & 0 & \cdots & \dfrac{\partial N^p}{\partial X_3} & 0 & 0 \end{bmatrix} \tag{B.5}$$

The linear set of equations to be solved for $\Delta\underline{\boldsymbol{u}}$ iteratively is given by

$$[\boldsymbol{K}]^g \Delta\underline{\boldsymbol{u}} = \int_{\Omega_0} [\boldsymbol{N}^T]\{\boldsymbol{b}\} dV_0 + \int_{\partial\Omega_0^{tr}} [\boldsymbol{N}]^T \{\boldsymbol{t}\} dS_0 - \int_{\Omega_0} [\boldsymbol{B}]^T \{\boldsymbol{P}\} dV_0 \tag{B.6}$$

where $[\boldsymbol{K}]^g$ is the global tangent matrix in Eq. (1.63) and Eq. (1.67) and $\{\boldsymbol{P}\}$ is the Boussinesq stress tensor. $\{\boldsymbol{b}\}$ and $\{\boldsymbol{t}\}$ denote the reference body force and surface traction fields, respectively.

B.2 Tensorial micromorphic elastoplasticity at small strain

The purpose of this appendix is to present briefly the finite element implementation of micromorphic models based on symmetric second-order tensors. Different shape functions are used to interpolate the degrees of freedom: displacement $\underline{\boldsymbol{u}}$ and micromorphic variable $\underset{\sim}{\chi}$. The list of degrees of freedom is arranged in an arrow as

$$\{DOF\}^T = \{u_1 \quad u_2 \quad u_3 \quad \chi_{11} \quad \chi_{22} \quad \chi_{33} \quad \chi_{12} \quad \chi_{23} \quad \chi_{31}\} \tag{B.7}$$

The degrees of freedom $\{DOF\}$ are interpolated form nodal values $\{DOF_{node}\}$ using shape functions denoted by $[N]$ as

$$\{DOF\} = \sum_{i=1}^{p} [N]\{DOF_{node}\} \tag{B.8}$$

where

$$[N] = \begin{bmatrix}
{}^uN_1 & 0 & 0 & 0 & 0 & 0 & 0 & 0 & 0 & \cdots & {}^uN_p & 0 & 0 & 0 & 0 & 0 & 0 & 0 & 0 \\
0 & {}^uN_1 & 0 & 0 & 0 & 0 & 0 & 0 & 0 & \cdots & 0 & {}^uN_p & 0 & 0 & 0 & 0 & 0 & 0 & 0 \\
0 & 0 & {}^uN_1 & 0 & 0 & 0 & 0 & 0 & 0 & \cdots & 0 & 0 & {}^uN_p & 0 & 0 & 0 & 0 & 0 & 0 \\
0 & 0 & 0 & {}^\chi N_1 & 0 & 0 & 0 & 0 & 0 & \cdots & 0 & 0 & 0 & {}^\chi N_p & 0 & 0 & 0 & 0 & 0 \\
0 & 0 & 0 & 0 & {}^\chi N_1 & 0 & 0 & 0 & 0 & \cdots & 0 & 0 & 0 & 0 & {}^\chi N_p & 0 & 0 & 0 & 0 \\
0 & 0 & 0 & 0 & 0 & {}^\chi N_1 & 0 & 0 & 0 & \cdots & 0 & 0 & 0 & 0 & 0 & {}^\chi N_p & 0 & 0 & 0 \\
0 & 0 & 0 & 0 & 0 & 0 & {}^\chi N_1 & 0 & 0 & \cdots & 0 & 0 & 0 & 0 & 0 & 0 & {}^\chi N_p & 0 & 0 \\
0 & 0 & 0 & 0 & 0 & 0 & 0 & {}^\chi N_1 & 0 & \cdots & 0 & 0 & 0 & 0 & 0 & 0 & 0 & {}^\chi N_p & 0 \\
0 & 0 & 0 & 0 & 0 & 0 & 0 & 0 & {}^\chi N_1 & \cdots & 0 & 0 & 0 & 0 & 0 & 0 & 0 & 0 & {}^\chi N_p
\end{bmatrix} \tag{B.9}$$

${}^uN$ and ${}^\chi N$ denote shape functions chosen for displacement and the micromorphic variable $\underset{\sim}{\chi}$, respectively. Strain tensors are computed from degrees of freedom as

$$\{STRAIN\} = [B][DOF] \tag{B.10}$$

The expression of the matrix $[B]$ is given by

$$[B] = \begin{bmatrix} {}^uB & 0 \\ 0 & {}^\chi N \\ 0 & {}^\chi B \end{bmatrix} \tag{B.11}$$

where

$$[{}^{u}\boldsymbol{B}] = \begin{bmatrix} \dfrac{\partial\, {}^{u}N_1}{\partial x_1} & 0 & 0 \\ 0 & \dfrac{\partial\, {}^{u}N_1}{\partial x_2} & 0 \\ 0 & 0 & \dfrac{\partial\, {}^{u}N_1}{\partial x_3} \\ \dfrac{1}{\sqrt{2}}\dfrac{\partial\, {}^{u}N_1}{\partial x_2} & \dfrac{1}{\sqrt{2}}\dfrac{\partial\, {}^{u}N_1}{\partial x_1} & 0 \\ 0 & \dfrac{1}{\sqrt{2}}\dfrac{\partial\, {}^{u}N_1}{\partial x_3} & \dfrac{1}{\sqrt{2}}\dfrac{\partial\, {}^{u}N_1}{\partial x_2} \\ \dfrac{1}{\sqrt{2}}\dfrac{\partial\, {}^{u}N_1}{\partial x_3} & 0 & \dfrac{1}{\sqrt{2}}\dfrac{\partial\, {}^{u}N_1}{\partial x_1} \end{bmatrix} \quad , \quad [{}^{\chi}\boldsymbol{B}] = \begin{bmatrix} \dfrac{\partial\, {}^{\chi}N_1}{\partial x_1} & 0 & 0 & 0 & 0 & 0 \\ \dfrac{\partial\, {}^{\chi}N_1}{\partial x_2} & 0 & 0 & 0 & 0 & 0 \\ \dfrac{\partial\, {}^{\chi}N_1}{\partial x_3} & 0 & 0 & 0 & 0 & 0 \\ 0 & \dfrac{\partial\, {}^{\chi}N_1}{\partial x_1} & 0 & 0 & 0 & 0 \\ 0 & \dfrac{\partial\, {}^{\chi}N_1}{\partial x_1} & 0 & 0 & 0 & 0 \\ 0 & \dfrac{\partial\, {}^{\chi}N_1}{\partial x_1} & 0 & 0 & 0 & 0 \\ & & \dots & & & \\ 0 & 0 & 0 & 0 & 0 & \dfrac{\partial\, {}^{\chi}N_1}{\partial x_1} \\ 0 & 0 & 0 & 0 & 0 & \dfrac{\partial\, {}^{\chi}N_1}{\partial x_2} \\ 0 & 0 & 0 & 0 & 0 & \dfrac{\partial\, {}^{\chi}N_1}{\partial x_3} \end{bmatrix} \tag{B.12}$$

Accordingly, stress tensors are computed as

$$\{STRESS\} = [K]\{STRAIN\} \tag{B.13}$$

where [K] is the consistent tangent matrix (see C.4) and

$$\begin{aligned} \{STRESS\}^T = \{ & \sigma_{11}\ \sigma_{22}\ \sigma_{33}\ \sqrt{2}\sigma_{12}\ \sqrt{2}\sigma_{23}\ \sqrt{2}\sigma_{31}\ a_{11}\ a_{22}\ a_{33}\ \sqrt{2}a_{12}\ \sqrt{2}a_{23}\ \sqrt{2}a_{31} \\ & b_{111}\ b_{112}\ b_{113}\ b_{221}\ b_{222}\ b_{223}\ b_{331}\ b_{332}\ b_{333}\ \sqrt{2}b_{121}\ \sqrt{2}b_{122}\ \sqrt{2}b_{123} \\ & \sqrt{2}b_{231}\ b_{232}\ \sqrt{2}b_{233}\ \sqrt{2}b_{311}\ \sqrt{2}b_{312}\ \sqrt{2}b_{313}\} \end{aligned} \tag{B.14}$$

$$\begin{aligned} \{STRAIN\}^T = \{ & \varepsilon_{11}\ \varepsilon_{22}\ \varepsilon_{33}\ \sqrt{2}\varepsilon_{12}\ \sqrt{2}\varepsilon_{23}\ \sqrt{2}\varepsilon_{31}\ \chi_{11}\ \chi_{22}\ \chi_{33}\ \sqrt{2}\chi_{12}\ \sqrt{2}\chi_{23}\ \sqrt{2}\chi_{31} \\ & K_{111}\ K_{112}\ K_{113}\ K_{221}\ K_{222}\ K_{223}\ K_{331}\ K_{332}\ K_{333}\ \sqrt{2}K_{121}\ \sqrt{2}K_{122}\ \sqrt{2}K_{123} \\ & \sqrt{2}K_{231}\ K_{232}\ \sqrt{2}K_{233}\ \sqrt{2}K_{311}\ \sqrt{2}K_{312}\ \sqrt{2}K_{313}\} \end{aligned} \tag{B.15}$$

Appendix C

Tangent matrices

C.1 Finite strain multi-mechanism plasticity

The Jacobian matrix is required to integrate the constitutive equations at the Gauss point level. The block form of the Jacobian matrix writes

$$\begin{pmatrix} \dfrac{\partial \mathscr{R}_{el}}{\partial \Delta \underset{\sim}{\boldsymbol{F}}^{e}} & \dfrac{\partial \mathscr{R}_{el}}{\partial \Delta p_i} & \dfrac{\partial \mathscr{R}_{el}}{\partial \Delta \boldsymbol{\alpha}_i} \\ \dfrac{\partial \mathscr{R}_{p_i}}{\partial \Delta \underset{\sim}{\boldsymbol{F}}^{e}} & \dfrac{\partial \mathscr{R}_{p_i}}{\partial \Delta p_i} & \dfrac{\partial \mathscr{R}_{p_i}}{\partial \Delta \boldsymbol{\alpha}_i} \\ \dfrac{\partial \mathscr{R}_{\boldsymbol{\alpha}_i}}{\partial \Delta \underset{\sim}{\boldsymbol{F}}^{e}} & \dfrac{\partial \mathscr{R}_{\boldsymbol{\alpha}_i}}{\partial \Delta p_i} & \dfrac{\partial \mathscr{R}_{\boldsymbol{\alpha}_i}}{\partial \Delta \boldsymbol{\alpha}_i} \end{pmatrix} \tag{C.1}$$

where the residuals are taken as

$$\mathscr{R}_{el} = \Delta \underset{\sim}{\boldsymbol{F}}^{e} - \Delta \underset{\sim}{\boldsymbol{F}} \underset{\sim}{\boldsymbol{F}}^{-1} \underset{\sim}{\boldsymbol{F}}^{e} + \underset{\sim}{\boldsymbol{F}}^{e} \sum_{i=0}^{N} \Delta p_i \underset{\sim}{\boldsymbol{N}}_i \tag{C.2}$$

$$\mathscr{R}_{p_i} = f_i \qquad \text{or} \qquad \mathscr{R}_{p} = \Delta p_i - \Delta t \frac{\partial \Omega}{\partial f_i} \tag{C.3}$$

$$\mathscr{R}_{\boldsymbol{\alpha}_i} = \Delta \boldsymbol{\alpha}_i - \Delta p_i \boldsymbol{m_i} + \Delta \boldsymbol{q_i} \tag{C.4}$$

The terms related to the global part of the Jacobian (the first row and the first column) are given by

$$\frac{\partial \mathscr{R}_{el}}{\partial \Delta \underset{\sim}{\boldsymbol{F}}^{e}} = \underset{\approx}{\boldsymbol{1}} - (\Delta \underset{\sim}{\boldsymbol{F}} \underset{\sim}{\boldsymbol{F}}^{-1}) \underline{\otimes} \underset{\sim}{\boldsymbol{1}} + \sum_{i=0}^{N} \Delta p_i \left(\underset{\sim}{\boldsymbol{1}} \underline{\otimes} \underset{\sim}{\boldsymbol{N}}_i^{T} \right) + \theta \underset{\sim}{\boldsymbol{F}}^{e} \left[\sum_{i=0}^{N} \Delta p_i \frac{\partial \underset{\sim}{\boldsymbol{N}}_i}{\partial \underset{\sim}{\boldsymbol{M}}} \right] : \frac{\partial \underset{\sim}{\boldsymbol{M}}}{\partial \underset{\sim}{\boldsymbol{F}}^{e}} \tag{C.5}$$

$$\frac{\partial \mathscr{R}_{el}}{\partial \Delta p_i} = \underset{\sim}{\boldsymbol{F}}^{e} \underset{\sim}{\boldsymbol{N}}_i + \Delta p_i \frac{\partial \underset{\sim}{\boldsymbol{N}}_i}{\partial \boldsymbol{A}_i} \frac{\partial \boldsymbol{A}_i}{\partial p_i} \tag{C.6}$$

$$\frac{\partial \mathscr{R}_{el}}{\partial \Delta \boldsymbol{\alpha}_i} = \theta \underset{\sim}{\boldsymbol{F}}^{e} \sum_{i=0}^{N} \Delta p_i \left(\frac{\partial \underset{\sim}{\boldsymbol{N}}_i}{\partial \boldsymbol{A}_i} \frac{\partial \boldsymbol{A}_i}{\partial \boldsymbol{\alpha}_i} \right) \tag{C.7}$$

$$\frac{\partial \mathscr{R}_{p}}{\partial \Delta \underset{\sim}{\boldsymbol{F}}^{e}} = \theta \frac{\partial f}{\partial \underset{\sim}{\boldsymbol{M}}} : \frac{\partial \underset{\sim}{\boldsymbol{M}}}{\partial \underset{\sim}{\boldsymbol{F}}^{e}} \qquad \text{or} \qquad \frac{\partial \mathscr{R}_{p}}{\partial \Delta \underset{\sim}{\boldsymbol{F}}^{e}} = -\theta \Delta t \frac{\partial \dot{p}_i}{\partial f_i} \left(\frac{\partial f}{\partial \underset{\sim}{\boldsymbol{M}}} : \frac{\partial \underset{\sim}{\boldsymbol{M}}}{\partial \underset{\sim}{\boldsymbol{F}}^{e}} \right) \tag{C.8}$$

$$\frac{\partial \mathscr{R}_{\boldsymbol{\alpha}_i}}{\partial \Delta \underset{\sim}{\boldsymbol{F}}^{e}} = -\theta \Delta p_i \frac{\partial \boldsymbol{m_i}}{\partial \underset{\sim}{\boldsymbol{M}}} : \frac{\partial \underset{\sim}{\boldsymbol{M}}}{\partial \underset{\sim}{\boldsymbol{F}}^{e}} \tag{C.9}$$

where

$$\frac{\partial \underset{\sim}{\boldsymbol{M}}}{\partial \underset{\sim}{\boldsymbol{F}}^{e}} = \underset{\sim}{\boldsymbol{1}} \bar{\otimes} (\underset{\sim}{\boldsymbol{\Pi}}^{e} \underset{\sim}{\boldsymbol{F}}^{eT}) + \underset{\sim}{\boldsymbol{F}}^{eT} \underline{\otimes} \underset{\sim}{\boldsymbol{\Pi}}^{e} + \underset{\sim}{\boldsymbol{F}}^{eT} \underset{\sim}{\boldsymbol{F}}^{e} \frac{\partial \underset{\sim}{\boldsymbol{\Pi}}^{e}}{\partial \underset{\sim}{\boldsymbol{E}}^{e}} : \frac{\partial \underset{\sim}{\boldsymbol{E}}^{e}}{\partial \underset{\sim}{\boldsymbol{F}}^{e}} \tag{C.10}$$

$$\frac{\partial \underset{\sim}{\boldsymbol{E}}^{e}}{\partial \underset{\sim}{\boldsymbol{F}}^{e}} = \frac{1}{2} \left(\underset{\sim}{\boldsymbol{1}} \bar{\otimes} \underset{\sim}{\boldsymbol{F}}^{eT} + \underset{\sim}{\boldsymbol{F}}^{eT} \underline{\otimes} \underset{\sim}{\boldsymbol{1}} \right) \tag{C.11}$$

Recall that $\theta \in [0,1]$ is a parameter of the integration method. Next, the block of the Jacobian related to the internal variable evolution equations writes

$$\frac{\partial \mathscr{R}_{p_i}}{\partial \Delta p_i} = \theta \frac{\partial f}{\partial p} \qquad \text{or} \qquad \frac{\partial \mathscr{R}_{p_i}}{\partial \Delta p_i} = 1 - \theta \Delta t \frac{\partial \dot{p}_i}{\partial f_i}\frac{\partial f_i}{\partial p_i} \tag{C.12}$$

$$\frac{\partial \mathscr{R}_{p_i}}{\partial \Delta \boldsymbol{\alpha}_i} = \frac{\partial f}{\partial \boldsymbol{\alpha}_i}\frac{\partial \boldsymbol{\alpha}_i}{\partial \Delta \boldsymbol{\alpha}_i} \qquad \text{or} \qquad \frac{\partial \mathscr{R}_{p_i}}{\partial \Delta \boldsymbol{\alpha_i}} = -\theta \Delta t \frac{\partial \dot{p}_i}{\partial f_i}\frac{\partial f}{\partial \boldsymbol{A}_i}\frac{\partial \boldsymbol{A}_i}{\partial \boldsymbol{\alpha}_i} \tag{C.13}$$

$$\frac{\partial \mathscr{R}_{\boldsymbol{\alpha}_i}}{\partial \Delta p_i} = -\boldsymbol{m_i} - \theta \Delta p_i \frac{\partial \boldsymbol{m_i}}{\partial p_i} \tag{C.14}$$

$$\frac{\partial \mathscr{R}_{\boldsymbol{\alpha}_i}}{\partial \Delta \boldsymbol{\alpha}_i} = \boldsymbol{1} - \theta \left(\Delta p_i \frac{\partial \boldsymbol{m_i}}{\partial \boldsymbol{A}_i} + \Delta t \frac{\partial \boldsymbol{q_i}}{\partial \boldsymbol{A}_i} \right) \frac{\partial \boldsymbol{A}_i}{\partial \boldsymbol{\alpha}_i} - \theta \Delta p_i \frac{\partial \boldsymbol{m_i}}{\partial \boldsymbol{\alpha}_i} \tag{C.15}$$

The interaction terms are given by

$$\frac{\partial \mathscr{R}_{p_i}}{\partial \Delta p_j} = \theta \frac{\partial f_i}{\partial p_j} \qquad \text{or} \qquad \frac{\partial \mathscr{R}_{p_i}}{\partial \Delta p_j} = -\theta \Delta t \frac{\partial \dot{p}_i}{\partial f_i}\frac{\partial f_i}{\partial p_j} \tag{C.16}$$

$$\frac{\partial \mathscr{R}_{p_i}}{\partial \Delta \boldsymbol{\alpha}_i} = \theta \frac{\partial f}{\partial \boldsymbol{A}_i}\frac{\partial \boldsymbol{A}_i}{\partial \boldsymbol{\alpha_j}} \qquad \text{or} \qquad \frac{\partial \mathscr{R}_{p_i}}{\partial \Delta \boldsymbol{\alpha}_i} = -\theta \Delta t \frac{\partial \dot{p}_i}{\partial f_i}\frac{\partial f}{\partial \boldsymbol{A}_i}\frac{\partial \boldsymbol{A}_i}{\partial \boldsymbol{\alpha_j}} \tag{C.17}$$

$$\frac{\partial \mathscr{R}_{\boldsymbol{\alpha}_i}}{\partial \Delta p_i} = \boldsymbol{0} \tag{C.18}$$

$$\frac{\partial \mathscr{R}_{\boldsymbol{\alpha}_i}}{\partial \Delta \boldsymbol{\alpha}_j} = \boldsymbol{1} - \theta \left(\Delta p_i \frac{\partial \boldsymbol{m_i}}{\partial \boldsymbol{A}_i} + \Delta t \frac{\partial \boldsymbol{q_i}}{\partial \boldsymbol{A}_i} \right) \frac{\partial \boldsymbol{A}_i}{\partial \boldsymbol{\alpha_j}} \tag{C.19}$$

The matrix $\dfrac{\partial \boldsymbol{A}_i}{\partial \boldsymbol{\alpha_j}}$ accounts for interactions between the hardening variables.

The second method to integrate constitutive equations relies upon the following definition of the residual in Eq. (C.2)

$$\mathscr{R}_{el} = \underset{\sim}{\boldsymbol{F}}^e \underset{\sim}{\boldsymbol{F}}^p - \underset{\sim}{\boldsymbol{F}} \tag{C.20}$$

$\underset{\sim}{\boldsymbol{F}}^p$ is the solution of the following differential equation

$$\dot{\underset{\sim}{\boldsymbol{F}}}{}^p = \underset{\sim}{\overline{\boldsymbol{L}}}{}^p \underset{\sim}{\boldsymbol{F}}^p \tag{C.21}$$

So $\underset{\sim}{\boldsymbol{F}}^p$, at increment $n+1$, can be estimated by using the exponential mapping [Weber and Anand, 1990] as

$$\underset{\sim}{\boldsymbol{F}}{}^p_{n+1} = \exp\left(\Delta \underset{\sim}{\overline{\boldsymbol{L}}}{}^p\right) \underset{\sim}{\boldsymbol{F}}{}^p_n \tag{C.22}$$

Accordingly, the plastic incompressibility, *i.e.* $\operatorname{trace}(\underset{\sim}{\overline{\boldsymbol{L}}}{}^{\mathrm{p}}) = 0$ or $\det\left(\underset{\sim}{\boldsymbol{F}}^p\right) = 1$, is satisfied since

$$\det\left(\exp \underset{\sim}{\boldsymbol{A}}\right) = \exp\left(\operatorname{tr} \underset{\sim}{\boldsymbol{A}}\right) \tag{C.23}$$

The first row of the Jacobian matrix in Eq. (C.1) is rewritten

$$\frac{\partial \mathscr{R}_{el}}{\partial \Delta \underset{\sim}{\boldsymbol{F}}^e} = \underset{\sim}{\boldsymbol{1}} \underline{\otimes} \underset{\sim}{\boldsymbol{F}}^{pT} + \theta \underset{\sim}{\boldsymbol{F}}^e \left[\frac{\partial \exp\left(\Delta \underset{\sim}{\overline{\boldsymbol{L}}}{}^p\right)}{\partial \Delta \underset{\sim}{\overline{\boldsymbol{L}}}{}^p} : \left(\sum_{i=0}^{N} \Delta p_i \frac{\partial \underset{\sim}{\boldsymbol{N}}{}_i}{\partial \underset{\sim}{\boldsymbol{M}}} \right) : \frac{\partial \underset{\sim}{\boldsymbol{M}}}{\partial \underset{\sim}{\boldsymbol{F}}^e} \right] \underset{\sim}{\boldsymbol{F}}{}^p_n \tag{C.24}$$

$$\frac{\partial \mathscr{R}_{el}}{\partial \Delta p_i} = \underset{\sim}{\boldsymbol{F}}^e \left(\frac{\partial \exp\left(\Delta \underset{\sim}{\overline{\boldsymbol{L}}}{}^p\right)}{\partial \Delta \underset{\sim}{\overline{\boldsymbol{L}}}{}^p} : \underset{\sim}{\boldsymbol{N}}{}_i \right) \underset{\sim}{\boldsymbol{F}}{}^p_n \tag{C.25}$$

$$\frac{\partial \mathscr{R}_{el}}{\partial \Delta \boldsymbol{\alpha}_i} = \underset{\sim}{\boldsymbol{F}}^e \left[\frac{\partial \exp\left(\Delta \underset{\sim}{\overline{\boldsymbol{L}}}{}^p\right)}{\partial \Delta \underset{\sim}{\overline{\boldsymbol{L}}}{}^p} : \left(\sum_{i=0}^{N} \Delta p_i \frac{\partial \underset{\sim}{\boldsymbol{N}}{}_i}{\partial \Delta \boldsymbol{\alpha}_i} \right) \right] \underset{\sim}{\boldsymbol{F}}{}^p_n \tag{C.26}$$

C.2 Single crystal plasticity

Two ways of integrating constitutive equations of single crystal plasticity are presented. The first approach considers kinematic variables associated with each slip system as auxiliary variables α^s and to be calculated directly from increments of γ^s. The second way relies on the assumption that α^s are independent variables, and are therefore considered as integrable variables.

C.2.1 First approach

The constitutive equations at $t+\theta\Delta t$ are given by

$$\begin{cases} \mathscr{R}_{el} & = \Delta \underset{\sim}{\boldsymbol{F}}^e - \Delta \underset{\sim}{\boldsymbol{F}}\,\underset{\sim}{\boldsymbol{F}}^{p-1} + \underset{\sim}{\boldsymbol{F}}^e \underset{\sim}{\overline{\boldsymbol{L}}}^p \\ \mathscr{R}_{\gamma^s} & = \Delta\gamma^s - \Delta t \left\langle \dfrac{f^s}{K} \right\rangle^n \operatorname{sign}(\underset{\sim}{\boldsymbol{M}} : \underset{\sim}{\boldsymbol{N}}^s - x^s) \end{cases} \tag{C.27}$$

The value of x^s at $t+\theta\Delta t$ is given by

$$x^s_{t+\theta\Delta t} = x_0 + C\alpha^s_{t+\theta\Delta t} \tag{C.28}$$

where

$$\Delta\alpha^s_{t+\theta\Delta t} = \alpha^s_{t+\theta\Delta t} - \alpha^s_t = \Delta\gamma^s_{t+\theta\Delta t} - D|\Delta\gamma^s_{t+\theta\Delta t}|\alpha^s_{t+\theta\Delta t} \tag{C.29}$$

or

$$\alpha^s_{t+\theta\Delta t} = \frac{\alpha^s_t + \theta\Delta\gamma^s_{t+\theta\Delta t}}{1 + D|\Delta\gamma^s_{t+\theta\Delta t}|} \tag{C.30}$$

The Jacobian matrix is defined as

$$\begin{array}{c|cccccccc}
 & & & \overbrace{\qquad\qquad\qquad}^{\text{slip system family 1}} & & & & \overbrace{\qquad\qquad\qquad}^{\text{slip system family n}} & \\
\hline
 & \dfrac{\partial\mathscr{R}_{el}}{\partial\Delta\underset{\sim}{\boldsymbol{F}}^e} & \dfrac{\partial\mathscr{R}_{el}}{\partial\Delta\gamma^1} & \cdots & \dfrac{\partial\mathscr{R}_{el}}{\partial\Delta\gamma^{N_1}} & \cdots & \dfrac{\partial\mathscr{R}_{el}}{\partial\Delta\gamma^{N-N_n+1}} & \cdots & \dfrac{\partial\mathscr{R}_{el}}{\partial\Delta\gamma^{N}} \\
 & \dfrac{\partial\mathscr{R}_{\gamma^1}}{\partial\Delta\underset{\sim}{\boldsymbol{F}}^e} & \dfrac{\partial\mathscr{R}_{\gamma^1}}{\partial\Delta\gamma^1} & \cdots & \dfrac{\partial\mathscr{R}_{\gamma^1}}{\partial\Delta\gamma^{N_1}} & \cdots & \dfrac{\partial\mathscr{R}_{\gamma^1}}{\partial\Delta\gamma^{N-N_n+1}} & \cdots & \dfrac{\partial\mathscr{R}_{\gamma^1}}{\partial\Delta\gamma^{N}} \\
\text{slip system family 1} & \vdots & \vdots & \ddots & \vdots & \vdots & \vdots & \vdots & \vdots \\
 & \dfrac{\partial\mathscr{R}_{\gamma^{N_1}}}{\partial\Delta\underset{\sim}{\boldsymbol{F}}^e} & \dfrac{\partial\mathscr{R}_{\gamma^{N_1}}}{\partial\Delta\gamma^1} & \cdots & \dfrac{\partial\mathscr{R}_{\gamma^{N_1}}}{\partial\Delta\gamma^{N_1}} & \cdots & \dfrac{\partial\mathscr{R}_{\gamma^{N_1}}}{\partial\Delta\gamma^{N-N_n+1}} & \cdots & \dfrac{\partial\mathscr{R}_{\gamma^{N_1}}}{\partial\Delta\gamma^{N}} \\
 & \vdots & \vdots & \cdots & \vdots & \ddots & \vdots & \vdots & \vdots \\
 & \dfrac{\partial\mathscr{R}_{\gamma^{N-N_n+1}}}{\partial\Delta\underset{\sim}{\boldsymbol{F}}^e} & \dfrac{\partial\mathscr{R}_{\gamma^{N-N_n+1}}}{\partial\Delta\gamma^1} & \cdots & \dfrac{\partial\mathscr{R}_{\gamma^{N-N_n+1}}}{\partial\Delta\gamma^{N_1}} & \cdots & \dfrac{\partial\mathscr{R}_{\gamma^{N-N_n+1}}}{\partial\Delta\gamma^{N-N_n+1}} & \cdots & \dfrac{\partial\mathscr{R}_{\gamma^{N-N_n+1}}}{\partial\Delta\gamma^{N}} \\
\text{slip system family n} & \vdots & \vdots & \vdots & \vdots & \vdots & \vdots & \ddots & \vdots \\
 & \dfrac{\partial\mathscr{R}_{\gamma^{N}}}{\partial\Delta\underset{\sim}{\boldsymbol{F}}^e} & \dfrac{\partial\mathscr{R}_{\gamma^{N}}}{\partial\Delta\gamma^1} & \cdots & \dfrac{\partial\mathscr{R}_{\gamma^{N}}}{\partial\Delta\gamma^{N_1}} & \cdots & \dfrac{\partial\mathscr{R}_{\gamma^{N}}}{\partial\Delta\gamma^{N-N_n+1}} & \cdots & \dfrac{\partial\mathscr{R}_{\gamma^{N}}}{\partial\Delta\gamma^{N}}
\end{array} \tag{C.31}$$

N_i denotes the number of slip systems for the i-th family and $N = \sum_{i=0}^{i=n} N_i$ is the total number of slip systems. The blocks of the Jacobian matrix are given by

$$\begin{cases} \dfrac{\partial \mathscr{R}_{el}}{\partial \Delta \underset{\sim}{\boldsymbol{F}}^e} & = \underset{\approx}{\boldsymbol{1}} - (\Delta \underset{\sim}{\boldsymbol{F}} \underset{\sim}{\boldsymbol{F}}^{-1}) \underline{\otimes} \underset{\sim}{\boldsymbol{1}} + \underset{\sim}{\boldsymbol{1}} \underline{\otimes} \underset{\sim}{\overline{\boldsymbol{L}}}^{pT} \\ \dfrac{\partial \mathscr{R}_{el}}{\partial \Delta \gamma^r} & = \underset{\sim}{\boldsymbol{F}}^e \underset{\sim}{\boldsymbol{N}}^r \\ \dfrac{\partial \mathscr{R}_{\gamma^s}}{\partial \Delta \underset{\sim}{\boldsymbol{F}}^e} & = \Delta t \dfrac{n}{K} \left\langle \dfrac{f^s}{K} \right\rangle^{n-1} \dfrac{\partial f^s}{\partial \underset{\sim}{\boldsymbol{M}}} \dfrac{\partial \underset{\sim}{\boldsymbol{M}}}{\partial \Delta \underset{\sim}{\boldsymbol{F}}^e} \operatorname{sign}(\underset{\sim}{\boldsymbol{M}} : \underset{\sim}{\boldsymbol{N}}^s - x^s) \\ \dfrac{\partial \mathscr{R}_{\gamma^s}}{\partial \Delta \gamma^r} & = 1 - \Delta t \dfrac{n}{K} \left\langle \dfrac{f^r}{K} \right\rangle^{n-1} \left(\operatorname{sign}(\underset{\sim}{\boldsymbol{M}} : \underset{\sim}{\boldsymbol{N}}^r - x^r) \dfrac{\partial \tau_c^s}{\partial \Delta \gamma^r} + \dfrac{\partial x^s}{\partial \Delta \gamma^r} \right) \end{cases} \tag{C.32}$$

where

$$\frac{\partial f^s}{\partial \underset{\sim}{\boldsymbol{M}}} = \operatorname{sign}(\underset{\sim}{\boldsymbol{M}} : \underset{\sim}{\boldsymbol{N}}^s - x^s) \underset{\sim}{\boldsymbol{N}}^s \tag{C.33}$$

$$\frac{\partial \tau_c^s}{\partial \Delta \gamma^r} = H^{sr} \exp\left(-b^{\mathscr{F}(r)} \gamma^r_{cum} \right) \operatorname{sign}(\underset{\sim}{\boldsymbol{M}} : \underset{\sim}{\boldsymbol{N}}^s - x^s) \tag{C.34}$$

$$\frac{\partial x^s}{\partial \Delta \gamma^r} = C \left(1 - D \operatorname{sign}(\underset{\sim}{\boldsymbol{M}} : \underset{\sim}{\boldsymbol{N}}^s - x^s) \alpha^s \right) \tag{C.35}$$

C.2.2 Second approach

The second way to integrate constitutive equations is to consider kinematic hardening variables α^s as integrable. For the sake of simplicity, the Jacobian matrix of a model with only one mechanism (*i.e.* one slip system family) is detailed in the following. The supplementary residual equation required to integrate α^s is given by

$$\mathscr{R}_{\alpha^s} = \Delta \alpha^s - \Delta \gamma^s \left(1 - D \operatorname{sign}(\underset{\sim}{\boldsymbol{M}} : \underset{\sim}{\boldsymbol{N}}^s - x^s) \alpha^s \right) \tag{C.36}$$

The Jacobian matrix of this model is derived as follows

$$\begin{pmatrix} \dfrac{\partial \mathscr{R}_{el}}{\partial \Delta \underset{\sim}{\boldsymbol{F}}^e} & \dfrac{\partial \mathscr{R}_{el}}{\partial \Delta \gamma^1} & \cdots & \dfrac{\partial \mathscr{R}_{el}}{\partial \Delta \gamma^N} & \dfrac{\partial \mathscr{R}_{el}}{\partial \Delta \alpha^1} & \cdots & \dfrac{\partial \mathscr{R}_{el}}{\partial \Delta \alpha^N} \\ \dfrac{\partial \mathscr{R}_{\gamma^1}}{\partial \Delta \underset{\sim}{\boldsymbol{F}}^e} & \dfrac{\partial \mathscr{R}_{\gamma^1}}{\partial \Delta \gamma^1} & \cdots & \dfrac{\partial \mathscr{R}_{\gamma^1}}{\partial \Delta \gamma^N} & \dfrac{\partial \mathscr{R}_{\gamma^1}}{\partial \Delta \alpha^1} & \cdots & \dfrac{\partial \mathscr{R}_{\gamma^1}}{\partial \Delta \alpha^N} \\ \vdots & \vdots & \ddots & \vdots & \vdots & \vdots & \vdots \\ \dfrac{\partial \mathscr{R}_{\gamma^N}}{\partial \Delta \underset{\sim}{\boldsymbol{F}}^e} & \dfrac{\partial \mathscr{R}_{\gamma^N}}{\partial \Delta \gamma^1} & \cdots & \dfrac{\partial \mathscr{R}_{\gamma^N}}{\partial \Delta \gamma^N} & \dfrac{\partial \mathscr{R}_{\gamma^N}}{\partial \Delta \alpha^1} & \cdots & \dfrac{\partial \mathscr{R}_{\gamma^N}}{\partial \Delta \alpha^N} \\ \dfrac{\partial \mathscr{R}_{\alpha^1}}{\partial \Delta \underset{\sim}{\boldsymbol{F}}^e} & \dfrac{\partial \mathscr{R}_{\alpha^1}}{\partial \Delta \gamma^1} & \cdots & \dfrac{\partial \mathscr{R}_{\alpha^1}}{\partial \Delta \gamma^N} & \dfrac{\partial \mathscr{R}_{\alpha^1}}{\partial \Delta \alpha^1} & \cdots & \dfrac{\partial \mathscr{R}_{\alpha^1}}{\partial \Delta \alpha^N} \\ \vdots & \vdots & \vdots & \vdots & \vdots & \ddots & \vdots \\ \dfrac{\partial \mathscr{R}_{\alpha^N}}{\partial \Delta \underset{\sim}{\boldsymbol{F}}^e} & \dfrac{\partial \mathscr{R}_{\alpha^N}}{\partial \Delta \gamma^1} & \cdots & \dfrac{\partial \mathscr{R}_{\alpha^N}}{\partial \Delta \gamma^N} & \dfrac{\partial \mathscr{R}_{\alpha^N}}{\partial \Delta \alpha^1} & \cdots & \dfrac{\partial \mathscr{R}_{\alpha^N}}{\partial \Delta \alpha^N} \end{pmatrix} \tag{C.37}$$

where

$$\begin{cases} \dfrac{\partial \mathscr{R}_{\gamma^s}}{\partial \Delta \alpha^r} & = \Delta t \, C \dfrac{n}{K} \left\langle \dfrac{f^s}{K} \right\rangle^{n-1} \operatorname{sign}(\underset{\sim}{\boldsymbol{M}} : \underset{\sim}{\boldsymbol{N}}^s - x^s) \\ \dfrac{\partial \mathscr{R}_{\alpha^s}}{\partial \Delta \gamma^r} & = D\alpha^s - \operatorname{sign}(\underset{\sim}{\boldsymbol{M}} : \underset{\sim}{\boldsymbol{N}}^s - x^s) \\ \dfrac{\partial \mathscr{R}_{\gamma^s}}{\partial \Delta \gamma^r} & = \dfrac{n}{K} \left\langle \dfrac{f^s}{K} \right\rangle^{n-1} \left(\operatorname{sign}(\underset{\sim}{\boldsymbol{M}} : \underset{\sim}{\boldsymbol{N}}^s - x^s) \dfrac{\partial \tau_c^s}{\partial \Delta \gamma^r} \right) \\ \dfrac{\partial \mathscr{R}_{\alpha^s}}{\partial \Delta \alpha^r} & = \theta D |\Delta \gamma^s| \end{cases} \tag{C.38}$$

C.3 Scalar micromorphic elastoplasticity

Here, the derivation of the consistent tangent matrix for a time-independent plastic model is illustrated. For the sake of brevity, only the model with a micromorphic variable associated with cumulative plastic strain is detailed in the following. The tangent matrix writes

$$[\boldsymbol{K}] = \frac{\partial \Delta \mathscr{V}_{OUT}}{\partial \Delta \mathscr{V}_{IN}} - \frac{\partial \Delta \mathscr{V}_{OUT}}{\partial \Delta \mathscr{V}_{int}} \left(\frac{\partial \mathscr{R}}{\partial \Delta \mathscr{V}_{int}} \right)^{-1} \frac{\partial \mathscr{R}}{\partial \Delta \mathscr{V}_{IN}} \tag{C.39}$$

where

$$\frac{\partial \Delta \mathscr{V}_{OUT}}{\partial \Delta \mathscr{V}_{IN}} = \begin{bmatrix} \dfrac{\partial \Delta \underset{\sim}{\boldsymbol{P}}}{\partial \Delta \underset{\sim}{\boldsymbol{F}}} & \dfrac{\partial \Delta \underset{\sim}{\boldsymbol{P}}}{\partial \Delta \chi} & \dfrac{\partial \Delta \underset{\sim}{\boldsymbol{P}}}{\partial \Delta \underline{\boldsymbol{K}}} \\ \dfrac{\partial \Delta a}{\partial \Delta \underset{\sim}{\boldsymbol{F}}} & \dfrac{\partial \Delta a}{\partial \Delta \chi} & \dfrac{\partial \Delta a}{\partial \Delta \underline{\boldsymbol{K}}} \\ \dfrac{\partial \Delta \underline{\boldsymbol{b}}}{\partial \Delta \underset{\sim}{\boldsymbol{F}}} & \dfrac{\partial \Delta \underline{\boldsymbol{b}}}{\partial \Delta \chi} & \dfrac{\partial \Delta \underline{\boldsymbol{b}}}{\partial \Delta \underline{\boldsymbol{K}}} \end{bmatrix} = \begin{bmatrix} J(\underset{\sim}{\boldsymbol{\sigma}} \underset{\sim}{\boldsymbol{F}}^{-T}) \otimes \underset{\sim}{\boldsymbol{F}}^{-T} - J(\underset{\sim}{\boldsymbol{\sigma}} \bar{\otimes} \underset{\sim}{\boldsymbol{1}}) : (\underset{\sim}{\boldsymbol{F}}^{-T} \underset{-}{\otimes} \underset{\sim}{\boldsymbol{F}}^{-1}) & \boldsymbol{0} & \boldsymbol{0} \\ \boldsymbol{0} & H_\chi & \boldsymbol{0} \\ \boldsymbol{0} & 0 & \underset{\sim}{\underline{\boldsymbol{A}}} \end{bmatrix} \tag{C.40}$$

$$\frac{\partial \Delta \mathscr{V}_{OUT}}{\partial \Delta \mathscr{V}_{int}} = \begin{bmatrix} \dfrac{\partial \Delta \underset{\sim}{\boldsymbol{P}}}{\partial \Delta \underset{\sim}{\boldsymbol{F}}^e} & \dfrac{\partial \Delta \underset{\sim}{\boldsymbol{P}}}{\partial \Delta p} \\ \dfrac{\partial \Delta a}{\partial \Delta \underset{\sim}{\boldsymbol{F}}^e} & \dfrac{\partial \Delta a}{\partial \Delta p} \\ \dfrac{\partial \Delta \underline{\boldsymbol{b}}}{\partial \Delta \underset{\sim}{\boldsymbol{F}}^e} & \dfrac{\partial \Delta \underline{\boldsymbol{b}}}{\partial \Delta p} \end{bmatrix} = \begin{bmatrix} \dfrac{\partial \Delta \underset{\sim}{\boldsymbol{P}}}{\partial \Delta \underset{\sim}{\boldsymbol{\sigma}}} : \dfrac{\partial \Delta \underset{\sim}{\boldsymbol{\sigma}}}{\partial \Delta \underset{\sim}{\boldsymbol{F}}^e} & 0 \\ 0 & -H_\chi \\ 0 & 0 \end{bmatrix} \tag{C.41}$$

with

$$\frac{\partial \Delta \underset{\sim}{\boldsymbol{P}}}{\partial \Delta \underset{\sim}{\boldsymbol{\sigma}}} = J \underset{\sim}{\boldsymbol{1}} \underset{-}{\otimes} \underset{\sim}{\boldsymbol{F}}^{-1} \tag{C.42}$$

$$\begin{aligned} \frac{\partial \Delta \underset{\sim}{\boldsymbol{\sigma}}}{\partial \Delta \underset{\sim}{\boldsymbol{F}}^e} = & -\frac{1}{J^e} (\underset{\sim}{\boldsymbol{F}}^e \underset{\sim}{\boldsymbol{\Pi}}^e \underset{\sim}{\boldsymbol{F}}^{eT}) \otimes \underset{\sim}{\boldsymbol{F}}^{e-T} + \frac{1}{J^e} \underset{\sim}{\boldsymbol{1}} \underset{-}{\otimes} (\underset{\sim}{\boldsymbol{F}}^e \underset{\sim}{\boldsymbol{\Pi}}^e) + \frac{1}{2J^e} \left(\underset{\sim}{\boldsymbol{F}}^e \underset{-}{\otimes} \underset{\sim}{\boldsymbol{F}}^e \right) : \frac{\partial \underset{\sim}{\boldsymbol{\Pi}}^e}{\partial \underset{\sim}{\boldsymbol{E}}^e} : \left(\underset{\sim}{\boldsymbol{1}} \bar{\otimes} \underset{\sim}{\boldsymbol{F}}^{eT} + \underset{\sim}{\boldsymbol{F}}^{eT} \underset{-}{\otimes} \underset{\sim}{\boldsymbol{1}} \right) \\ & + \frac{1}{J^e} ((\underset{\sim}{\boldsymbol{F}}^e \underset{\sim}{\boldsymbol{\Pi}}^e) \underset{-}{\otimes} \underset{\sim}{\boldsymbol{1}}) : (\underset{\sim}{\boldsymbol{1}} \bar{\otimes} \underset{\sim}{\boldsymbol{1}}) \end{aligned} \tag{C.43}$$

$$\frac{\partial \mathscr{R}}{\partial \Delta \mathscr{V}_{IN}} = \begin{bmatrix} \dfrac{\partial \mathscr{R}_e}{\partial \Delta \underset{\sim}{\boldsymbol{F}}} & \dfrac{\partial \mathscr{R}_e}{\partial \Delta \chi} & \dfrac{\partial \mathscr{R}_e}{\partial \Delta \underline{\boldsymbol{K}}} \\ \dfrac{\partial \mathscr{R}_p}{\partial \Delta \underset{\sim}{\boldsymbol{F}}} & \dfrac{\partial \mathscr{R}_p}{\partial \Delta \chi} & \dfrac{\partial \mathscr{R}_p}{\partial \Delta \underline{\boldsymbol{K}}} \end{bmatrix} = \begin{bmatrix} -\underset{\sim}{\boldsymbol{1}} \underset{-}{\otimes} (\underset{\sim}{\boldsymbol{F}}^{-1} \underset{\sim}{\boldsymbol{F}}^e)^T + (\Delta \underset{\sim}{\boldsymbol{F}} \underset{-}{\otimes} \underset{\sim}{\boldsymbol{F}}^{eT}) : (\underset{\sim}{\boldsymbol{F}}^{-1} \underset{-}{\otimes} \underset{\sim}{\boldsymbol{F}}^{-T}) & \boldsymbol{0} & \boldsymbol{0} \\ \boldsymbol{0} & 1 & \boldsymbol{0} \end{bmatrix} \tag{C.44}$$

At Gauss point level, constitutive equations are integrated using a θ-method [Besson et al., 2009]. The values of all integrated variables evaluated at an intermediate time designated by $\theta \in [0,1]$ are

$$\mathscr{V}_{int}^{t+\theta\Delta t} = \mathscr{V}_{int}^{t} + \theta\Delta\mathscr{V}_{int} \tag{C.45}$$

The set of equations (2.56) can be gathered in the following form

$$\mathscr{R}(\mathscr{V}_{int}^{t+\theta\Delta t}, \Delta\mathscr{V}_{int}) = 0 \tag{C.46}$$

Since Eq. (C.46) is highly nonlinear, it is usually solved by means of a Newton method which requires the calculation of the Jacobian matrix

$$\frac{\partial\mathscr{R}}{\partial\Delta\mathscr{V}_{int}} = \begin{bmatrix} \dfrac{\partial\mathscr{R}_e}{\partial\Delta\underset{\sim}{\boldsymbol{F}}^e} & \dfrac{\partial\mathscr{R}_e}{\partial\Delta p} \\ \dfrac{\partial\mathscr{R}_p}{\partial\Delta\underset{\sim}{\boldsymbol{F}}^e} & \dfrac{\partial\mathscr{R}_p}{\partial\Delta p} \end{bmatrix} = \begin{bmatrix} \underset{\approx}{\boldsymbol{1}} - \theta\underset{\sim}{\boldsymbol{L}} \underset{-}{\otimes} \underset{\sim}{\boldsymbol{1}} + \theta\Delta p\underset{\sim}{\boldsymbol{N}} + \theta\Delta p\dfrac{\partial\underset{\sim}{\boldsymbol{N}}}{\partial\underset{\sim}{\boldsymbol{M}}}\dfrac{\partial\underset{\sim}{\boldsymbol{M}}}{\partial\underset{\sim}{\boldsymbol{F}}^e} & \underset{\sim}{\boldsymbol{F}}^e\underset{\sim}{\boldsymbol{N}} \\ \theta\underset{\sim}{\boldsymbol{N}} : \dfrac{\partial\underset{\sim}{\boldsymbol{M}}}{\partial\underset{\sim}{\boldsymbol{F}}^e} & -\dfrac{\theta}{H_\chi}\dfrac{\partial R}{\partial p} \end{bmatrix} \tag{C.47}$$

where $\underset{\sim}{\boldsymbol{N}} = \dfrac{\partial f}{\partial\underset{\sim}{\boldsymbol{M}}}$ is the normal to the yield surface.

C.4 Tensorial micromorphic elastoplasticity (small strains)

The consistent tangent matrix in C.39 is derived for a micromorphic model based on a symmetric second order tensor for rate-independent plasticity. The integrated variables $\mathscr{V}_{int} = \{\underset{\sim}{\boldsymbol{\varepsilon}}^e, p\}$, the output variables $\mathscr{V}_{OUT} = \{\underset{\sim}{\boldsymbol{\sigma}}, \underset{\sim}{\boldsymbol{a}}, \underset{\underset{-}{\sim}}{\boldsymbol{b}}\}$ and input variable $\mathscr{V}_{IN} = \{\underset{\sim}{\boldsymbol{\varepsilon}}, \underset{\sim}{\boldsymbol{\chi}}, \nabla\underset{\sim}{\boldsymbol{\chi}}\}$. Supplementary integrated variables can be considered, *e.g.* $\underset{\sim}{\boldsymbol{\alpha}}$ for kinematic hardening.

C.4.1 Total strain based model

Constitutive equations are written in the form of residuals as

$$\mathscr{R}^e = \Delta\underset{\sim}{\boldsymbol{\varepsilon}}^e - \Delta\underset{\sim}{\boldsymbol{\varepsilon}} + \Delta p\,\underset{\sim}{\boldsymbol{n}} = 0 \tag{C.48}$$

$$\mathscr{R}^p = f = 0 \tag{C.49}$$

Note that in this case no normalization of the plastic residual is required since it does not involve the penalization term (see Eq. (3.12)). The Jacobian matrix is given by

$$\mathscr{J} = \frac{\partial\mathscr{R}}{\partial\Delta\mathscr{V}_{int}} = \begin{bmatrix} \dfrac{\partial\mathscr{R}^e}{\partial\Delta\underset{\sim}{\boldsymbol{\varepsilon}}^e} & \dfrac{\partial\mathscr{R}^e}{\partial\Delta p} \\ \dfrac{\partial\mathscr{R}^p}{\partial\Delta\underset{\sim}{\boldsymbol{\varepsilon}}^e} & \dfrac{\partial\mathscr{R}^p}{\partial\Delta p} \end{bmatrix} = \begin{bmatrix} \underset{\sim}{\boldsymbol{1}} & \underset{\sim}{\boldsymbol{n}} \\ \underset{\sim}{\boldsymbol{n}} : \underset{\approx}{\mathbb{C}} & -\dfrac{\partial R}{\partial p} \end{bmatrix} \tag{C.50}$$

and

$$\frac{\partial\mathscr{R}}{\partial\Delta\mathscr{V}_{IN}} = \begin{bmatrix} \dfrac{\partial\mathscr{R}^e}{\partial\Delta\underset{\sim}{\boldsymbol{\varepsilon}}} & \dfrac{\partial\mathscr{R}^e}{\partial\Delta\underset{\sim}{\boldsymbol{\chi}}} & \dfrac{\partial\mathscr{R}^e}{\partial\Delta\nabla\underset{\sim}{\boldsymbol{\chi}}} \\ \dfrac{\partial\mathscr{R}^p}{\partial\Delta\underset{\sim}{\boldsymbol{\varepsilon}}} & \dfrac{\partial\mathscr{R}^p}{\partial\Delta\underset{\sim}{\boldsymbol{\chi}}} & \dfrac{\partial\mathscr{R}^p}{\partial\Delta\nabla\underset{\sim}{\boldsymbol{\chi}}} \end{bmatrix} = \begin{bmatrix} -\underset{\sim}{\boldsymbol{1}} & 0 & 0 \\ 0 & 0 & 0 \end{bmatrix} \tag{C.51}$$

$$\frac{\partial\Delta\mathscr{V}_{OUT}}{\partial\Delta\mathscr{V}_{IN}} = \begin{bmatrix} \dfrac{\partial\Delta\underset{\sim}{\boldsymbol{\sigma}}}{\partial\Delta\underset{\sim}{\boldsymbol{\varepsilon}}} & \dfrac{\partial\Delta\underset{\sim}{\boldsymbol{\sigma}}}{\partial\Delta\underset{\sim}{\boldsymbol{\chi}}} & \dfrac{\partial\Delta\underset{\sim}{\boldsymbol{\sigma}}}{\partial\Delta\nabla\underset{\sim}{\boldsymbol{\chi}}} \\ \dfrac{\partial\Delta\underset{\sim}{\boldsymbol{a}}}{\partial\Delta\underset{\sim}{\boldsymbol{\varepsilon}}} & \dfrac{\partial\Delta\underset{\sim}{\boldsymbol{a}}}{\partial\Delta\underset{\sim}{\boldsymbol{\chi}}} & \dfrac{\partial\Delta\underset{\sim}{\boldsymbol{a}}}{\partial\Delta\nabla\underset{\sim}{\boldsymbol{\chi}}} \\ \dfrac{\partial\Delta\underset{\simeq}{\boldsymbol{b}}}{\partial\Delta\underset{\sim}{\boldsymbol{\varepsilon}}} & \dfrac{\partial\Delta\underset{\simeq}{\boldsymbol{b}}}{\partial\Delta\underset{\sim}{\boldsymbol{\chi}}} & \dfrac{\partial\Delta\underset{\simeq}{\boldsymbol{b}}}{\partial\Delta\nabla\underset{\sim}{\boldsymbol{\chi}}} \end{bmatrix} = \begin{bmatrix} \underset{\approx}{\boldsymbol{H}}_{\chi} & -\underset{\approx}{\boldsymbol{H}}_{\chi} & \mathbf{0} \\ -\underset{\approx}{\boldsymbol{H}}_{\chi} & \underset{\approx}{\boldsymbol{H}}_{\chi} & \mathbf{0} \\ \mathbf{0} & \mathbf{0} & \underset{\underset{\sim}{\approx}}{\boldsymbol{A}} \end{bmatrix} \tag{C.52}$$

$$\frac{\partial\Delta\mathscr{V}_{OUT}}{\partial\Delta\mathscr{V}_{int}} = \begin{bmatrix} \dfrac{\partial\Delta\underset{\sim}{\boldsymbol{\sigma}}}{\partial\Delta\underset{\sim}{\boldsymbol{\varepsilon}}^{e}} & \dfrac{\partial\Delta\underset{\sim}{\boldsymbol{\sigma}}}{\partial\Delta p} \\ \dfrac{\partial\Delta\underset{\sim}{\boldsymbol{a}}}{\partial\Delta\underset{\sim}{\boldsymbol{\varepsilon}}^{e}} & \dfrac{\partial\Delta\underset{\sim}{\boldsymbol{a}}}{\partial\Delta p} \\ \dfrac{\partial\Delta\underset{\simeq}{\boldsymbol{b}}}{\partial\Delta\underset{\sim}{\boldsymbol{\varepsilon}}^{e}} & \dfrac{\partial\Delta\underset{\simeq}{\boldsymbol{b}}}{\partial\Delta p} \end{bmatrix} = \begin{bmatrix} \underset{\approx}{\mathbb{C}} & \mathbf{0} \\ \mathbf{0} & \mathbf{0} \\ \mathbf{0} & \mathbf{0} \end{bmatrix} \tag{C.53}$$

C.4.2 Plastic strain based model

Constitutive equations are written in the form of residuals as

$$\mathscr{R}^{e} = \Delta\underset{\sim}{\boldsymbol{\varepsilon}}^{e} - \Delta\underset{\sim}{\boldsymbol{\varepsilon}} + \Delta p\,\underset{\sim}{\boldsymbol{n}} = 0 \tag{C.54}$$

$$\mathscr{R}^{p} = \frac{f}{H_{\chi}} = 0 \quad \text{where} \quad \underset{\approx}{\boldsymbol{H}}_{\chi} = H_{\chi}\underset{\approx}{\mathbf{1}} \tag{C.55}$$

The Jacobian matrix

$$\mathscr{J} = \frac{\partial\mathscr{R}}{\partial\Delta\mathscr{V}_{int}} = \begin{bmatrix} \dfrac{\partial\mathscr{R}^{e}}{\partial\Delta\underset{\sim}{\boldsymbol{\varepsilon}}^{e}} & \dfrac{\partial\mathscr{R}^{e}}{\partial\Delta p} \\ \dfrac{\partial\mathscr{R}^{p}}{\partial\Delta\underset{\sim}{\boldsymbol{\varepsilon}}^{e}} & \dfrac{\partial\mathscr{R}^{p}}{\partial\Delta p} \end{bmatrix} = \begin{bmatrix} \underset{\sim}{\mathbf{1}} & \underset{\sim}{\boldsymbol{n}} \\ \underset{\sim}{\boldsymbol{n}} : \underset{\approx}{\mathbb{C}} & -\dfrac{1}{H_{\chi}}\dfrac{\partial R}{\partial p} \end{bmatrix} \tag{C.56}$$

and

$$\frac{\partial\mathscr{R}}{\partial\Delta\mathscr{V}_{IN}} = \begin{bmatrix} \dfrac{\partial\mathscr{R}^{e}}{\partial\Delta\underset{\sim}{\boldsymbol{\varepsilon}}} & \dfrac{\partial\mathscr{R}^{e}}{\partial\Delta\underset{\sim}{\boldsymbol{\chi}}} & \dfrac{\partial\mathscr{R}^{e}}{\partial\Delta\nabla\underset{\sim}{\boldsymbol{\chi}}} \\ \dfrac{\partial\mathscr{R}^{p}}{\partial\Delta\underset{\sim}{\boldsymbol{\varepsilon}}} & \dfrac{\partial\mathscr{R}^{p}}{\partial\Delta\underset{\sim}{\boldsymbol{\chi}}} & \dfrac{\partial\mathscr{R}^{p}}{\partial\Delta\nabla\underset{\sim}{\boldsymbol{\chi}}} \end{bmatrix} = \begin{bmatrix} -\underset{\sim}{\mathbf{1}} & 0 & 0 \\ 0 & \underset{\sim}{\boldsymbol{n}} : \underset{\approx}{\boldsymbol{H}}_{\chi} & 0 \end{bmatrix} \tag{C.57}$$

$$\frac{\partial\Delta\mathscr{V}_{OUT}}{\partial\Delta\mathscr{V}_{IN}} = \begin{bmatrix} \dfrac{\partial\Delta\underset{\sim}{\boldsymbol{\sigma}}}{\partial\Delta\underset{\sim}{\boldsymbol{\varepsilon}}} & \dfrac{\partial\Delta\underset{\sim}{\boldsymbol{\sigma}}}{\partial\Delta\underset{\sim}{\boldsymbol{\chi}}} & \dfrac{\partial\Delta\underset{\sim}{\boldsymbol{\sigma}}}{\partial\Delta\nabla\underset{\sim}{\boldsymbol{\chi}}} \\ \dfrac{\partial\Delta\underset{\sim}{\boldsymbol{a}}}{\partial\Delta\underset{\sim}{\boldsymbol{\varepsilon}}} & \dfrac{\partial\Delta\underset{\sim}{\boldsymbol{a}}}{\partial\Delta\underset{\sim}{\boldsymbol{\chi}}} & \dfrac{\partial\Delta\underset{\sim}{\boldsymbol{a}}}{\partial\Delta\nabla\underset{\sim}{\boldsymbol{\chi}}} \\ \dfrac{\partial\Delta\underset{\simeq}{\boldsymbol{b}}}{\partial\Delta\underset{\sim}{\boldsymbol{\varepsilon}}} & \dfrac{\partial\Delta\underset{\simeq}{\boldsymbol{b}}}{\partial\Delta\underset{\sim}{\boldsymbol{\chi}}} & \dfrac{\partial\Delta\underset{\simeq}{\boldsymbol{b}}}{\partial\Delta\nabla\underset{\sim}{\boldsymbol{\chi}}} \end{bmatrix} = \begin{bmatrix} \mathbf{0} & \mathbf{0} & \mathbf{0} \\ \mathbf{0} & \underset{\approx}{\boldsymbol{H}}_{\chi} & \mathbf{0} \\ \mathbf{0} & \mathbf{0} & \underset{\underset{\sim}{\approx}}{\boldsymbol{A}} \end{bmatrix} \tag{C.58}$$

$$\frac{\partial\Delta\mathscr{V}_{OUT}}{\partial\Delta\mathscr{V}_{int}} = \begin{bmatrix} \dfrac{\partial\Delta\underset{\sim}{\boldsymbol{\sigma}}}{\partial\Delta\underset{\sim}{\boldsymbol{\varepsilon}}^{e}} & \dfrac{\partial\Delta\underset{\sim}{\boldsymbol{\sigma}}}{\partial\Delta p} \\ \dfrac{\partial\Delta\underset{\sim}{\boldsymbol{a}}}{\partial\Delta\underset{\sim}{\boldsymbol{\varepsilon}}^{e}} & \dfrac{\partial\Delta\underset{\sim}{\boldsymbol{a}}}{\partial\Delta p} \\ \dfrac{\partial\Delta\underset{\simeq}{\boldsymbol{b}}}{\partial\Delta\underset{\sim}{\boldsymbol{\varepsilon}}^{e}} & \dfrac{\partial\Delta\underset{\simeq}{\boldsymbol{b}}}{\partial\Delta p} \end{bmatrix} = \begin{bmatrix} \underset{\approx}{\mathbb{C}} & \mathbf{0} \\ \mathbf{0} & -\underset{\approx}{\boldsymbol{H}}_{\chi} : \underset{\sim}{\boldsymbol{n}} \\ \mathbf{0} & \mathbf{0} \end{bmatrix} \tag{C.59}$$

Bibliography

Abatour, M. (2019). Comportement et rupture à basse température de la gaine en polyéthylène de tuyaux flexibles destinés au transfert en mer de gaz naturel liquéfié (GNL). Master's thesis, Mines Paris.

Aifantis, E. C. (1984). On the microstructural origin of certain inelastic models. *Journal of Engineering Materials and Technology*, 106(4):326–330.

Anand, L., Aslan, O., and Chester, S. A. (2012). A large-deformation gradient theory for elastic–plastic materials: Strain softening and regularization of shear bands. *International Journal of Plasticity*, 30-31:116–143.

Aravas, N. (1994). Finite-strain anisotropic plasticity and the plastic spin. *Modelling and Simulation in Materials Science and Engineering*, 2(3A):483–504. Publisher: IOP Publishing.

Armstrong, P. and Frederick, C. (1966). A mathematical representation of the multiaxial Bauschinger effect. C.E.G.B. Report RD/B/ N 731, Berkeley Nuclear Laboratories, Berkeley, UK.

Ashby, M. F. (1970). The deformation of plastically non-homogeneous materials. *The Philosophical Magazine: A Journal of Theoretical Experimental and Applied Physics*, 21(170):399–424.

Aslan, O., Cordero, N., Gaubert, A., and Forest, S. (2011). Micromorphic approach to single crystal plasticity and damage. *International Journal of Engineering Science*, 49(12):1311–1325.

Auffray, N., Bouchet, R., and Bréchet, Y. (2009). Derivation of anisotropic matrix for bi-dimensional strain-gradient elasticity behavior. *International Journal of Solids and Structures*, 46(2):440–454.

Auffray, N., Bouchet, R., and Bréchet, Y. (2010). Strain gradient elastic homogenization of bidimensional cellular media. *International Journal of Solids and Structures*, 47(13):1698–1710.

Bažant, Z. P. and Jirásek, M. (2002). Nonlocal integral formulations of plasticity and damage: survey of progress. *Journal of Engineering Mechanics*, 128(11):1119–1149.

Bernstein, B. (1960). Hypo-elasticity and elasticity. *Archive for Rational Mechanics and Analysis*, 6(1):89–104.

Bertram, A. (1999). An alternative approach to finite plasticity based on material isomorphisms. *International Journal of Plasticity*, 15(3):353–374.

Bertram, A. (2003). Finite thermoplasticity based on isomorphisms. *International Journal of Plasticity*, 19(11):2027–2050.

Besson, J., Cailletaud, G., Chaboche, J.-L., and Forest, S. (2009). *Non-Linear Mechanics of Materials*. Solid Mechanics and Its Applications. Springer Netherlands.

Boehler, J. P. (1987). *Applications of tensor functions in solid mechanics*. CISM Courses and Lectures No. 292, Udine, Springer Verlag, Wien.

Botta, A. S., Venturini, W. S., and Benallal, A. (2005). BEM applied to damage models emphasizing localization and associated regularization techniques. *Engineering Analysis with Boundary Elements*, 29(8):814–827.

Bouby, C., Kondo, D., and de Saxcé, G. (2015). A comparative analysis of two formulations for non linear hardening plasticity models: Application to shakedown analysis. *European Journal of Mechanics - A/Solids*, 53:48–61.

Boyce, M. C., Montagut, E. L., and Argon, A. S. (1992). The effects of thermomechanical coupling on the cold drawing process of glassy polymers. *Polymer Engineering & Science*, 32(16):1073–1085.

Brepols, T., Vladimirov, I. N., and Reese, S. (2014). Numerical comparison of isotropic hypo- and hyperelastic-based plasticity models with application to industrial forming processes. *International Journal of Plasticity*, 63:18–48.

Brepols, T., Wulfinghoff, S., and Reese, S. (2017). Gradient-extended two-surface damage-plasticity: Micromorphic formulation and numerical aspects. *International Journal of Plasticity*, 97:64–106.

Cailletaud, G. (2017). *Multi-mechanism modeling of inelastic material behavior*. ISTE Ltd/John Wiley and Sons Inc, Hoboken, NJ.

Cailletaud, G. and Saï, K. (1995). Study of plastic/viscoplastic models with various inelastic mechanisms. *International Journal of Plasticity*, 11(8):991–1005.

Callister, W. D. and Rethwisch, D. G. (2013). *Materials Science and Engineering: An Introduction*. Wiley, Hoboken, NJ, 9e édition edition.

Chaboche, J. (2008). A review of some plasticity and viscoplasticity constitutive theories. *International Journal of Plasticity*, 24:1642–1693.

Chen, Y., Lorentz, E., and Besson, J. (2020). Crack initiation and propagation in small-scale yielding using a nonlocal GTN model. *International Journal of Plasticity*, 130:102701.

Chen, Y., Lorentz, E., Dahl, A., and Besson, J. (2022). Simulation of ductile tearing during a full size test using a non local Gurson–Tvergaard–Needleman (GTN) model. *Engineering Fracture Mechanics*, 261:108226.

Chevalier, J. (2018). *Micromechanics of an epoxy matrix for fiber reinforced composites : experiments and physics-based modelling*. PhD thesis, UCL - Université Catholique de Louvain.

Chevalier, J., Camanho, P. P., Lani, F., and Pardoen, T. (2019). Multi-scale characterization and modelling of the transverse compression response of unidirectional carbon fiber reinforced epoxy. *Composite Structures*, 209:160–176.

Ciarlet, P. G. (1988). *Three-Dimensional Elasticity*. Elsevier.

Clifton, R. J. (1972). On the Equivalence of FeFp and FpFe. *Journal of Applied Mechanics*, 39(1):287–289. Publisher: American Society of Mechanical Engineers Digital Collection.

Cordero, N. M., Forest, S., and Busso, E. P. (2016). Second strain gradient elasticity of nano-objects. *Journal of the Mechanics and Physics of Solids*, 97:92–124.

Cordero, N. M., Gaubert, A., Forest, S., Busso, E. P., Gallerneau, F., and Kruch, S. (2010). Size effects in generalised continuum crystal plasticity for two-phase laminates. *Journal of the Mechanics and Physics of Solids*, 58(11):1963–1994.

Dafalias, Y. F. (1983). Corotational rates for kinematic hardening at large plastic deformations. *Journal of Applied Mechanics*, 50(3):561–565.

Dafalias, Y. F. (1984). The plastic spin concept and a simple illustration of its role in finite plastic transformations. *Mechanics of Materials*, 3(3):223–233.

Dafalias, Y. F. (1993). On multiple spins and texture development. Case study: kinematic and orthotropic hardening. *Acta Mechanica*, 100(3):171–194.

Davaze, V., Vallino, N., Feld-Payet, S., Langrand, B., and Besson, J. (2020). Plastic and fracture behavior of a dual phase steel sheet under quasi-static and dynamic loadings. *Engineering Fracture Mechanics*, 235:107165.

De Borst, R. and Mühlhaus, H.-B. (1992). Gradient-dependent plasticity: Formulation and algorithmic aspects. *International Journal for Numerical Methods in Engineering*, 35(3):521–539.

de Borst, R., Pamin, J., and Geers, M. G. D. (1999). On coupled gradient-dependent plasticity and damage theories with a view to localization analysis. *European Journal of Mechanics - A/Solids*, 18(6):939–962.

de Borst, R., Pamin, J., and Sluys, L. J. (1995). Computational issues in gradient plasticity. *Continuum models for materials with microstructure*, pages 159–200. Publisher: Wiley.

de Saxcé, G. (1992). Une généralisation de l'inégalité de Fenchel et ses applications aux lois constitutives. *C.R. Acad. Sci. Paris*, 314.

Dettmer, W. and Reese, S. (2004). On the theoretical and numerical modelling of Armstrong–Frederick kinematic hardening in the finite strain regime. *Computer Methods in Applied Mechanics and Engineering*, 193(1):87–116.

Diamantopoulou, E., Liu, W., Labergère, C., Badreddine, H., Saanouni, K., and Hu, P. (2017). Micromorphic constitutive equations with damage applied to metal forming. *International Journal of Damage Mechanics*, 26(2):314–339. Publisher: SAGE Publications Ltd STM.

Dienes, J. K. (1979). On the analysis of rotation and stress rate in deforming bodies. *Acta Mechanica*, 32(4):217–232.

Dillard, T., Forest, S., and Ienny, P. (2006). Micromorphic continuum modelling of the deformation and fracture behaviour of nickel foams. *European Journal of Mechanics - A/Solids*, 25(3):526–549.

Dogui, A. and Sidoroff, F. (1985). Kinematic hardening in large elastoplastic strain. *Engineering Fracture Mechanics*, 21(4):685–695.

Duchene, L., Lelotte, T., Flores, P., Bouvier, S., and Habraken, A. (2008). Rotation of axes for anisotropic metal in FEM simulations. *International Journal of Plasticity*, 24(3):397–427.

Eringen, A. C., editor (2002). *Nonlocal continuum field theories*. Springer, New York, NY.

Eringen, A. C. and Edelen, D. G. B. (1972). On nonlocal elasticity. *International Journal of Engineering Science*, 10(3):233–248.

Eringen, A. C. and Suhubi, E. S. (1964). Nonlinear theory of simple micro-elastic solids–I. *International Journal of Engineering Science*, 2(2):189–203.

Fares, N. and Dvorak, G. J. (1991). Large elastic-plastic deformations of fibrous metal matrix composites. *Journal of the Mechanics and Physics of Solids*, 39(6):725–744.

Fassin, M., Eggersmann, R., Wulfinghoff, S., and Reese, S. (2019). Gradient-extended anisotropic brittle damage modeling using a second order damage tensor - Theory, implementation and numerical examples. *International Journal of Solids and Structures*, 167:93 – 126.

Felder, S., Kopic-Osmanovic, N., Holthusen, H., Brepols, T., and Reese, S. (2022). Thermo-mechanically coupled gradient-extended damage-plasticity modeling of metallic materials at finite strains. *International Journal of Plasticity*, 148:103142.

Fergoug, M., Parret-Fréaud, A., Feld, N., Marchand, B., and Forest, S. (2022). Multiscale analysis of composite structures based on higher-order asymptotic homogenization with boundary layer correction. *European Journal of Mechanics - A/Solids*, 96:104754.

Fleck, N. and Hutchinson, J. (1997). Strain gradient plasticity. *Adv. Appl. Mech.*, 33:295–361.

Fleck, N. A. and Hutchinson, J. W. (1993). A phenomenological theory for strain gradient effects in plasticity. *Journal of the Mechanics and Physics of Solids*, 41(12):1825–1857.

Fleck, N. A., Muller, G. M., Ashby, M. F., and Hutchinson, J. W. (1994). Strain gradient plasticity: Theory and experiment. *Acta Metallurgica et Materialia*, 42(2):475–487.

Foerch, R., Besson, J., Cailletaud, G., and Pilvin, P. (1997). Polymorphic constitutive equations in finite element codes. *Computer Methods in Applied Mechanics and Engineering*, 141(3):355–372.

Forest, S. (2009). Micromorphic approach for gradient elasticity, viscoplasticity, and damage. *Journal of Engineering Mechanics*, 135(3):117–131.

Forest, S. (2016). Nonlinear regularization operators as derived from the micromorphic approach to gradient elasticity, viscoplasticity and damage. *Proceedings of the Royal Society A: Mathematical, Physical and Engineering Sciences*, 472(2188):20150755.

Forest, S. and Aifantis, E. C. (2010). Some links between recent gradient thermo-elasto-plasticity theories and the thermomechanics of generalized continua. *International Journal of Solids and Structures*, 47(25):3367–3376.

Forest, S., Ammar, K., and Appolaire, B. (2011). Micromorphic vs. phase-field approaches for gradient viscoplasticity and phase transformations. In Pfeiffer, F., Wriggers, P., and Markert, B., editors, *Advances in Extended and Multifield Theories for Continua*, volume 59, pages 69–88. Springer Berlin Heidelberg, Berlin, Heidelberg. Series Title: Lecture Notes in Applied and Computational Mechanics.

Forest, S. and Sievert, R. (2003). Elastoviscoplastic constitutive frameworks for generalized continua. *Acta Mechanica*, 160(1):71–111.

Forest, S. and Sievert, R. (2006). Nonlinear microstrain theories. *International Journal of Solids and Structures*, 43(24):7224–7245.

Frederick, C. and Armstrong, P. (2007). A mathematical representation of the multiaxial bauschinger effect. *Materials at High Temperatures*, 24:1–26.

Friedlein, J., Mergheim, J., and Steinmann, P. (2022). Observations on additive plasticity in the logarithmic strain space at excessive strains. *International Journal of Solids and Structures*, 239-240:111416.

Frémond, M. and Nedjar, B. (1996). Damage, gradient of damage and principle of virtual power. *International Journal of Solids and Structures*, 33(8):1083–1103.

Geers, M., Borst, R., d., Brekelmans, W., and Peerlings, R. (1998). Strain-based transient-gradient damage model for failure analyses. *Computer Methods in Applied Mechanics and Engineering*, 160(1-2):133–153.

Geers, M. G., Engelen, R. A., and Ubachs, R. J. (2001). On the numerical modelling of ductile damage with an implicit gradient-enhanced formulation. *Revue Européenne des Éléments Finis*, 10(2-4):173–191.

Geers, M. G. D. (2004). Finite strain logarithmic hyperelasto-plasticity with softening: a strongly non-local implicit gradient framework. *Computer Methods in Applied Mechanics and Engineering*, 193(30):3377–3401.

Geers, M. G. D., Ubachs, R. L. J. M., and Engelen, R. A. (2003). Strongly non-local gradient-enhanced finite strain elastoplasticity. *International Journal for Numerical Methods in Engineering*, 56(14):2039–2068.

Germain, P. (1973). The method of virtual power in continuum mechanics. part 2: microstructure. *SIAM Journal on Applied Mathematics*, 25(3):556–575. Publisher: Society for Industrial and Applied Mathematics.

Green, A. E. and Naghdi, P. M. (1965). A general theory of an elastic-plastic continuum. *Archive for Rational Mechanics and Analysis*, 18(4):251–281.

Gudmundson, P. (2004). A unified treatment of strain gradient plasticity. *Journal of the Mechanics and Physics of Solids*, 52(6):1379–1406.

Gurtin, M. E. and Anand, L. (2005). The decomposition F=FeFp, material symmetry, and plastic irrotationality for solids that are isotropic-viscoplastic or amorphous. *International Journal of Plasticity*, 21(9):1686–1719.

Gurtin, M. E. and Anand, L. (2009). Thermodynamics applied to gradient theories involving the accumulated plastic strain: The theories of Aifantis and Fleck and Hutchinson and their generalization. *Journal of the Mechanics and Physics of Solids*, 57(3):405–421.

Halary, J.-L., Lauprêtre, F., and Monnerie, L. (2011). *Polymer materials: macroscopic properties and molecular interpretations*. Wiley, Hoboken, N.J.

Halphen, B. and Son Nguyen, Q. (1975). Sur les matériaux standard généralisés. *Journal de Mécanique*, 14:39–63.

Hashemi, R., Abrinia, K., and Assempour, A. (2013). The strain gradient approach to predict necking in tube hydroforming. *Journal of Manufacturing Processes*, 15(1):51–55.

Hashiguchi, K. (2019). Multiplicative hyperelastic-based plasticity for finite elastoplastic deformation/sliding: a comprehensive review. *Archives of Computational Methods in Engineering*, 26(3):597–637.

Hashiguchi, K. (2020). *Nonlinear continuum mechanics for finite elasticity plasticity: multiplicative decomposition with subloading surface model*. Elsevier, Amterdam, Netherlands ; Cambridge, MA.

Hibbitt, H., Marcal, P., and Rice, J. (1970). A finite element formulation for problems of large strain and large displacement. *International Journal of Solids and Structures*, 6(8):1069–1086.

Hien Poh, L. and Swaddiwudhipong, S. (2009). Over-nonlocal gradient enhanced plastic-damage model for concrete. *International Journal of Solids and Structures*, 46(25):4369–4378.

Hirschberger, C. B. and Steinmann, P. (2009). Classification of Concepts in Thermodynamically Consistent Generalized Plasticity. *Journal of Engineering Mechanics*, 135(3):156–170.

Holthusen, H., Brepols, T., Reese, S., and Simon, J.-W. (2022). A two-surface gradient-extended anisotropic damage model using a second order damage tensor coupled to additive plasticity in the logarithmic strain space. *Journal of the Mechanics and Physics of Solids*, 163:104833.

Holzapfel, G. A. (2000). *Nonlinear Solid Mechanics: A Continuum Approach for Engineering*. Wiley.

Itskov, M. and Aksel, N. (2004). A constitutive model for orthotropic elasto-plasticity at large strains. *Archive of Applied Mechanics*, 74(1):75–91.

Jebahi, M., Cai, L., and Abed-Meraim, F. (2020). Strain gradient crystal plasticity model based on generalized non-quadratic defect energy and uncoupled dissipation. *International Journal of Plasticity*, 126:102617.

Jebahi, M. and Forest, S. (2021). Scalar-based strain gradient plasticity theory to model size-dependent kinematic hardening effects. *Continuum Mechanics and Thermodynamics*, 33(4):1223–1245.

Jiao, Y. and Fish, J. (2017). Is an additive decomposition of a rate of deformation and objective stress rates passé? *Computer Methods in Applied Mechanics and Engineering*, 327:196–225.

Jiao, Y. and Fish, J. (2018). On the equivalence between the multiplicative hyper-elasto-plasticity and the additive hypo-elasto-plasticity based on the modified kinetic logarithmic stress rate. *Computer Methods in Applied Mechanics and Engineering*, 340:824–863.

Kamlah, M. and Tsakmakis, C. (1999). Use of isotropic thermoelasticity laws in finite deformation viscoplasticity models. *Continuum Mechanics and Thermodynamics*, 11(2):73–88.

Kiefer, B., Waffenschmidt, T., Sprave, L., and Menzel, A. (2018). A gradient-enhanced damage model coupled to plasticity-multi-surface formulation and algorithmic concepts. *International Journal of Damage Mechanics*, 27:253–295.

Kirchner, N. and Steinmann, P. (2005). A unifying treatise on variational principles for gradient and micromorphic continua. *Philosophical Magazine*, 85(33-35):3875–3895.

Kocks, U. and Mecking, H. (2003). Physics and phenomenology of strain hardening: the FCC case. *Progress in Materials Science*, 48(3):171–273.

Kojić, M. and Bathe, K.-J. (1987). Studies of finite element procedures—Stress solution of a closed elastic strain path with stretching and shearing using the updated Lagrangian Jaumann formulation. *Computers & Structures*, 26(1):175–179.

Kratochvíl, J. (1973). On a finite strain theory of elastic-inelastic materials. *Acta Mechanica*, 16(1):127–142.

Kröner, E. (1959). Allgemeine Kontinuumstheorie der Versetzungen und Eigenspannungen. *Archive for Rational Mechanics and Analysis*, 4(1):273–334.

Langenfeld, K. and Mosler, J. (2020). A micromorphic approach for gradient-enhanced anisotropic ductile damage. *Computer Methods in Applied Mechanics and Engineering*, 360:112717.

Le, L. T., Ammar, K., and Forest, S. (2020). Efficient simulation of single and poly-crystal plasticity based on the pencil glide mechanism. *Comptes Rendus Mécanique*, 348:846–876.

Lee, E. H. and Liu, D. T. (1967). Finite strain elastic-plastic theory with application to plane-wave analysis. *Journal of Applied Physics*, 38(1):19–27.

Lemaitre, J. and Chaboche, J.-L. (1994). *Mechanics of Solid Materials*. Cambridge University Press.

Lin, R. C., Schomburg, U., and Kletschkowski, T. (2003). Analytical stress solutions of a closed deformation path with stretching and shearing using the hypoelastic formulations. *European Journal of Mechanics - A/Solids*, 22(3):443–461.

Ling, C., Forest, S., Besson, J., Tanguy, B., and Latourte, F. (2018). A reduced micromorphic single crystal plasticity model at finite deformations. Application to strain localization and void growth in ductile metals. *International Journal of Solids and Structures*, 134:43–69.

Lion, A. (2000). Constitutive modelling in finite thermoviscoplasticity: a physical approach based on nonlinear rheological models. *International Journal of Plasticity*, 16(5):469–494.

Lorentz, E. and Benallal, A. (2005). Gradient constitutive relations: numerical aspects and application to gradient damage. *Computer Methods in Applied Mechanics and Engineering*, 194(50):5191–5220.

Loret, B. (1983). On the effects of plastic rotation in the finite deformation of anisotropic elastoplastic materials. *Mechanics of Materials*, 2(4):287–304.

Lu, S. C. H. and Pister, K. S. (1975). Decomposition of deformation and representation of the free energy function for isotropic thermoelastic solids. *International Journal of Solids and Structures*, 11(7):927–934.

Lubarda, V. A. (1991). Constitutive analysis of large elasto-plastic deformation based on the multiplicative decomposition of deformation gradient. *International Journal of Solids and Structures*, 27(7):885–895.

Lubarda, V. A. (1999). Duality in constitutive formulation of finite-strain elastoplasticity based on $F = F^e F^p$ and $F = F^p F^e$ decompositions. *International Journal of Plasticity*, 15(12):1277–1290.

Lubarda, V. A. (2004). Constitutive theories based on the multiplicative decomposition of deformation gradient: Thermoelasticity, elastoplasticity, and biomechanics. *Applied Mechanics Reviews*, 57(2):95–108. Publisher: American Society of Mechanical Engineers Digital Collection.

Mandel, J., editor (1972). *Plasticité classique et viscoplasticité*. Springer Verlag, Wien - New York. OCLC: 64315623.

Mandel, J. (1973). Équations constitutives et directeurs dans les milieux plastiques et viscoplastiques. *International Journal of Solids and Structures*, 9(6):725–740.

Martinez-Paneda, E. and Niordson, C. (2016). On fracture in finite strain gradient plasticity. *International Journal of Plasticity*, 80:154–167.

Martínez-Pañeda, E., Deshpande, V. S., Niordson, C. F., and Fleck, N. A. (2019). The role of plastic strain gradients in the crack growth resistance of metals. *Journal of the Mechanics and Physics of Solids*, 126:136–150.

Mazière, M. and Forest, S. (2015). Strain gradient plasticity modeling and finite element simulation of Lüders band formation and propagation. *Continuum Mechanics and Thermodynamics*, 27(1):83–104.

Mecking, H. and Kocks, U. F. (1981). Kinetics of flow and strain-hardening. *Acta Metallurgica*, 29(11):1865–1875.

Menzel, A., Ekh, M., Runesson, K., and Steinmann, P. (2005). A framework for multiplicative elastoplasticity with kinematic hardening coupled to anisotropic damage. *International Journal of Plasticity*, 21(3):397–434.

Méric, L., Poubanne, P., and Cailletaud, G. (1991). Single crystal modeling for structural calculations. Part 1: Model presentation. *Journal of Engineering Materials and Technology*, 113:162–170.

Miehe, C. (1996). Multisurface thermoplasticity for single crystals at large strains in terms of eulerian vector updates. *International Journal of Solids and Structures*, 33(20):3103–3130.

Miehe, C., Apel, N., and Lambrecht, M. (2002). Anisotropic additive plasticity in the logarithmic strain space: modular kinematic formulation and implementation based on incremental minimization principles for standard materials. *Computer Methods in Applied Mechanics and Engineering*, 191(47):5383–5425.

Mindlin, R. D. (1964). Micro-structure in linear elasticity. *Archive for Rational Mechanics and Analysis*, 16(1):51–78.

Morelle, X. P., Chevalier, J., Bailly, C., Pardoen, T., and Lani, F. (2017). Mechanical characterization and modeling of the deformation and failure of the highly crosslinked RTM6 epoxy resin. *Mechanics of Time-Dependent Materials*, 21(3):419–454.

Mu, Y., Zhang, X., Hutchinson, J., and Meng, W. (2016). Dependence of confined plastic flow of polycrystalline Cu thin films on microstructure. *MRS Communications*, 6:289–294.

Méric, L. and Cailletaud, G. (1991). Single crystal modeling for structural calculations: Part 2—finite element implementation. *Journal of Engineering Materials and Technology*, 113(1):171–182.

Naghdi, P. M. (1990). A critical review of the state of finite plasticity. *Zeitschrift für angewandte Mathematik und Physik ZAMP*, 41(3):315–394.

Needleman, A. (1988). Material rate dependence and mesh sensitivity in localization problems. *Computer Methods in Applied Mechanics and Engineering*, 67(1):69–85.

Nemat-Nasser, S. (1979). Decomposition of strain measures and their rates in finite deformation elastoplasticity. *International Journal of Solids and Structures*, 15(2):155–166.

Neto, E. A. d. S., Peric, D., and Owen, D. R. J. (2008). *Computational Methods for Plasticity: Theory and Applications*. John Wiley & Sons.

Nouailhas, D. and Cailletaud, G. (1995). Tension-torsion behavior of single-crystal superalloys: experiment and finite element analysis. *International Journal of Plasticity*, 11(4):451–470.

Nye, J. (1953). Some geometrical relations in dislocated crystals. *Acta Metallurgica*, 1:152–162.

Pardoen, T., Klavzer, N., Gayot, S., Van Loock, F., Chevalier, J., Morelle, X., Destoop, V., Lani, F., Camanho, P., Brassart, L., Nysten, B., and Bailly, C. (2021). Nanomechanics serving polymer-based composite research. *Comptes Rendus. Physique*, 22(S3):331–352.

Peerlings, R. H. J. (2007). On the role of moving elastic–plastic boundaries in strain gradient plasticity. *Modelling and Simulation in Materials Science and Engineering*, 15(1):S109–S120.

Peerlings, R. H. J., de Borst, R., Brekelmans, W. a. M., and De Vree, J. H. P. (1996). Gradient enhanced damage for quasi-brittle materials. *International Journal for Numerical Methods in Engineering*, 39(19):3391–3403.

Peeters, B., Hoferlin, E., Van Houtte, P., and Aernoudt, E. (2001). Assessment of crystal plasticity based calculation of the lattice spin of polycrystalline metals for FE implementation. *International Journal of Plasticity*, 17(6):819–836.

Poh, L. H., Peerlings, R. H. J., Geers, M. G. D., and Swaddiwudhipong, S. (2011). An implicit tensorial gradient plasticity model – Formulation and comparison with a scalar gradient model. *International Journal of Solids and Structures*, 48(18):2595–2604.

Raoult, A. (1986). Non-polyconvexity of the stored energy function of a Saint Venant-Kirchhoff material. *Aplikace matematiky*, 31(6):417–419.

Ree, F., Ree, T., and Eyring, H. (1958). Relaxation theory of transport problems in condensed systems. *Industrial & Engineering Chemistry*, 50(7):1036–1040. Publisher: American Chemical Society.

Ren, S., Mazière, M., Forest, S., Morgeneyer, T. F., and Rousselier, G. (2017). A constitutive model accounting for strain ageing effects on work-hardening. Application to a C–Mn steel. *Comptes Rendus Mécanique*, 345(12):908–921.

Rezaee-Hajidehi, M., Sadowski, P., and Stupkiewicz, S. (2022). Deformation twinning as a displacive transformation: Finite-strain phase-field model of coupled twinning and crystal plasticity. *Journal of the Mechanics and Physics of Solids*, 163:104855.

Russo, R., Phalke, V., Croizet, D., Ziane, M., Forest, S., Girot Mata, F., Chang, H., and Roos, A. (2022). Regularization of shear banding and prediction of size effects in manufacturing operations: A micromorphic plasticity explicit scheme. *International Journal of Material Forming*, 15:21.

Saanouni, K. and Hamed, M. (2013). Micromorphic approach for finite gradient-elastoplasticity fully coupled with ductile damage: Formulation and computational aspects. *International Journal of Solids and Structures*, 50(14):2289–2309.

Scherer, J., Besson, J., Forest, S., Hure, J., and Tanguy, B. (2019). Strain gradient crystal plasticity with evolving length scale: Application to voided irradiated materials. *European Journal of Mechanics - A/Solids*, 77:103768.

Scherer, J.-M., Phalke, V., Besson, J., Forest, S., Hure, J., and Tanguy, B. (2020). Lagrange multiplier based vs micromorphic gradient-enhanced rate-(in)dependent crystal plasticity modelling and simulation. *Computer Methods in Applied Mechanics and Engineering*, 372:113426.

Shutov, A. V. and Ihlemann, J. (2014). Analysis of some basic approaches to finite strain elasto-plasticity in view of reference change. *International Journal of Plasticity*, 63:183–197.

Sprave, L. and Menzel, A. (2020). A large strain gradient-enhanced ductile damage model: finite element formulation, experiment and parameter identification. *Acta Mechanica*, 231:5159–5192.

Steinmann, P. (1999). Formulation and computation of geometrically non-linear gradient damage. *International Journal for Numerical Methods in Engineering*, 46(5):757–779.

Stölken, J. S. and Evans, A. G. (1998). A microbend test method for measuring the plasticity length scale. *Acta Materialia*, 46(14):5109–5115.

Suhubi, E. S. and Eringen, A. C. (1964). Nonlinear theory of micro-elastic solids—II. *International Journal of Engineering Science*, 2(4):389–404.

Svendsen, B., Arndt, S., Klingbeil, D., and Sievert, R. (1998). Hyperelastic models for elastoplasticity with non-linear isotropic and kinematic hardening at large deformation. *International Journal of Solids and Structures*, 35(25):3363–3389.

Teodosiu, C. and Sidoroff, F. (1976). A theory of finite elastoviscoplasticity of single crystals. *International Journal of Engineering Science*, 14(2):165–176.

Truesdell, C. (1955). Hypo-elasticity. *Journal of Rational Mechanics and Analysis*, 4:83–1020. Publisher: Indiana University Mathematics Department.

Truesdell, C. and Noll, W. (1965). The non-linear field theories of mechanics. In Truesdell, C. and Noll, W., editors, *The Non-Linear Field Theories of Mechanics / Die Nicht-Linearen Feldtheorien der Mechanik*, Encyclopedia of Physics / Handbuch der Physik, pages 1–541. Springer, Berlin, Heidelberg.

Tsakmakis, C. (1996a). Kinematic hardening rules in finite plasticity Part I: A constitutive approach. *Continuum Mechanics and Thermodynamics*, 8(4):215–231.

Tsakmakis, C. (1996b). Kinematic hardening rules in finite plasticity Part II: Some examples. *Continuum Mechanics and Thermodynamics*, 8(4):233–246.

Tsakmakis, C. and Willuweit, A. (2004). A comparative study of kinematic hardening rules at finite deformations. *International Journal of Non-Linear Mechanics*, 39(4):539–554.

Ubachs, R. L. J. M., Schreurs, P. J. G., and Geers, M. G. D. (2004). A nonlocal diffuse interface model for microstructure evolution of tin–lead solder. *Journal of the Mechanics and Physics of Solids*, 52(8):1763–1792.

Ulz, M. H. (2011). A finite isoclinic elasto-plasticity model with orthotropic yield function and notion of plastic spin. *Computer Methods in Applied Mechanics and Engineering*, 200(21):1822–1832.

Van der Giessen, E. (1991). Micromechanical and thermodynamic aspects of the plastic spin. *International Journal of Plasticity*, 7(5):365–386.

Venkatraman, R. and Bravman, J. C. (1992). Separation of film thickness and grain boundary strengthening effects in Al thin films on Si. *Journal of Materials Research*, 7(8):2040–2048.

Vladimirov, I. N., Pietryga, M. P., and Reese, S. (2008). On the modelling of non-linear kinematic hardening at finite strains with application to springback—Comparison of time integration algorithms. *International Journal for Numerical Methods in Engineering*, 75(1):1–28.

Vladimirov, I. N., Pietryga, M. P., and Reese, S. (2010). Anisotropic finite elastoplasticity with nonlinear kinematic and isotropic hardening and application to sheet metal forming. *International Journal of Plasticity*, 26(5):659–687.

Vujošević, L. and Lubarda, V. (2002). Finite-strain thermoelasticity based on multiplicative decomposition of deformation gradient. *Theoretical and Applied Mechanics*, 28-29:379–399.

Wallin, M. and Ristinmaa, M. (2005). Deformation gradient based kinematic hardening model. *International Journal of Plasticity*, 21(10):2025–2050.

Wallin, M., Ristinmaa, M., and Ottosen, N. S. (2003). Kinematic hardening in large strain plasticity. *European Journal of Mechanics - A/Solids*, 22(3):341–356.

Weber, G. and Anand, L. (1990). Finite deformation constitutive equations and a time integration procedure for isotropic, hyperelastic-viscoplastic solids. *Computer Methods in Applied Mechanics and Engineering*, 79(2):173–202.

Wulfinghoff, S., Bayerschen, E., and Böhlke, T. (2014). Conceptual difficulties in plasticity including the gradient of one scalar plastic field variable. *PAMM*, 14(1):317–318.

Wulfinghoff, S. and Böhlke, T. (2012). Equivalent plastic strain gradient enhancement of single crystal plasticity: theory and numerics. *Proceedings of the Royal Society A: Mathematical, Physical and Engineering Sciences*, 468(2145):2682–2703. Publisher: Royal Society.

Xiao, H., Bruhns, O. T., and Meyers, A. (1998). On objective corotational rates and their defining spin tensors. *International Journal of Solids and Structures*, 35(30):4001–4014.

Xiao, H., Bruhns, O. T., and Meyers, A. (1999). Existence and uniqueness of the integrable-exactly hypoelastic equation $\overset{\circ}{\underset{\sim}{\tau}} = \lambda(tr\underset{\sim}{D})\underset{\sim}{1} + 2\mu\underset{\sim}{D}$ and its significance to finite inelasticity. *Acta Mechanica*, 138(1):31–50.

Yu, J.-S., Maniatty, A. M., and Knorr, D. B. (1997). Model for predicting thermal stresses in thin polycrystalline films. *Journal of the Mechanics and Physics of Solids*, 45(4):511–534.

Z-set (2022). Non-linear material & structure analysis suite. `www.zset-software.com`.

Zhang, Y., Lorentz, E., and Besson, J. (2018). Ductile damage modelling with locking-free regularised GTN model. *International Journal for Numerical Methods in Engineering*, 113(13):1871–1903.

Zheng, Q.-S. (1994). Theory of representations for tensor functions—a unified invariant approach to constitutive equations. *Applied Mechanics Reviews*, 47(11):545–587.

RÉSUMÉ

La simulation numérique par éléments finis des phénomènes de localisation de la déformation plastique s’accompagne en général d’une forte dépendance au maillage ainsi qu’aux algorithmes utilisés. Cette difficulté est liée au caractère mal posé du problème aux limites dans le cas d’un fort adoucissement à cause de la perte d’ellipticité des équations différentielles en jeu. L’enjeu principal de cette thèse est de proposer et d’implémenter une méthode systématique permettant de régulariser ce genre de simulations, en s’appuyant sur des théories à gradient. Cela nécessite une formulation cohérente et robuste intégrant l’élastoplasticité en transformations finies. La plupart des codes industriels et de recherche existants s’appuient sur des formulations hypoélastiques définies à l’aide des dérivées objectives. Ces lois, ne garantissant pas l’existence d’un potentiel d’élasticité, engendrent des artefacts vu leur caractère non-conservatif. La description de l’anisotropie, à l’aide de ces formulations, reste limitée vu que les axes d’anisotropie tournent avec le repère corotationnel en l’absence de la notion du taux de rotation des directeurs de la matière dû à la plasticité.

Nous proposons une méthode d’extension systématique des lois de comportement établies dans le cadre des petites déformations aux transformations finies. L’approche préconisée se base sur la décomposition multiplicative du gradient de la transformation et sur les principes de la thermodynamique des milieux continus. Les informations requises pour l’extension des lois formulées en petites déformations au cas général sont le choix d’un potentiel hyperélastique, un potentiel de dissipation viscoplastique, les types d’écrouissage et dans le cas anisotrope, l’évolution du taux de rotation des directeurs. Une comparaison systématique entre la formulation proposée et les modèles hypoelastiques a été menée dans le cas de plusieurs applications telles que la simulation de l’emboutissage et le fluage d’une aube de turbine.

La régularisation des modèles élastoplastiques en grandes déformations s’appuient sur la théorie des milieux micromorphes. Cette théorie se base sur l’introduction de longueurs caractéristiques associées à la dimension physique caractéristique des zones de localisation (taille de grain, espacement entre cavités, etc.). En effet, elle consiste à introduire des degrés de liberté supplémentaires indépendants associés à des variables internes du modèle classique. Cette approche peut être appliquée aux effets d’échelle dans le cas de la plasticité durcissante et à la localisation des déformations en plasticité adoucissante. Cela nécessite le choix des variables de plasticité, de nature scalaire ou tensorielle. Le choix de la nature du gradient (Eulérien, Lagrangien ou transporté sur la configuration intermédiaire) est étudié en grandes déformations. Le fait de considérer une formulation par rapport à la configuration intermédiaire introduit un terme d’écrouissage cinématique supplémentaire. L’approche micromorphe de la plasticité à gradient est comparée également à une approche de pénalité qui permet à travers des multiplicateurs de Lagrange d’imposer l’égalité (au sens faible) entre la variable locale et la variable micromorphe associée. Cette approche a été appliquée pour la simulation d’un composite à matrice polymère. Une longueur interne a été identifiée à travers les résultats expérimentaux issus d’un essai de compression transverse d’un composite unidirectionnel.

MOTS CLÉS

Transformations finies, décomposition multiplicative, thermo-élastoviscoplasticité, localisation de la déformation, la théorie micromorphe, longueur interne, régularisation, effets d’échelle.

ABSTRACT

The finite element simulation of plastic strain localization phenomena generally exhibits a strong dependency on the mesh and on the integration schemes. This difficulty is related to the ill-posedness of the boundary problem in the case of strong softening due to the loss of ellipticity of the considered differential equations. This thesis aims to propose and implement a systematic method to regularize such simulations, based on gradient theories. This requires a consistent and robust formulation for elastoplasticity at finite deformations. Most of the existing industrial and research FEM codes rely on hypoelastic formulations defined using objective derivatives. These formulations, for which the existence of an elastic potential is not guaranteed, lead to artefacts under complex cyclic loading conditions. The description of the anisotropy, using these formulations, remains limited because the axes of anisotropy spin with the corotational reference frame and the absence of the plastic spin notion.

We propose a systematic and thermodynamically consistent extension of small strain constitutive equations to finite strains. The proposed approach is based on the multiplicative decomposition of the deformation gradient. The required ingredients consist of a hyperelastic potential, a viscoplastic dissipation potential, internal variables for isotropic and kinematic hardening and in the anisotropic case, the plastic spin of the material’s directors. A systematic comparison between the proposed formulation and the hypoelastic models was carried out for several applications.

The regularization of elastoplastic models in large deformations is based on the theory of micromorphic media. This theory introduces characteristic lengths associated with the physical dimension associated to the microstructure (grain size, spacing between cavities, etc.). It consists in introducing additional independent degrees of freedom associated with the internal variables of the classical model. This approach can be applied to size effects in the case of hardening plasticity and to the localization of deformations in softening plasticity. This requires the choice of micromorphic variables, either scalar or tensorial. The choice of the gradient (Eulerian, Lagrangian or the gradient convected to the intermediate configuration) is studied in large deformations. The fact of considering a formulation with respect to the intermediate configuration introduces an additional kinematic hardening term. The micromorphic approach to gradient plasticity is also compared with a penalty approach that imposes a weak equality between the local variable and the associated micromorphic variable through Lagrange multipliers. This approach has been applied to the simulation of a polymer matrix composite. An internal length was identified through experimental results from a transverse compression test of a unidirectional composite.

KEYWORDS

Finite deformations, multiplicative decomposition, thermo-elastoviscoplasticity, strain localization, micromorphic theory, internal length, regularization, size effects.